



Passenger Vehicles with In-Wheel Motors: Fundamentals, Potentials and Limitations

by
Andrés Eduardo Rojas Rojas

Doctoral Thesis
submitted to the Faculty of Mechanical Engineering and Economic Sciences
Graz University of Technology
Austria

Tutor: Univ.-Prof. Dr.techn. Wolfgang Hirschberg
Institute of Automotive Engineering, TU Graz, Austria

Assessor: Prof. Dr.-Ing. Günther Prokop
Institute of Automotive Engineering, TU Dresden, Germany



Institute of Automotive Engineering

Member of
[FSI Frank Stronach Institute]

Graz, Austria, June 2012

Acknowledgement

The present thesis was developed as part of my work as scientific researcher at the Institute of Automotive Engineering at Graz University of Technology in Austria, in the context of a project in cooperation with MAGNA Powertrain AG & Co KG. Hereby I want to thank the persons who have significantly supported me and this work along these years.

My eternal gratitude goes to my parents María Orfa Rojas Losada and Jorge Eduardo Rojas Quintana and to my sister María Carolina Rojas Rojas for their everlasting love, unconditional support along my entire life, and for planting in my the seed of overcoming. Finally I would like to express my heartfelt gratefulness to my wife, Wilma Carolina Vargas Velandia, for her love, her tireless patience, her understanding, and for supporting me along this trip full of privations.

My most sincere thanks go to my tutor and mentor Univ.-Prof. Dr.techn. Wolfgang Hirschberg not only for his valuable technical advice and precise scientific orientation, but even more for his unconditional personal support, guidance and encouragement. His generous and straightforward supervising and leading style gave me the needed freedom not only to develop my own ideas related with this thesis, but also to explore other non-directly related fields which have surely shaped my way of thinking, strengthened my character and influenced my scientific and professional approach to the world. Furthermore, I want to thank him and his family for their valuable personal support given to my wife and to me as a foreign family in Austria. The present work would not have been possible without all his support.

I would also like to thanks Prof. Dr.-Ing. Gunther Prokop, director of the Institute of Automotive Engineering at Dresden University of Technology, for his disposition to serve as assessor of my work, for his interest in it and for the related meticulous discussion.

I am very grateful with my colleges at the Institute of Automotive Engineering for the professional discussions, for the great working atmosphere and for their support beyond technical aspects.

Many thanks are addressed to MAGNA Powertrain AG & Co KG, specially to Dipl.-Ing. Franz Gratzner and his team of the department of research and development, for supporting this research project.

Andrés Eduardo Rojas Rojas
Graz - Austria, June 2012

Abstract

As oil reservoirs are being depleted, new energy sources are needed in order to guarantee the mobility of future generations. From the current point of view, electric energy seems to be the most appropriate energy form to be used in vehicles. Furthermore, due to the new design possibilities that can be opened by using in-wheel motors, they are seen as a promising and visionary technology toward the electrification of vehicles. Nevertheless, in-wheel motors are related with a series of open questions that need to be solved before this technology can go into series production.

This thesis offers a systematic, founded and wide analysis of in-wheel motors for applications in electric passenger vehicles with the aim of giving answer to some of the open questions related with this technology. With the objective to determine the main characteristics of the battery as well as of induction and synchronous electric motors, an approach based on performance requirements given for different vehicle classes is introduced. Furthermore, the potentials and limitations of in-wheel motors to enhance the lateral vehicle dynamics are determined, and the effect of the related increased non-suspended masses on ride comfort and driving safety are extensively analyzed. Therefore, a theoretical approach complemented by the subjective perception of normal drivers and experienced test drivers while driving with a vehicle with increased non-suspended masses is introduced. Finally, a novel automated approach for the mechanical integration of in-wheel motors in modern single wheel suspension systems is presented.

Statutory declaration

I declare that I have authored this thesis independently, that I have not used other than the declared sources / resources, and that I have explicitly marked all material which has been quoted either literally or by content from the used sources.

Date: _____

Signature: _____

Contents

Acknowledgement	iii
Abstract	v
Nomenclature	xv
1. Introduction	1
1.1. Motivation	4
1.2. In-wheel motors: State of the art	6
1.3. Outline and objectives of this work	9
2. Simulation environment	13
2.1. Driver-vehicle-environment	13
2.2. Coordinate systems	15
2.3. General principles of linear and angular momentum for a moving body .	16
2.4. Vehicle model	18
2.4.1. Equations of motion for the suspended mass	18
2.4.2. Equations of motion for the non-suspended masses	21
2.4.3. Equations of motion for additional masses	23
2.5. Tire model	24
2.5.1. Model for the horizontal tire dynamics	25
2.5.2. Model for the vertical tire dynamics	32
2.5.3. Outputs of the tire model	40
2.6. Road model	40
2.6.1. Curved regular grid road with obstacles	40
2.6.2. Road roughness	41
2.7. Passive suspension system model	47
2.7.1. Suspension spring	48
2.7.2. Shock absorber	51

2.8. Model validation	56
3. Longitudinal dynamics	63
3.1. Equations of motion	63
3.2. Approaches toward the electrification of the vehicle powertrain	66
3.3. Driving cycles	67
3.4. Energy storage	70
3.4.1. Energy storage device	71
3.4.2. Energy and power demand in a driving cycle	72
3.4.3. Battery capacity and mass estimation	73
3.5. Electric motors	75
3.5.1. Torque-speed diagram of induction and synchronous motors	75
3.5.2. Weight of electric motors	77
3.5.3. Energy recuperation	78
3.5.4. Power balance	79
3.5.5. Maximum speed	81
3.5.6. Power defined climbing and acceleration ability	83
3.5.7. Elasticity	85
3.5.8. Determination of the electric motor torque and power characteristics	86
3.6. Power demand of auxiliaries for electric vehicles	87
3.7. Results	88
3.7.1. Considered vehicle classes	89
3.7.2. Powertrain architectures	90
3.7.3. General properties of the electric powertrain components	90
3.7.4. Performance requirements	92
3.7.5. Energy demand and needed battery mass	92
3.7.6. Dimensioning of electric motors	96
4. Lateral dynamics	105
4.1. Driving maneuvers	105
4.1.1. Step steer	106
4.1.2. Open-loop sinusoidal steering input	107
4.1.3. Open-loop frequency response	108
4.2. Control concept of a torque vectoring system for vehicles with in-wheel motors	110
4.2.1. Reference values generator	111
4.2.2. Horizontal dynamics controller	113

4.2.3.	Optimal longitudinal force allocation algorithm	117
4.3.	Results	122
4.3.1.	General maneuver conditions	122
4.3.2.	Step steer	127
4.3.3.	Open-loop sinusoidal steering input	129
4.3.4.	Open-loop frequency response	131
5.	Vertical dynamics	135
5.1.	Assessment of ride comfort and driving safety	135
5.1.1.	Ride comfort assessment	136
5.1.2.	Driving safety assessment	138
5.1.3.	Trade-off between ride comfort and driving safety	139
5.2.	Influence of increased non-suspended mass on ride comfort and driving safety	141
5.2.1.	Influence of the relation of the suspended to the non-suspended mass on the assessment criteria	142
5.2.2.	Subjective comfort assessment and correlation with simulation results	143
5.2.3.	Equivalence between the subjective ride comfort perception with increased non-suspended masses and increased tire inflation pressure	148
5.3.	Suspension systems to enhance the ride comfort and the driving safety .	150
5.3.1.	Passive suspension systems	150
5.3.2.	Semi-active suspension system	154
5.3.3.	Active suspension system	157
5.3.4.	Comparison	157
5.4.	Driving safety enhancement of vehicles with in-wheel motors through torque vectoring	161
5.4.1.	Maneuver definition	161
5.4.2.	Alternative driving safety assessment criteria	163
5.4.3.	Results	166
6.	Mechanical component integration	175
6.1.	Suspension characterization process and previous definitions	176
6.2.	Suspension Kinematics Optimization System - KOS	177
6.2.1.	Module 1: Reference values	180
6.2.2.	Module 2: Suspension system to be optimized	180
6.2.3.	Module 3: Suspension kinematics optimization	181

6.3. Application cases	184
6.3.1. Control blade suspension system	186
6.3.2. Double wishbone suspension system	187
7. Summary and conclusions	193
A. Appendix: Optimization methods and mathematics	199
A.1. Relative cumulative frequency	199
B. Appendix: Simulation environment	201
B.1. Vehicle parameters	201
B.2. Tire parameters	201
B.3. Road parameters	201
B.4. Single-mass oscillator model parameters	204
B.5. Passive suspension system parameters	205
C. Appendix: Longitudinal dynamics	207
C.1. Equations of motion for the longitudinal vehicle dynamics	207
C.2. Determination of the reduced moment of inertia	211
C.3. Driving cycles	212
C.3.1. ARTEMIS	212
C.3.2. HYZEM	212
C.3.3. INRETS	212
C.3.4. NEDC	213
C.3.5. FTP-75	213
C.3.6. Japan-10-15	213
C.3.7. Energy storage device	213
C.4. Electric motors	216
C.4.1. Induction motor	218
C.4.2. Synchronous motor	219
C.4.3. Comparison of the structural and operational characteristics of synchronous and induction motors	221
C.4.4. Efficiency of induction and synchronous electric motors	221
C.4.5. Comparison between the traction force diagrams of a vehicle with internal combustion engine and a vehicle with electric motor(s)	224
C.5. Power electronics	226
C.6. Dimensioning of electric motors: Four-wheel drive powertrain architecture	228

C.7. Weight of different electric vehicles (EV) in comparison with their counterparts with internal combustion engine (ICE)	228
D. Appendix: Lateral dynamics	231
D.1. Single track vehicle model	231
E. Appendix: Vertical dynamics	235
E.1. Frequency filter for the seat in vertical direction	235
E.2. Quarter vehicle model	236
E.3. Test drives with additional non-suspended masses	239
E.3.1. Device to increase the non-suspended masses for test drives . . .	239
E.3.2. Questionnaire to collect the subjective ride comfort perception of test drivers	239
F. Appendix: Mechanical component integration	243
F.1. Control blade suspension system	243
F.2. Double wishbone suspension system	244
Bibliography	247
List of Figures	271
List of Tables	283

Nomenclature

To facilitate reading this work, it was written using a self explaining text, i.e. the used variables are directly explained where they are defined. Nevertheless, the abbreviations, indexes and symbols have the meaning presented in the following unless something else is indicated directly where they are defined in the document body.

It must be highlighted, that, in this work, all variables are expressed in the international system of units unless something else is specified.

Notation

In this work, a logical structure to designate each variable was used. To determine the meaning of a certain variable, it would be necessary to search for the meaning of its symbol and of its index(es) separately. Furthermore, following notation is used to identify a single variable V :

$${}^1_2 V^5_3,$$

where the variable can be

V	...	a scalar magnitude or
\mathbf{V}	...	a vector or a matrix.

Additionally, the indexes are used for:

1	...	Maximum (max) or minimum (min); also used to refer to a specific
---	-----	--

- system (e.g. *semi* for the *semi-active* suspension system) or to a specific variable characteristic (e.g. *nominal* or infinity).
- 2 ... Coordinate system in which \mathbf{V} is defined.
- 3 ... Used to indicate the instance (e.g. body, direction, distance from a point P_1 to a point P_2 ($d_{P_1 \rightarrow P_2}$) or position) to which \mathbf{V} is related
- 4 ... Exponent, transposition mark T , inversion mark $^{-1}$ or characteristics like static S .
- 5 ... Reserved to e.g. derivative marks, mean values.

In the case two or more variables $V_k \dots V_n$ differ only in the instance they are referring to (i.e. k or n), only one variable is written using the notation $V_{k/\dots/n}$.

Abbreviations

Abbreviation	Meaning
ABS	Anti-lock B raking S ystem
AC	A ssessment C riterium, or A lternating C urrent (depending on context)
ARTEMIS	A ssessment and R eliability of T ransport E mission M odels and I nventory S ystems
AWD	A ll W heel D rive
CAD	C omputer A ided D esign
CG	C enter of G ravity
CNG	C ompressed N atural G as
CRG	C urved R egular G rid
CSP	C haracteristic S uspension P arameter
DC	D irect C urrent
DP	D esired D riving P erformance P arameter
EM	E lectric M otor
EV	E lectric V ehicle
ESP	E lectronic S tability P rogram
FTP	F ederal T est P rocedure
FWD	F our W heel D rive
GPS	G lobal P ositioning S ystem

Abbreviation	Meaning
GUI	G raphical U ser I nterface
ICR	I ntantaneous C enter of R otation
HYZEM	H Ybrid Z ero E mission M obility
ICE	I nternal C ombustion E ngine
IM	I nduction M otor
INRETS	I nstitut N ational de R echerche sur les T ransports et leur S écurité
KOS	Suspension K inematics O ptimization S ystem
MOVES ²	M Odular V ehicle S imulation S ystem
NEDC	N ew E ropean D riving C ycle
PC	P ersonal C omputer
OEM	O riginal E quipment M anufacturer
RAM	R andom A ccess M emory
RWD	R ear W heel D rive
SM	S ynchronous M otor <u>with permanent magnets</u>
SOC	S tate O f C harge
TRFE	T ire R oad F riction E stimator
TVS	T orque V ectoring S ystem
VDC	V ehicle D ynamics C ontroller

Frequently used indexes

Index	Meaning
0	Initial value
<i>aero</i>	Aerodynamic
<i>act</i>	Relative to the active mass of an electric motor, or relative to an active suspension system (depending on context)
<i>air</i>	Relative to the air
<i>assum</i>	Assumed quantity
<i>A</i>	Relative to the suspended mass
<i>Add</i>	Additional
<i>AP</i>	Attachment point
<i>Aq</i>	Relative to the quarter vehicle
<i>Aux</i>	Relative to the auxiliaries

Index	Meaning
<i>b</i>	Relative to the body or suspended mass
<i>b₀</i>	Relative to the limit of the linear behavior of the suspension spring in bound
<i>B</i>	Body or Braking action (depending on context)
<i>Batt</i>	Relative to the battery
<i>charge</i>	Relative to a situation in which the battery is charging
<i>clash</i>	Relative to a collision situation
<i>climb</i>	Relative to the climbing resistance
<i>comp</i>	Quantity to be compared
<i>cycle</i>	Relative to a driving cycle
<i>C</i>	Wheel center axis system
<i>C₀</i>	Relative to the limit of the region for low deflection speeds of the shock absorber in compression
<i>discharge</i>	Relative to a situation in which the battery is discharging
<i>dyn</i>	Dynamic
<i>d</i>	Relative to the shock absorber, or desired quantity (depending on context)
<i>demand</i>	Demanded quantity
<i>driving</i>	Relative to a driving condition
<i>D</i>	Driving action or dynamic (depending on context)
<i>DM</i>	Relative to the <i>damping mass</i> suspension system
<i>e</i>	Ellipse
<i>energy</i>	Relative to a variable determined based on energy considerations
<i>eq</i>	Equivalent
<i>ex</i>	Excess quantity
<i>E</i>	Earth-fixed axis system
<i>EM</i>	Relative to an electric motor
<i>f</i>	Relative to the front
<i>gearbox</i>	Relative to the gearbox
<i>generator</i>	Relative to a condition in which an electric motor is working as generator
<i>h</i>	Horizontal
<i>hs</i>	Relative to the distance from the vehicle's center of gravity to the position of the optic speed sensor
<i>h_{load}</i>	Half loaded condition

Index	Meaning
<i>i</i>	Counter for the wheels (unless something else is indicated)
<i>init</i>	Initial value
<i>inverter</i>	Relative to the inverter or the power electronics
<i>IM</i>	Relative to an induction motor
I_0	Relative to the lower limit of the linear region of the suspension spring
III_0	Relative to the upper limit of the linear region of the suspension spring
<i>j</i>	Counter
<i>k</i>	Counter, or relative to the kinetic energy (depending on context)
<i>l</i>	Relative to the left
<i>lat</i>	Relative to the lateral dynamics or to the lateral direction
<i>linear</i>	Linear behavior
<i>load</i>	Relative to a certain loaded condition
<i>loss</i>	Relative to energetic losses
<i>L</i>	Leveled axis system
<i>m</i>	Counter
<i>max</i>	Maximum
<i>mean</i>	Mean value
<i>min</i>	Minimum
<i>motor</i>	Relative to a condition in which an electric motor is driving
<i>mtvv</i>	Maximum transient vibration value
<i>n</i>	Counter, relative to the electric motor in nominal service, or normalized quantity (depending on context)
<i>needed</i>	Relative to a needed quantity
<i>nom</i>	Nominal or relative to nominal conditions
n_c	Relative to the exponential coefficient of suspension spring
<i>offer</i>	Offered quantity
<i>ol</i>	Relative to the electric motor in overload service
<i>om</i>	Order of magnitude
<i>p</i>	Counter
<i>peak</i>	Relative to a peak value
<i>pert</i>	Relative to a perturbation
<i>power</i>	Relative to a variable determined based on power considerations
<i>proj</i>	Projected

Index	Meaning
<i>r</i>	Relative to the rear or to the right (depending on context)
<i>recuperating</i>	Relative to a condition with energy recuperation
or <i>rec</i>	
<i>red</i>	Reduced
<i>ref</i>	Reference quantity
<i>res</i>	Reserve
<i>rmf</i>	Relative to the rotatory magnetic field
<i>rms</i>	Root mean square
<i>road</i>	Relative to the road
<i>roll</i>	Relative to the rolling resistance
<i>rot</i>	Relative to the rotor of an electric motor
<i>rrms</i>	Running root mean square
r_0	Relative to the limit of the linear behavior of the suspension spring in rebound
<i>R</i>	Random reference system
<i>RC</i>	Relative to the instantaneous roll center
<i>semi</i>	Relative to a semi-active suspension system
<i>sky</i>	Relative to the sky-hook control strategy
<i>specific</i>	Relative to a specific quantity
<i>stat</i>	Relative to the stator of an electric motor
<i>supp</i>	Relative to the power supply
<i>susp</i>	Relative to the suspension system
<i>syn</i>	Relative to the synchronous speed
<i>S</i>	Steady state or static (depending on context)
<i>SM</i>	Relative to a synchronous motor
<i>t</i>	Relative to the trajectory
<i>th</i>	Theoretical quantity
<i>tires</i>	Relative to the tires
<i>T</i>	Tire or relative to it
<i>TA</i>	Relative to the trailing arm
T_0	Relative to the limit of the region for low deflection speeds of the shock absorber in tension
<i>u</i>	Counter
<i>v</i>	Relative to the vehicle
<i>V</i>	Vehicle axis system

Index	Meaning
w	Wheel or frequency weighted quantity (depending on context)
ws	Relative to the suspension system of a wheel
W	Wheel contact point
\overline{W}	Road tangential axis system
x	Longitudinal direction
y	Lateral direction
z	Vertical direction
∞	Saturation value

Latin characters

Variable	Meaning
a_e	Parameter of the tire enveloping model
A	TMsimple coefficient related to the initial slope of the tire force, or area (depending on context)
b_e	Parameter of the tire enveloping model
b_{road}	Distance from middle road track to another one
B	TMsimple coefficient related to the saturation value of the tire force
c	Stiffness
c_b^*	Equivalent spring coefficient
C_d	Drag coefficient
C_l	Lift coefficient
$C_{mw \rightarrow p}$	Proportionality factor used for the equivalence between tire inflation pressure and increased non-suspended mass
C_s	Lateral drag coefficient
$\mathbb{C}_{T\omega}$	Function considering the <i>tire hardening</i> with the rotational speed
d	Distance or damping (depending on context)
dY_0	Initial slope of the tire force
e	Mass factor
E	Energy
f	Temporal frequency, or temporal natural frequency (depending on context)
f_{cu}	Cumulative frequency

Variable	Meaning
f_{OL}	Overload factor for an electric motor
f_{roll}	Rolling resistance coefficient
f_{κ_d}	Force factor in the non-linear region of the shock absorber
\mathcal{F}	Function
${}_V\widehat{F}_{A, x}$	Reference control longitudinal force at the center of gravity of the suspended mass
G	Transfer function
\mathbb{G}	Conversion factor for the slip angle
I	Inertia moment
j	Imaginary unit
J	Fitness function
K	TMsimple coefficient related to the maximum of the tire force
K_{F_x}	Gain parameter for the total longitudinal force ${}_V\widehat{F}_{A, x}$
K_I	Integral control parameter
K_P	Proportional control parameter
l_f, l_r	Distance from the vehicle's center of gravity to the front (f) and the rear (r) axle
l	Length
l_s	Length of the tire contact patch
${}^{susp}\Delta L$	Wheel base alteration
m	Mass
$m_{v_{running\ order}}$	Vehicle mass in running order according to [Com92]
$m_{EM\ total}$	Mass of all electric motors installed in a vehicle
M	Moment or torque
M_b	Breakdown torque of an electric motor
M_N	Total torque acting at the wheel hub
${}_V\widehat{M}_{A, z}$	Reference control yaw moment around the vertical axis of the suspended mass
n_p	Pneumatic trail
n_c	Exponential coefficient of the suspension spring
n_d	Exponential coefficient of the shock absorber
n_{FWR}	Exponential factor for the torque of the electric motor in the field weakening region
N_{EM}	Number of installed electric motors
O	Origin of a coordinate system

Variable	Meaning
\mathcal{O}	Overshoot
p	Road inclination in [%]
p_{EM}	Number of pole-pairs of an electric motor
p_T	Tire pressure
P	Arbitrary point, or power (depending on context)
\mathcal{P}	Coefficient related to the vertical tire model
$Q_{\Delta\beta}$	Weighting factor to prioritize the driving stability
$Q_{\Delta\psi}$	Weighting factor to prioritize the vehicle driving behavior
$Q_{\dot{\psi},ch}$	Yaw acceleration characteristic value
r	Tire radius
$^{susp}r_{\sigma}$	Scrub radius
$^{susp}r_{\tau}$	Caster offset
s	Traveled distance
s	Vehicle track
sl	Tire slip
$^{susp}\Delta s$	Track change
s^*	Generalized tire slip
t	Time
T	Time period, reaction time, or time delay (depending on context)
TB	Vehicle factor
T_o	Observation time
v	Horizontal vehicle speed
v^*	Transport speed
v_N	Artificial velocity
v	Arbitrary state variable
V	Voltage
w	Unevenness or waviness exponent
W_k, W_d, W_c	Frequency filters to obtain the frequency weighted acceleration
x	Longitudinal direction
X	Slip quantity
y	Lateral direction
$^{susp}y_{RC}$	Roll center transversal position
Y	Tire force quantity
Δy_{1s}	Deviation from reference trajectory one second after perturbation occurs

Variable	Meaning
z	Vertical direction
z	Amplitude of individual harmonic signals used to describe a road
z_e	Vertical position of a point in the ellipse used for the enveloping model
${}^{susp}z_{RC}$	Roll center height

Greek characters

Variable	Meaning
α	Slip angle
α_{road}	Road inclination (depending on context)
β	Sideslip angle
β_{sl}	Angle of the horizontal tire force vector
β_P	Shape coefficient of <i>J. G. Parchilowskij</i>
β_{wy}	Effective forward slope of the effective road surface
γ_d	Relation between the shock absorber forces during bound and rebound
γ_{road}	Coherence function of left and right road tracks
${}^{susp}\gamma$	Camber angle
δ	Difference or deviation (depending on context)
δ_{st}	Steering wheel angle
${}^{susp}\delta$	Toe angle
Δ	Difference or deviation (depending on context)
${}^{susp}\varepsilon$	Anti-dive angle
ζ	Arbitrary parameter related to the suspension movement
η	Efficiency
θ	Pitch angle
κ_d	Coefficient related to the force behavior in the non-linear region of the shock absorber during bound and rebound
κ_{road}	Correlation factor of <i>J. F. Parkhilowskij</i> for left and right road tracks
${}^{susp}\kappa$	Anti-squat angle
λ_{road}	Wave length of a road signal
μ	Friction coefficient
ξ_d	Damping ratio

Variable	Meaning
χ_{Fz_i}	Relation between the mean and the nominal value of the tire vertical contact force
χ_{wl_i}	Wheel load factor of wheel i
ρ_z	Effective vertical tire deflection
$^{susp}\sigma$	Kingpin inclination
τ	Time constant
$^{susp}\tau$	Caster angle
ϕ	Roll angle
φ	Phase angle or phase delay
Φ	Power spectral density of the road
Φ_{stat}	Magnetic flux in the stator
ψ	Yaw angle
ω	Angular or rotational velocity, or angular frequency (depending on context)
Ω	Angular spatial frequency

Matrices and vectors

Symbol	Meaning
$\mathbf{0}$	Zero matrix
\mathbf{A}	System matrix
\mathbf{B}	Input matrix
\mathbf{B}_c	Controllable input matrix
\mathbf{e}	Error vector
\mathbf{F}	General force vector
\mathbf{G}	Gravity vector
\mathbf{I}	Identity matrix or moment of inertia tensor (depending on context)
${}^v\mathbf{I}_{CG_A}$	Moment of inertia tensor for the suspended mass
\mathbf{J}	Jacobian matrix
\mathbf{K}_c	Controller matrix
\mathbf{M}	General moment vector
\mathbf{n}_{traj}	Unit vector perpendicular to the tangent to the reference trajectory
\mathbf{P}_{lat}	Solution matrix of the matrix Riccati equation
\mathbf{Q}_{lat}	Weighting matrix for the error in the state variables

Symbol	Meaning
\mathbf{r}	Position vector, or reference vector (depending on context)
$\widehat{\mathbf{R}}_{\beta}$	Three-dimensional map (matrix) for the steady state values of the sideslip angle
\mathbf{R}_{lat}	Weighting matrix for the controllable inputs
$\widehat{\mathbf{R}}_{\dot{\psi}}$	Three-dimensional map (matrix) for the steady state values of the yaw rate
\mathbf{u}	Input vector
\mathbf{u}_c	Controllable input vector
\mathbf{x}	State vector
\mathbf{y}	Vector of measured state variables

Considered vehicle classes

Vehicle classes definition according to [oE11].

Symbol	Vehicle class
A^-	Minicompact
A	Subcompact
B	Compact
D	Large

1. Introduction

The essential components for the use of electrical energy as driving energy source in vehicles were developed in the 19th century. The electric battery was invented by Alessandro Volta in the year 1800. The battery technology was then improved by Gaston Planté and Camille Faure in 1859 and 1881 respectively leading to the lead-acid battery [KS09]. Furthermore, the direct current motor (DC-motor) was invented by Joseph Henry in 1831. Using this inventions, Gustave Trouvé presented the first electric vehicle at the international exhibition of electricity in Paris in 1881 [Høy08] with a driving range of 26 km and a maximum speed of 12 km/h. One year later, W. E. Ayrton and J. Perry presented an electric tricycle (see figure 1.1) with a driving range of 40 km and a maximum speed of 14 km/h [Geo08].

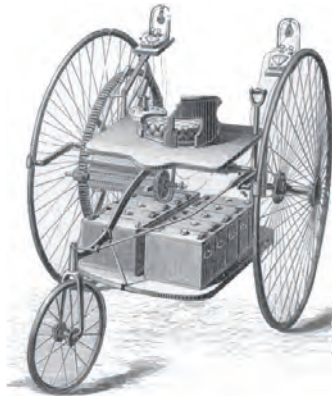


Figure 1.1.: Electric tricycle presented by W. E. Ayrton and J. Perry in 1882 [Geo08].

At the turn from the 19th to the 20th century approximately 38 % of all motorized vehicles in the United States of America were powered by electrical energy [Sov09] (see figure 1.2). They were highly valued because of its cleanliness (no emissions), low noise and vibration levels, simplicity and easy operation compared with vehicles powered by internal combustion or steam engines. Nevertheless, economical, political, socio-cultural and technical factors, particularly the huge amount of energy content of the

used fuels rather than the associated technology itself, inclined the balance toward the internal combustion engines. They became the most significant power source technology worldwide by the beginning of the 1940s. Furthermore, modern studies [She09, dB09] show that vehicles using only internal combustion engines as power source will account for just about 40 % of all vehicles worldwide in the year 2030. As can be seen in figure 1.2, all other vehicles will use electrical energy as primary or secondary driving energy source for the powertrain.

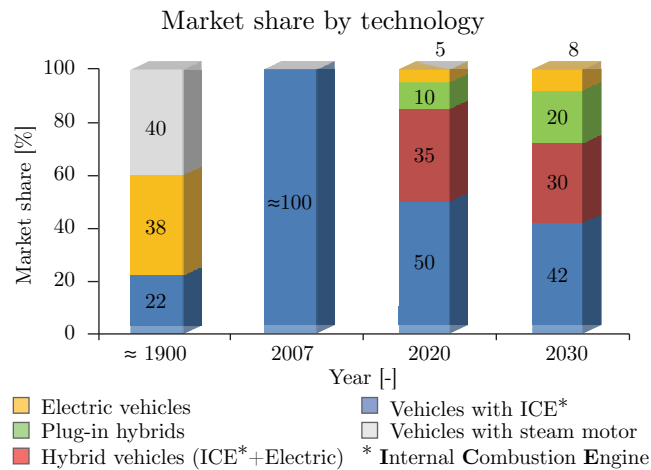


Figure 1.2.: Market share by technology at the turn from the 19th to the 20th century (see [Sov09]) and in the coming decades (see [She09] and [dB09]).

As can be deduced from figure 1.2, the internal combustion engine has been continuously developed for over hundred years. Since its invention, its efficiency has been nearly doubled and the specific fuel consumption¹ has, therefore, been reduced. Nevertheless, further efficiency improvements and fuel consumption reductions can be hardly anticipated since they are related with exponentially growing technological efforts that are getting closer to the economically reasonable limits. Moreover, as can be seen in figure 1.3, even according to the most optimistic scenarios the crude oil production world wide will reach its maximum somewhen in the next two decades. These facts together with volatile oil prices, increased environmental sensitivity and political concerns have moved the attention of governments, automobile manufacturers and customers to alternative powertrains. Some of the most promising concepts for future vehicles are based on the conversion of electrical into mechanical energy [WFO09].

Since there are several technical, political and economical aspects that must be cleared

¹Defined as the fuel consumption per unit of power [l/kW] (see e.g. [Pis04]).

Prognosis of world crude oil production in the 21st century

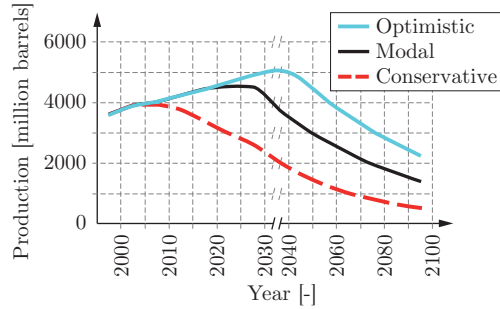


Figure 1.3.: Oil production forecast worldwide (see [MC09] and [Kon09]).

on the way toward the "re"-electrification of vehicles, hybrid technologies comprising an internal combustion engine working together with one or more electric machines (as motor or generator) have been being developed since several decades. Depending on how the internal combustion engine and the electric motor(s) are connected and how they provide the power to move the vehicle, hybrid powertrains can be classified in series, parallel or mixed. Additionally, depending on the relation between the power provided by the internal combustion engine and the power provided by the electric motor(s), it can be distinguished between micro, mild and full hybrids. Further information on these classifications can be found in [Hof09] and [Kel10]. Furthermore, as schematically presented in figure 1.4, hybrids can be seen as an intermediate step between the mature internal combustion engine technology and the upcoming clean² and more efficient electric vehicles. Nevertheless, as shown in figure 1.2, it can be expected that internal combustion engines, hybrids and electric vehicles will coexist in the future to cope with the different mobility demands of the coming generations.

There are different powertrain configurations for pure electric vehicles (see also [KSS11]). The most representative ones are presented schematically in figure 1.5. With one electric *central motor*, a differential is used to transmit the power to the wheels of an axle. If more than one electric motor is considered, two alternatives arise. On the one hand, it is possible to place the electric motors directly on the suspended mass and use shafts to transmit the power to the wheels. On the other hand, the electric motors can be placed directly within the wheel. This leads to the concept of *in-wheel motors* this work focuses on.

²Based on a *tank-to-wheel* analysis. In comparison, in a *well-to-wheel* analysis, the emissions of electric vehicles depend on the mixture of primary energy sources used to generate the electric energy [Wei08].

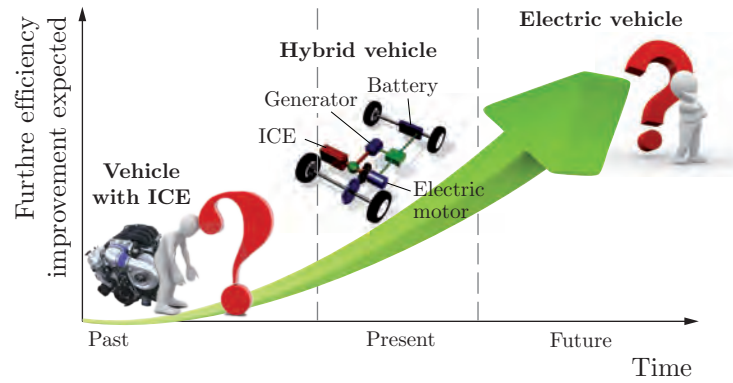


Figure 1.4.: Development and establishment of technologies on the way toward the vehicle electrification.

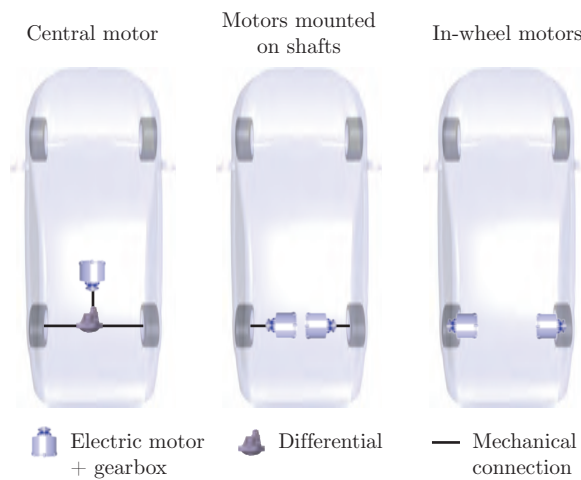


Figure 1.5.: Electric powertrain architectures (rear wheel drive is shown exemplarily).

1.1. Motivation

In-wheel motors are an old idea as well as a visionary solution for future powertrains and an interesting concept toward vehicle electrification that provides also high potentials to improve vehicle dynamics and handling (see e.g. [RNH11], [RNW11a], [HEG11] and [LSW00]). Nevertheless they are related with a series of open questions needing further research and technical development to be answered (see e.g. [RNH11], [RNW10], [RNW11a], [RA11], [GFH10] [GHKP12]). A summary of both advantages and open questions is presented in table 1.1 (see also [RNH11] and [RNW11a]).

In-wheel motors constitute the shortest possible powertrain. In comparison with a con-

Table 1.1.: Advantages and open questions related with in-wheel motors in comparison with a traditional powertrain architecture with internal combustion engine.

Advantages	Open questions
Visionary solution for future powertrains	Higher non-suspended masses ^a
Shortest possible powertrain	Packaging within the rim ^b
Less mechanical components	Fail safe behavior ^c
New passenger cell design possibilities	Cooling system ^d
Higher powertrain efficiency	Difficult operation environment for motor
More degrees of freedom for design	Complex control of individual motors ^e
Well suited for additional functionalities ^f	Higher production costs at present

^a Dealt with in chapter 5.

^b Dealt with in chapter 6.

^c See e.g. [NDR11], [NDR11].

^d See e.g. [Wil11].

^e Dealt with in section 4.2 of chapter 4.

^f For example **Torque Vectoring** (see section 4.2 of chapter 4 and also section 5.4 of chapter 5) or **All-Wheel Drive**.

ventional powertrain architecture with central motor (see figure 1.5), less mechanical components are needed and some electric components are added (battery, inverter, electric motors). Due to the higher efficiency of the used components (see chapter 3), the entire efficiency of the powertrain can be improved. While the tank to wheel efficiency of a conventional powertrain is about 20 % [Gös08], that of an electric vehicle with in-wheel motors amounts approximately 80 % [NBW06] (depending on the driving cycle and driving conditions). Furthermore, since much less mechanical components are needed to connect the power source with the wheels, new possibilities for the design of the passenger cell and for placing the electric components are opened. In addition, by integrating the propulsion system and maybe other functions (e.g. steering system as presented in [Nie11], [Nie10], [NR10b] and [NDR11]) in the wheel, some simplifications in the assembly line can be expected. It must be also noticed, that since the mechanical connection between the wheels of an axle disappears, in-wheel motors introduce additional degrees of freedom into the system *vehicle*. This makes concepts using in-wheel motors well suited to implement functionalities like torque vectoring (see section 4.2 and also e.g. [RND11], [NLER11] and [Nie11]; compared with a mechanical system e.g. in [SBRH11]), all-wheel-drive, electronic stability control, ABS (see e.g. [RKuML11])

or hill start aid.

However, in-wheel motors are also related with some open questions like the effect of the increased non-suspended masses on ride comfort (see chapter 5 and also e.g. [RNW10] and [RNH11]) and driving safety (see chapter 5 and also e.g. [RND11]), the mechanical integration of the components in the wheel (see chapter 6 and also e.g. [RNA11a], [RN11], [RNA11b] and [Apo10]) and the fail-safe behavior (see e.g. [RND11], [Nie10], [NDR11], [EBMG10], [JW06] and [KTSY07]). Moreover, since in-wheel motors are placed directly within the rim, they are exposed to strong environmental working conditions comprising, for example, mechanical vibrations induced by the road unevenness, an abrasive atmosphere (e.g. dust and water) or difficult cooling conditions for the electric components (see e.g. [Wil11]). Furthermore, complex algorithms are needed to control the additional degrees of freedom introduced by in-wheel motors³ and effectively profit from their advantages (see section 4.2 in chapter 4 as well as e.g. [Nie11], [JA08], [JAJT10], [AB06], [And07], [BA06] and [FAL04] and [AKB06]). Finally, due to the fact that in-wheel motors and other components needed for their operation (e.g. battery) are still being developed, they are related with high production costs. Nevertheless, cost reductions can be expected if the production rises. However, to provide beneficial conditions for series production, the open questions related in table 1.1 must be answered. Some of these aspects are analyzed in this work and some solutions are presented (see section 1.3).

1.2. In-wheel motors: State of the art

In-wheel motors were widespread at the beginning of the automotive history. In 1889, Ferdinand Porsche developed a pure electric vehicle with two in-wheel motors mounted on the front wheels (see figure 1.6). This vehicle was able to reach a maximum speed of 50 km/h and the used lead-acid battery provided a range of approximately 50 km (see e.g. [Hof09]). Porsche's technology was applied in different vehicle concepts ranging from series hybrid racing cars (see [Gom07]) over series hybrid four-wheel drive vehicles (see e.g. the "*Mixte*" in [Hof09]) up to commercial vehicles (see e.g. [KA10]). Because of the degrees of freedom in-wheel motors introduce into the system *vehicle*, they were also selected as main components for the powertrain of the *lunar roving vehicle* used by the NASA for the lunar missions at the beginning of the 1970s [WJ02]. A summary of

³Wheels of an axle are not mechanically connected any more.

recent concepts and research activities in the field of in-wheel motors for automotive applications is presented in tables 1.2 and 1.3, from which the *Advanced Dynamic Damper Motor* prototype of Bridgestone, the *Active Wheel* prototype of Michelin, the *eCorner* concept of Siemens VDO, and the *Autonomous Corner Module* concept of Volvo can be highlighted (see figure 1.7). As presented in tables 1.2 and 1.3, some of these mentioned concepts not only include the traction and electric braking support functions made possible by the in-wheel motors but also additional functions that arise through the integration of other mechatronic systems within the wheel (like the steering, the brake and/or suspension system). The wheel acquires a new meaning, for which the term *corner module* is used (see e.g. [Zet02], [Jon07] and [Nie11]).



Figure 1.6.: Lohner-Porsche "Semper Vivus": Pure electric vehicle with two DC-in-wheel motors mounted on the front wheels.

The *Advanced Dynamic Damper Motor* prototype of Bridgestone (see e.g. [MTI⁺06] and [NIT08]) represent the simplest stage of a mechatronic *corner module*. With the aim of enhancing riding comfort and driving safety, the in-wheel motor is suspended on the wheel carrier by a spring and damper suspension system (see the *damping mass* concept in section 5.3.1). The torque is transmitted to the wheel through a flexible coupling.

In contrast, the in-wheel motor is coupled rigidly with the wheel in the *Active Wheel* prototype of Michelin (see [BDD⁺06], and [LSW00]). Aiming to improve ride comfort and driving safety, this prototype additionally integrates an active suspension system (see also section 5.3.3).

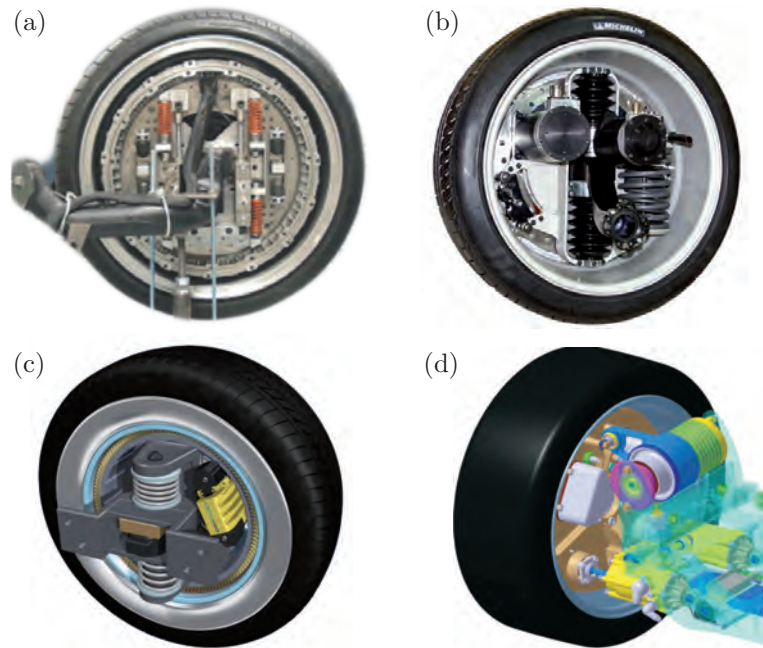


Figure 1.7.: Representative research and development projects in the field of electro-mechanical corner modules: (a) the *Advanced Dynamic Damper Motor* prototype of Bridgestone (see [MTI⁺06] and [NIT08]), (b) the *Active Wheel* prototype of Michelin (see [BDD⁺06], and [LSW00]), (c) the *eCorner* concept of Siemens VDO (see [Gom07] and [Gom10]), and (d) the *Autonomous Corner Module* concept of Volvo (see [Zet02] and [Jon07]).

The *eCorner* of Siemens VDO (see [Gom07] and [Gom10]) additionally includes an electric single wheel steering system and a mechatronic brake (*Electronic Wedge Brake* [GG06]). Nevertheless, it is still in the concept stage and only the in-wheel motor and the mechatronic brake system have been presented as prototypes.

Additionally to the functions integrated by the approaches outlined before, the *Autonomous Corner Module* concept of Volvo (see [Zet02] and [Jon07]) further includes a mechatronic system to actively change the camber angle. This concept constitutes the utmost stage within the *corner module* family.

As can be observed in tables 1.2 and 1.3 (see also [Gom07]), not only several Original Equipment Manufacturers (referred in the following as OEMs) are investing efforts in the research and development of in-wheel motors. Due to the multiple advantages of this technology (see table 1.1), also scientists at different universities and research institutions throughout the world are interested in giving answer to the open questions

related with it. The Japanese *Keio University* as well as the German *Fraunhofer Institute*, *German Aerospace Center (DLR)*, *University of Applied Sciences Offenburg* and *University of Paderborn* have developed research prototypes. The North American *Massachusetts Institute of Technology* goes a little bit further and develops a whole new idea of mobility for the 21st century based on vehicles with in-wheel motors including rational use of materials, intelligent car sharing concepts, innovative traffic solutions and ownership models.

This huge landscape of recent research activities reflects the high potentials of in-wheel motors. Nevertheless, the fact that there is still no series production evidences, at the same time, a big lack on knowledge regarding in-wheel motors.

1.3. Outline and objectives of this work

The approaches presented in this work aim to give a founded answer to some of the open questions summarized in table 1.1 that are directly related with the mechanical integration of in-wheel motors in electric passenger vehicles. The advantages and limitations related with in-wheel motors are analyzed based on simulations. In the case of the effect of increased non-suspended masses on ride comfort, the simulation results are complemented and compared with field experiments. As result of the presented analysis, fundamental knowledge as well as some practical solutions are offered as basis for the further development of in-wheel motors for passenger vehicles on the way toward series production. Due to the different physical effects that characterize commercial vehicles (see e.g. [HSA⁺08]), a direct extrapolation of the approaches and results presented in this work is not recommended.

After this introductory chapter, the simulation environment developed as basis for the analysis of vehicles with in-wheel motors is presented in chapter 2. The modeling approach used for the vehicle, the tire, the road and the passive suspension system as well as the model validation is presented in detail.

In chapter 3, the longitudinal dynamics of vehicles with in-wheel motors is analyzed. The key aspect in this chapter is the definition of the characteristics of the electric motors and the battery as main electric components of a vehicle with in-wheel motors. Therefore, two optimization approaches are presented and used to determine the motor and battery characteristics for vehicles belonging to different vehicle classes. Further-

more, the estimated weight of the electric motors is used as basis for the analysis of the effects of the increased non-suspended masses presented in chapter 5.

Chapter 4 focuses on the vehicle lateral dynamics of electric vehicles with in-wheel motors. A control strategy for a torque vectoring system for vehicles with in-wheel motors is presented. The potentials and limitations of this system to enhance handling and safety of vehicles with in-wheel motors are analyzed.

The effect of the increased non-suspended masses is analyzed in chapter 5 both from the theoretical objective and the subjective point of view. This analysis gives a founded insight into what is considered to be the most critical and criticized aspect related with the in-wheel motors, i.e. the effect of increased non-suspended masses on ride comfort and driving safety. Moreover, selected alternative passive suspension systems as well as semi-active and active ones are analyzed with the aim of giving a basis for the decision making regarding possible measurements to enhance driving safety and ride comfort of vehicles with in-wheel motors. Finally, the potentials and limitations of the torque vectoring system introduced in chapter 4 to enhance the driving safety of vehicles with in-wheel motors are presented.

Before presenting the summary and conclusions in chapter 7, an approach for the mechanical integration of in-wheel motors in different single wheel suspension systems is introduced in chapter 6. This approach changes the position of the suspension hard-points aiming, on the one hand, to keep the driving behavior of the vehicle in which the in-wheel motors must be integrated, and to avoid collisions between the components, on the other hand. The integration of in-wheel motors into a control blade suspension system and into a double wishbone suspension system for rear axles is presented as representative application scenario.

1.3. Outline and objectives of this work

Table 1.2.: Recent concepts and research activities in the field of in-wheel motors for automotive applications in **Asia** and **North America**.

Company or institution	Project name ^a	Powertrain ^b	E-Components ^c	State ^d	Source	
Asia	Mitsubishi	MIEV ^e (2005)	EV	P	Pt	[TYSS06]
	Bridgestone	ADM ^f (2004)	n.a.	P, B	Pt	[MTI ⁺ 06] [NIT08]
	Nissan	Pivo (2005)	EV	P, St	Pt	[Aso08] [Nis]
	KIA	Fuel Cell EV Platform	FC	P	Pt	[KIA]
	Honda	FCX (2005)	FC	P	Pt	[Hon]
	Toyota	Fine N (2005)	FC	P, St	C	[Gom07]
		Supra HR-V (2007)	PH	P	Pt	[Hof09]
	Keio University	Luciole, Eliica (1997, 2004)	EV	P	Pt	[Shi05] [KTSY07]
North America	General Motors	Autonomy, Hy-wire, Sequel (2002, 2002, 2005)	FC	P, Su, St, B	C, C, Pt	[BBS08]
	TM4	Wheel motor	n.a.	P	Pt	[TM4]
	MIT ^g	Hiriko CityCar (2006)	EV	P, St	Pt	[MBBB10]

^a If known, date of introduction of initial concept is indicated.

^b **EV**: Electric vehicle, **SH**: Series hybrid, **PH**: Parallel hybrid, **XH**: Mixed hybrid, **FC**: Fuel cell, **FH**: Full hybrid, -: Classification criterium does not apply.

^c Mechatronic components included, as **P**: Powertrain, **Su**: Suspension system, **St**: Steering system, **B**: Brake system.

^d Development state indicated as **Pt**: Prototype, **C**: Concept, **s-ft**: Small series production or fleet tests.

^e **M**itsubishi **I**nnovative **E**lectric **V**ehicle.

^f **A**dvanced **D**ynamic **D**amper **M**otor.

^g **M**assachusetts **I**nstitute of **T**echnology.

Table 1.3.: Recent concepts and research activities in the field of in-wheel motors for automotive applications in **Europe**.

Company or institution	Project name ^a	Powertrain ^b	E-Components ^c	State ^d	Source
KTH Royal Institute of Technology /	Autonomous Corner Module (2002)	n.a.	P, Su, St, B	C	[Zet02] [Jon07]
Volvo	Recharge (2007)	SH, FH	P	Pt	[Vol]
Michelin	Active wheel, Hy-Light (2004)	n.a., EV	P, Su	s-ft	[BDD ⁺ 06] [LSW00]
PML Flightlink	Hi-Pa Drive	n.a.	P	s-ft	[Pro]
Fiat	Downtown (1993)	FC	P	C	[Cor08]
Siemens VDO	eCorner (2006)	n.a.	P, Su, St, B	C	[Gom07] [Gom10]
Volkswagen	twinDRIVE (2008)	XH	P	Pt	[HLSB08] [Hof09]
ZF Friedrichshafen	Axle AVE 130 for buses	n.a.	P	s-ft	[Hof09]
Fraunhofer-Institute	Frecc0 (2010)	EV	P	Pt	[GHKP12] [KH11]
Schaeffler	eWheelDrive (2010)	n.a.	P	C	[GFH10]
Industrie-service Just	Scheibenläufermotor (2008)	n.a.	P	C	[Bes09]
Hochschule Offenburg	In-wheel motors (2006)	n.a.	P	Pt	[KWLH10]
eTraction	TheWheel TM	n.a.	P, Su, St, B	Pt	[Hei01] [eTr]
DLR ^e	Romo	EV	P, St	Pt	[BHS ⁺ 11] [SBBH11]
TU Paderborn	X-by-Wire Demonstrator	EV	P, Su, St, B	Pt	[NJT08]

^a If known, date of introduction of initial concept is indicated.

^b **EV**: Electric vehicle, **SH**: Series hybrid, **PH**: Parallel hybrid, **XH**: Mixed hybrid, **FC**: Fuel cell, **FH**: Full hybrid, -: Classification criterium does not apply.

^c Mechatronic components included, as **P**: Powertrain, **Su**: Suspension system, **St**: Steering system, **B**: Brake system.

^d Development state indicated as **Pt**: Prototype, **C**: Concept, **s-ft**: Small series production or fleet tests.

^e German Aerospace Center (**D**eutsches **Z**entrum für **L**uft und **R**aumfahrt).

2. Simulation environment

2.1. Driver-vehicle-environment

The simulation environment **MO**dular **V**ehicle **S**imulation **S**ystem - MOVES² - has been developed at the Institute of Automotive Engineering of Graz University of Technology in the frame of the present research project. It is a modular and flexible platform to model and simulate the entire driver-vehicle-environment system (see figure 2.1) with different model complexities and modeling depths according to the task being currently analyzed (see [RNFD11]). Models with different complexity at component (see e.g. [NDR11], [RNW10] or [RNW11b]), system see e.g. ([Mar09] and [Nie11]) and vehicle level (see e.g. [KK12]) can be simulated.

The vehicle is assumed to be composed of a suspended and non-suspended bodies (wheels). As a central element between the vehicle and the road, the horizontal and vertical dynamics of the tires are also modeled (see [RNW10] and [RND11]). It is also possible to consider several bodies attached directly or via a suspension system (spring and/or damper) to the suspended mass (see [Mar09]). The effect of the axle kinematics on the vehicle dynamics for different axle systems can be taken into account thanks to the *Kinematics Optimization System - KOS* - module (see chapter 6 as well as [RNA11b], [RNH11], [RNA11a] and [RN11]). Furthermore, several subordinated control systems (e.g. ABS, ESP or a *Vehicle Dynamics Control System* [Nie11]) as well as different sensors and actuators (see e.g. [RNW10], [RND11], [NLER11], [NDR11], [NRD11], [RNW11b], [NR10a] and [LEH11]) can be implemented.

Within the simulation environment, it is possible to simulate standardized open-loop and closed-loop maneuvers (e.g. double lane change, step steer, constant radius cornering, J-turn) as well as to create new maneuvers using an implemented *maneuver builder* (see [Fer11]). These maneuvers are characterized by speed and trajectory profiles as functions of time or displacement. To follow these profiles, a flexible driver model structure split in

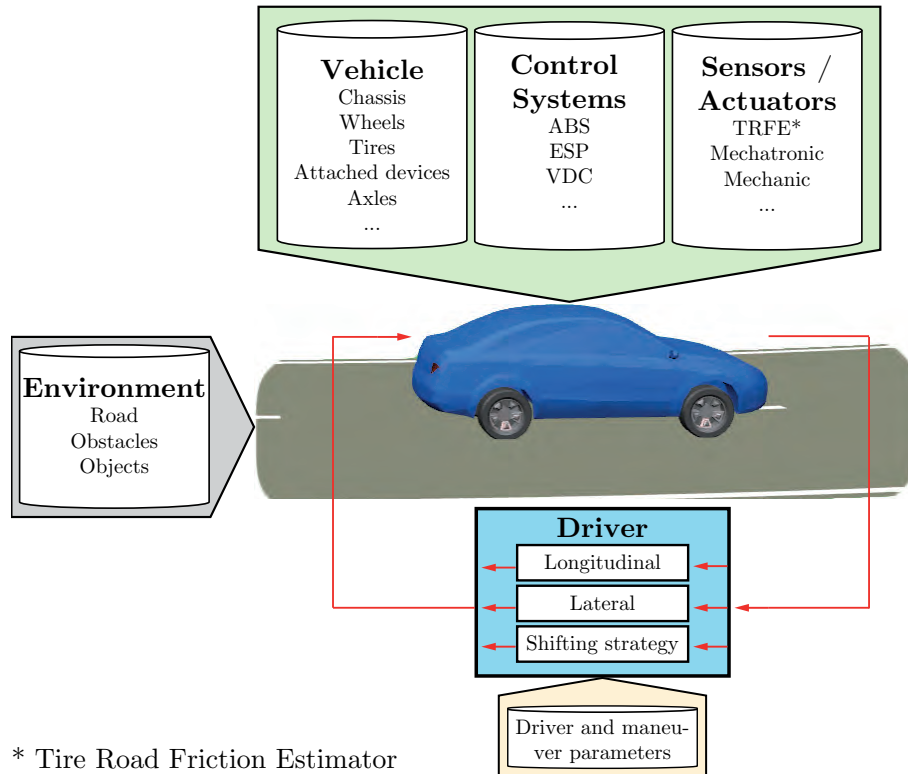


Figure 2.1.: Driver-vehicle-environment system (control loop).

different longitudinal and lateral controls as well as in a shifting strategy is implemented (see [Nie11], [MW04], [PE07] and [EPRT07]).

The road is the most important aspect concerning the environment. It is composed by a series of straight and curved elements with certain roughness, friction coefficients and road obstacles (e.g. bumps or sinusoidal perturbations) as well as different slope and banking attributes (see [RNW10], [Fer11]). Furthermore, using the implemented *scenario builder*, it is also possible to place static objects (e.g. cones, trees, houses or other static vehicles) on or beside the road [Fer11].

The results can be visualized during and/or after the simulation in a virtual reality environment (see [Fer11]). Due to the real-time capability of the models, they are suitable to be used, for example, in driving simulators or for rapid control prototyping. Furthermore, since the entire driver-vehicle-environment can be simulated, it is also possible to analyze the effectiveness of driver assistance systems (see e.g. [NLER11]). Co-simulation with other simulation environments is also possible (see [NDR11]).

Due to the high relevance for this work, the vehicle, tire and road model will be described more in detail in the following sections. For other topics mentioned to be related with the driver-vehicle-environment system, the reader is referred to the literature. The presented models have been validated based on measured data obtained with the test vehicle (*Opel Combo 1.6 CNG*) and are presented in [Dür11], [RNW10] and [Mar09].

2.2. Coordinate systems

Figure 2.2 shows the different orthogonal right-handed coordinate systems, based on the German standard DIN 70000 [fN94], used to describe the vehicle movement. The left subscript indicates the coordinate system to which an axis is referred to or on which a variable is defined.

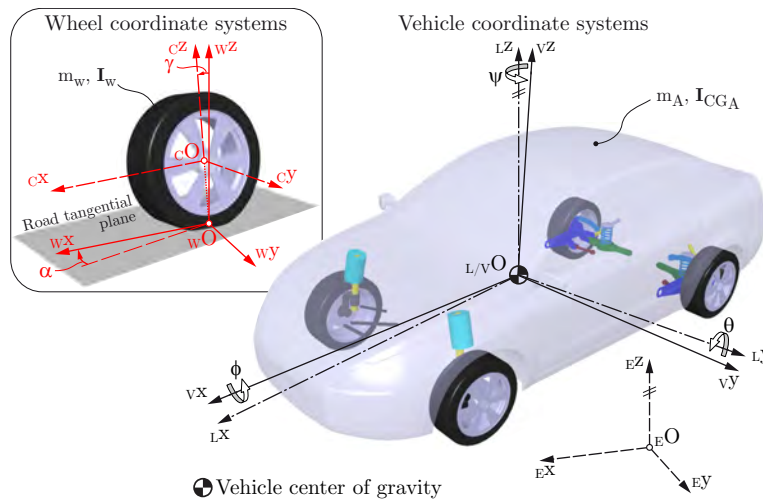


Figure 2.2.: Vehicle and wheel coordinate systems (based on the German standard [fN94]).

Earth-fixed axis system $\{E O; E x, E y, E z\}$

Inertial coordinate system. The $E z$ axis is directed upwards.

Leveled axis system $\{L O; L x, L y, L z\}$

This coordinate system moves with the vehicle body. Its origin $L O$ is placed on the vehicle center of gravity $C G$, its $L z$ axis is parallel to the $E z$ axis and its $L x$ is directed to the front of the vehicle, so that $L x$ and $V x$ (see vehicle axis system) are always in a vertical plane.

Vehicle axis system $\{_V O; _V x, _V y, _V z\}$

Coordinate system fixed to the suspended mass. The origin $_V O$ is placed at the vehicle center of gravity CG , the $_V x$ axis is directed to the vehicle front and the $_V z$ axis upwards. The angular position of the vehicle axis system results from the successive (ordered) *partial* rotations around the $_E z$ axis (yaw movement), the $_L y$ axis (pitch movement) and $_V x$ axis (roll movement), which result in the *Cardan* angles with modified sequence of rotation ψ, θ, ϕ (see [Hir09a] and [fN94]).

Wheel center axis system $\{_C O; _C x, _C y, _C z\}$

Non-rotating coordinate system whose origin $_C O$ is placed on the center of the wheel and whose $_C x - _C z$ plane is parallel to the wheel circumference.

Wheel axis system $\{_W O; _W x, _W y, _W z\}$

Non-rotating coordinate system whose origin $_W O$ is placed at the contact point W between the tire and the road and whose $_W x - _W y$ plane is parallel to the road tangential plane (see figure 2.7).

Road tangential plane axis system $\{\overline{W} O; \overline{W} x, \overline{W} y, \overline{W} z\}$ (not depicted in figure 2.2)

Non-rotating coordinate system whose origin $\overline{W} O$ is always located on the road tangential plane¹ (see figure 2.7), its $\overline{W} x$ axis is parallel to the $_W x$ axis and its $\overline{W} z$ axis is collinear with the $_W z$ axis. This axis system is mainly used by the model for the vertical tire dynamics (see chapter 2.5.2).

Assumption 2.1: *In this work, the camber angle is neglected. Consequently, the axes $_W z$ and $_C z$ are assumed as collinear and $_W y$ and $_C y$ as parallel.*

2.3. General principles of linear and angular momentum for a moving body

The general principles of linear and angular momentum for a body B describing both a translational and a rotational movement in space under the influence of external forces and moments can be written respectively as:

¹In this work, the road tangential plane is assumed to be the base flat road without any unevenness (see figure 2.7).

$$\sum {}_R\mathbf{F} = m_B \cdot {}_R\mathbf{a}_{_B O}, \quad (2.1)$$

$$\sum {}_B\mathbf{M} = {}_B\mathbf{I} \cdot {}_B\dot{\boldsymbol{\omega}} + {}_B\boldsymbol{\omega} \times {}_B\mathbf{I} \cdot {}_B\boldsymbol{\omega}, \quad (2.2)$$

where the equation for the linear momentum is written in a general form in an arbitrary reference coordinate system $\{{}_R O; {}_R x, {}_R y, {}_R z\}$, and the sum of moments in the equation of angular momentum is referred to the origin of the body coordinate system ${}_B O$. Moreover, m_B is the mass of the body and ${}_B\mathbf{I}$ denotes the moment of inertia tensor of the body in the coordinate system B attached to it. The angular velocity and angular acceleration of the body correspond to ${}_B\boldsymbol{\omega}$ and ${}_B\dot{\boldsymbol{\omega}}$ respectively. The acceleration of the center of gravity CG of the body in the reference coordinate system is indicated with ${}_R\mathbf{a}_{_B O}$, since it is assumed, that the origin of the coordinate system of the body ${}_B O$ coincides its center of gravity.

Furthermore, the acceleration ${}_R\mathbf{a}_P$ of any static or moving² point P of the body can be described in the reference coordinate system in a general way as (see [BJ88]):

$$\begin{aligned} {}_R\mathbf{a}_P = {}_R\mathbf{a}_{_B O} + \underbrace{{}_R\dot{\boldsymbol{\omega}} \times {}_R\mathbf{r}_{_B O \rightarrow P} + {}_R\boldsymbol{\omega} \times {}_R\boldsymbol{\omega} \times {}_R\mathbf{r}_{_B O \rightarrow P}}_{{}_R\mathbf{a}_{P^*}} + \\ \underbrace{2 \cdot {}_R\boldsymbol{\omega} \times {}_R\dot{\mathbf{r}}_{_B O \rightarrow P}}_{{}_R\mathbf{a}_{cor}} + \underbrace{{}_R\ddot{\mathbf{r}}_{_B O \rightarrow P}}_{{}_R\mathbf{a}_{P \setminus B}}, \quad (2.3) \end{aligned}$$

where ${}_R\mathbf{a}_{_B O}$ indicates the acceleration of the origin of the body coordinate system ${}_B O$ (coincident with the center of gravity of the body) in the reference coordinate system ${}_R O$, ${}_R\mathbf{a}_{P \setminus B}$ represents the acceleration of the point P as seen from the body coordinate system ${}_B O$ but described in the reference coordinate system ${}_R O$, ${}_R\mathbf{a}_{cor}$ is the Coriolis acceleration and ${}_R\mathbf{a}_{P^*}$ stands for the acceleration (described in the reference coordinate system) of a point P^* belonging to the body that, at the considered instant, coincides with the point P moving relative to the body B . Furthermore, ${}_R\mathbf{r}_{_B O \rightarrow P}$, ${}_R\dot{\mathbf{r}}_{_B O \rightarrow P}$ and ${}_R\ddot{\mathbf{r}}_{_B O \rightarrow P}$ correspond to the position, velocity and acceleration vectors of the point P as seen from the body coordinate system ${}_B O$ but described in the reference coordinate system ${}_R O$.

²The movement of the point P can also be described in its own coordinate system ${}_P O$.

2.4. Vehicle model

In this chapter, the equations of motion of the suspended body, the non-suspended bodies (wheels) and the additional bodies attached to the suspended one by a suspension system are presented. In the following, the word *mass* is used to refer to the different bodies *body* for a better understanding throughout this work. Details regarding, for example, the influence of the suspension kinematics are presented by *Dürnberger* [Dür11].

2.4.1. Equations of motion for the suspended mass

In this section, the equations of motion for the suspended mass are presented. It must be mentioned, that in this work, the expression *suspended mass* can be used to refer to the chassis wherever it is advantageous. The right subscript A is used to refer to variables belonging to the suspended mass. Furthermore, since the angular velocity ${}_V\boldsymbol{\omega}_A$ and the angular acceleration ${}_V\dot{\boldsymbol{\omega}}_A$ of the suspended mass appear in the equations of linear momentum (implicitly in the acceleration ${}_V\mathbf{a}_{{}_V O}$ of the vehicle center of gravity) and angular momentum (explicitly), and since their definition is not straightforward, they are going to be presented separately.

Equation of linear momentum for the suspended mass

According to equations 2.1 and 2.3, the equation of linear momentum for the suspended mass (mass m_A) referred to coordinate system $\{{}_V O; {}_V x, {}_V y, {}_V z\}$ can be written as

$$\sum {}_V \mathbf{F}_A = m_A \cdot \left({}_V \dot{\boldsymbol{\omega}}_A \times {}_V \mathbf{r}_{{}_E O \rightarrow {}_V O} + {}_V \boldsymbol{\omega}_A \times {}_V \boldsymbol{\omega}_A \times {}_V \mathbf{r}_{{}_E O \rightarrow {}_V O} \right), \quad (2.4)$$

since the first and the last two terms of equation 2.3 vanish. The term on the right side of equation 2.4 is a function of the angular velocity ${}_V \boldsymbol{\omega}_A$ (see equation 2.9) and the angular acceleration ${}_V \dot{\boldsymbol{\omega}}_A$ (see equation 2.11). The sum of forces $\sum {}_V \mathbf{F}_A$ comprises all external forces acting on the suspended mass, i.e. the reaction forces ${}_V \mathbf{F}_{ws_i}$ induced by the n wheels on the suspended mass through the suspension system³, the aerodynamic force

³It groups the forces on the linkages of the suspension system as well as applied forces of any passive, semi-active or active element belonging to it.

${}^V\mathbf{F}_{aero}$, the forces ${}^V\mathbf{F}_{Add_j}$ induced by k additional devices attached to the suspended mass as well as the gravitational force ${}^V\mathbf{G}_A = m_A \cdot \mathbf{g}$:

$$\sum {}^V\mathbf{F}_A = \sum_{i=1}^n {}^V\mathbf{F}_{ws_i} + {}^V\mathbf{F}_{aero} + \sum_{j=1}^k {}^V\mathbf{F}_{Add_j} + {}^V\mathbf{G}_A. \quad (2.5)$$

Equation of angular momentum for the suspended mass

According to equation 2.2, the equation of angular momentum for the suspended mass can be written as:

$$\sum {}^V\mathbf{M}_A = {}^V\mathbf{I}_{CG_A} \cdot {}^V\dot{\boldsymbol{\omega}}_A + {}^V\boldsymbol{\omega}_A \times {}^V\mathbf{I}_{CG_A} \cdot {}^V\boldsymbol{\omega}_A, \quad (2.6)$$

where the angular velocity ${}^V\boldsymbol{\omega}_A$ and the angular acceleration ${}^V\dot{\boldsymbol{\omega}}_A$ are given by the equations 2.9 and 2.11 respectively, the moment of inertia tensor ${}^V\mathbf{I}_{CG_A}$ can be written as a function of the principal moments of inertia (${}^V I_{CG_A x}$, ${}^V I_{CG_A y}$ and ${}^V I_{CG_A z}$)

$${}^V\mathbf{I}_{CG_A} = \begin{bmatrix} {}^V I_{CG_A x} & 0 & 0 \\ 0 & {}^V I_{CG_A y} & 0 \\ 0 & 0 & {}^V I_{CG_A z} \end{bmatrix}, \quad (2.7)$$

when the coordinate system of the vehicle $\{{}^V O; {}^V x, {}^V y, {}^V z\}$ coincides with the principal axes, and the sum $\sum {}^V\mathbf{M}_A$ comprises all external moments acting on the suspended mass:

$$\sum {}^V\mathbf{M}_A = \underbrace{\sum_{i=1}^n ({}^C\mathbf{r}_{V O \rightarrow AP_{wi}} \times {}^V\mathbf{F}_{ws_i})}_{{}^V\mathbf{M}_{ws_i}} + \underbrace{{}^V\mathbf{r}_{V O \rightarrow P_{aero}} \times {}^V\mathbf{F}_{aero}}_{{}^V\mathbf{M}_{aero}} + \underbrace{\sum_{j=1}^k ({}^V\mathbf{r}_{j, V O \rightarrow Add_j} \times {}^V\mathbf{F}_{Add_j})}_{{}^V\mathbf{M}_{Add}}. \quad (2.8)$$

The terms in equation 2.8 correspond to the sum of the cross products of the individual

forces of equation 2.5 with the position vectors⁴ ${}_V \mathbf{r}_m$ from the vehicle coordinate system to the application point of the corresponding force ${}_V \mathbf{F}_m$.

Angular acceleration, velocity and position of the suspended mass

The angular velocity ${}_V \boldsymbol{\omega}_A$ of the suspended mass can be written as:

$${}_V \boldsymbol{\omega}_A = {}_V \begin{bmatrix} \omega_x & \omega_y & \omega_z \end{bmatrix}_A^T = {}_V \mathbf{J} \cdot \begin{bmatrix} \dot{\psi} & \dot{\theta} & \dot{\phi} \end{bmatrix}^T, \quad (2.9)$$

where ${}_V \mathbf{J}$ is the Jacobian matrix used to express the angular velocity ${}_V \boldsymbol{\omega}_A$ as a function of the time derivatives of the Cardan angles (ψ for the yaw movement, θ for the pitch movement and ϕ for roll movement) and is given by (see [Hir09a]):

$${}_V \mathbf{J} = \begin{bmatrix} -\sin \theta & 0 & 1 \\ \cos \theta \cdot \sin \phi & \cos \phi & 0 \\ \cos \theta \cdot \cos \phi & -\sin \phi & 0 \end{bmatrix}. \quad (2.10)$$

Taking the time derivative of equation 2.9 yields to

$${}_V \dot{\boldsymbol{\omega}}_A = {}_V \begin{bmatrix} \dot{\omega}_x & \dot{\omega}_y & \dot{\omega}_z \end{bmatrix}_A^T = {}_V \dot{\mathbf{J}} \cdot \begin{bmatrix} \dot{\psi} & \dot{\theta} & \dot{\phi} \end{bmatrix}^T + {}_V \mathbf{J} \cdot \begin{bmatrix} \ddot{\psi} & \ddot{\theta} & \ddot{\phi} \end{bmatrix}^T, \quad (2.11)$$

with the time derivative of the Jacobian matrix ${}_V \dot{\mathbf{J}}$ given by:

$${}_V \dot{\mathbf{J}} = \begin{bmatrix} -\dot{\theta} \cdot \cos \theta & 0 & 0 \\ -\dot{\theta} \cdot \sin \theta \cdot \sin \phi + \dot{\phi} \cdot \cos \theta \cdot \cos \phi & -\dot{\phi} \cdot \sin \phi & 0 \\ -\dot{\theta} \cdot \sin \theta \cdot \cos \phi - \dot{\phi} \cdot \cos \theta \cdot \sin \phi & -\dot{\phi} \cdot \cos \phi & 0 \end{bmatrix}. \quad (2.12)$$

Finally, the position angles ψ , θ and ϕ , needed to describe the orientation of the suspended mass in space, are determined using numerical methods (see e.g. [Sim06] and [Sch03]) to solve the system of nonlinear differential equations

$$\begin{bmatrix} \dot{\psi} & \dot{\theta} & \dot{\phi} \end{bmatrix}^T = {}_V \mathbf{J}^{-1} \cdot {}_V \begin{bmatrix} \omega_x & \omega_y & \omega_z \end{bmatrix}_A^T, \quad (2.13)$$

⁴Here AP_{wi} corresponds to the attachment point of the wheel i , P_{aero} to the application point of the aerodynamical force, and Add_j to the attachment point of the j additional mass.

which is obtained by inverting equation 2.9. In equation 2.13, ${}_V\mathbf{J}^{-1}$ corresponds to the inverse matrix of the Jacobian matrix of equation 2.10:

$${}_V\mathbf{J}^{-1} = \frac{1}{\cos \theta} \cdot \begin{bmatrix} 0 & \sin \phi & \cos \phi \\ 0 & \cos \theta \cdot \cos \phi & -\cos \theta \cdot \sin \phi \\ \cos \theta & \sin \theta \cdot \sin \phi & \sin \theta \cdot \cos \phi \end{bmatrix}. \quad (2.14)$$

It is evident from equation 2.14 that there is a singularity for $\theta = \pi/2$, i.e. when the vehicle is rolling over by turning around the transversal axis ${}_L y$. This can be easily solved by setting a threshold a little bit smaller than $\pi/2$ when θ is reaching this value and changing to the complementary angle when $\theta > \pi/2$. An alternatively solution is to use quaternions instead of Cardan angles (see e.g. [Wil07]).

2.4.2. Equations of motion for the non-suspended masses

In this section, the equations of linear and angular momentum for the non-suspended masses are presented. The non-suspended mass includes not only the wheel, the tire, the brake disc and the calliper but also part of the mass of the suspension linkages. Nevertheless, the expressions *wheel* and *non-suspended mass* are used indistinctly in this work unless something else is explicitly indicated.

Equation of linear momentum for the non-suspended masses

According to equation 2.1, the equation of linear momentum for a non-suspended mass m_{w_i} can be written as:

$$\sum {}_C\mathbf{F}_{w_i} = m_{w_i} \cdot {}_C\mathbf{a}_{_C O}, \quad (2.15)$$

where the sum ${}_C\mathbf{F}_{w_i}$ comprises all external forces acting on the analyzed wheel, i.e. the tire forces ${}_C\mathbf{F}_{T_i}$, the reaction forces ${}_C\mathbf{F}_{ws_i}$ induced by the suspended mass on the wheel through the suspension system (as mentioned before, it groups the forces on the linkages of the suspension system as well as forces of any passive, semi-active or active element belonging to it) and the gravitational force ${}_C\mathbf{G}_{w_i} = m_{w_i} \cdot \mathbf{g}$:

$$\sum {}_C\mathbf{F}_{w_i} = {}_C\mathbf{F}_{T_i} - {}_C\mathbf{F}_{ws_i} + {}_C\mathbf{G}_{w_i}. \quad (2.16)$$

Assumption 2.2: In the simulation environment MOVES², it is assumed, as simplification, that the non-suspended masses can move only parallel to ${}_E z$.

According to assumption 2.2, equations 2.15 and 2.16 simplify to:

$${}_C F_{T_i, z} - {}_C F_{ws_i, z} + {}_C G_{w_i, z} = m_{w_i} \cdot {}_C a_{_C O, z}. \quad (2.17)$$

Furthermore, the horizontal components of the acceleration of the wheel are correspondingly the same as the acceleration for the attachment point AP_{w_i} of the wheel to the suspended mass, which, according to equation 2.3, is given by:

$${}_C a_{AP_{w_i}} = {}_C a_{_V O} + {}_C \dot{\omega}_A \times {}_C r_{_V O \rightarrow AP_{w_i}} + {}_C \omega_A \times {}_C \omega_A \times {}_C r_{_V O \rightarrow AP_{w_i}}. \quad (2.18)$$

The acceleration vector of the wheel w_i can then be written as:

$${}_C a_{_C O} = \left[{}_C a_{AP_{w_i}, x} \quad {}_C a_{AP_{w_i}, y} \quad {}_C a_{_C O, z} \right]^T. \quad (2.19)$$

Equation of angular momentum for the non-suspended masses

Additionally to the vertical movement relative to the suspended mass, a wheel is considered to have also a rotational freedom degree around its ${}_C y$ axis. Thus, according to equation 2.2, the equation of angular momentum for a wheel can then be written as:

$$\sum {}_C M_{w_i} = {}_C I_{CGw_i} \times {}_C \dot{\omega}_{w_i}. \quad (2.20)$$

The sum $\sum {}_C M_{w_i}$ comprises all external moments acting on the wheel:

$$\sum {}_C M_{w_i} = {}_C M_{D/B, i} + \underbrace{{}_C r_{_C O \rightarrow AP_{w_i}} \times {}_C F_{ws_i}}_{{}_C M_{ws_i}} + {}_C M_{T_i}, \quad (2.21)$$

where ${}_C M_{ws_i}$ is the moment vector due to the reaction forces induced by the suspended mass on the wheel through the suspension, ${}_C M_{T_i}$ correspond to the tire moments (see chapter 2.5 and take into account assumption 2.1, from which follows that ${}_C z$ becomes

parallel to ${}_Wz$) and the driving/braking moment vector ${}_C\mathbf{M}_{D/B, i}$ is given by

$${}_C\mathbf{M}_{D/B, i} = {}_C \begin{bmatrix} 0 & M_{D/B, i} & 0 \end{bmatrix}^T. \quad (2.22)$$

The driving (subscript D) and braking (subscript B) are supposed to act only in the ${}_Cy$ axis with $M_{D, i} > 0$ and $M_{B, i} < 0$. Furthermore, the moment of inertia tensor ${}_C\mathbf{I}_{CGw_i}$ for a wheel, present on the right side of equation 2.20, can be approximated as:

$${}_C\mathbf{I}_{CGw_i} = \begin{bmatrix} {}_C I_{CGw_i, x} & 0 & 0 \\ 0 & {}_C I_{CGw_i, y} & 0 \\ 0 & 0 & {}^{red}{}_C I_{CGw_i, z} \end{bmatrix}, \quad (2.23)$$

where ${}^{red}{}_C I_{CGw_i, z}$ corresponds the reduced moment of inertia including the powertrain components considered to be connected to the wheel i (see appendix C.2).

2.4.3. Equations of motion for additional masses

It is considered that j additional masses m_{Add_j} (e.g. combustion engine, occupants or a battery) can be attached to the suspended mass using a rigid connection or a suspension system composed of a spring and a damper in parallel (see [Mar09]). Furthermore, it is assumed that these masses have only one degree of freedom, i.e. a relative vertical movement with respect to the suspended mass. For example, modeling the vertical vibration behavior of the internal combustion engine improves the simulation results of the overall vertical vibration behavior of the vehicle (see e.g. [Mar09], [RNW10], [MK98]). Additionally, since the moment of inertia of the suspended devices is neglected, they are modeled as punctual masses and not as bodies.

Equation of linear momentum for the additional masses

According to equation 2.1, the equation of linear momentum for an additional mass m_{Add_j} attached to the suspended mass can be written as:

$$\sum_V \mathbf{F}_{Add_j} = m_{Add_j} \cdot {}_V \mathbf{a}_{Add_j}, \quad (2.24)$$

where the sum $\sum_V \mathbf{F}_{Add_j}$ correspond to the forces of the joint between the additional mass and the suspended mass⁵. Moreover, the acceleration ${}_V \mathbf{a}_{Add_j}$ of the additional mass is given by:

$$\begin{aligned}
 {}_V \mathbf{a}_{Add_j} = & {}_V \mathbf{a}_{VO} + \underbrace{{}_V \dot{\boldsymbol{\omega}} \times {}_V \mathbf{r}_{VO \rightarrow P_{Add_j}} + {}_V \boldsymbol{\omega} \times ({}_V \boldsymbol{\omega} \times {}_V \mathbf{r}_{VO \rightarrow P_{Add_j}})}_{{}_V \mathbf{a}_{P_{Add_j}^*}} + \\
 & \underbrace{2 \cdot {}_V \boldsymbol{\omega} \times {}_V \dot{\mathbf{r}}_{VO \rightarrow P_{Add_j}}}_{{}_V \mathbf{a}_{cor}} + \underbrace{{}_V \ddot{\mathbf{r}}_{VO \rightarrow P_{Add_j}}}_{{}_V \mathbf{a}_{P_{Add_j} \setminus V}}. \quad (2.25)
 \end{aligned}$$

The sum of forces $\sum_V \mathbf{F}_{Add_j}$ acting on the suspended mass causes a moment on it as indicated by the last term on the right hand side of equation 2.6.

2.5. Tire model

There are several models used in the automotive industry for different applications to represent the behavior of a pneumatic tire. An overview can be found in [Hir09c] and [HW06]. According to the framework used to model the tire, these models range from physical over semi-physical up to empirical ones. The physical models are very accurate, use generally a large number of model parameters and are time consuming and computationally intensive. Some examples are RMOD-K (see [Oer11] and [OF01]), FTire (see [Gip05]) and CDTire (see [GB07] [GCDB05]). The empirical models use often parameters without or with only a minor physical meaning to approximate the tire behavior by means of mathematical equations. The high computing efficiency is a big advantage of this kind of models. The most widespread empirical model is based on the so-called *magic formula* (see e.g. [Pac06] and [PB97]). The semi-physical tire models combine the advantages of the physical and empirical ones. They can be as computing efficient as the empirical models while using fewer still meaningful parameters as the physical tire models. TMeasy [HRW07], TMsimple [Hir09b], MF-Tyre (see e.g. [Pac06]) and MF-SWIFT (see [SBJ07], [Sch04] and [Sch01]) are examples of semi-physical tire models.

⁵As mentioned before, the additional mass can be rigidly attached to the suspended mass or over a spring and damper system with one degree of freedom, i.e. the relative vertical movement with respect to the suspended mass (see [Mar09]).

In order to fulfill the specific requirements of the present research work and be able to simulate the horizontal and vertical tire dynamics needed to investigate the potential and limits as well as the advantages and disadvantages of vehicles with in-wheel motors, a tire model was developed and implemented. Special attention was paid to minimize the number of model parameters and required computational resources to be able to use the model in real time applications. While for the horizontal dynamics a model based on the TMsimple (see [Hir09b]) and the TMeasy (see [HRW07] and [HRW02]) tire models of *Hirschberg et al.* was implemented, the semi-physical approach of *Schmeitz* (see [Sch04] and [Sch01]) used in the MF-SWIFT tire model was used as basis to depict the tire vertical dynamics. Thus, the limits of conventional tire models for horizontal dynamics and handling were extended for rough road applications.

Figure 2.3 presents a schematic representation of the interaction between the implemented vehicle, road and tire models. The model of the vertical tire dynamics takes two inputs: on the one hand, the coordinates ${}_E[x, y, z]_{road}^T$ of the grid of points defining the road; on the other hand, the position ${}_E[x, y]_{w_i}^T$ and the speed ${}_E[\dot{x}, \dot{y}]_{w_i}^T$ as well as the steering angle δ_{st} of each wheel w_i . The output comprises the vertical contact force ${}_W F_{T_i, z}$, the vertical position ${}_E z_{w_i}({}_E x, {}_E y)_{road}$ of the tire contact point W_i , the dynamic length of the tire contact patch $l_{s_{dyn_i}}$ and the dynamic tire radius r_{dyn_i} . These outputs are transferred to the model of the horizontal tire dynamics together with the horizontal speed ${}_W[\dot{x}, \dot{y}]_{w_i}^T$ of the tire contact point⁶ W and the angular speed ${}_C \omega_{w_i, y}$ around the ${}_C y$ axis of each wheel w_i . The outputs of the model of the horizontal tire dynamics are the tire forces ${}_W \mathbf{F}_{T_i}$ and torques ${}_W \mathbf{M}_{T_i}$ at the tire contact point W_i , which are, in turn, inputs to the vehicle model (see chapter 2.4.2).

The values of the tire model parameters are presented in appendix B.2.

2.5.1. Model for the horizontal tire dynamics

For a considered tire i , the steady state values of the combined longitudinal ${}_W F_{T_i, x}^S$ and the lateral ${}_W F_{T_i, y}^S$ tire forces for a certain vertical contact force ${}_W F_{T_i, z}$ between tire and ground are approximated based on the TMsimple tire model [Hir09b]. According to this model, the individual⁷ longitudinal ${}_W F_{T_i, x}^{S*}$ and lateral tire forces ${}_W F_{T_i, y}^{S*}$ (both

⁶From assumption 2.1, it follows that ${}_W \dot{x}_{w_i} \approx {}_C \dot{x}_{w_i}$ and ${}_W \dot{y}_{w_i} \approx {}_C \dot{y}_{w_i}$ (see also chapter 2.4.2).

⁷In contrast to the individual longitudinal ${}_W F_{T_i, x}^{S*}$ and lateral ${}_W F_{T_i, y}^{S*}$ tire forces, the combined longitudinal ${}_W F_{T_i, x}^S$ and lateral ${}_W F_{T_i, y}^S$ tire forces act simultaneously at the W point. They are correspondingly equal for pure longitudinal or transversal motion of the tire.

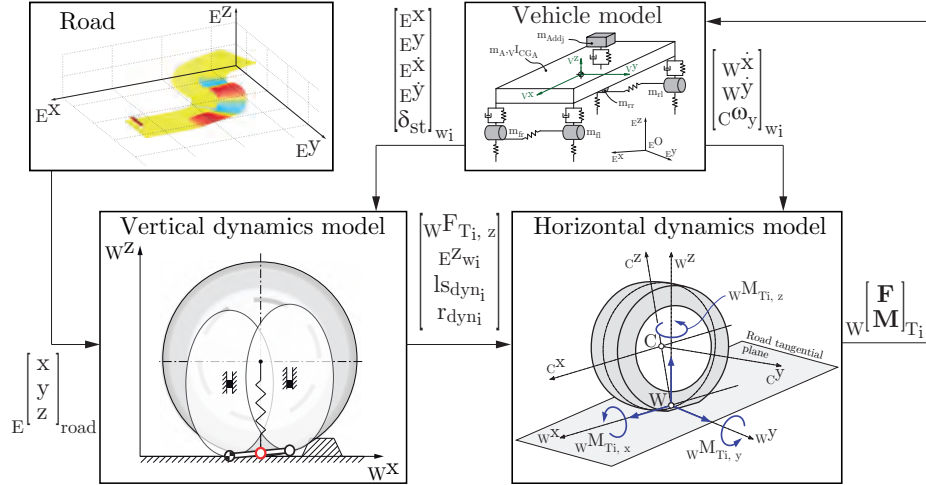


Figure 2.3.: Schematic representation of the interaction between implemented vehicle, road and tire models.

designated as Y) for a constant contact force ${}_W F_{T_i, z}$, can be expressed as a function of the (longitudinal or lateral) slip quantity X as:

$$Y = K \cdot \sin \left[B \cdot \left(1 - e^{-|X|/A} \right) \cdot \text{sign}(X) \right]. \quad (2.26)$$

The coefficients A , B and K are functions of the maximum or peak value ${}^{max}Y$, the saturation value ${}^{\infty}Y$ and the initial stiffness dY_0 as shown in equations 2.27:

$$K = {}^{max}Y, \quad (2.27a)$$

$$B = \pi - \arcsin \left(\frac{{}^{\infty}Y}{{}^{max}Y} \right), \quad (2.27b)$$

$$A = \frac{1}{dY_0} \cdot K \cdot B. \quad (2.27c)$$

With equations 2.26 and 2.27, the tire force Y can be obtained as a function of the relating slip quantity X as presented in figure 2.4.

In the TMsimple model, the polynomial

$$\mathbb{D}({}_W F_{T_i, z}) = d_1 \cdot \left(\frac{{}_W F_{T_i, z}}{{}_W F_{T_i, z}^{nom}} \right) + d_2 \cdot \left(\frac{{}_W F_{T_i, z}}{{}_W F_{T_i, z}^{nom}} \right)^2 \quad (2.28)$$

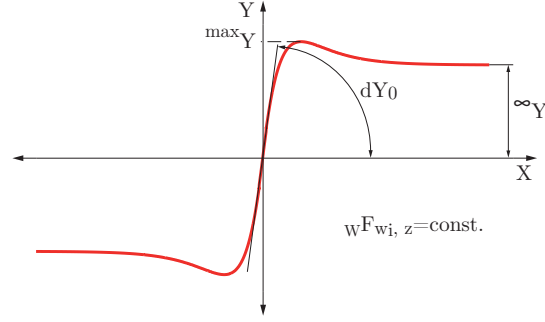


Figure 2.4.: Individual tire force vs. slip; approach according to TMsimple [Hir09b].

is used to account for the declining influence of the vertical contact force⁸ ${}_W F_{T_i, z}$, where $\mathbb{D}({}_W F_{T_i, z})$ correspond to ${}^{max}Y({}_W F_{T_i, z})$, $dY_0({}_W F_{T_i, z})$ or ${}^\infty Y({}_W F_{T_i, z})$. The coefficients \mathfrak{d}_1 and \mathfrak{d}_2 are calculated for ${}^{max}Y$, dY_0 and ${}^\infty Y$ according to:

$$\mathfrak{d}_1 = 2 \cdot \mathbb{D}_1 - 0.5 \cdot \mathbb{D}_2, \quad (2.29a)$$

$$\mathfrak{d}_2 = 0.5 \cdot \mathbb{D}_2 - \mathbb{D}_1, \quad (2.29b)$$

for given values \mathbb{D}_1 and \mathbb{D}_2 for ${}_W F_{T_i, z \text{ nom}}$ and $2 \cdot {}_W F_{T_i, z \text{ nom}}$ respectively, where ${}_W F_{T_i, z \text{ nom}}$ correspond to the nominal vertical contact force. The values \mathbb{D}_1 and \mathbb{D}_2 are determined experimentally based on measurements (see e.g. [HBWH11], [Hir09a], [HEG11] and [HW06]).

The slip quantity X of equation 2.26 correspond to the longitudinal sl_{x_i} or to the lateral sl_{y_i} slip for each tire i as given by:

$$sl_{x_i} = \frac{r_{dyn} \cdot C \omega_{w_i, y} - C \dot{x}_{w_i}}{v^* + v_N}, \quad (2.30a)$$

$$sl_{y_i} = \arctan\left(\frac{W \dot{y}_{w_i}}{v^* + v_N}\right) \cdot \frac{1}{G}, \quad (2.30b)$$

with the transport speed v^* given by:

$$v^* = \begin{cases} r_{dyn} \cdot |C \omega_{w_i, y}|; & \text{for driving,} \\ |C \dot{x}_{w_i}|; & \text{for braking.} \end{cases} \quad (2.31)$$

⁸The vertical contact force ${}_W F_{T_i, z}$ is determined by the model for the vertical tire dynamics (see chapter 2.5.2).

The artificial velocity⁹ v_N is added in the denominator of equations 2.30 to avoid numerical problems when the wheel locks (i.e. ${}_C\omega_{w_i, y} = 0$) or when the vehicle stops (i.e. ${}_C\dot{x}_{w_i} = 0$). Additionally, the conversion factor

$$\mathbb{G} = \frac{dY_{0x}}{dY_{0y}} = \frac{A_y \cdot K_x \cdot B_x}{A_x \cdot K_y \cdot B_y} \quad (2.32)$$

in equation 2.30b transforms the slip angle

$$\alpha_{w_i} = \arctan\left(\frac{W\dot{y}_{w_i}}{v^* + v_N}\right) \quad (2.33)$$

into the lateral slip sl_{y_i} , which is a quantity comparable with the longitudinal slip sl_{x_i} . The slip vector $\mathbf{sl} = [sl_{x_i}, sl_{y_i}]^T$, acting in the direction given by the angle

$$\beta_{sl} = \arctan\left(\frac{sl_{y_i}}{sl_{x_i}}\right), \quad (2.34)$$

is the basis for the calculation of the steady state value of the combined tire forces; i.e. the longitudinal and lateral tire forces (${}_W F_{T_i, x}^S$ and ${}_W F_{T_i, y}^S$ respectively) acting simultaneously at the contact point W (for example, when driving or braking in a curve). The steady state value of the resulting horizontal force ${}_W F_{T_i, h}^S$ assumed to act in the opposite direction of the slip vector \mathbf{sl} can be approximated using the following interpolation function (see also figure 2.5):

$${}_W F_{T_i, h}^S = {}_W F_{T_i, x}^{S*} \cdot \sin^2(\beta_{sl}) + {}_W F_{T_i, y}^{S*} \cdot \cos^2(\beta_{sl}). \quad (2.35)$$

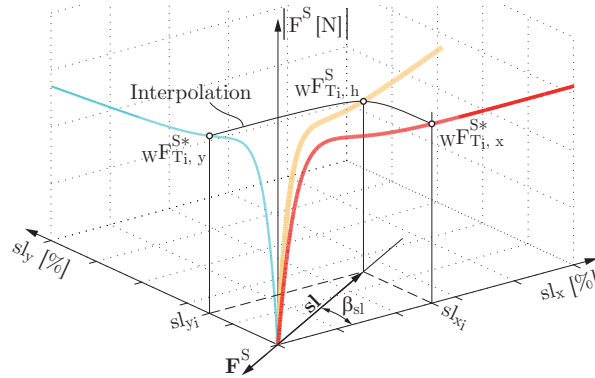


Figure 2.5.: Interpolation of the combined tire forces in steady state [Hir09b].

⁹A suited value for the artificial velocity is e.g. $v_N = 0.01 \text{ m/s}$

Finally, the steady state value of the combined longitudinal ${}_W F_{T_i, x}^S$ and lateral ${}_W F_{T_i, y}^S$ forces can be expressed as:

$${}_W F_{T_i, x}^S = {}_W F_{T_i, h}^S \cdot \cos(\beta_{sl}) , \quad (2.36a)$$

$${}_W F_{T_i, y}^S = {}_W F_{T_i, h}^S \cdot \sin(\beta_{sl}) . \quad (2.36b)$$

Following model extensions are based on the TMeasy tire model presented by *Hirschberg et al.* (see [HRW02] and [HRW07]):

First order tire dynamics

Tire dynamics can be approximated by a first order system (see [HRW07], [HWJ00] and [Hir09c]) given by the following differential equation or by the transfer function $G_{x/y}(s)$:

$$\tau_{x/y} \cdot \dot{{}_W F_{T_i, x/y}^D}(t) = {}_W F_{T_i, x/y}^S - {}_W F_{T_i, x/y}^D \quad \bullet \quad G_{x/y}(s) = \frac{{}_W F_{T_i, x/y}^D}{{}_W F_{T_i, x/y}^S} = \frac{1}{1 + \tau_{x/y} \cdot s} . \quad (2.37)$$

These equations describe the dynamical tire force ${}_W F_{T_i, x/y}^D$ as a function of its steady state value ${}_W F_{T_i, x/y}^S$ (given by equations 2.36) and the time constant

$$\tau_{x/y} = \frac{1}{r_{dyn} \cdot |C \omega_{w_i, x/y}|} \cdot \frac{1}{c_{T_i, x/y}} \cdot \frac{\partial {}_W F_{T_i, x/y}^S}{\partial sl_{x/y}} . \quad (2.38)$$

The right subscript x/y denotes the considered direction (${}_W x$ or ${}_W y$ axis respectively) and the term $c_{T_i, x/y}$ corresponds to the tire stiffness in the respective direction. In order to avoid numerical overflow, the partial derivative of the steady state tire forces with respect to the slip (the third term on the right in equation 2.38) can be approximated by their global derivatives:

$$\frac{\partial {}_W F_{T_i, x/y}^S}{\partial sl_{x/y}} \approx \frac{{}_W F_{T_i, x/y}^S}{sl_{x/y}} . \quad (2.39)$$

Thus, no specific fitting parameters are necessary except the known ones.

Friction coefficient

As mentioned before, the tire parameters ^{max}Y , dY_0 or $^{\infty}Y$ are determined experimentally based on measurements, which can be obtained using different devices such as a roller drum or a flat band test rig as well as a tire measurement vehicle (see e.g. [HBWH11], [Hir09a], [HEG11] and [HW06]). In any case, the tire is in contact either with a surface simulating a given road or with the road itself. In both cases, a certain nominal friction coefficient μ_0 is present in the contact area. Nevertheless, different friction conditions could be of interest. To account for different local friction coefficients μ_{w_i} along a given road and for a considered wheel i and since the friction coefficient mainly influences the maximum ^{max}Y and the sliding force $^{\infty}Y$ values while leaving the initial slope dY_0 nearly unchanged, ^{max}Y and $^{\infty}Y$ can be modified according to

$$^{max}Y ({}_W F_{T_i, z}) \rightarrow ^{max}Y ({}_W F_{T_i, z}) \cdot \frac{\mu_{w_i}}{\mu_0}, \quad (2.40a)$$

$$^{\infty}Y ({}_W F_{T_i, z}) \rightarrow ^{\infty}Y ({}_W F_{T_i, z}) \cdot \frac{\mu_{w_i}}{\mu_0}. \quad (2.40b)$$

Rolling resistance torque

Due to the asymmetrical pressure distribution in the tire latch, the resultant vertical contact force ${}_W F_{T_i, z}$ does not act at the contact point W but ahead, for ${}_C \dot{x} > 0$, or behind it, for ${}_C \dot{x} < 0$ (see e.g. [Hir09a], [Wal06] or [MW04]). This results in a rolling resistance torque given by

$${}_W M_{T_i, y} = r_{dyn} \cdot {}_W F_{T_i, z} \cdot f_{roll} \cdot \text{sign} ({}_C \omega_{w_i, y}), \quad (2.41)$$

where f_{roll} represents the rolling resistance coefficient and r_{dyn} the dynamic tire radius (see [Wal04]).

Self aligning torque and pneumatic trail

During cornering, a lateral shear stress distribution arises in the tire contact patch (see e.g. [Hir09a], [Wal06] or [MW04]). The resultant lateral tire force ${}_W F_{T_i, y}^D$ is situated in the centroid of this distribution. The distance between this force and the tire contact point W along the ${}_W x$ axis is called pneumatic trail¹⁰ n_{p_i} . The shear stress distribution and hence the pneumatic trail are influenced by the lateral slip sl_{y_i} (see figure 2.6). For small values of the lateral slip, most tire particles in the latch are adhered to the ground and the application point of the lateral force lies behind the W point, i.e. the pneumatic trail is positive. For increasing values of the lateral slip, this point moves forward. As the shear stress increases with the lateral slip, more tire particles in the latch start to slide and the application point can even move ahead the W point. In the limit situation, when all particles are sliding in the lateral direction (along the ${}_W y$ axis), the pneumatic trail becomes zero. The self aligning torque, i.e. the torque around the ${}_W z$ axis, is related with the resultant lateral tire force ${}_W F_{T_i, y}^D$ and the pneumatic trail n_{p_i} by:

$${}_W M_{T_i, z}(sl_{y_i}) = -n_{p_i}(sl_{y_i}) \cdot {}_W F_{T_i, y}^D(sl_{y_i}) . \quad (2.42)$$

The pneumatic trail n_{p_i} can be approximated by [Ril94]:

$$n_{p_i} = \begin{cases} \left(\frac{n_{p_i}}{ls_i}\right)_0 \cdot \left(1 - \frac{|sl_{y_i}|}{sl_{y_i}^0}\right); & \text{for } |sl_{y_i}| \leq sl_{y_i}^0, \\ -\left(\frac{n_{p_i}}{ls_i}\right)_0 \cdot \left(\frac{|sl_{y_i}| - sl_{y_i}^0}{sl_{y_i}^0}\right) \cdot \left(\frac{sl_{y_i}^S - |sl_{y_i}|}{sl_{y_i}^S - sl_{y_i}^0}\right); & \text{for } sl_{y_i}^0 < |sl_{y_i}| \leq sl_{y_i}^S, \\ 0; & \text{for } |sl_{y_i}| > sl_{y_i}^S, \end{cases} \quad (2.43)$$

where ls_i denotes the length of the tire contact patch, and the slip values $sl_{y_i}^0$ and $sl_{y_i}^S$ indicate the limits between the adhesion, transition and sliding zones mentioned before (see figure 2.6). The term $(n_{p_i}/ls_i)_0$ correspond to the value of the pneumatic trail for $|sl_{y_i}| = 0$ %.

To depict the dependency of the characteristic parameters $sl_{y_i}^0$, $sl_{y_i}^S$ and $(n_{p_i}/L_{T_i})_0$ from the vertical contact force ${}_W F_{T_i, z}$, *Rill* [Ril94] proposes the following interpolation ap-

¹⁰Must not be mistaken with the mechanical trail.

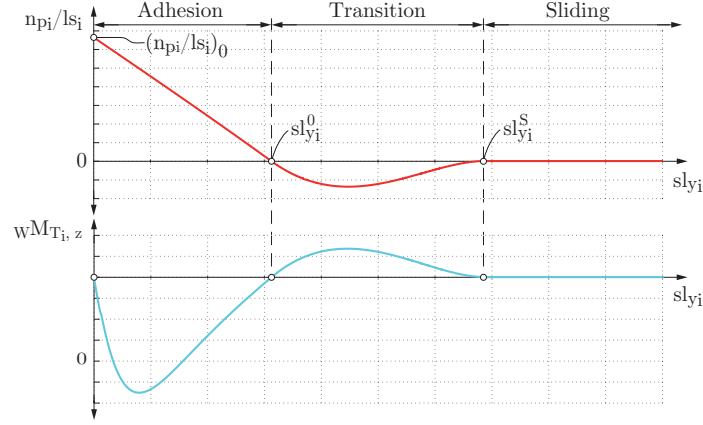


Figure 2.6.: Pneumatic trail n_{pi}/l_{s_i} and self aligning torque $w M_{T_i, z}$ as a function of the lateral slip $s l_{y_i}$.

proach

$$\mathbb{E}(w F_{T_i, z}) = \mathbb{E}_1 + (\mathbb{E}_2 - \mathbb{E}_1) \cdot \left(\frac{w F_{T_i, z}}{w F_{T_i, z}^{nom}} - 1 \right), \quad (2.44)$$

where the desired parameter $\mathbb{E}(s l_{y_i}^0, s l_{y_i}^S$ or $(n_{pi}/L_{T_i})_0$) for a given vertical contact force $w F_{T_i, z}$ can be calculated given values \mathbb{E}_1 for the nominal force $w F_{T_i, z}^{nom}$ and \mathbb{E}_2 for $2 \cdot w F_{T_i, z}^{nom}$ respectively.

2.5.2. Model for the vertical tire dynamics

As mentioned before, the inputs for the vertical tire dynamics model are the coordinates of the road points, the position $[_E x_{w_i}, _E y_{w_i}]$ and the speed $[_E \dot{x}_{w_i}, _E \dot{y}_{w_i}]$ of the tire contact point W in the earth-fixed coordinate system $\{_E O; _E x, _E y, _E z\}$, as well as the steering angle δ_{st, w_i} for each wheel i . Based on this information, the contact force between tire and ground $w F_{T_i, z}$, the vertical position $w z_{w_i}$ of the contact point W as well as the dynamic value of the tire radius r_{dyn_i} and the latch length l_{s_i} are calculated.

The model for the vertical tire dynamics is composed of three modules interacting continuously between each other, as presented in figure 2.7. The *location algorithm* is used to correlate the position $[_E x_{w_i, p}, _E y_{w_i, p}]$ of a given point P_p^* with the grid of points defining the road in order to establish the corresponding road height $_E z_{w_i, p}$. The *enveloping model* is based on the approach proposed by *Schmeitz* (see [Sch01] and [Sch04]) and is used to scan the road and determine the vertical movement of the wheel

while driving over an uneven road. Finally, a simple *single-mass oscillator model* is used to depict the vertical tyre dynamics. These modules are going to be explained in more detail in the following sections.

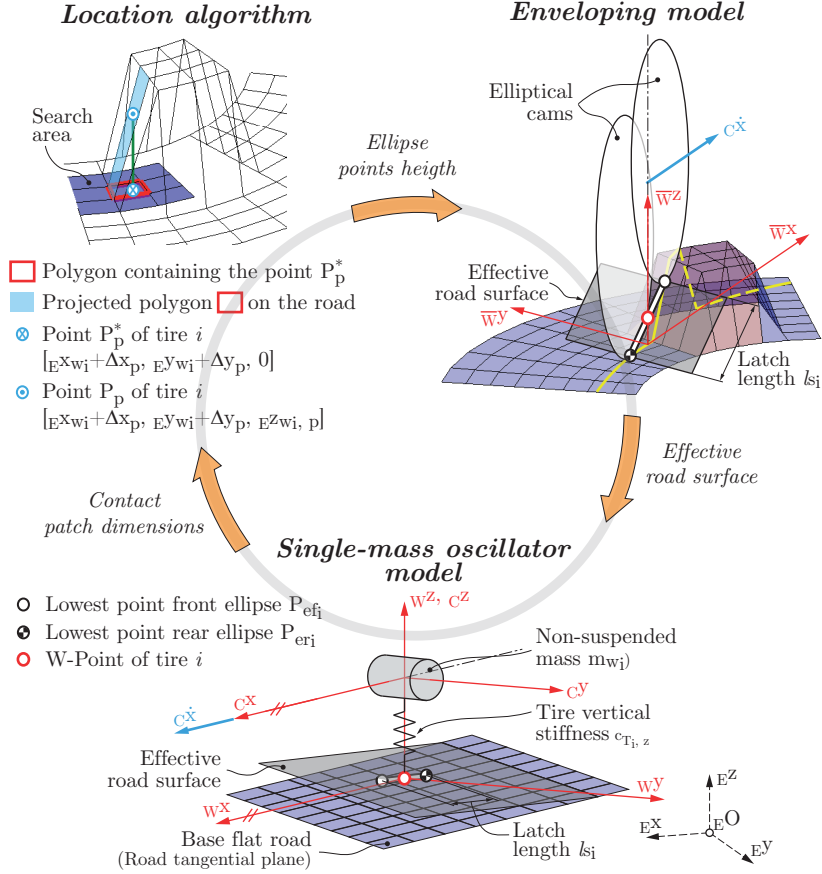


Figure 2.7.: Schematic representation of the tire model for the vertical tire dynamics consisting of the location algorithm, the enveloping model and the single-mass oscillator model.

Location algorithm

In this work, a simple and efficient approach to correlate the position $[E^x w_i, p, E^y w_i, p]$ of a given point P_p^* with the grid of points $E[x, y, z]_{road}^T$ defining the road in order to establish the corresponding road height $E^z w_i, p$ is proposed. The road can be seen, in a mathematical context, as a three-dimensional matrix containing the coordinates $E[x, y, z]_{road}$ of the knot points defining the road. An interpolation method seems to be the easiest way to determine the height of the road $E^z_{road, p}$ at any given position $[E^x_p, E^y_p]$.

Nevertheless, the open question is related with the road points ${}_E[x, y]_{road}$ to be used to perform this interpolation. This can be translated into the task of determining the polygon within which $[_E x_p, _E y_p]$ is found.

Consider the point $P_p^* = [_E x_p, _E y_p, 0]$ belonging to the *base flat road*, i.e. the road on which the tire is moving but with zero vertical component (${}_E z_{road} = 0$). To determine if the point P_p^* lies within a polygon defined by the points $[P_1, P_2, P_3, P_4]_{road}$, each point is connected with P_p^* building triangles (see figure 2.8-a). The point P_p^* is within the polygon if and only if the sum $\sum_{u=1}^4 A_u$ of the area of the single triangles is the same as the area of the polygon $A_{[P_1, P_2, P_3, P_4]_{road}}$ plus a term ε_A introduced to account for the numerical rounding:

$$\text{Point is within polygon} \leftrightarrow \sum_{u=1}^4 A_u = A_{[P_1, P_2, P_3, P_4]_{road}} + \varepsilon_A . \quad (2.45)$$

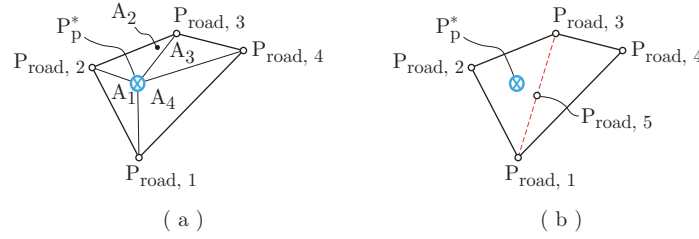


Figure 2.8.: Triangulation method to determine whether a point is within a polygon or not.

To improve the computational efficiency of the algorithm, a search area around the point P_p^* can be defined depending on its velocity. Once the polygon containing the point P_p^* has been found, it is divided in two triangles as shown in figure 2.8-b. Using the fictitious point $P_{road, 5}$ (midpoint between $P_{road, 1}$ and $P_{road, 3}$) and with the help of the algorithm described by equation 2.45, the triangle containing the point P_p^* is determined. The vertical coordinate ${}_E z_{w_i, p}$ of the point P_p can finally be found projecting the point P_p^* on the corresponding triangle belonging to the road:

$${}_E z_{w_i, p} = {}_E z_{\Delta P_1} + \frac{\left({}_E y_{w_i, p} - {}_E y_{\Delta P_1} \right) \cdot [a_x \cdot b_z - a_z \cdot b_x] - \left({}_E x_{w_i, p} - {}_E x_{\Delta P_1} \right) \cdot [a_y \cdot b_z - a_z \cdot b_y]}{a_x \cdot b_y - a_y \cdot b_x} , \quad (2.46)$$

with

$$a_{\mathbf{c}} = E^{\mathbf{c}}_{\Delta P_2} - E^{\mathbf{c}}_{\Delta P_1} , \quad (2.47a)$$

$$b_{\mathbf{c}} = E^{\mathbf{c}}_{\Delta P_3} - E^{\mathbf{c}}_{\Delta P_1} , \quad (2.47b)$$

as the difference of the corresponding coordinate \mathbf{c} (where \mathbf{c} correspond to x , y or z) of the vertices ΔP_1 , ΔP_2 and ΔP_3 of the triangle containing P_p .

Furthermore, it is worth noting that any other arbitrary quantity, like the friction coefficient μ (see also chapter 2.5.1), can be determined analogously using the presented algorithm.

Enveloping model

A tire acts as a low-pass filter on road excitations, as expressed by equation 2.38. Those excitations with short wavelengths are filtered out. Roughly speaking, wavelengths shorter than the length of the contact area (i.e. approximately 0.1 m) have little influence on the vertical movement of a vehicle and excitations with a wavelength greater than 100 m do not produce any appreciable effect on the vehicle suspension [Fia06]. It means, that only those excitations with wavelengths between approximately 0.1 m and 100 m are relevant for the analysis of the vertical vehicle dynamics. Nevertheless, even those excitations are somehow filtered by a real pneumatic (deformable) tire. This is called enveloping behavior.

To depict the enveloping behavior of a tire, several approaches are proposed in the literature. A summary of them are presented by *Schmeitz* [Sch04]. He presents also a semi-physical approach based on several cams used to scan the road (see [Sch04] and [Sch01]). This approach constitutes the basis for the enveloping model with two cams implemented in this work and shown in figure 2.9-a. It filters the road signal Ez_{road} by transforming it in the excitation $\overline{W}z_{w_i}$ (defined in the *road tangential plane axis system* $\{\overline{W}O; \overline{W}x, \overline{W}y, \overline{W}z\}$ - see chapter 2.2) acting on the spring representing the (statical) tire vertical stiffness $c_{T_i, z}^S$, as can be seen in figure 2.9-b.

The two elliptical cams are contained in the $x_W - z_W$ -plane and have only one degree of freedom, i.e. to move in the vertical direction. Furthermore, their lowest points P_{ef_i} (front ellipsis) and P_{er_i} (rear ellipsis) are connected through a fictitious extensible bar symbolizing the length ls_{dyn_i} of the contact patch, which is given as a function of the

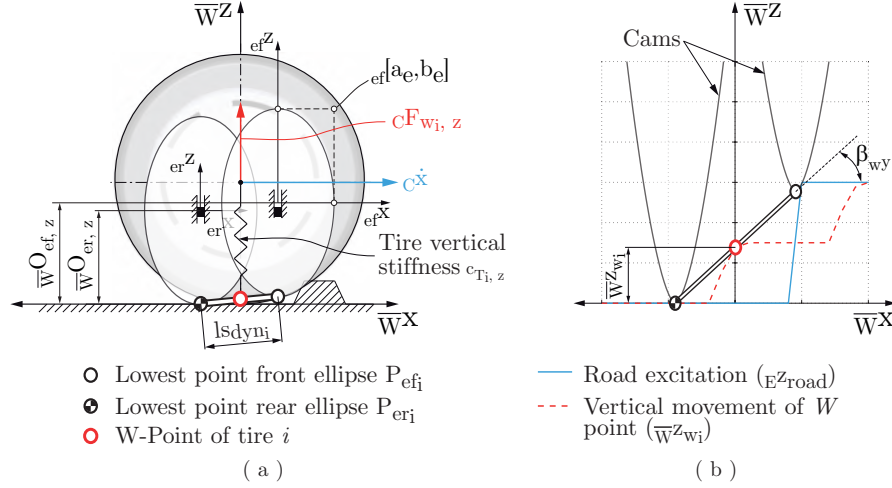


Figure 2.9.: Enveloping model: Two cams model (a) and movement of the W point (b).

spring force¹¹ ${}_W F_{T_i, z}$:

$$l_{s_{dyn_i}} = 2 \cdot \mathcal{P}_{l_{s_0}} \cdot \left(\mathcal{P}_{l_{s_1}} \cdot {}_W F_{T_i, z} + \mathcal{P}_{l_{s_2}} \cdot \sqrt{{}_W F_{T_i, z}} \right), \quad (2.48)$$

where the parameters $\mathcal{P}_{l_{s_0/1/2}}$ are specific for each tire type (see appendix B.2).

The front and rear ellipses (the subscript f/r is used to refer to any of them) are mathematically described by

$$\left(\frac{ef/er \cdot x_e}{a_e} \right)^{\mathcal{P}_c} + \left(\frac{ef/er \cdot z_e}{b_e} \right)^{\mathcal{P}_c} = 1, \quad (2.49)$$

with the tire specific exponent parameter \mathcal{P}_c (see appendix B.2) and the minor a_e and the major b_e semiaxes given as functions of the unloaded tire radius r_0 :

$$a_e = \mathcal{P}_a \cdot r_0, \quad (2.50a)$$

$$b_e = \mathcal{P}_b \cdot r_0. \quad (2.50b)$$

Solving equation 2.49 for the distance $ef/er \cdot z_e$ from any point on the ellipsis to the local

¹¹According to assumption 2.1, the magnitude of the spring force is equal to the magnitude of the tire contact force, i.e. $C F_{w_i, z} = {}_W F_{T_i, z}$

longitudinal axis ${}_{ef/er}x$ results in:

$${}_{ef/er}z_e = \left| b_e \cdot \left[1 - \left(\frac{|{}_{ef/er}x_e|}{a_e} \right)^{\mathcal{P}_c} \right]^{1/\mathcal{P}_c} \right|. \quad (2.51)$$

The vertical position $\overline{W}O_{ef/er, z}$ of the front or rear ellipsis center is given by

$$\overline{W}O_{ef/er, z} = \max \left[E z_{road} \left(P_{ef/eri, \overline{W}x} + {}_{ef/er}x \right) + {}_{ef/er}z_e \left({}_{ef/er}x \right) \right], \quad (2.52)$$

where the height of the road $E z_{road}$ at the position $P_{ef/eri, \overline{W}x} + {}_{ef/er}x$ of each point of the considered ellipsis in the earth-fixed coordinate system can be determined with the algorithm described in chapter 2.5.2 and ${}_{ef/er}z_e({}_{ef/er}x)$ is given by equation 2.51 for the position ${}_{ef/er}x$ of the considered point on the ellipsis' own coordinate system. Equation 2.52 indicates that the point at which an ellipsis contacts the road is given by the maximum of the sum of the point's vertical coordinate ${}_{ef/er}z_e$ and the road height $E z_{road}$ under each ellipsis point $P_e = [{}_{ef/er}x, {}_{ef/er}z_e]$. Therefore, this condition must be evaluated for at least all points P_e on the lower half-ellipse.

Having determined the positions $\overline{W}O_{ef/er, z}$ of the centers of the ellipses, the effective height $\overline{W}z_{w_i} = E z_{w_i}$ (see definition of the coordinate systems in chapter 2.2) of the contact point W corresponding to the height of the midpoint of the fictitious extensible bar connecting the points P_{ef_i} and P_{er_i} can be expressed as:

$$E z_{w_i} = \frac{\overline{W}O_{ef, z} + \overline{W}O_{er, z}}{2} - b_e. \quad (2.53)$$

According to *Schmeitz* [Sch04], the dynamic tire radius r_{dyn_i} can be expressed in terms of the vertical contact force ${}_W F_{T_i, z}$ and the tire specific parameters $\mathcal{P}_{r_{0/1/2/3}}$ (see appendix B.2 for the parameter values) as:

$$r_{dyn_i} = \mathcal{P}_{r_3} \cdot ({}_W F_{T_i, z})^{3/2} + \mathcal{P}_{r_2} \cdot {}_W F_{T_i, z} + \mathcal{P}_{r_1} \cdot ({}_W F_{T_i, z})^{1/2} + \mathcal{P}_{r_0} + r_{dyn_i, 0} \cdot [\cos(\beta_W y) - 1] - \rho_{z_i} \cdot r_{dyn_i, 0} \cdot \frac{d\beta_W y}{d_W x}. \quad (2.54)$$

The initial dynamic radius $r_{dyn_i, 0}$ (given for the simulation time $t = 0$) is given for the

nominal load ${}_W F_{T_i, z}^{nom}$ as a function of the unloaded tire radius r_0 and the initial static tire radius $r_{stat, 0}$ [Hir09c]:

$$r_{dyn_i, 0} = \frac{2}{3} \cdot r_0 + \frac{1}{3} \cdot r_{stat, 0} . \quad (2.55)$$

The effective deflection ρ_{z_i} of the spring representing the (statical) tire vertical stiffness $c_{T_i, z}^S$ is calculated as a function of the absolute road height ${}_{E}z_{road}$ at the considered point $[{}_{E}x_{w_i}, {}_{E}y_{w_i}]$, the absolute vertical position ${}_{E}z_{w_i}$ of the tire contact point and the absolute vertical position of the center of the considered wheel ${}_{E}z_{C_i}$ according to:

$$\rho_{z_i} = {}_{E}z_{road}({}_{E}x_{w_i}, {}_{E}y_{w_i}) + {}_{E}z_{w_i} - {}_{E}z_{C_i} . \quad (2.56)$$

The effective forward slope $\beta_{_W y}$ of the effective road surface (see figure 2.7) is given by:

$$\beta_{_W y} = \arctan \left(\frac{\overline{W}O_{er, z} + \overline{W}O_{ef, z}}{l_{s_{dyn_i}} + l_{s^*}} \right) , \quad (2.57)$$

where the small fictitious term l_{s^*} is introduced to avoid numerical instabilities when $l_{s_{dyn_i}}$ becomes zero (i.e. when ${}_W F_{T_i, z} = 0$).

Finally, the last term in equation 2.54, i.e. the variation of the effective forward slope with respect to the traveled distance, can be approximated for two consecutive integration steps $t - \Delta t$ and t with $\Delta t \rightarrow 0$ as:

$$\frac{d\beta_{_W y}}{d_W x} \approx \lim_{\Delta_W x \rightarrow 0} \frac{\Delta \beta_{_W y}(t)}{\Delta_W x(t)} = \frac{\beta_{_W y}(t) - \beta_{_W y}(t - \Delta t)}{{}_W x(t) - {}_W x(t - \Delta t)} , \quad (2.58)$$

with the initial condition

$$\left. \frac{d\beta_{_W y}}{d_W x} \right|_{t=0} = 0 . \quad (2.59)$$

Single-mass oscillator model

The implemented model consists of a single-mass oscillator composed by the non-suspended mass m_{w_i} of each wheel i , and by a spring representing the statical tire vertical stiffness $c_{T_i, z}^S$. The tire damping was neglected since it is more than one order of magnitude lower than that of the shock absorber of the suspension system and therefore has a

marginal effect on the vibration behavior of the vehicle (see e.g. [RS86]). While rolling over the effective road surface determined by the enveloping model (see chapter 2.5.2), the movement of the tire contact point W_i excites the spring resulting in the tire contact force given as a function \mathcal{F}_{cT}^* of the effective deflection ρ_{z_i} (see equation 2.56), the rotational speed of the wheel ${}^C\omega_{w_i, y}$ and the tire inflation pressure p_{T_i} :

$${}^W F_{T_i, z} = \mathcal{F}_{cT}^* (\rho_{z_i}, {}^C\omega_{w_i, y}, p_{T_i}) . \quad (2.60)$$

Considering the *tire lifting* as the most important nonlinear effect (see figure 2.10), equation 2.60 can be written as:

$${}^W F_{T_i, z} = \begin{cases} \mathcal{F}_{cT} (\rho_{z_i}, {}^C\omega_{w_i, y}, p_{T_i}) ; & \text{if } p_{T_i} \geq 0 \text{ (tire in contact with the ground)} \\ 0 ; & \text{otherwise (tire lifting).} \end{cases} \quad (2.61)$$

While for most preliminary analyses the effect of the rotational speed of the wheel ${}^C\omega_{w_i, y}$ and the tire inflation pressure p_{T_i} are neglected and the function \mathcal{F}_{cT} (and some times even \mathcal{F}_{cT}^*) is taken as a linear function of the effective deflection ρ_{z_i} and the statical tire vertical stiffness $c_{T_i, z}^S$

$${}^{linear} {}^W F_{T_i, z} = c_{T_i, z}^S \cdot \rho_{z_i} , \quad (2.62)$$

for more accurate results the following polynomial

$${}^W F_{T_i, z} = \mathbb{C}_{T\omega} ({}^C\omega_{w_i, y}) \cdot \left[c_{T_i, z}^S (p_{T_i}) \cdot \rho_{z_i} + c_{T_i, z}^D (p_{T_i}) \cdot \rho_{z_i}^2 \right] , \quad (2.63)$$

is proposed in this work based on the approach according to *Hirschberg and Waser* [HW09], which considers the force ${}^W F_{T_i}$ to be a function of a statical $c_{T_i, z}^S$ and a dynamical $c_{T_i, z}^D$ tire stiffness coefficient. This approach is modified by introducing the term $\mathbb{C}_{T\omega}$, which considers the *tire hardening* due to the effect of the centrifugal force on the carcass, the belt and tread of the tire when the rotational speed ${}^C\omega_{w_i, y}$ increases (see [RSB01] and [Wal06]). Additionally, in the approach presented in this work, the tire stiffness coefficients $c_{T_i, z}^S$ and $c_{T_i, z}^D$ are supposed to be pressure dependent. The behavior of the proposed functions $\mathbb{C}_{T\omega} ({}^C\omega_{w_i, y})$, $c_{T_i, z}^S (p_{T_i})$ and $c_{T_i, z}^D (p_{T_i})$ is presented in appendix B.4 (see also [Mar09]).

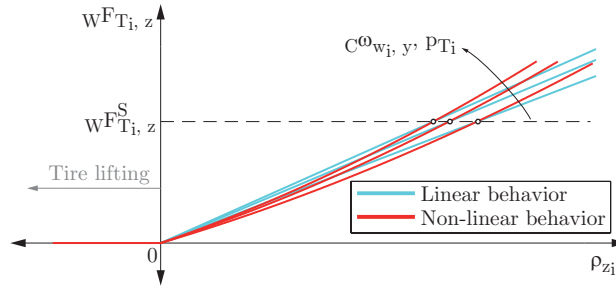


Figure 2.10.: Model of the tire vertical contact force $W F_{T_i, z}$.

2.5.3. Outputs of the tire model

Taking into account the dynamic horizontal tire forces (see chapter 2.5.1) and the vertical contact force $W F_{T_i, z}$ between tire and ground (see chapter 2.5.2) as well as the self aligning torque $W M_{T_i, z}$ the output vectors corresponding to the tire forces and moments defined in the wheel axis system $\{W O; W x, W y, W z\}$ are given by:

$$W \mathbf{F}_{T_i} = \begin{bmatrix} W F_{T_i, x}^D & W F_{T_i, y}^D & W F_{T_i, z} \end{bmatrix}^T, \quad (2.64a)$$

$$W \mathbf{M}_{T_i} = \begin{bmatrix} W M_{T_i, x} & W M_{T_i, y} & W M_{T_i, z} \end{bmatrix}^T, \quad (2.64b)$$

where $W M_{T_i, x} = 0$ in the implemented model.

2.6. Road model

In the implemented simulation environment MOVES², a road can be seen as a superposition of a three-dimensional road with banking, slope and obstacles (e.g. bumps or sinusoidal perturbations) and a grid of points with stochastic height (road roughness) and a certain friction coefficient.

2.6.1. Curved regular grid road with obstacles

A three-dimensional road without obstacles is defined in the present work as a group of straight and curved segments with certain slope and banking. In general, there are sev-

eral tools to generate the group of straight and curved segments without obstacles, like Cosin/3Droad [ss10], RoadXML© [Duc04] or OpenCRG® (see [Gmb10] and [Rau08]). This last option was integrated in the simulation environment MOVES² due to following reasons (see [RNFD11] and [Fer11]): it is open source, it is developed in the same language as the environment itself (MATLAB), its development is supported by many *original equipment manufacturers - OEMs*, and it is compatible with several tire models (e.g. MF-Tyre and MF-SWIFT [VS10], FTire [GH10], RMOD-K [FS10]) and other road generation tools and formats - even with measured road data - (see e.g. [GH10] and [Grä10]). With OpenCRG®, roads are generated based on a *Curved Regular Grid - CRG*, i.e. a grid of points regularly spaced and defined in a cartesian coordinate system that is afterwards stretched along a curved line defining the road center line (see e.g. [RMB08], [Ma95] and [Atk02]). This approach enhances the computational efficiency while running simulations and reduces the amount of information needed to describe a road [RMB08]. With the integration of OpenCRG® in the simulation environment MOVES², obstacles (e.g. ramps, potholes, bumps or sinusoidal perturbations) can be added to the three-dimensional generated roads, as can be seen in figure 2.11.

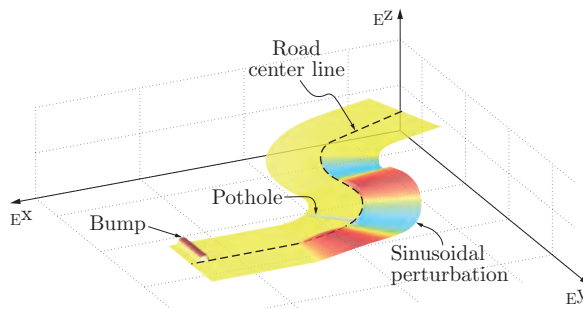


Figure 2.11.: Three-dimensional road with obstacles generated with the *Curved Regular Grid* approach of OpenCRG® and the simulation environment MOVES².

2.6.2. Road roughness

In the first part of this chapter, a short introduction to the description of road surfaces based on its power spectral density Φ_{road} is given. Afterwards, a method to generate a three-dimensional grid of points from a given spectral density is presented. This grid of points can be used in the simulation environment together with the vehicle and the tire models (see chapters 2.4 and 2.5 respectively) to simulate driving maneuvers on roads with a certain superficial roughness.

Power spectral density of a road

Isotropic road surfaces can be seen as stochastic signals described by stationary, normally distributed, ergodic random processes [Hir09a]. In turn, these processes can be seen as a superposition of an infinite number of harmonic signals with different amplitudes, frequencies and phase angles. The power spectral density¹² Φ_{road} is used to describe the distribution of amplitudes of the harmonic signals $E^{Z_{road}}$ composing a given random process (in this case, a road surface $E^{Z_{road}}$) with respect to the frequency. It specifies the square of the effective value¹³ $E^{Z_{road}, rms}$ of the amplitude of the expected harmonic signal in a considered frequency range Δf

$$\Phi_{road}(f) = \frac{(E^{Z_{road}, rms})^2}{\Delta f} = \frac{(E^{\hat{Z}_{road}})^2}{2 \cdot \Delta f}, \quad (2.65)$$

where $E^{\hat{Z}_{road}} = \sqrt{2} \cdot E^{Z_{road}, rms}$ corresponds to the amplitude of an individual harmonic signal $E^{Z_{road}}$ considered.

Since the time frequency f [Hz] depends on the vehicle speed $v \cdot \dot{x}$ when driving over a harmonic signal, the angular spatial frequency Ω [rad/m], given by

$$\Omega = \frac{2 \cdot \pi}{v \cdot \dot{x}} \cdot f, \quad (2.66)$$

is used instead. The units of the spectral density Φ_{road} depend only on the units of the considered signal. In case of the road unevenness $E^{Z_{road}}$ [m], called displacement spectral density, it is then given in¹⁴ [m²·m/cycle]. The classification and characterization of roads is specified in the international standard ISO 8608:1995(E) [fSI95]. In figure 2.12 the power spectral density of some typical roads is shown.

In the mentioned international standard, following method to approximate real displacement spectral densities is proposed:

$$\Phi_{road}(\Omega) = \Phi_{road}(\Omega_0) \cdot \left(\frac{\Omega_0}{\Omega} \right)^w, \quad (2.67)$$

where Ω_0 is the reference angular spatial frequency and is equal to 1 rad/m. The displace-

¹²Strictly speaking it corresponds to the one sided power spectral density; nevertheless the term *power spectral density* will be used to refer to the two sided case.

¹³Also known as *root mean square* - rms - in mathematics.

¹⁴The description in [m³] or [cm³] is also widespread (see for example [MW04]).

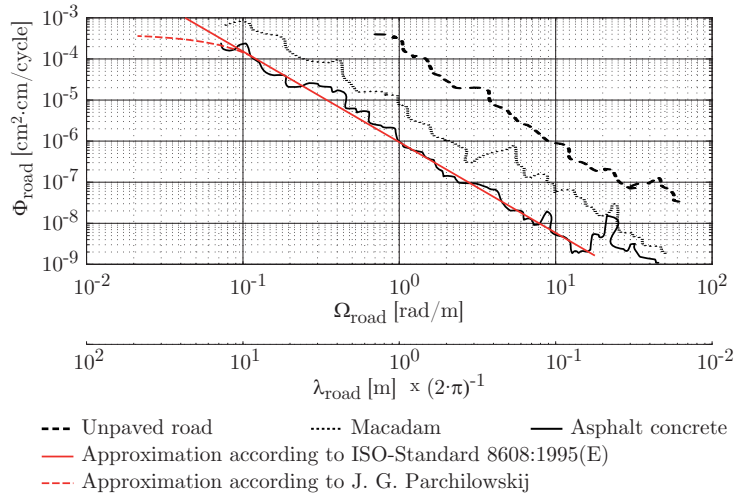


Figure 2.12.: Power spectral density of some common road types and approximation according to the international standard ISO 8608:1995(E) [fSI95] and to J. G. Parchilowskij (see [MW04]).

ment spectral density $\Phi_{road}(\Omega_0)$ and the waviness exponent w are used to characterize the road (the value of w oscillates around 2 [MW04]). Furthermore, roads can be classified from *A* (e.g. good paved road) to *H* (e.g. rough gravel road) according to the value of $\Phi_{road}(\Omega_0)$, which can be determined according to (see also [fSI95]):

$$\Phi_{road}(\Omega_0) = 4^{\mathbb{R}}, \quad (2.68)$$

where the exponent \mathbb{R} corresponds to the position of the letter representing the considered road type within the alphabet (e.g. $\mathbb{R} = 1$ for road type *A* and $\mathbb{R} = 3$ for road type *C*).

Nevertheless, the approximation given by equation 2.67 results in $\Phi_{road}(\Omega) \rightarrow \infty$ for $\Omega \rightarrow 0$, i.e. for wave lengths $\lambda_{road} \rightarrow \infty$. Since this does not correspond to the reality, *J. G. Parchilowskij* introduced the shape coefficient β_P in equation 2.65

$$\Phi_{road}(\Omega) = \Phi_{road}(\Omega_0) \cdot \left(\frac{\Omega_0^w}{\Omega^w + \beta_P^w} \right), \quad (2.69)$$

which results in finite values for infinite wave lengths (see figure 2.12).

Reconstruction of a road based on a given power spectral density

In this section a computationally efficient method to reconstruct an uneven road described as a stationary, normally distributed and ergodic random process is presented. Stationary means that the statistical values (e.g. mean value or standard deviation) of the road are time independent, the normal distribution concerns the height of the road points and the ergodic character indicates that it is possible to deduce the properties and characteristic values of every road belonging to certain road class (see [fSI95] based on only one of them. In the first part of this section, the two dimensional approach to reconstruct roads is presented; afterwards, it is extended to the three dimensional case.

Two dimensional method There are several methods to reconstruct the excitation signal Ez_{road} from the displacement spectral density $\Phi_{road}(\Omega)$ approximated by equation 2.69 (see for example [Hir09a], [Dór06], [BPR0] and [Bog06]). A computationally efficient method was proposed by S. O. Rice in 1952 [Ric52] (see also [Hir09a] and [Bau87]). According to this method, the given power spectral density is divided in n frequency bands with identical area A_c (see figure 2.13).

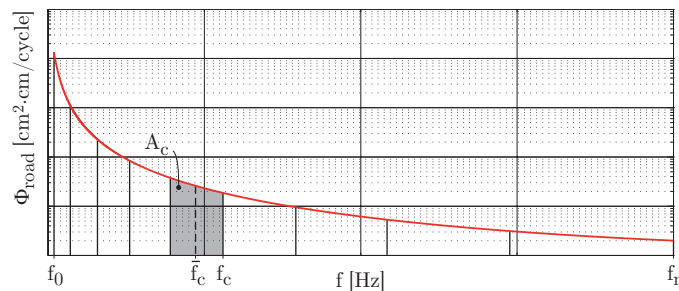


Figure 2.13.: Rice method to reconstruct a road based on a given power spectral density.

A signal $z(t)$ in the time domain characterized by the power spectral density $\Phi(f)$ given by¹⁵

$$\Phi(f) = \frac{2 \cdot \pi}{v \dot{x}} \cdot \Phi(\Omega) \quad (2.70)$$

¹⁵Analogously, the power spectral density can be expressed as a function of the angular frequency $\omega = 2 \cdot \pi \cdot f$ as $\Phi(\omega) = \frac{1}{v \dot{x}} \cdot \Phi(\Omega)$.

can be approximated as the sum of n cosine functions

$$z(t) = \sum_{c=1}^n C_c \cdot \cos(2 \cdot \pi \cdot \bar{f}_c \cdot t - \varphi_c) , \quad (2.71)$$

where \bar{f}_c corresponds to the central frequency of the considered frequency band c and the coefficients C_c are expressed as:

$$C_c = \sqrt{2 \cdot A_c} , \quad (2.72)$$

with the area of each frequency band generally calculated as

$$A_c = \int_{f_{c-1}}^{f_c} \Phi(f) df . \quad (2.73)$$

Nevertheless, since frequency bands with equal area are assumed, A_c correspond to a constant value and the equation 2.73 simplifies to:

$$A_c = \frac{1}{n} \cdot \int_{f_0}^{f_n} \Phi(f) df . \quad (2.74)$$

Since the information about the phase angle φ is not contained in the power spectral density $\Phi(f)$, the individual values φ_c in equation 2.71 can be obtained with a random generator with uniform distribution in the range $[0, 2 \cdot \pi)$.

Three dimensional method The approach of *J. F. Parkhilowski* is used to generate a three dimensional road (see figure 2.14). According to this approach, there is no correlation between the pure lifting and the pure rolling excitation signals of a real road (see [MW04] and [Bau87]) and the entire road can be described based on the power spectral density of the middle track $\Phi_{z_m}(\Omega)$ and the angle $\Phi_{\delta_{road}}(\Omega)$:

$$\Phi_{z_m}(\Omega) = \frac{1}{1 + \kappa_{road}} \cdot \Phi_{road}(\Omega_0) \cdot \left(\frac{\Omega_0^w}{\Omega^w + \beta_{P_1}^w} \right) , \quad (2.75a)$$

$$\Phi_{\delta_{road}}(\Omega) = \frac{\kappa_{road}}{b_{road}^2 \cdot (1 + \kappa_{road})} \cdot \Phi_{road}(\Omega_0) \cdot \left(\frac{\Omega_0^w}{\Omega^w + \beta_{P_2}^w} \right) , \quad (2.75b)$$

where b_{road} represents the distance from the middle track to the considered track to be reconstructed, β_{P_1} and β_{P_2} are analogous to the shape coefficient β_P introduced by *J. G.*

Parchilowskij in equation 2.69 to avoid infinite values of Φ_{road} for $\lambda_{road} \rightarrow \infty$, and the parameter κ_{road} is a measure of the correlation between the track on the left $Ez_{road, l}$ and the corresponding (i.e. at the same distance b_{road}) track on the right $Ez_{road, r}$.

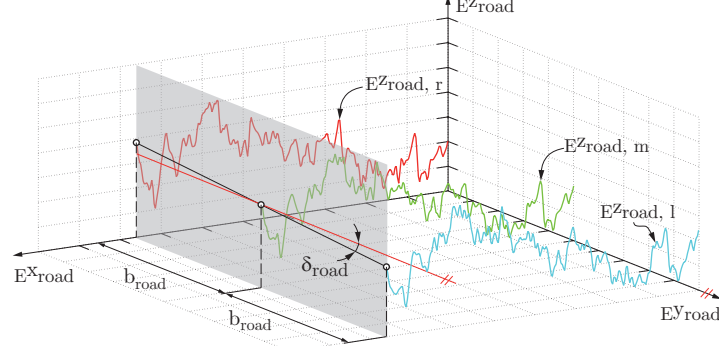


Figure 2.14.: Three-dimensional road model according to *J. F. Parkhilowskij* (see [Hir09a] and [Bau87]).

The correlation parameter κ_{road} is related with the coherence function γ_{road} , which is a widespread measure for the relation between a track to the left and a track to the right of the middle track, by (for details see [Bau87]):

$$\gamma_{road} = \frac{\Phi_{z_m}(\Omega) - b_{road}^2 \cdot \Phi_{\delta_{road}}}{\Phi_{z_m}(\Omega) + b_{road}^2 \cdot \Phi_{\delta_{road}}} = \frac{(1 - \kappa_{road}) \cdot \Omega^w - \kappa_{road} \cdot \beta_{P_1}^w + \beta_{P_2}^w}{(1 + \kappa_{road}) \cdot \Omega^w + \kappa_{road} \cdot \beta_{P_1}^w + \beta_{P_2}^w}. \quad (2.76)$$

From equation 2.76 it is clear, that the far two tracks are from each other (i.e. the greater b_{road}), the lower is their correlation for all values of the angular spatial frequency Ω and for a constant κ_{road} . Furthermore, for $\kappa_{road} = 0$ is the coherence function $\gamma_{road} = 1$ for all values of Ω , i.e. the tracks on both sides of the middle track correlate totally. Additionally, increasing κ_{road} results in lower values of γ_{road} for a constant Ω . Other models relating the coherence function with the distance b_{road} from any track to the middle track and the angular spatial frequency Ω can be found in [Bog08].

Using the method explained in section 2.6.2, it is possible to reconstruct the signals for the middle track $z_m(t)$ and for the angle $\delta_{road}(t)$ and use them to reconstruct any track at the left $Ez_{road, l}$ or at the right $Ez_{road, r}$ of the middle track:

$$Ez_{road, l}(t) = z_m(t) - b_{road} \cdot \delta_{road}(t), \quad (2.77a)$$

$$Ez_{road, r}(t) = z_m(t) + b_{road} \cdot \delta_{road}(t). \quad (2.77b)$$

By varying the distance b_{road} from zero to the desired road width, a regular grid of points representing a straight road with the roughness described by the given power spectral density Φ_{road} is obtained. This grid can be overlapped with a curved regular grid generated with *OpenCRG*® (see chapter 2.6.1) to obtain any curved road with a desired roughness (some examples are presented in [Fer11]).

2.7. Passive suspension system model

In this section, the models for the suspension spring and the shock absorber belonging to a passive suspension system, as those of the test vehicle (see appendix B), are presented (see also [RNW10]). Special attention was given to the balance of the complexity and accuracy between the different components. The goal was to model the different components in the simplest way assuring an acceptable correspondence with the reality at the same time. The values of all model parameters are presented in chapter B.5 of appendix B. Furthermore, following assumption was made:

Assumption 2.3: *In the assumption 2.2 was stated, that only the vertical movement of the non-suspended masses is considered. Accordingly, it is assumed here that the forces induced by the suspension spring and by the shock absorber are only functions of the relative vertical displacement and relative vertical speed between the considered wheel (non-suspended mass) and the suspension attachment point at the suspended mass respectively (see also chapter 2.4.2).*

Additionally, the forces induced in the suspension elements are considered to act directly over the tire wheel contact point W . Therefore, all suspension model parameters must be taken as *wheel-related*. To determine the corresponding values at element level, the suspension geometry must be taken into account (see e.g. [Wal06]). Based on this, total force of the passive suspension system ${}_C\mathbf{F}_{ws_i}$ (see chapter 2.4) is given by the sum of the (vertical) forces of the suspension spring ${}_C\mathbf{F}_{c_i}$ and the shock absorber ${}_C\mathbf{F}_{d_i}$:

$${}_C\mathbf{F}_{ws_i} = {}_C\mathbf{F}_{c_i} + {}_C\mathbf{F}_{d_i} . \quad (2.78)$$

2.7.1. Suspension spring

The suspension spring can be considered as a force element characterized by a continuously derivable function \mathcal{F}_c of the spring deformation $\Delta z_{c_i} = {}_C z_{C_i} - {}_C z_{AP_{wi}}$:

$${}_C \mathbf{F}_{c_i} = \mathcal{F}_c(\Delta z_{c_i}) = \mathcal{F}_c({}_C z_{C_i} - {}_C z_{AP_{wi}}), \quad (2.79)$$

where ${}_C z_{C_i}$ corresponds to the vertical position of the center point of the considered wheel and ${}_C z_{AP_{wi}}$ stands for the vertical position of the attachment point AP_{wi} of the corresponding suspension spring to the suspended mass (see also equation 2.18). The function \mathcal{F}_c is taken as linear

$${}^{linear}{}_C \mathbf{F}_{c_i} = c_{b_i}^S \cdot \Delta z_{c_i} = c_{b_i}^S \cdot ({}_C z_{C_i} - {}_C z_{AP_{wi}}) \quad (2.80)$$

in most of the preliminary investigations (with $c_{b_i}^S$ as suspension spring static coefficient - see also equation 2.83) and the results approximate quite well the behavior of a cylindrical coil spring with constant wire diameter and constant coil distance. However, even in the case of such a simple spring, it is reasonable to take into account the effect of other elastic elements used in real vehicle suspensions, such as additional rubber springs (*bump stops*) and elastic mountings if strong vertical acceleration values (shocks) are expected (e.g. while simulating a driving over potholes, square-edged bumps or curbs). On the other side, the consideration of the influence of all elastic elements of the vehicle suspension would lead to a complex model and increased simulation times. Therefore, a compromise between model simplicity and complexity is normally made. In this work, all the influences mentioned before are assumed to be summarized in a spring having a characteristic line divided in three regions, as can be seen in figure 2.15. In the approach used here, hysteresis effects are neglected. A description of some suspension springs with continuously nonlinear behavior like those with variable coil and wire diameter or variable coil distance as well as the gas and hydro-pneumatic springs can be found in [MW04] and [Wal06].

Furthermore, the design of the dynamic behavior of a spring must comply with three criteria: first, the deflection range (approximately the range covered by the region II in figure 2.15) must correspond to the available space in the wheel housing. Second, the static ground clearance $\Delta z_{c_i}^S$ should be enough to overcome obstacles present on the road under normal driving conditions. And third, a comfortable vehicle vibration behavior should be assured. To fulfill these conditions, a computationally efficient semi-

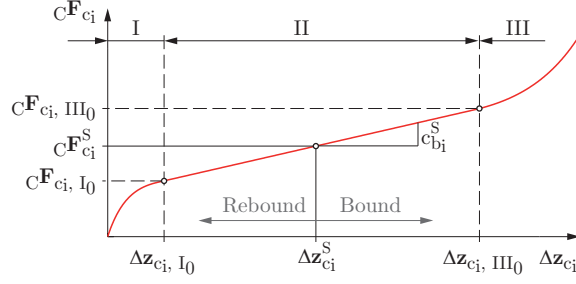


Figure 2.15.: Characteristic deformation-force curve of the suspension spring according to the developed model.

physical spring model is proposed in this work. The parameter values corresponding to the suspension springs at the front and the rear axle of the test vehicle as well as the obtained characteristic force-displacement curves are presented in appendix B.5.

Region II: Considering a quarter vehicle model (see section E.2 in appendix E), the natural frequency f_{Aq} of the vertical movement of the suspended mass¹⁶ m_{Aq} can be expressed as (see also [HW09]):

$$f_{Aq} = \frac{1}{2 \cdot \pi} \cdot \sqrt{\frac{c_b^*}{m_{Aq}}}, \quad (2.81)$$

where $1.0 \text{ Hz} \leq f_{Aq} \leq 1.2 \text{ Hz}$ (see e.g. [HW09] and [Wal06]), and c_b^* corresponds to the equivalent spring coefficient which considers the suspension spring (characterized by its static value $c_{b_i}^S$) and the statical tire vertical stiffness ($c_{T_i, z}^S$) in series:

$$c_b^* = \frac{c_{b_i}^S \cdot c_{T_i, z}^S}{c_{b_i}^S + c_{T_i, z}^S}. \quad (2.82)$$

As can be seen in equation 2.81, the natural frequency f_{Aq} varies with the suspended mass m_{Aq} . Since large variations in the natural frequency are related with low comfort levels (see e.g. [MW04]), the mass m_{Aq, h_load} corresponding to a quarter of the half loaded vehicle is employed to determine the value of the suspension spring static coefficient (see also [Hir09a]):

$$c_{b_i}^S = \frac{m_{Aq, h_load} \cdot (2 \cdot \pi \cdot f_{Aq})^2 \cdot c_{T_i, z}^S}{c_{T_i, z}^S - m_{Aq, h_load} \cdot (2 \cdot \pi \cdot f_{Aq})^2}. \quad (2.83)$$

¹⁶A quarter of the total suspended mass is considered by the quarter vehicle model. To indicate variables related with this model, the right subscript q is used.

The linear relationship

$${}_C\mathbf{F}_{c_i, II} = c_{b_i}^S \cdot \Delta z_{c_i, II} + {}_C\mathbf{F}_{c_i, I_0} \quad (2.84)$$

between suspension spring force ${}_C\mathbf{F}_{c_i, II}$ and the spring deflection

$$\Delta z_{c_i, II} = \Delta z_{c_i} - \Delta z_{c_i, I_0} \quad (2.85)$$

in this region leads to linear changes in the acceleration induced in the suspended mass, where ${}_C\mathbf{F}_{c_i, I_0}$ corresponds to the spring force at the limit $\Delta z_{c_i, I_0}$

$${}_C\mathbf{F}_{c_i, I_0} = {}_C\mathbf{F}_{c_i}^S - c_{b_i}^S \cdot (\Delta z_{c_i}^S - \Delta z_{c_i, I_0}) . \quad (2.86)$$

In the regions I and III, nonlinear changes in the body acceleration are induced. Since there is evidence showing that linear changes in the induced vertical acceleration yields to a better comfort perception (see e.g. [ST06]), the limits $\Delta z_{c_i, I_0}$ and $\Delta z_{c_i, III_0}$ of the region II must be set to account for most of the working conditions in the life of the suspension spring.

Region III: The effect of the additional rubber spring or *bump stop* on the suspension spring force ${}_C\mathbf{F}_{c_i, III}$ in this region can be modeled using an exponential coefficient $n_{c,III}$

$${}_C\mathbf{F}_{c_i, III} = c_{b_i}^S \cdot (\Delta z_{c_i, III})^{n_{c,III}} + {}_C\mathbf{F}_{c_i, III_0} , \quad (2.87)$$

as a function of the spring deflection

$$\Delta z_{c_i, III} = \Delta z_{c_i} - \Delta z_{c_i, III_0} + \Delta z_{c_i, n_{c,III}} \quad (2.88)$$

in this region and the spring force at the limit $\Delta z_{c_i, III_0}$

$${}_C\mathbf{F}_{c_i, III_0} = {}_C\mathbf{F}_{c_i}^S + c_{b_i}^S \cdot (\Delta z_{c_i, III_0} - \Delta z_{c_i}^S) , \quad (2.89)$$

where

$$\Delta z_{c_i, n_{c,III}} = \frac{\Delta z_{c_i}}{|\Delta z_{c_i}|} \cdot \left(\frac{1}{n_{c,III}} \right)^{(n_{c,III} - 1)^{-1}} \quad (2.90)$$

is a correction term to guarantee the same gradient at the limit between the regions II and III.

Region I: A similar approach as in the region III is used. The spring force in this region is expressed as

$${}_C\mathbf{F}_{c_i, I} = {}_C\mathbf{F}_{c_i, I_0} - c_{b_i}^S \cdot (\Delta z_{c_i, I_0} - \Delta z_{c_i})^{n_{c,I}} , \quad (2.91)$$

where the spring force ${}_C\mathbf{F}_{c_i, I_0}$ at the limit $\Delta z_{c_i, I_0}$ is given by equation 2.86. Nevertheless, the exponent $n_{c,I}$ must be selected in such a way that ${}_C\mathbf{F}_{c_i, I} = 0$ N for $\Delta z_{c_i, I} = 0$ m, i.e. when the suspension spring is not deflected, which leads to

$$n_{c,I} = \frac{\log_{10} ({}_C\mathbf{F}_{c_i, I_0} / c_{b_i}^S)}{\log_{10} (\Delta z_{c_i, I_0})} . \quad (2.92)$$

Total suspension spring force: The total suspension spring force can be expressed as:

$${}_C\mathbf{F}_{c_i} = \begin{cases} {}_C\mathbf{F}_{c_i, I}; & \text{if } \Delta z_{c_i} \leq \Delta z_{c_i, I_0}, \\ {}_C\mathbf{F}_{c_i, II}; & \text{if } \Delta z_{c_i, I_0} < \Delta z_{c_i} \leq \Delta z_{c_i, III_0}, \\ {}_C\mathbf{F}_{c_i, III}; & \text{if } \Delta z_{c_i, III_0} < \Delta z_{c_i}. \end{cases} \quad (2.93)$$

2.7.2. Shock absorber

Modeling the shock absorber behavior is a challenging task since it is characterized by a nonlinear and time-variant behavior [DSR97]. Several physical, semi-physical and empirical modeling approaches are presented in the literature (an overview can be found in [AHG06]). In this work, the computationally efficient semi-physical model presented schematically in figure 2.16 is proposed. The parameter values corresponding to the shock absorbers at the front and the rear axle of the test vehicle as well as the obtained characteristic speed-force curves are presented in appendix B.5.

In this model, the characteristic speed-force curve of the shock absorber is a continuously derivable function \mathcal{F}_d of its deformation speed $\Delta \dot{z}_{d_i} = {}_C\dot{z}_{C_i} - {}_C\dot{z}_{AP_{wi}}$:

$${}_C\mathbf{F}_{d_i} = \mathcal{F}_d(\Delta \dot{z}_{d_i}) = \mathcal{F}_d({}_C\dot{z}_{C_i} - {}_C\dot{z}_{AP_{wi}}) , \quad (2.94)$$

where ${}_C\dot{z}_{C_i}$ corresponds to the vertical speed of the center point of the considered wheel and ${}_C\dot{z}_{AP_{wi}}$ stands for the vertical speed of the attachment point AP_{wi} of the corresponding shock absorber to the suspended mass (see also equation 2.18). The

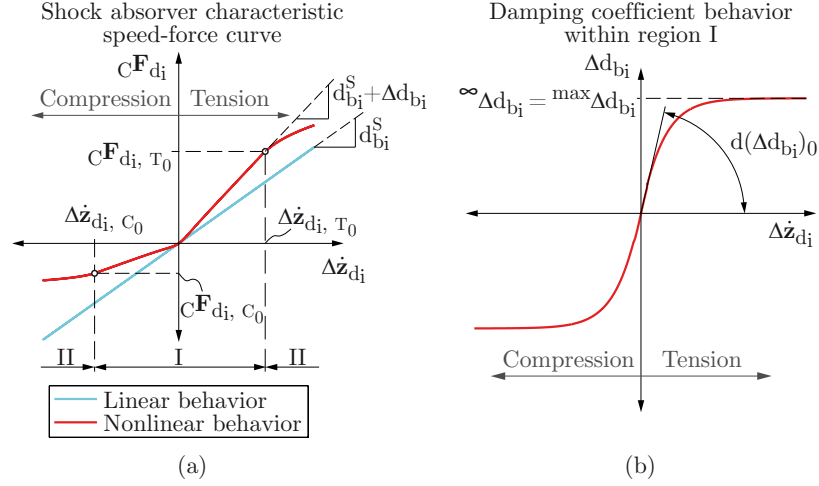


Figure 2.16.: Model of the shock absorber: characteristic speed-force curve divided in a region I of low and a region II of high deflection speeds (a) and behavior of the deviation Δd_{b_i} within the region I with respect to the value of the static damping coefficient $d_{b_i}^S$ (b).

function \mathcal{F}_d is taken as linear

$${}^{linear} C \mathbf{F}_{d_i} = d_{b_i}^S \cdot \Delta \dot{z}_{d_i} = d_{b_i}^S \cdot (C \dot{z}_{C_i} - C \dot{z}_{AP_{wi}}) \quad (2.95)$$

in most of the preliminary investigations (with $d_{b_i}^S$ as linear damping coefficient - see also equation 2.105) and the results can be used to explain fundamental phenomena. However, to obtain more accurate results, it is reasonable to take into account both the different behavior of the speed-force curve in tension and compression, and the behavior of this curve after the relief mechanisms of the damper (e.g. relief valves) are activated (see e.g. [HEG11]). To account for this, a shock absorber model consisting of two deflection speed regions is proposed. The two regions are limited by the deflection speeds $\Delta \dot{z}_{d_i, C_0}$ and $\Delta \dot{z}_{d_i, T_0}$ for which the relief valves open in bound and rebound respectively (see figure 2.16-a).

Region I: In this region, the different behavior of the shock absorber in tension and compression is depicted. When driving over a non-flat road, certain amount of energy is introduced into the vibrating system consisting of the suspended and the non-suspended masses. The function of the shock absorber is to dissipate this introduced energy reducing the oscillations and enhancing (primarily) hereby the riding comfort. The force of

the shock absorber in this region can be considered to be given as:

$${}_C\mathbf{F}_{d_i, I} = \begin{cases} {}_C\mathbf{F}_{d_i, C}; & \text{during compression, i.e. if } \Delta\dot{z}_{d_i, C_0} < \Delta\dot{z}_{d_i} \leq \mathbf{0}, \\ {}_C\mathbf{F}_{d_i, T}; & \text{during tension, i.e. if } \mathbf{0} < \Delta\dot{z}_{d_i} \leq \Delta\dot{z}_{d_i, T_0}. \end{cases} \quad (2.96)$$

During compression, it is desired to reduce the force ${}_C\mathbf{F}_{d_i, C}$ transmitted from the road excitation signal over the shock absorber into the suspended mass in order to avoid high vertical acceleration values and therefore to enhance the ride comfort perception. This can be observed in figure 2.16-a when comparing the characteristic curves of a shock absorber with linear and nonlinear behavior during compression. Nevertheless, a lower force during compression reduces the amount of dissipated energy from the vibrating system, extending, therefore, the period of time during which the suspended mass is oscillating. This would lead to a worse ride comfort perception. To avoid this undesired effect, more energy is dissipated during tension by introducing a higher shock absorber force ${}_C\mathbf{F}_{d_i, T}$ for a certain deflection speed $\Delta\dot{z}_{d_i}$ (compare linear and nonlinear behavior during tension in figure 2.16-a). *Wallentowitz* [Wal06] defines the relation between the shock absorber force during compression ${}_C\mathbf{F}_{d_i, C}$ and tension ${}_C\mathbf{F}_{d_i, T}$ in this region as:

$$\gamma_d = \frac{|{}_C\mathbf{F}_{d_i, T}|}{|{}_C\mathbf{F}_{d_i, T} + {}_C\mathbf{F}_{d_i, C}|}. \quad (2.97)$$

Assuming that the forces ${}_C\mathbf{F}_{d_i, C}$ and ${}_C\mathbf{F}_{d_i, T}$ can be expressed in a similar way as in equation 2.95 as a linear function of the deflection speed of the shock absorber $\Delta\dot{z}_{d_i}$ and a damping coefficient for compression $d_{b_i, C}$ and tension $d_{b_i, T}$ respectively

$${}_C\mathbf{F}_{d_i, C} = d_{b_i, C} \cdot \Delta\dot{z}_{d_i}, \quad (2.98a)$$

$${}_C\mathbf{F}_{d_i, T} = d_{b_i, T} \cdot \Delta\dot{z}_{d_i}, \quad (2.98b)$$

equation 2.97 can be rewritten as:

$$\gamma_d = \frac{d_{b_i, T}}{d_{b_i, T} + d_{b_i, C}}. \quad (2.99)$$

Furthermore, assuming that the damping coefficient during compression $d_{b_i, C}$ and tension $d_{b_i, T}$ can be written in terms of their difference Δd_{b_i} with respect to the linear

damping coefficient $d_{b_i}^S$ as

$$d_{b_i, C} = d_{b_i}^S - \Delta d_{b_i} , \quad (2.100a)$$

$$d_{b_i, T} = d_{b_i}^S + \Delta d_{b_i} , \quad (2.100b)$$

the difference Δd_{b_i} (see also figure 2.16-b) can be expressed as:

$$\Delta d_{b_i} = d_{b_i}^S \cdot (2 \cdot \gamma_d - 1) . \quad (2.101)$$

In this work, a similar function to that used in the horizontal tire model TMsimple (see equation 2.26 in chapter 2.5.1) is proposed to model the behavior of the difference Δd_{b_i} within the region I:

$$\Delta d_{b_i} = K_d \cdot \sin \left[B_d \cdot \left(1 - e^{-|\Delta \dot{z}_{d_i}|/A_d} \right) \cdot \text{sign}(\Delta \dot{z}_{d_i}) \right] , \quad (2.102)$$

with the coefficients K_d , B_d and A_d given by:

$$K_d = \Delta d_{b_i} , \quad (2.103a)$$

$$B_d = \pi - \arcsin \left(\frac{\infty \Delta d_{b_i}}{\max \Delta d_{b_i}} \right) = \pi - \arcsin(1) = \frac{\pi}{2} , \quad (2.103b)$$

$$A_d = \frac{1}{d(\Delta d_{b_i})_0} \cdot K_d \cdot B_d , \quad (2.103c)$$

where $d(\Delta d_{b_i})_0$ is defined in terms of the limit speeds $\Delta \dot{z}_{d_i, C_0}$ and $\Delta \dot{z}_{d_i, T_0}$ as:

$$d(\Delta d_{b_i})_0 = \min(\Delta \dot{z}_{d_i, C_0}, \Delta \dot{z}_{d_i, T_0})^{-1} . \quad (2.104)$$

Finally, considering a quarter vehicle model (see chapter E.2 in appendix E), the linear damping coefficient $d_{b_i}^S$ can be written as a function of the desired damping ratio ξ_d , the value of the suspension spring static coefficient¹⁷ $c_{b_i}^S$ (see equation 2.83) and the mass of the quarter vehicle m_{Aq} as:

$$d_{b_i}^S = 2 \cdot \xi_d \cdot \sqrt{c_{b_i}^S \cdot m_{Aq}} . \quad (2.105)$$

¹⁷It is assumed that the value of the static tire vertical stiffness $c_{T_i, z}^S$ is much larger than the static value of the suspension spring coefficient $c_{b_i}^S$, i.e. $c_{T_i, z}^S \gg c_{b_i}^S$ (see also [HW09] and appendix B).

Since $d_{b_i}^S$ depends on the vehicle mass which changes with the load situation, a suitable compromise is to assume the half loaded vehicle mass, i.e. $m_{Aq} \approx m_{Aq,h_load}$ (see e.g. [HW09]).

Region II: This region is characterized by faster shock absorber deflections as those present in region I. To avoid cavitation and damage of the shock absorber, additional relief devices (e.g. relief valves) can be opened (see e.g. [AHG06], [GWL11] and [HEG11]) at certain deflection speeds $\Delta\dot{z}_{d_i, C_0}$ and $\Delta\dot{z}_{d_i, T_0}$, which define the limits between regions I and II. To determine the force of the shock absorber in this region during compression and tension (see figure 2.16-a) an exponential model similar to that presented in chapter 2.7.1 for the suspension spring is proposed in this work:

$${}_C\mathbf{F}_{d_i, II} = f_{\kappa_d} \cdot d_{b_i, C/T} \cdot \frac{\Delta\dot{z}_{d_i} - \delta\Delta\dot{z}_{d_i}}{|\Delta\dot{z}_{d_i} - \delta\Delta\dot{z}_{d_i}|} \cdot (\Delta\dot{z}_{d_i} - \delta\Delta\dot{z}_{d_i})^{n_{d,T}} + \delta{}_C\mathbf{F}_{d_i, II}. \quad (2.106)$$

The exponent $n_{d,T}$ defines the behavior of the shock absorber force during tension. A progressive, linear or degressive behavior can be adjusted depending whether the value of $n_{d,T}$ is positive, negative or equal 1 (see also [Wal06]). Furthermore, since the behavior of the shock absorber force during compression and tension normally differs from each other in this region (see e.g. [GWL11]), the factor κ_d

$$\kappa_d = \frac{|{}_C\mathbf{F}_{d_i, T, II}|}{|{}_C\mathbf{F}_{d_i, T, II} + {}_C\mathbf{F}_{d_i, C, II}|} \quad (2.107)$$

can be defined. Based on this factor, the term f_{κ_d} accounting for the mentioned difference between the shock absorber force in compression and tension can be expressed as:

$$f_{\kappa_d} = \begin{cases} \frac{1 - \kappa_d}{\kappa_d}; & \text{during compression, i.e. if } \Delta\dot{z}_{d_i} \leq \Delta\dot{z}_{d_i, C_0}, \\ 1; & \text{during tension, i.e. if } \Delta\dot{z}_{d_i, T_0} < \Delta\dot{z}_{d_i}. \end{cases} \quad (2.108)$$

The term $d_{b_i, C/T}$ accounts for the different damping coefficients at the deflection speed limits $\Delta\dot{z}_{d_i, C_0}$ and $\Delta\dot{z}_{d_i, T_0}$ and can be obtained from equations 2.100 and 2.101 as:

$$d_{b_i, C/T} = \begin{cases} 2 \cdot d_{b_i}^S \cdot (1 - \gamma_d); & \text{during compression, i.e. if } \Delta\dot{z}_{d_i} \leq \Delta\dot{z}_{d_i, C_0}, \\ 2 \cdot d_{b_i}^S \cdot \gamma_d; & \text{during tension, i.e. if } \Delta\dot{z}_{d_i, T_0} < \Delta\dot{z}_{d_i}. \end{cases} \quad (2.109)$$

The terms $\delta\Delta\dot{z}_{d_i}$ and $\delta{}_C\mathbf{F}_{d_i, II}$ correspond to correction factors to guarantee the same gradient at the limits between the regions I and II. $\delta\Delta\dot{z}_{d_i}$ is defined as a function of the

deflection speed¹⁸ $\Delta\dot{z}_{d_i, n_d}$, with

$$\Delta\dot{z}_{d_i, n_d} = \frac{\Delta\dot{z}_{d_i}}{|\Delta\dot{z}_{d_i}|} \cdot \left(f_{\kappa_d} \cdot n_{d,T} \right)^{- (n_{d,T} - 1)}, \quad (2.110)$$

for which the exponential function proposed for region II has the same gradient as for the function defining the shock absorber force in region I, as:

$$\delta\Delta\dot{z}_{d_i} = \Delta\dot{z}_{d_i, C_0/T_0} - \Delta\dot{z}_{d_i, n_d} \quad (2.111)$$

Finally, the correction term $\delta_C \mathbf{F}_{d_i, II}$ accounting for different force values given by the models proposed for the regions I and II is defined as the difference between the force

$${}_C \mathbf{F}_{d_i, n_d} = f_{\kappa_d} \cdot d_{b_i, C/T} \cdot \frac{\Delta\dot{z}_{d_i, n_d}}{|\Delta\dot{z}_{d_i, n_d}|} \cdot (\Delta\dot{z}_{d_i, n_d})^{n_{d,T}} \quad (2.112)$$

given by the exponential model in region II, and the force

$${}_C \mathbf{F}_{d_i, C_0/T_0} = d_{b_i}^S \cdot \Delta\dot{z}_{d_i, C_0/T_0} \quad (2.113)$$

given by the model in the region I at the limits $\Delta\dot{z}_{d_i, C_0}$ and $\Delta\dot{z}_{d_i, T_0}$ between the regions I and II as:

$$\delta_C \mathbf{F}_{d_i, II} = {}_C \mathbf{F}_{d_i, C_0/T_0} - {}_C \mathbf{F}_{d_i, n_d}. \quad (2.114)$$

2.8. Model validation

To validate the different models presented in this chapter, the model parameters shown in appendix B corresponding to the test vehicle Opel Combo 1.6 CNG were used. As shown schematically in figure 2.17, the test vehicle was equipped with a wheel vector system to measure the wheel position and orientation, acceleration sensors at the front left and the rear right wheel as well as at all wheel housings, a measurement steering wheel, a three-dimensional fibre-optic gyroscope, an incremental GPS-Sensor¹⁹ and an optic speed over ground sensor. With this last sensor, the sideslip angle β can be determined as

$$\beta = \beta_0 + \Delta\beta = \arctan \left(\frac{V\dot{y}}{V\dot{x}} \right), \quad (2.115)$$

¹⁸The variable $\Delta\dot{z}_{d_i, n_d}$ is defined analogously to $\Delta z_{c_i, n_{c,III}}$ in equation 2.90.

¹⁹Global Positioning System.

where $\Delta\beta$ corresponds to the *difference sideslip angle*, which is obtained as a sensor output and is an approximation for the slip angle at the rear axle (see also equation 2.33 and [Hir09a]), and the *base sideslip angle* β_0

$$\beta_0 \approx \frac{l_{hs}}{R_t}, \quad (2.116)$$

which is a function of the longitudinal sensor position l_{hs} and the trajectory radius R_t .

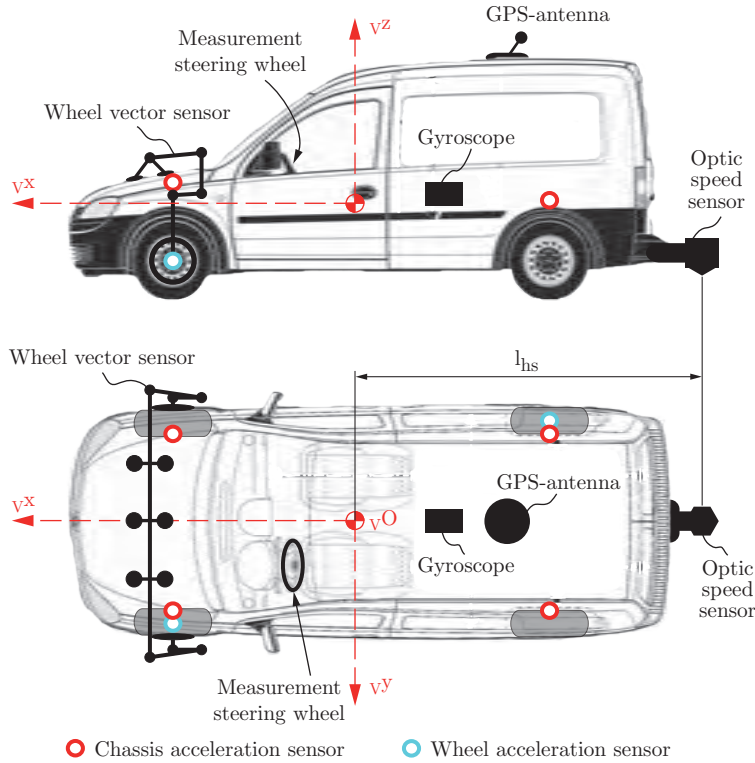


Figure 2.17.: Measurement system used for the model validation with the test vehicle (Opel Combo 1.6 CNG).

Different maneuvers were carried out to validate the stationary and the transient behavior of the vehicle as well as its oscillatory response when driving over a non-flat road. The filtered signals of the steering wheel angle δ_{st} and the longitudinal vehicle speed $v_{\dot{x}}$ were used as inputs for the vehicle model in all considered maneuvers. Further details regarding the validation of the different model components are presented in [Dür11], [Nie11] and [Mar09].

The validation of the stationary response of the vehicle model was carried out based on

a standardized steady state circular driving maneuver according to the International Standard ISO 4138 [fSI04]. Thereby and corresponding to the second method described in the mentioned standard, the trajectory radius $R_t = 44$ m was kept as constant as possible by varying the steering wheel angle δ_{st} while increasing the vehicle longitudinal speed $v\dot{x}$ from a value corresponding to approximately zero lateral acceleration $v\ddot{y}$ until reaching the maximum steady state value of it $^{max}v\ddot{y}$. Figure 2.18 shows the comparison between the measured data obtained with the test vehicle and the simulation results for this maneuver.

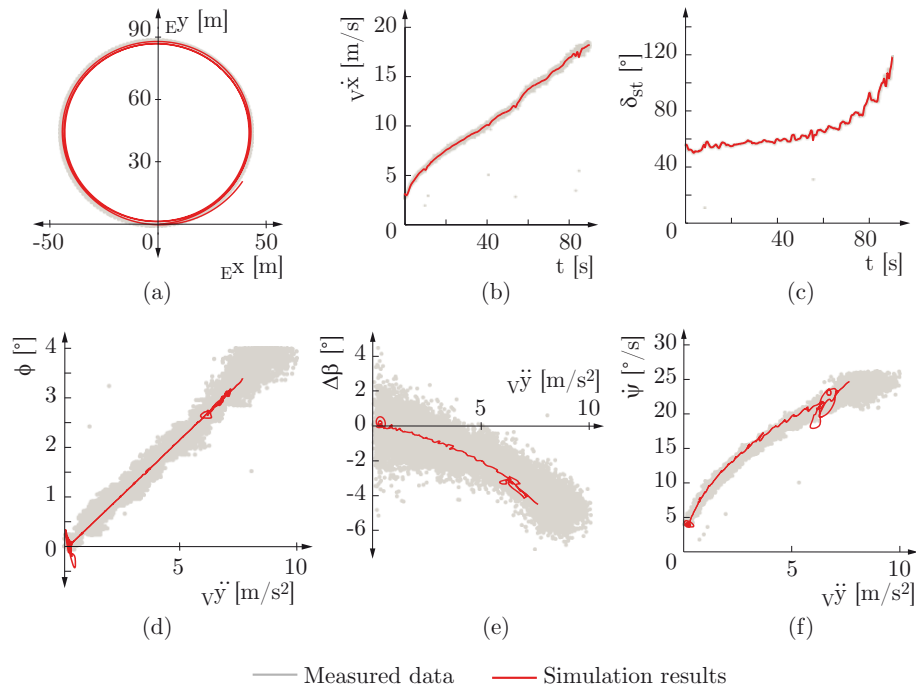


Figure 2.18.: Comparison between simulation results and measured data obtained with the test vehicle for the steady state circular driving maneuver with a constant reference trajectory radius $R_t = 44$ m and increasing longitudinal speed $v\dot{x}$: absolute position Ey vs. Ex of the center of gravity of the vehicle (a), longitudinal vehicle speed $v\dot{x}$ (b), steering wheel angle δ_{st} (c), roll angle ϕ (d), difference sideslip angle $\Delta\beta$ (e), and yaw rate $\dot{\psi}$ (f). Figures (d), (e) and (f) are plotted against the lateral acceleration $v\ddot{y}$ (see also [Dür11] and [Nie11]).

The understeering tendency of the test vehicle can be recognized observing the increasing deviation of the actual trajectory from the reference trajectory characterized by the constant radius $R_t = 44$ m (figure 2.18-a), while the value of the steering wheel an-

gle δ_{st} increases at the same time (figure 2.18-c). For the maximum achievable steady state value of the lateral acceleration ${}^{max}_V \ddot{y}^S \approx 7.4 \text{ m/s}^2$, the roll angle corresponds to $\phi \approx 3.5^\circ$. The results in this figure show a very good correlation between the measured data and the simulated results.

For the validation of the transient response of the vehicle, a dynamic maneuver with varying vehicle longitudinal speed ${}_V \dot{x}$ and an unsteady steering wheel angle input δ_{st} was selected. As can be seen in figure 2.19, the simulation results present a high correlation with the measured data both in amplitude and in phase angle.

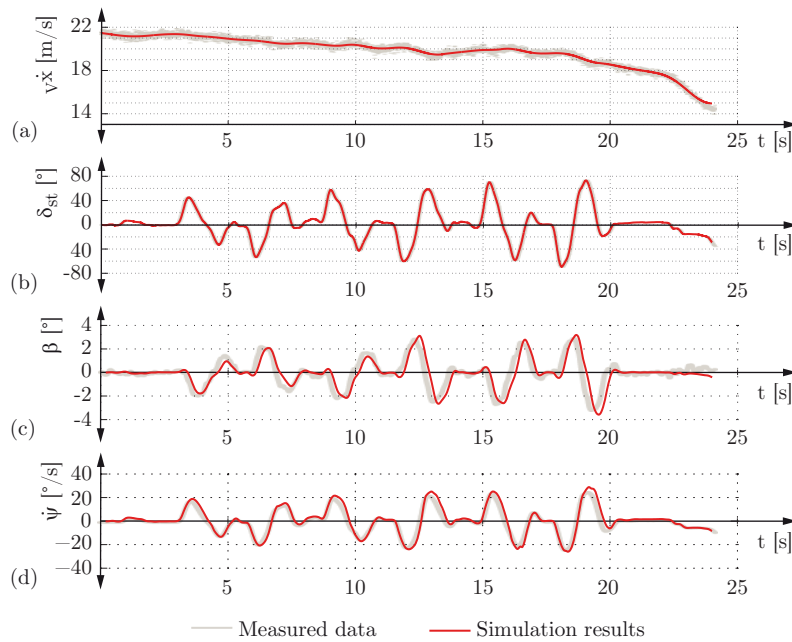


Figure 2.19.: Comparison between simulation results and measured data obtained with the test vehicle for a dynamic maneuver: vehicle longitudinal speed ${}_V \dot{x}$ (a), steering wheel angle δ_{st} (b), sideslip angle β (c) and yaw rate $\dot{\psi}$ (d) over the time t (see also [Dür11] and [Nie11]).

To validate the vertical dynamic behavior of the vehicle model, measurements with the test vehicle were taken by driving on the test track schematically presented in figure 2.20 consisting in a curb followed by a pothole with a height of ${}_E z_{road} = 27 \text{ mm}$. During these measurements, a longitudinal speed ${}_V \dot{x} = 11.11 \text{ m/s}$, a wheel mass $m_{w_i} = 40 \text{ kg}$, a tire inflation pressure $p_{T_i} = 2.6 \text{ bar}$ and no additional load mass ($m_{load} = 0 \text{ kg}$) were used. These conditions were reproduced in the simulation environment MOVES² using the parameters presented in appendix B.

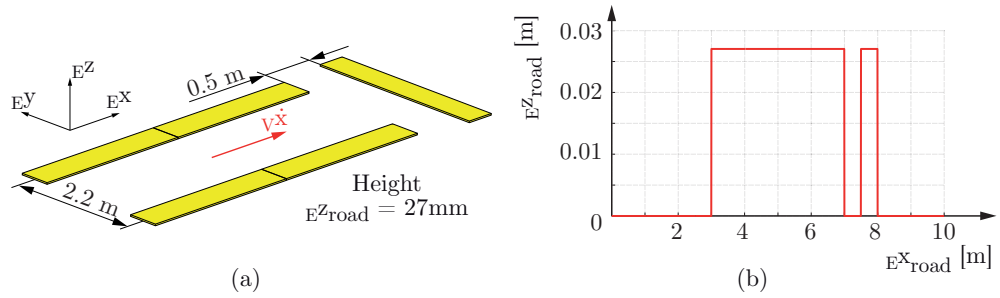


Figure 2.20.: Schematic representation of the test track consisting in a curb followed by a pothole with a height of $E^z_{road} = 27$ mm which was used to obtain the measured data taken as basis for the validation of the vertical dynamics behavior of the developed vehicle model (a), and corresponding road profile height E^z_{road} (b).

Furthermore, the acceleration of both the suspended ${}_V\ddot{z}_A$ and the non-suspended mass ${}_C\ddot{z}_C$ at the front left (right subscript *fl*) and rear right (right subscript *rr*) vehicle corners was taken as basis for the validation (see also figure 2.17 for the position of the acceleration sensors). Figure 2.21 shows the comparison between the measured data and the simulation results. It can be seen that the simulation model reproduces the vertical vehicle dynamics with good accuracy. A similar correlation level was found for different values of the suspended mass m_{w_i} (in the range from 40 kg to 70 kg - see also the device to simulate additional non-suspended masses on chapter E.3.1 in appendix E), the longitudinal vehicle speed (20 km/h and 40 km/h), the tire inflation pressure (2.6 bar and 3.6 bar) and for an additional load mass $m_{load} = 400$ kg (corresponding to approximately two thirds of the maximum authorized additional load mass - see table B.1 in appendix B) [Mar09]. The correlation between measured data and simulation results is strongly influenced by the vertical tire model, the consideration of the vibration behavior of both the engine and the gearbox, as well as by the modeling approach used for the suspension spring and the shock absorber [RNFD11].

Summary chapter 2: Simulation environment The developed simulation environment MOVES² involving the modular modeling of the *driver-vehicle-environment* system was introduced. The developed models of the vehicle, the tire, the road and the passive suspension system were described in detail. The vehicle model is considered to be composed of the suspended body and the non-suspended masses as well as of additional masses positioned on the suspended body via a spring-damper system. The tire model is divided into two sub-models: an extended model based on the tire models presented by

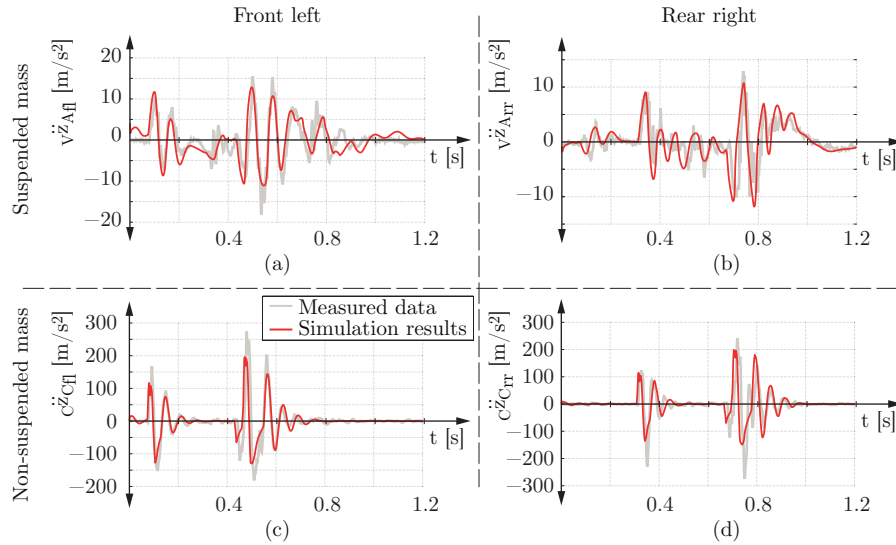


Figure 2.21.: Comparison between simulation results and measured data obtained with the test vehicle for driving over the synthetic road (figure 2.20) consisting in a curb followed by a pothole with a height of $Ez_{road} = 27$ mm: Suspended $v\ddot{z}_A$ and non-suspended mass $C\ddot{z}_C$ acceleration at the front left (a and c respectively - right subscript *fl*) and rear right (b and d respectively - right subscript *rr*) corners of the vehicle over the time t . Vehicle longitudinal speed $v\dot{x} = 11.11$ m/s, wheel mass $m_{w_i} = 40$ kg, tire inflation pressure $p_{T_i} = 2.6$ bar and no additional load mass $m_{load} = 0$ kg (see also [Mar09]).

Hirschberg et al. (see [Hir09b], [HRW02] and [HRW02]) was implemented for the horizontal tire dynamics. For the vertical tire dynamics, a complex tire model including a location algorithm, an enveloping model and a single-mass oscillator model was developed. The tire model is divided into two sub-models depicting the horizontal and vertical tire dynamics. To model the uneven road, the widespread open source program OpenCRG®, which is based on a *Curved Regular Grid* and is still being developed by several original equipment manufacturers, was implemented and extended. The road roughness was implemented additionally based on the approach of S. O. Rice [Ric52] and can be used to generate uneven roads with any given power spectral density (e.g. as proposed in the international standard ISO 8608:1995(E) [fSI95]).

The developed passive suspension system model is considered to be composed of a suspension spring and a shock absorber. For modeling the suspension spring, a nonlinear approach based on five physically meaningful parameters (e.g. desired natural frequency

of the suspended mass, or static ground clearance) was presented. To model the shock absorber, a nonlinear complex model based on the basic exponential trigonometrical function of the tire model TMsimple and adapted to depict the behavior of the damping coefficient was developed. The entire model was validated using measured data obtained with the test vehicle Opel Combo 1.6 CNG.

3. Longitudinal dynamics

Several aspects concerning the vehicle longitudinal dynamics, like the maximum longitudinal acceleration, the maximum speed or the climbing ability, play a very important role for the quality perception of vehicles by final customers. Beside these aspects, the fuel or energy efficiency has become more and more important in the last time. Upcoming technologies should fulfill the traditional customer's expectations at least until the driving and transportation culture changes toward a more environmentally conscious one.

In an electric vehicle, the requirements imposed on the vehicle longitudinal dynamics directly influence the characteristics of the entire electric powertrain. In this chapter, the analysis of the longitudinal vehicle dynamics of vehicles with in-wheel motors is focused on the determination of the main characteristics of the electric motors and the battery to fulfill given performance requirements. Furthermore, an overview of driving cycles used for longitudinal dynamics analysis as well as the energy consumption for some of them are presented.

3.1. Equations of motion

In this chapter, the simplified vehicle model presented in appendix C.1, which neglects the tire slip, is used to describe the quasi-stationary total resistance force $F_{x_{resistance}}$ that should be overcome in the quasi-stationary equilibrium in order to produce a certain instantaneous driving movement characterized by a given longitudinal vehicle speed ${}_V\dot{x}$ and acceleration ${}_V\ddot{x}$:

$$F_{x_{resistance}} = F_{{}_V\ddot{x}} + F_{roll} + F_{aero} + F_{climb} . \quad (3.1)$$

The inertial force $F_v \ddot{x}$ is given by

$$F_v \ddot{x} = e_i \cdot m_v \cdot \ddot{x} \quad (3.2)$$

as a function of the total vehicle mass in running order¹

$$m_v = m_A + m_{w_f} + m_{w_r} \quad (3.3)$$

and the mass factor² e_i for each gear i of the gearbox

$$e_i = 1 + \frac{{}^{red}I}{m_v \cdot r_{dyn}^2}, \quad (3.4)$$

where ${}^{red}I$ corresponds to the total reduced moment of inertia of the front and rear axles (see [Wal04] and equations C.14 and C.15 in chapter C.2) and r_{dyn} stands for the dynamic tire radius.

The rolling resistance force³ (see also equation 2.41 in chapter 2.5.1)

$$F_{roll} = G_v \cdot \cos(\alpha_{road}) \cdot f_{roll} \cdot \text{sign}(v \dot{x}) \quad (3.5)$$

depends on the inclination angle of the road α_{road} , on the rolling resistance factor f_{roll} and on the gravitational force of the entire vehicle G_v , which can be expressed as a function of the vehicle mass in running order m_v , any additional load mass m_{load} and the gravity g as:

$$G_v = (m_v + m_{load}) \cdot g. \quad (3.6)$$

The aerodynamic resistance force F_{aero} is a function of the air density ρ_{air} , the drag coefficient C_d , the projected frontal area of the vehicle A_w and the longitudinal vehicle speed $v \dot{x}$ (see table B.1 in appendix B for the value of the vehicle parameters):

$$F_{aero}(t) = 0.5 \cdot \rho_{air} \cdot C_d \cdot A_w \cdot |v \dot{x}| \cdot v \dot{x}. \quad (3.7)$$

¹Vehicle mass definitions according to the Council Directive 92/21/EEC of 31 March 1992 of the European Union [Com92].

²The mass factor comprises the translatory and rotatory inertia of the vehicle and the powertrain [Wal04]. Exemplarily values of the mass factor for vehicles with a powertrain with internal combustion engine can be found in [Hir09a] and [Wal04].

³The effect of the vehicle speed on the rolling resistance is neglected in this work.

3.1. Equations of motion

Here, the term $|\dot{v}_x| \cdot \dot{v}_x$ is used instead of \dot{v}_x^2 to account for driving forwards or backwards. Furthermore, the wind speed is neglected.

For a given road inclination angle α_{road} , the corresponding resistance force F_{climb} is given by:

$$F_{climb} = G_v \cdot \sin(\alpha_{road}) . \quad (3.8)$$

At this point, it is worth noting that the road inclination is often given in percentage p_{road} , which is related with the road inclination angle α_{road} by:

$$p_{road} = \tan(\alpha_{road}) \cdot 100 \% . \quad (3.9)$$

These resistance forces are schematically shown in figure 3.1 for a subcompact electric vehicle with a single stage gearbox (see tables 3.3 and 3.5) as a function of the longitudinal speed \dot{v}_x . It can be seen, that, even for relative small values of the longitudinal acceleration, the inertial force $F_{v\ddot{x}}$ is of high importance at low speeds. However, the aerodynamic resistance force F_{aero} becomes more relevant at higher speeds due to the quadratic influence of the longitudinal speed.

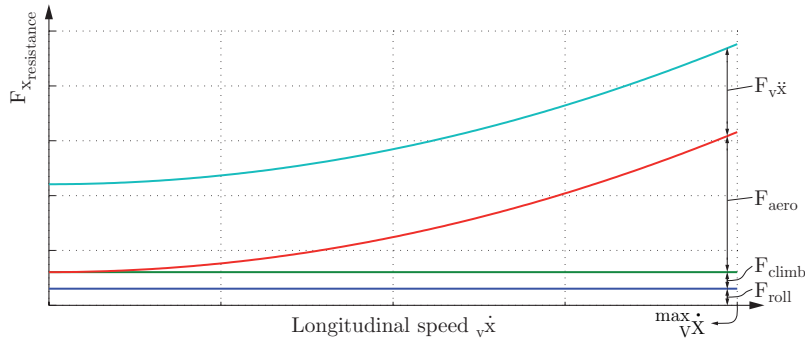


Figure 3.1.: Quasi-stationary total longitudinal resistance force $F_{xresistance}$ for a subcompact electric vehicle with a single stage gearbox (see tables 3.3 and 3.5) as function of the longitudinal speed \dot{v}_x while driving on a road with constant inclination ($\alpha_{road} = const.$) and with a longitudinal acceleration $\dot{v}_x = 0.5 \text{ m/s}^2$.

3.2. Approaches toward the electrification of the vehicle powertrain

There are two ways to electrify a vehicle (figure 3.2). The electric components (electric motors, battery, inverters) are the starting point of the first way, called analysis. Based on the characteristics of these components, the achievable driving performance can be determined in a simulation or in field tests using a prototype. The other possibility is to firstly set the performance requirements and then use them to derive the characteristics of the electric components. This process is called synthesis. In this work, a synthesis approach is presented, since this is probably the most interesting approach from the engineering point of view.

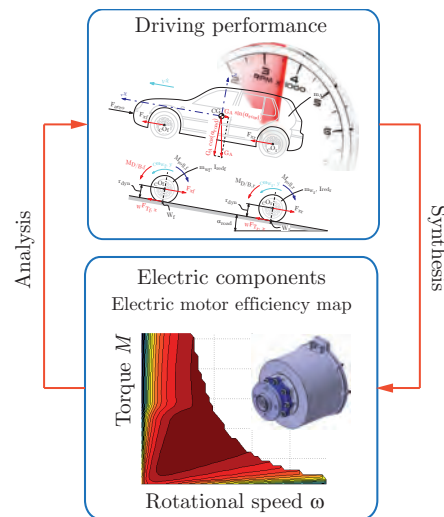


Figure 3.2.: Two different approaches toward the electrification of vehicles.

In the presented approach, the general characteristics of the battery and in-wheel motors are determined based on the desired driving performance. It can be described based on maximum speed ${}^{max}_V \dot{x}$ and desired acceleration values (expressed as the time Δt needed from standstill to a certain speed ${}_V \dot{x}_1$ or ${}_V \dot{x}_2$) as well as on climbing ability (expressed as the maximum road inclination to overcome ${}^{max} \alpha_{road}$), elasticity (time to accelerate from a certain speed ${}_V \dot{x}_{e1}$ different from zero to another one ${}_V \dot{x}_{e2}$) and driving range ${}^{max} s$. The maximum speed can be specified for driving on a plain terrain ${}^{max} \dot{x}_{\alpha_{road1}=0^\circ}$ or on a street with a certain inclination ${}^{max} \dot{x}_{\alpha_{road2} \neq 0^\circ}$. Furthermore, since, in general, the performance of electric motors depends on the operating condition (continuous or overload service mode), it is important to specify in which condition a given performance

requirement shall be reached. The aspects considered in this work to describe the desired driving performance can be seen in figure 3.3 (see also [Cho02]).

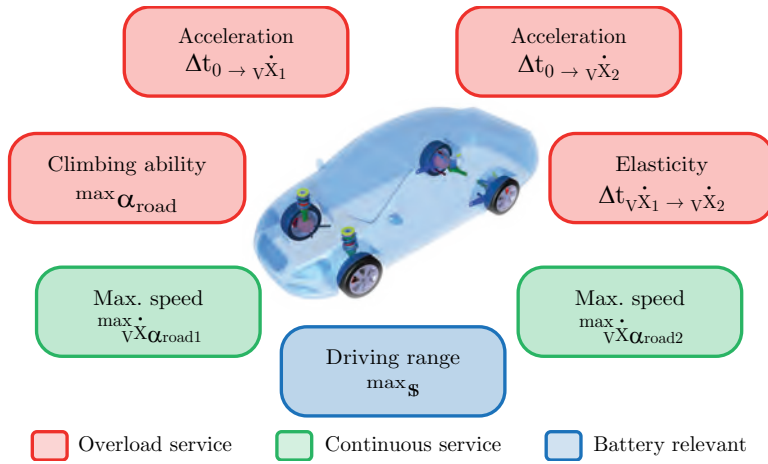


Figure 3.3.: Aspects considered to describe the desired driving performance.

3.3. Driving cycles

Basically, driving cycles describe the vehicle speed as a function of the cycle time. From this so-called speed profile, an acceleration profile can be derived. For additional fuel consumption considerations the gear shift information has to be taken into account in order to get comparable and reproducible results. Although many of them are used in the automotive industry, only few of them are mandatory or standardized (NEDC, FTP-75, Japan-10-15). There are several other driving cycles representing more realistic load requirements. These driving cycles have been stored in large databases ([And04], [And06]).

A simple way to classify driving cycles is based on their individual vehicle speed behavior. Cycles representing constant acceleration and constant speed sections are called modal cycles. Thus, cycles having unsteady acceleration and speed sections are generally known as transient cycles. Modal cycles do not effectively represent the driving behavior of common on-road use. As a consequence, transient cycles have been created representing modern driving patterns. Widely used standardized driving cycles are the *New European Driving Cycle* - NEDC, the North-American driving cycle FTP-75 and the Japanese cycle Japan-10-15. The ARTEMIS, HYZEM or INRETS (see [And04],

[And06]) are examples of groups of non-standardized transient driving cycles. A further classification scheme makes the distinction between standardized or non-standardized driving cycles. Moreover, some authors use classification criteria like mass-to-power-ratio or an analysis of parameters, like stop duration and stop rate, highest and average acceleration and highest and average speed (see e.g. [NBW06]). Driving cycles can be classified according to their application domain, which means cycles representing typical driving patterns of urban (city), road or highway cycles [And04], [And06], [NBW06], [AJV⁺06].

The standardized driving cycles NEDC, FTP-75 and Japan-10-15 as well as the non-standardized ARTEMIS, HYZEM and INRETS (as shown in figure 3.4) are used in this work as basis for further calculations regarding energy demand and determination of the electric components characteristics and will be described more in detail.

Table 3.1 presents an overview of the characteristic kinematic parameters of the considered driving cycles. Compared with the non-standardized driving cycles (ARTEMIS, HYZEM and INRETS), the standardized ones (NEDC, FTP-75 and Japan-10-15) are shorter, present lower speeds and accelerations and are characterized by more stops and longer distances between them. This points out the fact, that the non-standardized driving cycles represent more realistic driving patterns, as will be explained in the following sections. Among the standardized driving cycles, while the NEDC shows the highest maximum speed (120.0 km/h), the FTP-75 presents a higher value of the maximum acceleration (1.72 m/s²). Observing the non-standardized driving cycles, while the HYZEM driving cycle has the highest maximum speed (138.1 km/h) and maximum positive acceleration (3.19 m/s²) the INRETS driving cycle shows the strongest deceleration (−3.94 m/s²).

For a constant road inclination, the quasi-stationary total resistance force $F_{x_{resistance}}$ and therefore the demanded energy $E_{cycle\ tires}$ (see chapter 3.4.2) depend on the longitudinal speed $v\dot{x}$ and longitudinal acceleration $v\ddot{x}$. It can be expected that driving cycles characterized by higher accelerations at higher speeds demand higher amounts of energy. Figure 3.5 shows the maximum longitudinal acceleration $\overset{max}{v}\ddot{x}$ as a function of the longitudinal speed $v\dot{x}$ for the different driving cycles considered. It can be seen that non-standardized driving cycles (dotted and/or dashed lines) present higher longitudinal acceleration values along the entire speed range as the standardized ones (continuous lines). Some authors consider the low dynamic behavior as one of the biggest disadvantages of the standardized driving cycles [And04]. Among the standard-

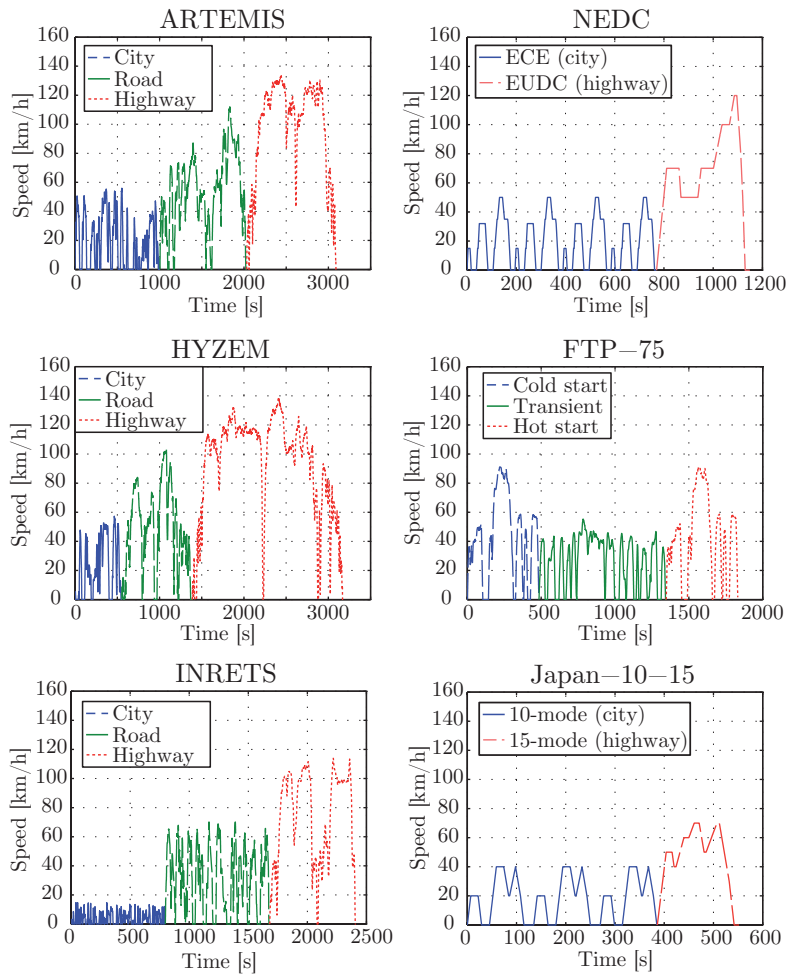


Figure 3.4.: Considered driving cycles: ARTEMIS, HYZEM, INRETS, NEDC, FTP-75 and Japan-10-15.

ized driving cycles, the NEDC presents the highest longitudinal accelerations at higher speeds. Based on this, it can be expected that higher amounts of energy and therefore a bigger battery is needed for the NEDC as for the FTP-75 or Japan-10-15 for the same driving range. Nevertheless, the highest amounts of required energy and therefore the heaviest batteries can be expected for the non-standardized and more realistic driving cycles ARTEMIS and HYZEM, which present the highest longitudinal accelerations at the highest longitudinal speeds among all considered driving cycles. More details of kinematic parameters of the selected driving cycles can be found in [And04], [NBW06] and [WRN09]. General information about the considered driving cycles is presented in

Table 3.1.: Characteristic kinematic parameters of the considered driving cycles.

			NEDC	FTP-75	Japan-10-15	ARTEMIS	HYZEM	INRETS
Duration	t_{cycle}	[s]	1168	1856	620	3108	3179	2410
Dead time	Absolute	[s]	268.1	317.1	167.1	320.1	243.1	387.1
	Relative	[%]	23.0	17.1	27.0	10.3	7.6	16.1
Stops	Number	[-]	14	23	8	28	17	50
	Δ Distance ^a	[m]	846.6	807.6	595.0	1832.9	3806.2	485.2
Traveled distance	s_{cycle}	[km]	11.0	17.8	4.2	49.5	60.9	23.8
Speed	Mean	$\left[\frac{\text{km}}{\text{h}}\right]$	33.9	34.5	24.2	57.3	69.0	35.5
	Maximum		120.0	91.2	70.0	133.9	138.1	113.9
Acceleration	Drive	Mean	0.534	0.483	0.527	0.434	0.427	0.586
		Max.	1.04	1.72	0.79	2.50	3.19	2.83
	Brake	Mean	-0.725	-0.530	-0.605	-0.483	-0.498	-0.576
		Min.	-1.39	-1.50	-0.83	-3.36	-4.61	-3.94

^a Mean distance between stops.

section C.3 in appendix C.

3.4. Energy storage

In the first part of this chapter, a short overview of different energy storage devices is given (see chapter 3.4.1). Afterwards, it is presented how the energy and power demands to drive a given cycle can be determined (see chapter 3.4.2). Finally, the developed approach to determine the battery characteristics based on any driving cycle is presented (see 3.4.3).

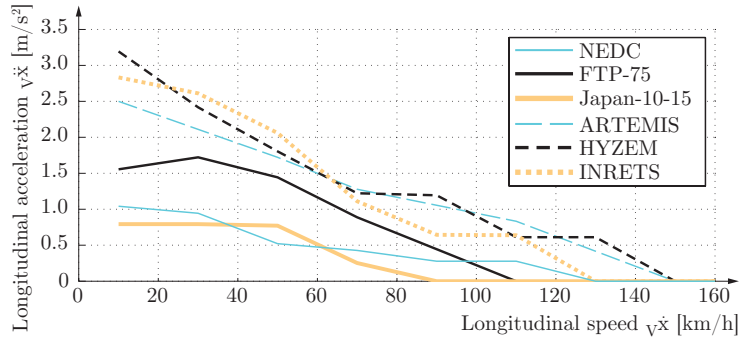


Figure 3.5.: Maximum longitudinal acceleration as function of the longitudinal speed for the different standardized (dotted and/or dashed lines) and non-standardized (continuous lines) driving cycles considered.

3.4.1. Energy storage device

The energy to move a vehicle must be stored properly to guarantee not only its movement but also a harmonic and adequate operation according to the requested performance (see also chapter 3.3). An overview of the different ways to store this energy in a vehicle is presented in section C.3.7 of appendix C. Beside the energy-to-mass and power-to-mass values, the state of charge SOC_{Batt} is an important characteristic parameter that must be taken into account to determine the battery dimensions and its operating conditions. It indicates the amount of energy stored in the battery E_{Batt, t_i} at a certain time t_i in relation to the nominal storable energy $^{nom}E_{Batt}$ of the battery:

$$SOC_{Batt} = \frac{E_{Batt, t_i}}{^{nom}E_{Batt}} \cdot 100 \% . \quad (3.10)$$

The state of charge SOC_{Batt} strongly influences the lifetime of batteries undergoing frequently load cycles (for example in electric and hybrid vehicles). While very narrow ranges of batteries for hybrid vehicles are used (e.g. 10 % of the battery capacity) to increase or at least maintain its lifetime, up to 80 % of the battery capacity of batteries for electric vehicles is used [Hof09]. This usable fraction of the total energy stored in the battery is known as SOC-Range ($SOC_{Batt \text{ range}}$). Further information about batteries and energy storage devices in general is presented in section C.3.7 of appendix C.

3.4.2. Energy and power demand in a driving cycle

The energy $E_{cycle\ tires}$ needed at the tires to drive a certain cycle, characterized by a longitudinal speed profile ${}_V\dot{x}(t)$ over the time, is given by the integral of the driving power $P(t)$ over the cycle duration t_{cycle} :

$$E_{cycle\ tires} = \int_0^{t_{cycle}} P(t) dt = \int_0^{t_{cycle}} F_{x_{resistance}}(t) \cdot {}_V\dot{x}(t) dt, \quad (3.11)$$

where $F_{x_{resistance}}(t)$ corresponds to the quasi-stationary total resistance force given by equation 3.1.

If it is assumed that the kinetic energy can be recuperated during braking (see chapter 3.5.3), it is important to take into account the efficiency of the chain not only from the battery to the wheels (driving) but also in the opposite direction (recuperation while braking) since the efficiency values are, in general, different in each case. Based on this, without considering any energy consuming aggregates like the air conditioning system, electric steering system or active/semi-active suspension systems (see also chapter 3.6), the total energy consumption for a given cycle E_{cycle} is given by:

$$E_{cycle} = E_{driving} - E_{recuperation}, \quad (3.12)$$

where the energy amounts while driving $E_{driving}$ and recuperating $E_{recuperating}$ are given by:

$$E_{driving} = \frac{E_{cycle\ tires, {}_V\ddot{x} \geq 0}}{\eta_{gearbox} \cdot \eta_{EM\ motor} \cdot \eta_{inverter} \cdot \eta_{Battery\ discharge}}, \quad (3.13)$$

$$E_{recuperation} = \frac{E_{cycle\ tires, {}_V\ddot{x} \leq 0}}{\eta_{gearbox} \cdot \eta_{EM\ generator} \cdot \eta_{inverter} \cdot \eta_{Battery\ charge}}. \quad (3.14)$$

It is assumed here, that electric motors have different nominal efficiencies while working as motor $\eta_{EM\ motor}$ or as generator $\eta_{EM\ generator}$. Moreover, also different nominal efficiencies are considered for the electric battery while charging $\eta_{Battery\ charge}$ and discharging $\eta_{Battery\ discharge}$. Additionally, the nominal efficiencies of the gearbox $\eta_{gearbox}$ and of the inverter $\eta_{inverter}$ are taken as constant. The used values are presented in table

3.4. Moreover, it is supposed in this approach, that braking is carried out completely by the electric motors and the intervention of the friction braking system is neglected.

Furthermore, to determine the energy while driving $E_{driving}$, driving phases with $v\ddot{x} \geq 0$ are considered. The recuperated energy $E_{recuperation}$ is related with negative accelerations $v\ddot{x} < 0$.

3.4.3. Battery capacity and mass estimation

In an early development phase of an electric vehicle, it is of high importance to estimate the battery capacity (amount of stored energy) needed to achieve a certain driving range under the consideration of a defined driving cycle (see [NBW06],[WRN09],[And04] and [FJM⁺98], and also section 3.3). Two facts must be taken into account to determine the battery capacity: On the one hand, the battery capacity is related with the battery mass and the battery mass depends on the energy needed to drive the cycle. On the other, the energy consumption on a given driving cycle depends on the total vehicle mass including the battery. Based on this, it is clear that the battery capacity depends on its own mass and in turn the battery mass depends on the battery capacity. Therefore, an iterative process must be used to determine the battery capacity and mass. The developed approach is presented in figure 3.6 and can be used to determine the battery characteristics based on any driving cycle (see also [RNH11]).

The starting point is an assumed battery mass $m_{Batt\ assum}$. In the first step of the iterative process, the power and energy demands needed to drive a given cycle can be determined in the section 3.4.2. Taking into account the energy-to-mass $E_{Batt\ specific}$ and the power-to-mass $P_{Batt\ specific}$ ratios (see e.g. [vdBVvM⁺06], and chapter 3.4.1), the needed battery mass to drive the cycle can then be calculated as:

$$m_{Batt\ needed} = \max(m_{Batt\ power}, m_{Batt\ energy}) , \quad (3.15)$$

where the needed battery mass to cope with the power $m_{Batt\ power}$ and with the energy requirements $m_{Batt\ energy}$ of the driving cycle is given by:

$$m_{Batt\ energy} = \frac{E_{cycle}}{E_{Batt\ specific}} \quad (3.16)$$

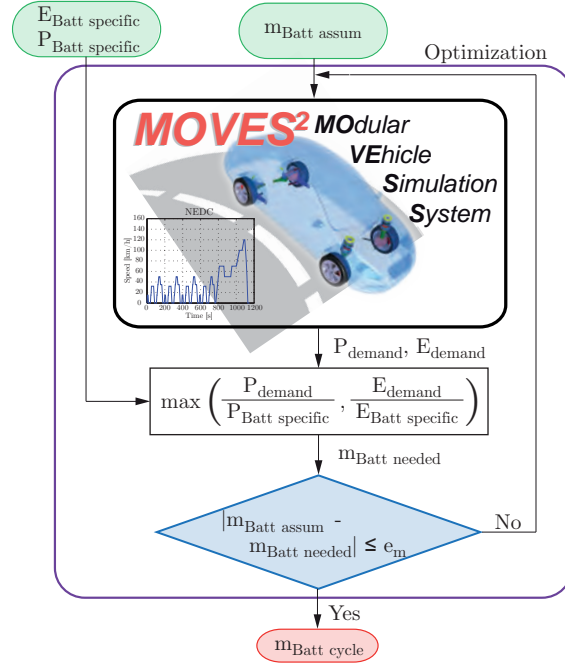


Figure 3.6.: Flow diagram of the iterative process used to determine the characteristics of the needed battery for a certain driving cycle (battery mass as well as power and energy capacities).

and

$$m_{Batt\ power} = \frac{P_{peak}}{P_{Batt\ specific}} . \quad (3.17)$$

Assuming that the battery can deliver as much power during discharging as it can store during charging, the maximum value P_{peak} of the needed power can be expressed as:

$$P_{peak} = \max(|P(t)|) . \quad (3.18)$$

The battery mass $m_{Batt\ cycle}$ to drive a certain cycle is found if the difference between the needed battery mass $m_{Batt\ needed}$ and the assumed battery mass $m_{Batt\ assum}$ is smaller than a specified threshold e_m . Otherwise, the algorithm must change the assumed value and start the iteration again.

The battery mass needed to travel a given maximum distance ^{max}s can be finally ap-

proximated based on the cycle distance s_{cycle} according to:

$$m_{Batt, s} = m_{Batt\ cycle} \cdot \frac{max\ s}{s_{cycle}}. \quad (3.19)$$

3.5. Electric motors

In this chapter, the synchronous motor with permanent magnets and the induction motor are described and analyzed since they seem to be the most attractive electric motor types for the automotive industry on the way toward the electrification of the powertrain of passenger vehicles (see e.g. [Wil11]). It must be pointed out that the expression *synchronous motor* is used in this work to refer to the synchronous motor with permanent magnets. The selection of most suitable electric motor technology for the electrification of the powertrain of a passenger vehicle depends not only on the general characteristics of the electric motor type (as presented in chapters C.4.1, C.4.2 and C.4.3) and its nominal efficiency (see chapter C.4.4) but also on the application scenario and the applied control strategy (see also [Wil11] and [WH10]). In appendix C, detailed information about these motor types (see section C.4) as well as an introduction to the power electronics needed to control them (see section C.5) is presented.

3.5.1. Torque-speed diagram of induction and synchronous motors

The achievable driving performance depends mainly on the full load curve of the considered electric motor. In comparison with internal combustion engines, electric motors can be overloaded for short periods of time. Nevertheless, the overload factor and the amount of time in which an electric motor can work in overload service depend mainly on the system's heat dissipation conditions, i.e. on the cooling system.

Figure 3.7 shows the torque-speed curves in nominal and overload service for the two motor types considered in this work. The curves of both motor types are characterized by a region of constant torque up to the nominal rotational speed ${}^n\omega$. For higher rotational speeds up to the maximum rotational speed ${}^{max}\omega$, i.e. in the field weakening region, the maximum torque in nominal and overload service is a function of the considered rotational speed ω . To describe the behavior of the torque in the entire speed range, following semi-phenomenological approach is proposed (see [Wil11] for a

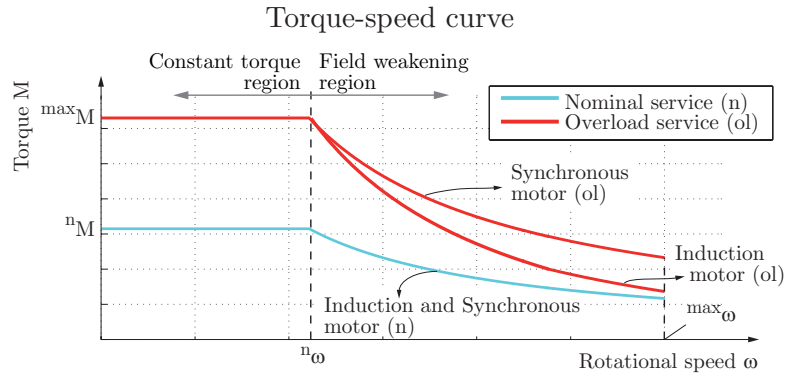


Figure 3.7.: Schematic steady state torque-speed curves for induction and synchronous motors in nominal and overload service.

phenomenological description):

$$M = \begin{cases} {}^0M; & \text{if } \omega \leq {}^n\omega \text{ (constant torque region),} \\ {}^0M \cdot \left(\frac{{}^n\omega}{\omega}\right)^{n_{FWR}}; & \text{if } \omega > {}^n\omega \text{ (field weakening region),} \end{cases} \quad (3.20)$$

where 0M corresponds to the torque (${}^{max}M$ for overload and nM for nominal service) at nominal speed ${}^n\omega$, and the exponent n_{FWR} depends on the motor type and the operating condition according to:

$$n_{FWR} = \begin{cases} 1; & \text{for } IM_n \text{ and } SM_n \text{ and } ol, \\ 2; & \text{for } IM_{ol}. \end{cases} \quad (3.21)$$

Here stands IM for induction motor, SM for synchronous motor, n for nominal service and ol for overload service.

An important aspect of electric machines concerns their ability to be operated (depending on the power electronics) to deliver positive and negative torque values in both rotation directions. This leads to the so called four-quadrants operation in which electric machines can be used to drive and brake in both rotational directions, as can be seen in figure 3.8. During braking, electric machines can work as generators to recuperate the kinetic energy of the vehicle they are installed on. In this work, a symmetric

field⁴ is assumed.

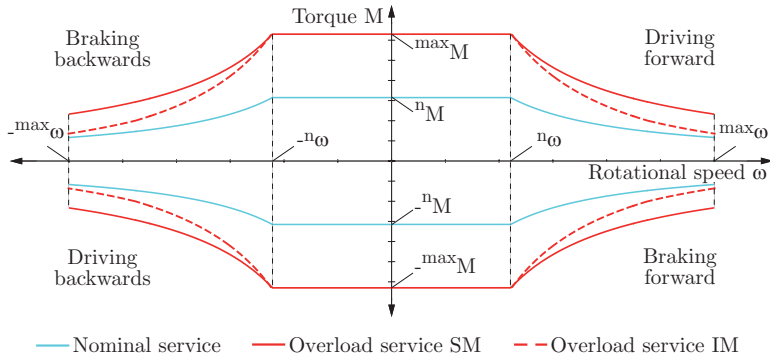


Figure 3.8.: Steady state four-quadrants operation of induction (IM) and synchronous motors (SM).

A comparison between the traction force diagrams⁵ of a vehicle with internal combustion engine and a vehicle with electric motor(s) is presented in section C.4.5 in appendix C.

3.5.2. Weight of electric motors

Since in-wheel motors increase the non-suspended mass and it tends to worsen ride comfort and driving safety, the weight of the electric motors for this kind of application is an important aspect to be considered (see e.g. [MW04] and chapter 5.2). Figure 3.9 presents the active mass⁶ of induction and synchronous motors as a function of its nominal torque nM for two different values of its nominal power nP . A tendency line for each case is also shown. The values were approximated using the approach presented by [Wil11].

It can be seen on this figure, that the weight of synchronous and induction motors depends mainly on its nominal torque nM rather than on its nominal power nP (see also [RNW10] and [Wil11]). Furthermore, due to the weight of the windings in the rotor, induction motors tend to be heavier than the synchronous ones.

⁴With the same absolute value of the maximum torque while braking and driving.

⁵See *traction force diagram* in chapter 3.5.4.

⁶Mass of all electromagnetic parts (see [Wil11]).

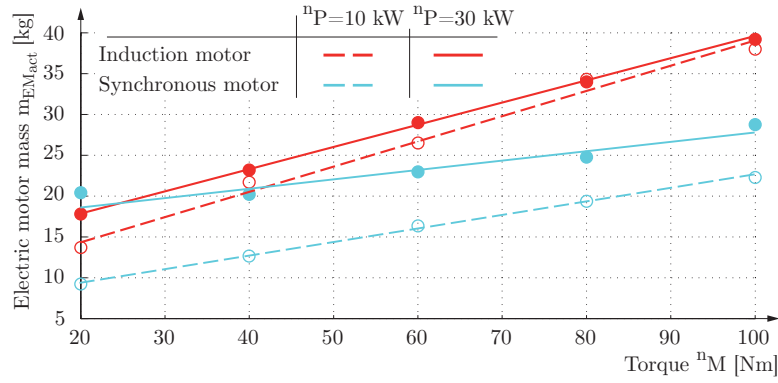


Figure 3.9.: Active mass $m_{EM_{act}}$ of induction and synchronous motors as function of the nominal torque nM and the nominal power nP .

3.5.3. Energy recuperation

As mentioned before, electric machines can be operated as generators while braking to recuperate kinetic energy. This energy can then be stored (see chapter 3.4) to be used later, for example, to drive the vehicle. This reduces the overall energy consumption. Nevertheless and regardless of the storage technology used (e.g. battery or capacitors), only a certain amount of the kinetic energy can be recuperated. Observing the equation 3.1, it is possible to notice that the rolling F_{roll} , climbing F_{climb} and aerodynamic F_{aero} forces still act on the moving vehicle while braking.

By multiplying the different force components F_{x_i} of equation 3.1 (i.e. F_{roll} , F_{aero} , F_{climb} and the inertial force $F_{v\ddot{x}}$) with the longitudinal speed $v\dot{x}$, it is possible to express the theoretical maximum recuperable kinetic power while braking $^{th,max}P_{rec,v\dot{x}_j}$ for a given longitudinal speed $v\dot{x}_j$ as (without considering losses in the powertrain while recuperating due to reduced mechanical and electrical efficiencies):

$$^{th,max}P_{rec,v\dot{x}_j} = \begin{cases} |P_{v\ddot{x}}| - P_{loss,v\dot{x}_j}; & \text{if } v\ddot{x} < 0 \text{ and } |P_{v\ddot{x}}| > P_{loss,v\dot{x}_j}, \\ 0; & \text{otherwise,} \end{cases} \quad (3.22)$$

where the total losses at the considered given speed are given by

$$P_{loss,v\dot{x}_j} = (P_{roll} + P_{climb} + P_{aero})_{v\dot{x}_j} \quad (3.23)$$

and, as stated before, the different power components can be expressed as:

$$P_j = F_{x_i} \cdot v \dot{x}_j. \quad (3.24)$$

If there were no rolling F_{roll} , climbing F_{climb} and aerodynamic F_{aero} forces acting during braking, the total power $P_{v \ddot{x}}$ related to the vehicle inertia could be recuperated. Nevertheless and as mentioned before, as this forces remain active, the theoretical maximum recuperable kinetic power $^{max}P_{th \ rec}$ is just a part of the power $P_{v \ddot{x}}$. This is shown in figure 3.10 for a given longitudinal speed $v \dot{x}_j$ (see also [WFO09]) and two different deceleration values $v \ddot{x}_1$ and $v \ddot{x}_2$. While there is only a small speed range where energy can be recuperated while braking with $v \ddot{x}_1$, energy can be recuperated in the entire speed range shown in figure 3.10 when braking with $v \ddot{x}_2$.

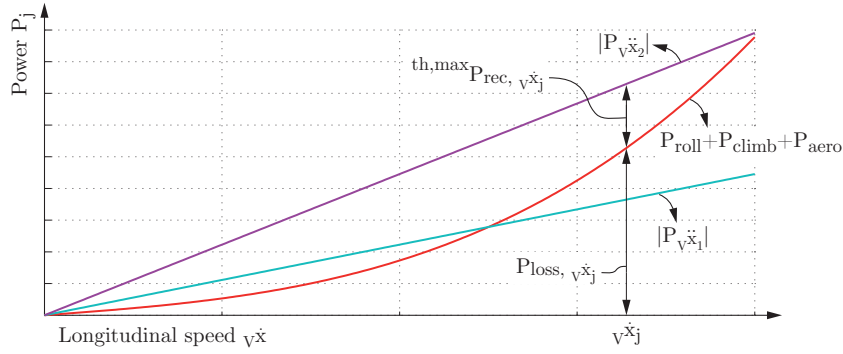


Figure 3.10.: Theoretical maximum recuperable kinetic energy while braking (steady state diagram).

3.5.4. Power balance

By considering the number N_{EM} of installed electric motors and the torque produced by each electric motor M_{EM} as well as the transmission ratio $i_{gearbox}$ and the efficiency $\eta_{gearbox}$ (assumed as constant) of the considered gearbox between the in-wheel motor and the wheel hub, the driving/braking force defined in the appendix C.1 can be expressed as:

$$\frac{M_{D/B}}{r_{dyn}} = \frac{N_{EM} \cdot M_{EM} \cdot \eta_{gearbox} \cdot i_{gearbox}}{r_{dyn}}. \quad (3.25)$$

This force can be expressed as a function of the vehicle longitudinal speed by considering the characteristic torque-speed curve of the installed electric motors (see chapter 3.5.1). Plotting this force together with the demanded traction force (see equation 3.1) leads to the so-called steady state⁷ traction force diagram. Figure 3.11 (a) shows, in a schematic way, the traction force diagram of both a synchronous and an induction motor for nominal and overload service. The quasi-stationary total resistance force $F_{x_{resistance}}$ is plotted as dashed lines for different road inclinations p . Due to the fact, that in the field weakening region, the torque of the induction motor in overload service decreases faster than the torque of the synchronous motor (see e.g. [Wil11] for a detailed explanation), the offered traction force of the synchronous motor in this region is greater than that of the induction motor.

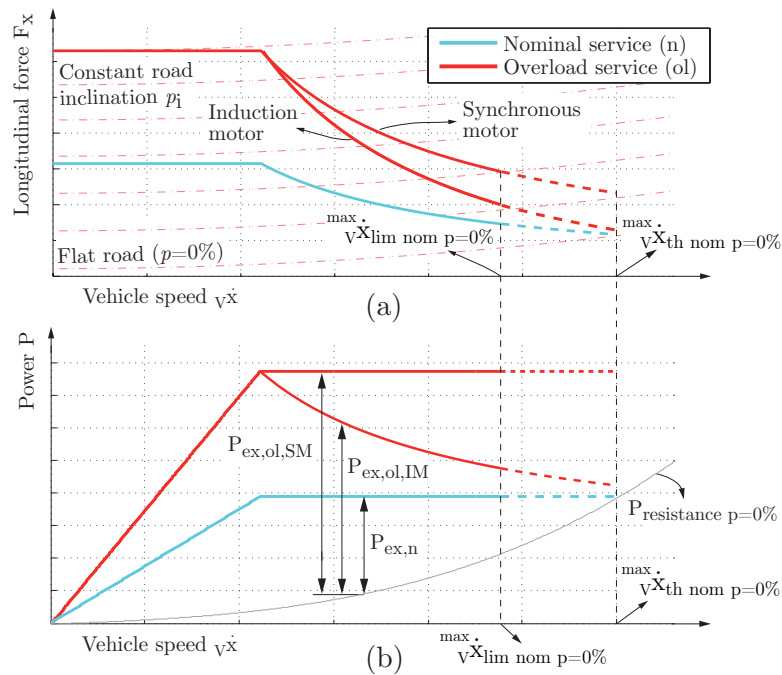


Figure 3.11.: Steady state traction force (a) and power (b) diagrams of a synchronous (SM) and an induction (IM) motor with an overspeed limited maximum speed on flat road $v_x^{lim nom p=0\%}$. The theoretical maximum speed on flat road in nominal service is also indicated $v_x^{th nom p=0\%}$.

The resistance $P_{resistance}$ as well as the offered P_{offer} power can be obtained based on equations 3.1 and 3.25 as a function of the vehicle longitudinal speed v_x and the

⁷In this work, the expression "traction force diagram" is used to indicate the corresponding diagrams in steady state.

rotational speed ${}_C\omega_{w_f/r, y}$ of the wheels as:

$$P_{resistance} = F_{x_{resistance}} \cdot V\dot{x} , \quad (3.26)$$

$$P_{offer} = M_{D/B,f} \cdot {}_C\omega_{w_f, y} + M_{D/B,r} \cdot {}_C\omega_{w_r, y} . \quad (3.27)$$

In this way, the driving performance diagram presented in figure 3.11-b can be obtained based on the traction force diagram. In this figure, the excess power P_{ex} is also indicated. It can be obtained as the difference between the demanded and offered power for a certain longitudinal speed and strongly influences the driving performance.

It should be remarked, that both diagrams are influenced by the transmission ratio $i_{gearbox}$ of the gearbox as indicated in the equation 3.25.

3.5.5. Maximum speed

In general, the higher the offered power, the higher the maximum speed that can be reached. This would suggest to design or select an electric motor (considering also the corresponding transmission) to reach the maximum desired speed in overload service. Nevertheless, due to the fact that an electric motor can be overloaded for a limited period of time because of thermic reasons (see e.g. [Wil11]), the maximum desired speed must be reached in nominal service if it must be hold for longer time periods. The excess power in overload service can then be used to overcome a higher demanded traction force (e.g. master a steeper road or drive against stronger headwind) during short time intervals. The maximum theoretical longitudinal speed on a flat road ${}^{max}V\dot{x}_{th\ nom\ p=0\%}$ for an electric motor working on nominal service is given by the intersection between the demanded traction force for a flat road ($p = 0\%$) and the offered traction force. It can also be expressed as the intersection between the lines of offered and demanded power.

Figure 3.12 presents different electric motor - gearbox layouts leading to different performance conditions. These three layouts are defined analogously as for vehicles with internal combustion engines (see e.g. [Wal04]). The same maximum offered power in nominal service is considered for each case. The three cases differ on the position of the overspeed point of the electric motor compared with the maximum theoretical longitudinal speed ${}^{max}V\dot{x}_{th\ nom\ p=0\%}$ (over the hyperbola of constant power for nominal service

in the traction force diagram).

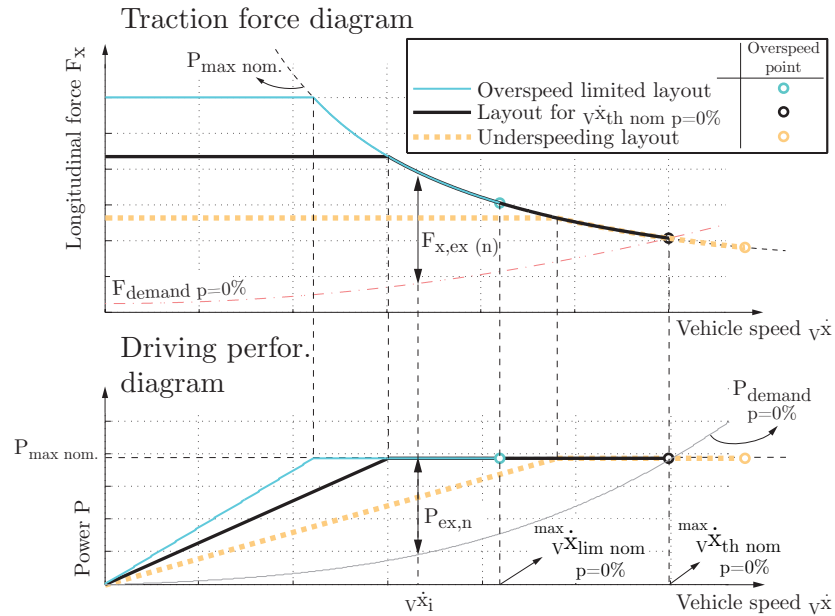


Figure 3.12.: Steady state traction force (a) and power (b) diagrams illustrating the different electric motor - gearbox layouts: layout for maximum theoretical speed $v_{x_{th}}^{max}$, electric motor overspeed limited layout, and underspeeding layout.

a) Layout for maximum theoretical longitudinal speed

The maximum theoretical longitudinal speed $v_{x_{th}}^{max}$ on a flat road can be reached for long periods of time. Nevertheless, the power excess immediately before the maximum speed available for acceleration climbing or driving against headwind is relatively small.

b) Electric motor overspeed limiting layout

If due to the combination of electric motor and gearbox, there are no intersection between the lines of offered and demanded power, the maximum achievable longitudinal driving speed is limited by the overspeed of the electric motor. In this case, the maximum theoretical longitudinal speed $v_{x_{th}}^{max}$ cannot be reached. However, the total area between the curves of offered and demanded power is greater than in the case

of the layout for ${}^{\text{max}}_V \dot{x}_{th}$. This leads to higher excess traction force values and therefore to a higher acceleration or climbing ability (see 3.5.6 chapter acceleration ability).

c) Underspeeding layout

In this case, the maximum desired longitudinal speed is reached by a rotational speed below the overspeed point of the electric motor. The maximum theoretical longitudinal speed ${}^{\text{max}}_V \dot{x}_{th \text{ nom } p=0\%}$ can be reached slower than in the other two cases because of the smaller area between the offer and demand curves. This fact represents a difference with the internal combustion engines, by which ${}^{\text{max}}_V \dot{x}_{th \text{ nom } p=0\%}$ cannot be reached with an underspeeding layout. Furthermore, the electric motor can be operated in a region of higher efficiency values, which leads to lower energy consumptions.

If a given desired maximum speed should be reached (as exposed in chapter 3.2), then the electric motor and the gearbox transmission design or selection should lead to one of the first two options discussed above.

3.5.6. Power defined climbing and acceleration ability

Based on the traction force diagram, the excess traction force $F_{x,ex}$ can be determined for a given longitudinal speed ${}_V \dot{x}_i$ as the difference between the demanded and the offered traction force (see figure 3.13):

$$F_{x,ex} = \frac{M_{D/B}}{r_{dyn}} - F_{demand} . \quad (3.28)$$

This excess traction force can be used to overcome a higher demanded traction force (e.g. reach a higher speed, master a steeper road or drive against stronger headwind).

Assuming a driving with constant speed (${}_V \ddot{x} = 0 \text{ m/s}^2$) and neglecting the influence of the road inclination on the rolling resistance (e.g. $\alpha_{road} \rightarrow 0^\circ \Rightarrow \cos(\alpha_{road}) \rightarrow 1$), the maximum road inclination that can be mastered for a given longitudinal speed ${}_V \dot{x}_i$ is given by (see e.g. [Wal04]):

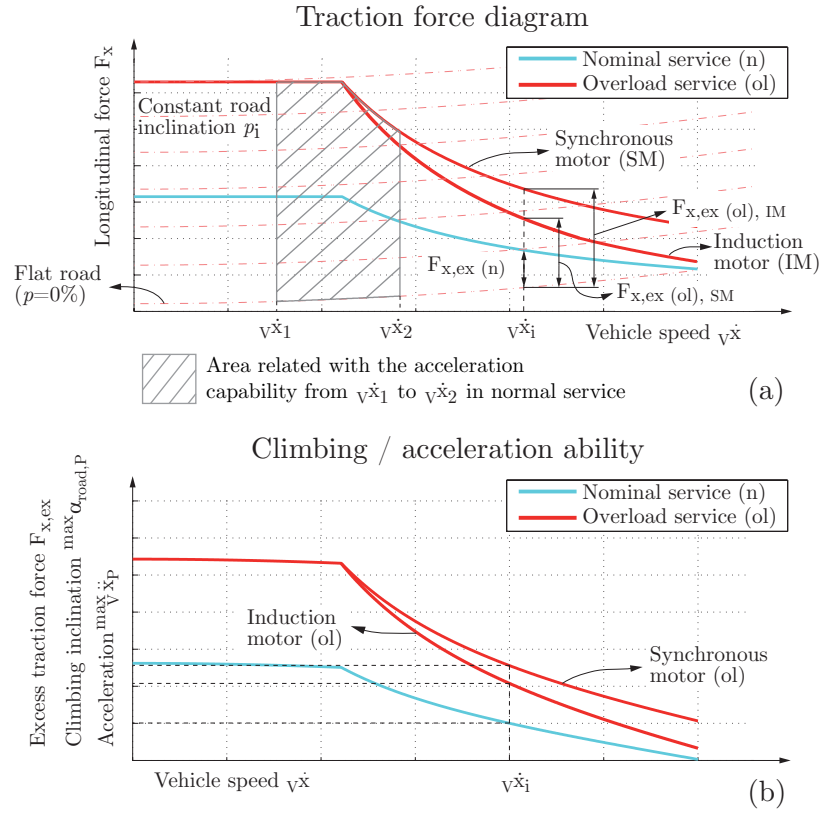


Figure 3.13.: (a) Steady state traction force diagram and excess traction force, (b) steady state power defined climbing and acceleration ability.

$$\alpha_{road,P}^{max} = \arcsin \left(\frac{F_{x,ex,v} \dot{x}_i}{(m_v + m_{load} + m_{battery}) \cdot g} \right). \quad (3.29)$$

Analogously, the maximum acceleration on a flat road is given by (see e.g. [Wal04]):

$$\ddot{v}_{\dot{x}P}^{max} = \frac{F_{x,ex,v} \dot{x}_i}{e_i \cdot m_v + m_{load} + m_{battery}}. \quad (3.30)$$

According to the torque-speed curve of electric motors (see figure 3.7), both the maximum road inclination and the maximum acceleration are available for $v_{\dot{x}} = 0$ km/h (compare with figure 3.13).

Influence of the vehicle mass on the power defined climbing and acceleration ability

According to equations 3.29 and 3.30 and observing the traction force diagram 3.13, it is evident that the power defined climbing and acceleration ability as well as the excess traction force $F_{x,ex}$ depend nonlinearly on the vehicle mass⁸ m_v (see also [Hir09a]). This nonlinear relation is shown exemplarily for a synchronous motor in Figure 3.14, which adds a new dimension to the traction force diagram presented in figure 3.11.

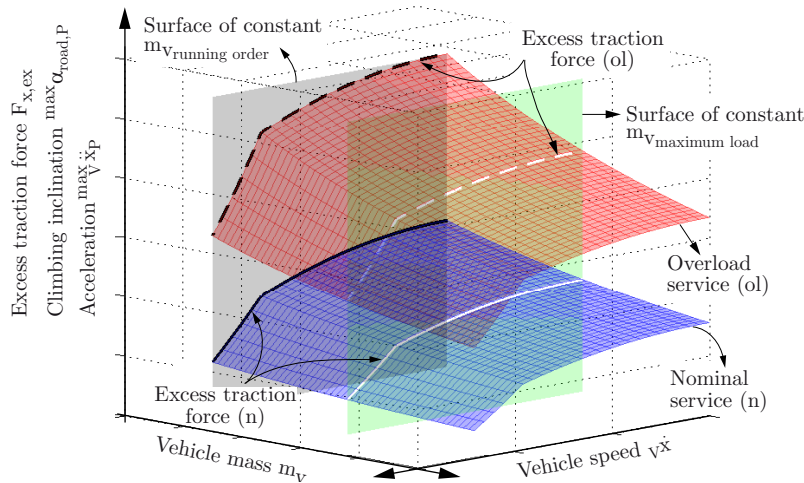


Figure 3.14.: Influence of the vehicle mass on the steady state power defined climbing and acceleration ability. The example is based on a synchronous motor. Vehicle mass definitions according to the Council Directive 92/21/EEC of 31 March 1992 of the European Union [Com92].

The excess traction force and therefore the climbing and acceleration ability decreases with increasing speed v_x and increasing vehicle mass m_v . While the influence of the vehicle speed depends mainly on the torque-speed curve of the considered electric motor, the effect of the vehicle mass is independent from the motor type.

3.5.7. Elasticity

The elasticity can be defined as the needed time to pass from a certain speed v_{x1} to a higher one v_{x2} . This is related with the acceleration ability of the vehicle and

⁸Vehicle mass definitions according to the Council Directive 92/21/EEC of 31 March 1992 of the European Union [Com92].

therefore with the excess traction force $F_{x,ex}$. Since $F_{x,ex}$ varies with the vehicle speed, the elasticity depends directly from the area limited by the offered force (see equation 3.25) and the quasi-stationary total resistance force $F_{x_{resistance}}$ between the two given speed values (see hatched area in figure 3.13). Furthermore, while the elasticity and therefore the speed development within the torque constant region depends on the nominal torque of the electric motor nM , in the field weakening region they depend on the nominal power nP .

3.5.8. Determination of the electric motor torque and power characteristics

To determine the suitable motor torque and power characteristics, an optimization process based on the simplex algorithm was developed. The flow diagram of the presented approach can be seen in figure 3.15. The desired performance requirements as well as initial values for the nominal torque ${}^{n,init}M$, nominal power ${}^{n,init}P$, number of electric motors N_{EM} and overload factor f_{OL} serve as inputs. Based on ${}^{n,init}M$ and ${}^{n,init}P$, the achievable driving performance is determined as described before. The values of nM and nP are varied by the optimization algorithm until the desired driving performance can be reached with the minimum nM and nP . Therefore, following fitness function to be minimized is proposed:

$$J_{EM} = \sum_1^{DP_i} \underbrace{b_i \cdot \Delta DP_i}_{\text{Performance parameters}} + \underbrace{b^n_M \cdot {}^nM}_{\text{Nominal torque}} + \underbrace{b^n_P \cdot {}^nP}_{\text{Nominal power}}. \quad (3.31)$$

The first term on the right side of this equation accounts for the difference between the desired driving performance parameters DP_i (see figure 3.3) and the obtained ones. Weighting factors b_i are introduced to be able to vary the relative importance of the considered performance parameters. The second term punishing the nominal torque nM is introduced since the torque is related with the weight of the electric motor and it influences directly the non-suspended masses tending to negatively affect ride comfort and driving safety (see chapter 5.2). The third term accounts for the minimization of the nominal power nP .

It must be pointed out, that while minimizing the nominal torque (weight) and installed power, the proposed fitness function allows the fulfillment of all desired performance

parameters or only some of them depending on the weighting factors b_i and on the threshold e_{EM} introduced in the algorithm. The torque and power characteristics of the electric motor are iteratively varied until the value J_{EM} of the fitness function is smaller than the threshold e_{EM} . The electric motor (or a group of them) with the obtained torque-speed curve fulfills the driving performance requirements for the analyzed vehicle as described before.

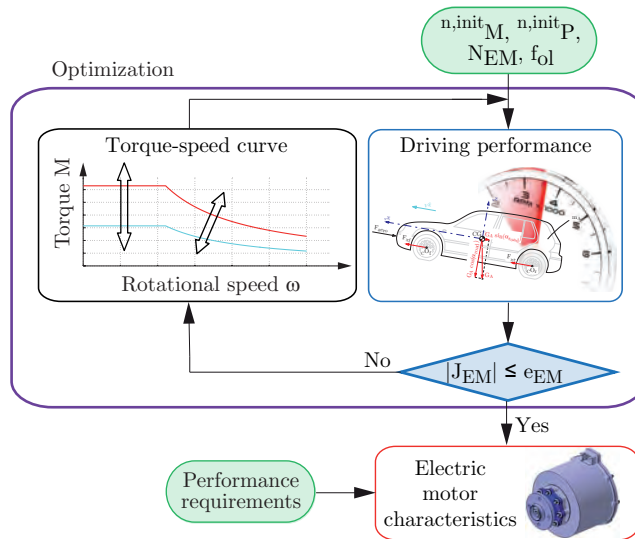


Figure 3.15.: Flow diagram of the optimization process used to determine the torque and power characteristics of an electric motor.

3.6. Power demand of auxiliaries for electric vehicles

In electric vehicles, traditional mechanical auxiliaries (e.g. the air conditioning compressor, the booster vacuum pump of the brake system and the power steering system) that are directly driven by the engine in vehicles with ICE, are normally replaced by electrical components. Among other aspects, this is due to the fact that they cannot be powered during standstill phases in which the electric motor used for traction is not moving. Wallentowitz et al. [WFO09] summarize the maximum power demand of these components as presented in table 3.2.

The operating factor introduced in table 3.2 is based on the experience of the automotive companies and accounts for the fact that auxiliaries are neither permanently working nor demanding the maximum power. More information about the power demand of

Table 3.2.: Average power demand of auxiliaries for an electric vehicle [WFO09].

		Minicompact to compact	Midsized to large
Air conditioning system		4.0	6.0
Power steering system	[kW]	1.0	1.2
Brake booster		0.2	
Operating factor	[%]	10.0	
Average power demand	P_{Aux} [kW]	0.52	0.74

auxiliaries can be found in [Lun09] and [Gös08]. Moreover, *Niederkofler* [Nie11] presents the power demand of a novel electrical single wheel steering system.

The energy for the auxiliaries is supplied from the main battery used to provide the energy to the electric traction motors. Since the voltage in the battery is normally higher than the needed one for the auxiliaries, a DC-DC-converter is needed. Assuming the same efficiency for the DC-DC-converters as for the DC-AC-converters ($\eta_{inverter}$) used for the electric traction motors (see chapter C.5) and based on the total power demand of auxiliaries P_{Aux} , the additional battery mass $\Delta m_{Batt_{Aux}}$ needed to cover their energy demand for a certain maximum range $^{max}\mathfrak{s}$ can be calculated based on the the energy-to-mass ratio $E_{Batt\ specific}$ and for the different driving cycles considered as:

$$\Delta m_{Batt_{Aux}} = P_{Aux} \cdot \frac{t_{cycle}}{E_{Batt\ specific}} \cdot \frac{^{max}\mathfrak{s}}{\mathfrak{s}_{cycle}} \cdot \frac{1}{\eta_{inverter} \cdot \eta_{Battery\ discharge} \cdot SOC_{Batt\ range}} \quad (3.32)$$

The SOC-Range $SOC_{Batt\ range}$ must be introduced in equation 3.32 to account for the fact that there is always a non-usable energy capacity in the battery, as stated before in chapter 3.4.1.

3.7. Results

In this chapter, the applicability of the approaches proposed in this work is discussed. Therefore, the considered vehicles and powertrain architectures as well as the general characteristics of the battery and electric motor(s) are presented in the first part of this chapter. Afterwards, the battery characteristics are determined for each vehicle based on the driving cycles presented in chapter 3.3 and according to the methodology

proposed in chapter 3.4.3. Finally, the electric motor characteristics are identified based on the approach proposed in chapter 3.5.8.

It must be pointed out, that the assumed values in chapters 3.7.1 and 3.7.3 are just representative examples of the technology available nowadays and are used only to discuss the applicability of the design methodology proposed in the mentioned chapters. They can be easily modified to consider any other scenario.

3.7.1. Considered vehicle classes

To analyze the influence of different vehicle characteristics on the dimensioning of battery and electric motors, different vehicle classes are considered. Since it can be expected, that electrified powertrains will become more common in small vehicles in the near future (see e.g. [WFO09]), three vehicles belonging to the minicompact (A^-), subcompact (A) and compact (B) classes⁹ are taken into account. The assumed characteristics of these vehicles can be observed in the table 3.3 and correspond to representative vehicles available in the market nowadays.

Table 3.3.: Assumed parameters of the considered vehicle classes.

		Minicompact	Subcompact	Compact	
		A^-	A	B	
Vehicle mass	In running order ^a m_v	850	1050	1200	
	Max. authorized ^a $max m_v$	1050	1550	1800	
	Mean (design) $mean m_v$	950	1300	1500	
Rolling resistance coefficient ^a	f_{roll}		0.01		
Drag coefficient ^b	C_d	0.26	0.27	0.28	
Frontal area ^b	A_w	[m ²]	2.0	2.2	2.3
Dynamic radius ^a	r_{dyn}	[m]	0.26	0.28	0.30
Inertia moment of one wheel ^a	I_w	[kg · m ²]	0.8	0.9	1.0
Air density ^a	ρ	[kg/m ³]		1.293	

^a Based on [BS07].

^b Based on [Huc05].

⁹Vehicle classes definition according to [oE11].

In table 3.3, the mean value

$$\text{mean } m_v = \frac{m_v + {}^{max}m_v}{2} \quad (3.33)$$

of the vehicle mass in running order m_v and maximum authorized mass ${}^{max}m_v$ is presented (see [Com92] for the definition of these concepts). This value will be used for further calculations since the total vehicle mass influences both longitudinal force and energy demands (see chapter 3.4.2).

3.7.2. Powertrain architectures

Figure 3.16 shows a schematic representation of the powertrain architectures considered. Two electric powertrain architectures are taken into account to analyze the advantages and limitations of in-wheel motors: a rear-wheel drive and a four-wheel drive powertrain. It must be mentioned, that the electric powertrain corresponding to the rear-wheel drive architecture can be used as add-on alternative to hybridize a vehicle with an internal combustion engine driving the front wheels. A comparison between rear-wheel and four-wheel drive mechanical powertrain architectures can be found in [HEG11] and [Sto04].

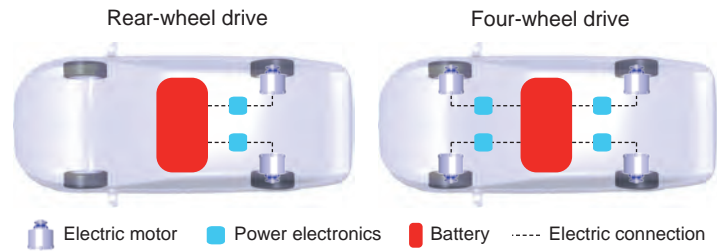


Figure 3.16.: Schematic representation of the considered powertrain architectures.

3.7.3. General properties of the electric powertrain components

The general properties of the electric powertrain components (battery, power electronics and electric motors) are presented in table 3.4.

The Energy-to-mass $E_{Batt \text{ specific}}$, the Power-to-mass $P_{Batt \text{ specific}}$ and the SOC-Range $SOC_{Batt \text{ range}}$ values correspond to a modern Li-ion battery with a high specific energy content for electric vehicles. The indicated efficiency values are lower than the nominal

Table 3.4.: General properties of the electric powertrain components.

Battery	Energy-to-mass ratio ^a	$E_{Batt\ specific}$	[Wh/kg]	150
	Power-to-mass ratio ^a	$P_{Batt\ specific}$	[W/kg]	300
	State of charge hub ^b	$SOC_{Batt\ range}$		70
	Efficiency ^b	Charge	$\eta_{Battery\ charge}$	[%]
Discharge		$\eta_{Battery\ discharge}$	88	
Power electronics	Efficiency ^c	$\eta_{inverter}$	[%]	95
Electric motor(s)	Max. rotational speed ^d	$^{max}\omega$	[rad/s]	11000 rpm, $\frac{2\cdot\pi}{60}$
	Red. moment of inertia ^e	$I_{EM\ Wheel}^*$	[kg · m ²]	0.75
	Efficiency ^d	As motor	$\eta_{EM\ motor}$	[%]
As generator		$\eta_{EM\ generator}$	82	

^a See figure C.3.

^b See e.g. [Hof09].

^c See e.g. [WFO09].

^d See e.g. [Wil11].

^e Estimated reduced moment of inertia of each electric motor and its transmission at wheel level as stated in appendix C.2 (see also [Wil11]).

ones indicated in chapter 3.4.1 to account for the efficiency reduction when the battery is working in a real driving cycle.

As indicated in chapter C.5, the efficiency of the power electronics is very high and around a value of 93 %. For further calculations, highly efficient power electronics are considered, as shown in table 3.4.

Based on the maximum rotational speed of the electric motor(s) $^{max}\omega$ and on the desired maximum speed of the vehicle $^{max}\dot{x}$ (see table 3.5), the transmission ratio $i_{gearbox}$ of the gearbox used between each electric motor and the wheel hub can be found as a function of the dynamic radius r_{dyn} according to:

$$i_{gearbox} = \frac{\omega_{max} \cdot r_{dyn}}{max\dot{x}}. \quad (3.34)$$

To take into account the moment of inertia of the electric motor on the energy requirements, a reduced moment of inertia at wheel level $I_{EM\ Wheel}^*$ (see section C.2) was

estimated for the assembly group consisting of electric motor and transmission¹⁰. Furthermore, as in the case of the battery, efficiency values lower than the nominal ones (see chapters C.4.1 and C.4.2) were assumed to account for efficiency reduction during real driving cycles away of the nominal point (see also [Wil11]).

3.7.4. Performance requirements

Table 3.5 shows the performance requirements for the different vehicle classes defined in chapter 3.7.1. The maximum speed $^{max}\dot{x}$ is defined for flat road ($p = 0\%$) and for a road with an inclination of $p = 4\%$ ¹¹. Two acceleration values ${}_V\ddot{x}_{0\rightarrow 50}$ and ${}_V\ddot{x}_{0\rightarrow 100}$ (from standstill to 50 km/h and 100 km/h respectively) are considered. To be able to overtake trucks on a highway, an elasticity ${}_V\ddot{x}_{80\rightarrow 100}$ is also specified. For all vehicles, the same climbing ability ^{max}p from standstill is required and the same overload factor f_{OL} is considered. Furthermore, since it is assumed that the considered vehicles are not going to be used to drive very long distances in one single trip, driving ranges up to 150 km (depending on the vehicle class) are set as requirement. The values presented in table 3.5 correspond to rational real world performance requirements (see also [Cho02], [BH11] and [Hir11]).

3.7.5. Energy demand and needed battery mass

According to chapter 3.6, table 3.6 presents the additional battery mass $\Delta m_{Batt_{Aux}}$ for the different driving cycles considered (see chapter 3.3) while taking into account the information on tables 3.1, 3.4 and 3.5.

Based on the methodology proposed in chapter 3.4.3 and on the information of tables 3.3, 3.4, 3.5 and 3.6, the energy and power demands as well as the needed battery for the different considered driving cycles were determined and are presented in table 3.7.

As it was expected (see chapter 3.3), the energy demand of non-standardized driving cycles (ARTEMIS, HYZEM and INRETS) is higher than for standardized ones

¹⁰The inertia moment of the rotor of synchronous and induction motors used for in-wheel applications is lower than 10^{-2} (see e.g. [Wil11]).

¹¹According to the German Federal Ministry of Transportation, the maximum inclination of roads designed for maximum speeds between 120 km/h and 130 km/h (maximum speed for the different considered vehicle classes) is 4% (see [Wal04]).

Table 3.5.: Driving performance requirements.

				EM service mode ^a	Load condition	Minicompact A ⁻	Subcompact A	Compact B
Maximum speed	Flat road	$\frac{max \dot{x}_{\alpha_{road}=0^\circ}}{}$	$\left[\frac{\text{km}}{\text{h}} \right]$	n		120	130	130
	Inclined road	$\frac{max \dot{x}_{\alpha_{road}=4^\circ}}{}$						
Climbing ability		$max p$	$[\%]$		$mean m_v$		25	
Acceleration	0 to 50 km/h	$\Delta t_{0 \rightarrow 50}$	$[\text{s}]$	ol		8	7	7
	0 to 100 km/h	$\Delta t_{0 \rightarrow 100}$				16	16	15
Elasticity	80 to 110 km/h	$\Delta t_{80 \rightarrow 110}$				15	12	12
Driving range		$max s$	$[\text{km}]$	-		100	120	150
Overload factor ^b		f_{OL}	$[-]$		-		2	

^a Service modi of electric motor(s): nominal (n) and overload (ol) service.

^b Based on [Wil11].

(NEDC, FTP-75 and Japan-10-15) independently from the vehicle class. While the NEDC present the highest energy demand among all standardized cycles, the ARTEMIS and HYZEM driving cycles show the highest demand among all considered cycles. As discussed in chapter 3.3, this behavior is due because of the highest accelerations at higher speeds.

For given battery specifications (see table 3.4), the dominant factor for the battery dimensioning depends mainly on the driving cycle. For example, if the determined energy content of the battery is equal to the energy demand in the considered driving cycle, it can be said that the dominant factor corresponds to the energy capacity of the battery. In such a case, both values are highlighted in table 3.7. The same occurs for the power demand of the considered driving cycle and the power of the battery. It can be seen that while the dominant factor for standardized driving cycles correspond to the battery energy capacity, the power demand tend to be the dominant factor for non-standardized driving cycles. This comes from the higher accelerations of the non-standardized driving cycles. The results agree with those presented in the literature (see e.g. [WFO09] and [Gös08]).

Table 3.6.: Additional battery mass $\Delta m_{BattAux}$ needed to cover the energy demand of electric auxiliaries for an electric vehicle belonging to the vehicle classes minicompact to compact in the different driving cycles.

	Additional battery mass $\Delta m_{BattAux}$ [kg]		
	Minicompact A^-	Subcompact A	Compact B
NEDC	0.60	0.72	0.90
FTP-75	0.44	0.53	0.66
Japan-10-15	0.98	1.18	1.47
ARTEMIS	0.16	0.19	0.24
HYZEM	0.10	0.12	0.15
INRETS	0.40	0.48	0.60

It must be mentioned at this point, that only the maximum power while driving was considered in the presented methodology (see chapter 3.4.3) for the dimensioning of the battery. Taking the maximum power while braking would lead to higher battery masses (around the double). Furthermore, the appearance of high decelerations while braking is very seldom with 98 % of all deceleration values being smaller than the maximum of the acceleration ones. This can be seen in figure 3.17, which shows the relative cumulative frequency (see appendix A.1) of the power while braking for the most extreme case, i.e. compact vehicle (B) in the HYZEM driving cycle. In this case, around 99.9 % of all cases concerning the power while braking can be covered with the maximum power while driving. Dimensioning the battery according to the maximum power while braking would thus lead to an overdimensioned battery. Correspondingly, the maximum power cannot be recovered but this is compensated with the energy saving arising from transporting a lighter battery all the time.

Table 3.8 summarizes the battery mass m_{Batt} needed for the considered vehicles based on the results of all analyzed driving cycles and to fulfill the driving range defined in table 3.5 (see battery properties in table 3.4). It must be remarked, that the results were obtained taking into account the mean value of the vehicle mass $^{mean}m_v$ and thus a lower or a higher energy demand (lighter or heavier battery) can be obtained for the mass in running order m_v and with the maximum authorized mass $^{max}m_v$ respectively.

3.7. Results

Table 3.7.: Energy and power demands as well as the needed battery mass for the different considered driving cycles. Highlighted background cells correspond to the dominant factor in the considered driving cycle.

		Energy				Power		Battery				
		Total required ^a	Net ^b		Recuperated	Max. driving	Max. braking	Energy capacity ^d	Power capacity	Mass for 100km	Mass for range ^e	Total mass ^f
			Final ^c	Maximum								
		[kWh/100 km]				[kW]		[kWh]	[kW]	[kg]		
NEDC	A ⁻	12.6	10.8	11.6	1.8	26.2	20.6	11.6	33.0	110.0	110.0	110.6
	A	16.0	13.7	14.7	2.4	32.6	27.8	14.7	41.9	139.6	167.5	168.2
	B	18.1	15.4	16.5	2.7	36.4	31.8	16.5	47.1	157.1	235.6	236.5
FTP-75	A ⁻	11.6	9.2	9.3	2.5	23.5	19.6	9.3	26.5	88.4	88.4	88.8
	A	15.2	11.9	12.0	3.3	31.0	26.2	12.0	34.4	114.5	137.4	137.9
	B	17.2	13.4	13.6	3.8	35.3	29.9	13.6	38.9	129.7	194.5	195.1
Japan-10-15	A ⁻	11.8	9.2	9.9	2.6	13.7	8.6	9.9	28.2	94.1	94.1	95.1
	A	15.4	12.0	12.9	3.5	18.1	11.5	12.9	36.8	122.8	147.4	148.6
	B	17.5	13.6	14.6	4.0	20.6	13.2	14.6	41.8	139.4	209.1	210.6
ARTEMIS	A ⁻	15.0	13.1	13.2	1.9	40.0	83.8	14.0	40.0	133.2	133.2	133.3
	A	19.0	16.4	16.5	2.6	51.5	111.6	18.0	51.5	171.7	206.0	206.2
	B	21.4	18.4	18.5	3.0	58.2	127.3	20.4	58.2	193.9	290.9	291.1
HYZEM	A ⁻	15.2	13.6	13.6	1.6	40.4	111.5	14.1	40.4	134.7	134.7	134.8
	A	19.0	16.9	16.9	2.2	51.3	147.9	17.9	51.3	170.9	205.1	205.2
	B	21.3	18.8	18.9	2.5	57.6	168.5	20.2	57.6	192.1	288.1	288.3
INRETS	A ⁻	16.1	12.9	13.1	3.3	35.9	65.2	13.1	37.4	124.8	124.8	125.2
	A	20.7	16.4	16.7	4.4	47.3	86.3	16.7	47.7	158.9	190.7	191.1
	B	23.4	18.4	18.8	5.0	53.8	98.4	18.8	53.8	179.3	269.0	269.6

^a Total energy required for the driving cycle without recuperation.

^b Energy required for the driving cycle with recuperation.

^c Measured at the end of the driving cycle.

^d Usable energy capacity according to the defined $SOC_{Batt\ range}$ (see table 3.4).

^e Battery mass required to reach the desired range (see table 3.5).

^f Total battery mass required to reach the desired range (see table 3.5) and considering the additional battery mass $\Delta m_{Batt\ Aux}$ needed to cover the energy demand of electric auxiliaries (see table 3.6).

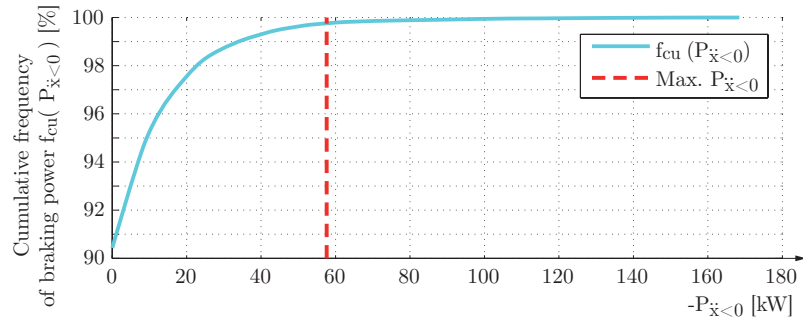


Figure 3.17.: Cumulative frequency of the power while braking $P_{\dot{x}<0}$ for a compact vehicle (B) during the HYZEM driving cycle (most extreme case from those presented in table 3.7).

Table 3.8.: Battery mass m_{Batt} needed for the considered vehicles in order to fulfill the driving range specified in table 3.5 (see battery properties in table 3.4).

		Battery mass m_{Batt} [kg]
Minicompact	A^-	135
Subcompact	A	205
Compact	B	290

3.7.6. Dimensioning of electric motors

According to equation 3.34 and taking into account the specified maximum rotational speed of the electric motors $^{max}\omega$ (see table 3.4), the dynamic radius r_{dyn} (see table 3.3) as well as the maximum desired speed on flat road $^{max}\dot{x}_{\alpha=0^\circ}$ (see table 3.5), the transmission ratio $i_{gearbox}$ of the gearbox used between each electric motor and the wheel hub was determined and is presented in table 3.9.

Table 3.9.: Transmission ratio of the gearbox used between the electric in-wheel motors and the wheel hub for the different vehicles considered.

		Transmission ratio $i_{gearbox}$ [-]
Minicompact	A^-	8.99
Subcompact	A	8.93
Compact	B	9.57

To determine the power and torque characteristics of the electric motors needed for

the different vehicle classes defined in table 3.3 to fulfill the performance requirements established in table 3.5, the weighting factors shown in table 3.10 were used for the fitness function of equation 3.31.

Table 3.10.: Weighting factors used to determine the power and torque characteristics of the electric motor(s).

		Weighting factor [-]			Weighting factor [-]
Nominal torque	b^n_M	0.5	Nominal power	b^n_P	0.5
Maximum speed	$b^{max}_{\dot{x}}$	2.0	Climbing ability	b^{max}_α	0.4
Acceleration	$b_{\Delta t_0 \rightarrow \dot{x}_i}$	2.0	Elasticity	$b_{\Delta t_{\dot{x}_1 \rightarrow \dot{x}_2}}$	2.0

Applying the proposed methodology presented in chapter 3.5.8, the torque and power characteristics as well as the achieved performance parameters presented in table 3.11 were obtained. In this table, the reserve ^{res}p , i.e. the inclination angle that can still be overcome at maximum speed (${}_V\dot{x}_i = ^{max}\dot{x}$ in equation 3.29), is also shown.

Comparing the results of table 3.11 with the performance requirements presented in table 3.5, it can be seen, that all performance requirements were achieved. The nominal torque and power of the electric in-wheel motors in a four-wheel drive architecture are more or less the half of those in a rear-wheel drive one. In the proposed methodology, even though the same vehicle mass was assumed for both powertrain architectures, the moment inertia of the additional electric motors and the transmission ratio of their corresponding gearboxes increase particularly the power demand.

To fulfill the requested performance requirements, while the nominal torque for the induction motors is almost the same as for the synchronous ones, the nominal power is higher. This can be explained using the traction force diagram presented in figure 3.18 for the case of vehicles with two in-wheel motors. It is required that the vehicles achieve certain acceleration and elasticity characteristics with the electric motors working in overload service. In the proposed methodology, it is assumed that the overload service corresponds to the curve of breakdown torque. Since the acceleration is related with the area between the demanded and offered force (see also chapter 3.5.6), and due to the fact that the curve of breakdown torque declines more rapidly for induction than for synchronous motors in the field weakening area (see chapter 3.5.1), a higher power is needed to achieve the required acceleration. As approximately the same driving performance is achieved with the presented induction and synchronous motors, it can

Table 3.11.: Electric motor characteristics for vehicles with two and four in-wheel motors.

E-motor		Max. speed ^b		Climbing ^c			Accel. ^c		Elast. ^c	Reserve ^c		
Torque	Power	Flat road	Inclined road	For m_v	For $mean m_v$	For $max m_v$	0-50 $\frac{km}{h}$	0-100 $\frac{km}{h}$	80-110 $\frac{km}{h}$	Inclination		
${}^n M$	${}^n P$	$max \dot{x}_{\alpha=0^\circ}$	$max \dot{x}_{\alpha=4^\circ}$	$max p$			$\Delta t_{0 \rightarrow 50}$	$\Delta t_{0 \rightarrow 100}$	$\Delta t_{80 \rightarrow 110}$	$res p$		
[Nm]	[kW]	[km/h]		[%]			[s]		[%]			
2 x IM ^a	A ⁻	17.0	11.2	120	105	28	25	22.5	6.3	16	9.9	3.2
	A	25.2	14.8	130	108	32	25	20.5	6.2	16	10.1	1.6
	B	29.1	17.9	130	112	32	25	20.5	6.1	15	8.6	2.5
2 x SM ^a	A ⁻	17.0	9.1	120	93	28	25	22.5	6.3	16	8.1	6.7
	A	25.2	11.8	130	93	32	25	20.5	6.2	16	8.2	5.3
	B	29.2	14.8	130	99	32	25	20.5	6.1	15	7.3	6.4
4 x IM ^a	A ⁻	8.5	5.7	120	106	28	25	22.5	6.5	16	9.7	3.5
	A	12.6	7.5	130	110	32	25	20.5	6.2	16	10	1.8
	B	14.6	9.1	130	114	32	25	20.5	6.2	15	8.6	2.7
4 x SM ^a	A ⁻	8.5	4.7	120	95	28	25	22.5	6.5	16	8.1	7.1
	A	12.6	6.0	130	94	32	25	20.5	6.2	16	8.1	5.6
	B	14.6	7.5	130	101	32	25	20.5	6.2	15	7.2	6.6

^a IM: Induction motor - SM: Synchronous motor

^b To be fulfilled with electric motor(s) working in nominal service.

^c To be fulfilled with electric motor(s) working in overload service.

be seen in figure 3.18 how the curves for the overload service are crossed in the field weakening area and more or less the same area arises between them and the total resistance force for a flat road ($p = 0 \%$). The traction force diagrams for the vehicles with four in-wheel motors are very similar to those for the vehicles with two electric motors and can be found in appendix C.6. It must be pointed out, that the obtained results agree with those presented recently by *Gombert et al.* [GFH10].

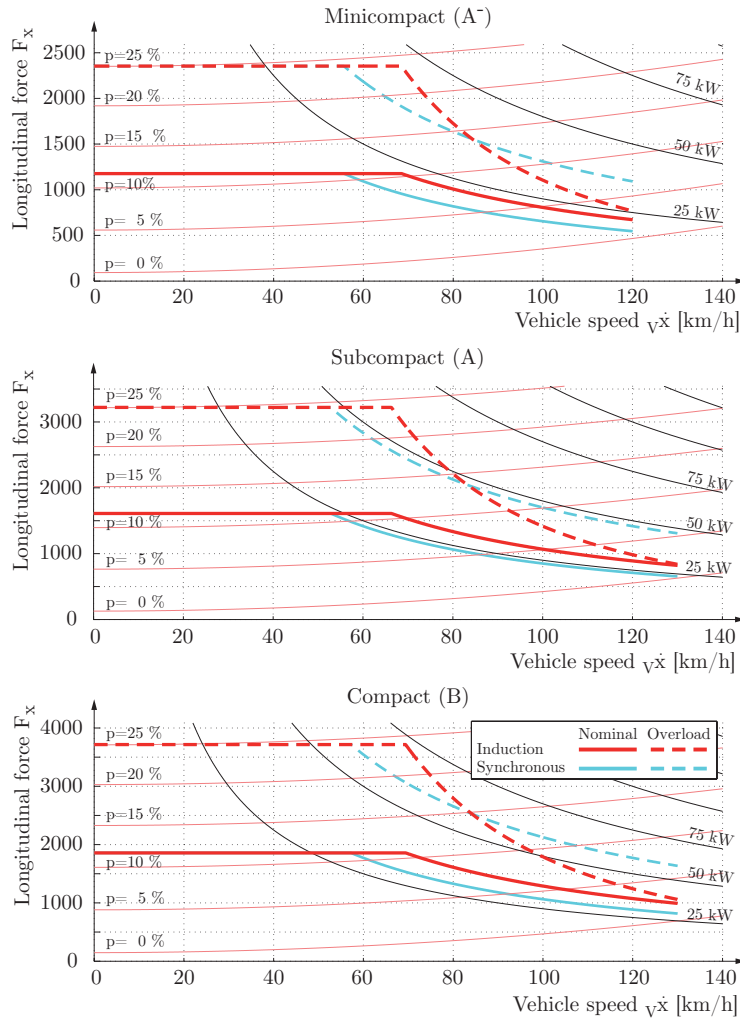


Figure 3.18.: Steady state traction force diagrams for the different vehicles considered with two in-wheel motors.

Figure 3.19 exemplarily shows, the operation points of the electric motors of a minicompact vehicle (A⁻) with a rear-wheel drive powertrain architecture for different driving cycles. The pictures for the other vehicle classes considered are quite similar and are

therefore omitted. As presented in figure 3.19, while the electric motors obtained with the proposed approach (see chapter 3.5.8) cover all the operating points for the standardized driving cycles (NEDC, FTP-75 and Japan-10-15), there are some operating points of the non-standardized cycles (ARTEMIS, HYZEM and INRETS) that cannot be covered. Some operating conditions demand higher traction forces and some other higher speeds. It must be taken into account, that the maximum speed defined for the minicompact segment (120 km/h) is lower than the highest speed of the ARTEMIS and HYZEM driving cycles, since it is assumed, that this kind of vehicle is mainly used in the city where those high speeds are normally not found. Nevertheless, the results show that over 95 % of all operating points corresponding to the non-standardized driving cycles can be covered for all considered vehicles (minicompact A^- , subcompact A and compact B). This fact agrees with the results of Wallentowitz [WFO09]. Additional aspects regarding the performance of electric motors in different driving cycles can be found in [WARN10].

All presented analyses are based on the assumption that the mass in running order of an electric vehicle $m_{v, EV}$ is the same as for a vehicle with internal combustion engine $m_{v, ICE}$. To validate this assumption, a short analysis was made for the case of a rear-wheel drive electric vehicle with two synchronous motors and is presented in table 3.12.

In the first part of table 3.12, the mass in running order of a vehicle with internal combustion engine $m_{v, ICE}$ is taken as basis to calculate the mass m_{v0} of a vehicle without mechanical powertrain or fuel tank. The term *powertrain* considers here not only the engine, the gearbox and the drive shafts but also the exhaust system. In the second part, the mass of the electric motors $m_{EM\ total}$, the power electronics $m_{PE\ total}$ and the battery m_{Batt} is added to m_{v0} to estimate the mass in running order $m_{v, EV}$ of an electric vehicle belonging to the different vehicle classes considered. To approximate the mass of the electric motors, the mass of one electric motor for the subcompact vehicle A was estimated as 25 kg based on chapter 3.5.2. The mass of one electric motor for the other vehicle classes considered was approximated proportionally to its individual nominal torque (see table 3.11). The values of the battery mass correspond to those presented in table 3.8. Following the same approach, the relative weight change for rear-wheel and four-wheel drive electric vehicles using also induction motors were determined (see table C.2 in appendix C.7). The results show only small changes ($|\Delta m_v| \leq 6.1\%$). Similar results were presented by *Eckstein et al.* [EGW11], who compared the weight of the *Mitsubishi i-MiEV* as the first series electric vehicle of a big automotive company

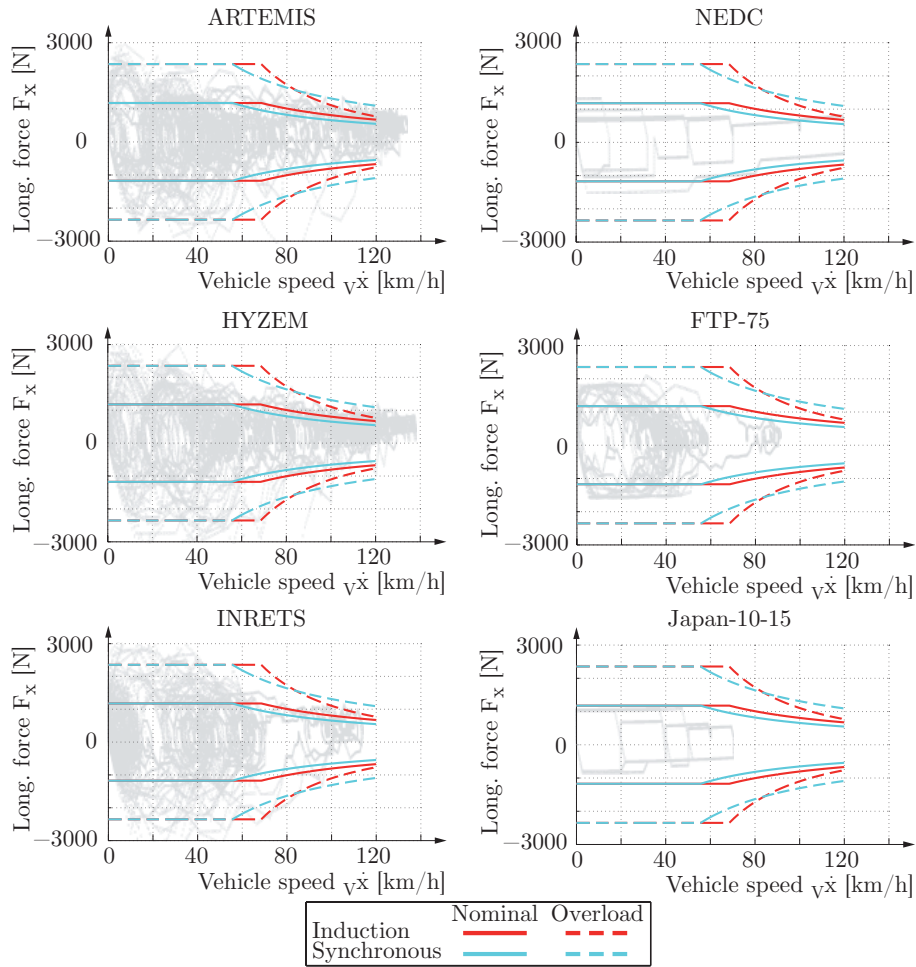


Figure 3.19.: Steady state operation points of the electric motors of a minicompact vehicle (A^-) with a rear-wheel drive powertrain architecture for different driving cycles.

(see [HY07]) with a traditional vehicle with internal combustion engine and similar driving performance. Based on this approach and taking the different operation ranges of both vehicles with ICE and electric vehicles into account, it can be concluded, that no appreciable weight change for an electric vehicle in comparison with its counterpart with internal combustion engine is to be expected. Therefore, the assumption made in this chapter concerning similar masses for these kind of vehicles can be assumed as valid for the presented calculations.

Table 3.12.: Comparison of the weight of a vehicle with internal combustion engine (ICE) and an electric vehicle (EV) with a rear-wheel drive powertrain architecture for the different vehicle classes considered.

Vehicle with internal combustion engine			A^-	A	B	
Vehicle mass in running order ^a	$m_{v, ICE}$		850	1050	1200	
Mechanical powertrain ^b		[kg]	210	300	360	
Fuel tank ^b			35	50	60	
Base vehicle mass ^c	m_{v0}		605	700	780	
Electric rear-wheel drive vehicle with two synchronous in-wheel motors			A^-	A	B	
Electric motors	Individual mass ^d	m_{EM}	16.9	25.0	28.9	
	Total mass	$m_{EM total}$	33.7	50.0	57.8	
Power electronics ^e	Individual mass	m_{PE}		15		
	Total mass	$m_{PE total}$		30		
Battery mass		m_{Batt}	135	205	290	
Approx. mass EV in running order ^f		$m_{v, EV}$	803.7	985.0	1157.8	
Relative weight change ^g		Δm_v	[%]	-5.4	-6.2	-3.5

^a See table 3.3 for the characteristics of the different vehicle classes considered and [Com92] for the terminology concerning the vehicle mass.

^b See [HEG11] for approximated weights of powertrain components and fuel tank.

^c Vehicle mass without mechanical powertrain and fuel tank.

^d The mass of an electric motor for the subcompact vehicle class was approximated to 25 kg taking into account the active mass of the electric motor (see chapter 3.5.2), bearings and housing. The mass of the electric motors for the other vehicle classes was obtained proportionally based on their nominal torque ⁿ M .

^e The same number of inverters as electric motors is assumed (see also chapter 3.7.2). The individual mass was approximated.

^f $m_{v, EV} = m_{v0} + m_{EM total} + m_{PE total} + m_{Batt}$

^g $\Delta m_v = (m_{v, EV} - m_{v, ICE})/m_{v, EV}$

Summary chapter 3: Longitudinal dynamics This chapter focused on the determination of the battery and electric motor characteristics for vehicles with in-wheel motors on the basis of given performance requirements (e.g. maximum speed for different road inclinations, driving range or acceleration and climbing ability). Therefore, optimization approaches using the Nelder-Mead simplex algorithm (see [NM65]) were developed and presented. In the first part of the chapter, the simplified equations of motion for the longitudinal vehicle dynamics were deduced from those corresponding to the three-dimensional vehicle model presented in chapter 2. Afterwards three standardized (NEDC, FTP-75 and Japan-10-15) and three non-standardized (ARTEMIS, HYZEM and INRETS) driving cycles were presented and analyzed. In the third part, a simplified approach was introduced to determine the battery mass based on the presented driving cycles and taking into account the theoretical recuperable kinetic energy as well as the power demand of auxiliaries for electric vehicles. After having analyzed the main aspects and boundary conditions that must be taken into account, an optimization approach to determine the nominal torque and power of induction and synchronous motors is presented hereafter. It corresponds to a synthesis process leading to the fulfilment of the driving performance requirements imposed.

The presented approaches were used to determine the characteristics of the mentioned electric components for vehicles belonging to three different vehicle classes: minicompact, subcompact and compact. Therefore two pure electric powertrain architectures (i.e. a rear-wheel and a four-wheel powertrain) were considered. In order to guarantee the customer acceptance of the synthesized vehicles with in-wheel motors, performance requirements corresponding to those present in modern vehicles with traditional internal combustion engine were assumed. Furthermore, a half loaded condition was considered to account for changing demands with the vehicle mass.

The results corresponding to the dimensioning of the battery showed that, while standardized cycles can be used to determine the energy capacity, the more dynamic non-standardized cycles determine the power capacity. Based on a regular modern Li-ion battery with an energy-to-mass ratio of 150 Wh/kg and a power-to-mass ratio of 300 W/kg a battery mass of 135 kg for the minicompact, 205 kg for the subcompact and 290 kg for the compact vehicle class were obtained.

Assuming a maximum rotational speed of 11000 rpm for the electric motors and based on the required maximum longitudinal speed for the different vehicle classes, transmission ratios around 9 were defined for the different vehicle classes considered. Induction

and electric motors were assumed to be able to work both in the region of constant torque and in the field weakening region. Due to the fact that the torque curve of induction motors is inversely proportional to the square of the rotational speed in the field weakening region, higher values of the nominal power are needed than for synchronous motors for which the torque is inversely proportional to its rotational speed. The nominal torque needed to fulfill the driving performance requirements was found to be almost the same for both electric motor technologies. Exemplarily, the results showed that two electric motors with about 17.0 Nm and 11.2 kW are needed to meet the driving performance requirements of a vehicle belonging to the minicompact class and a rear-wheel drive powertrain architecture. Although the driving cycles are not explicitly considered in the presented approach to synthesize electric motors, it was shown that the obtained motor characteristics do not only fulfill the imposed performance requirements but also the demands of all driving cycles described in this chapter.

Finally, a comparison between the weight of vehicles with internal combustion engines and vehicles with in-wheel motors belonging to the three different vehicle classes considered was presented. The results showed that a weight reduction of about (6 %) can be expected under the consideration of rational real world performance requirements covering most of the daily necessities of average drivers.

4. Lateral dynamics

In this chapter, the potential of in-wheel motors to improve the vehicle lateral dynamics is analyzed. The in-wheel motors are considered to be part of an electric torque vectoring system, which can allocate longitudinal tire forces wheel individually. Therefore, different driving maneuvers are simulated and characteristic lateral dynamics parameters evaluated. In the first part of the chapter, the driving maneuvers as well as the corresponding evaluation parameters are presented. Afterwards, the control system for the torque-vectoring system is presented. In the final part, results are presented and the potentials of in-wheel motors to improve lateral vehicle dynamics discussed.

4.1. Driving maneuvers

There are several standardized and non-standardized driving maneuvers used to assess the driving behavior of vehicles (see e.g. [fSI03] and [RH84]). They can be grouped in *open-loop* and *closed-loop* maneuvers (see e.g. [Hir09a] and [MW04]). The difference between them relies in the structure of the control loop considered (see also figure 2.1). While *closed-loop* maneuvers consider the driver as controller within the control loop, *open-loop* maneuvers exclude him. In this last group of maneuvers, it is not necessary to model and simulate the driver and the maneuver is reproducible and totally driven by the inputs corresponding to the steering wheel angle δ_{st} and the desired vehicle longitudinal speed $v\dot{x}^d$. In the maneuvers considered in this chapter, while the steering wheel angle δ_{st} is given as input and treated as in an *open-loop* maneuver, a controller (see section 4.2.2) is used to follow a desired profile of the longitudinal vehicle speed $v\dot{x}^d$ as in a *closed-loop* one. Time series corresponding to the steering wheel angle $\delta_{st}(t)$ are used directly in the simulations. A proportional-integral controller is used to regulate the longitudinal vehicle speed based on the corresponding input time series $v\dot{x}^d(t)$ (see chapter 4.2.2). In the following sections, the *open-loop* maneuvers considered in this chapter, i.e. *step steer*, *open-loop sinusoidal steering input* and *open-*

loop frequency response, are described. They are based on the recommendations of International Standard 7401:1988 [fSI03] but are adapted to the specific demands of the present work. Further information on driving maneuvers used to determine the dynamic behavior of vehicles are presented by *Rosinger* [Ros09].

4.1.1. Step steer

In relation with the control theory, it is a widespread praxis to analyze the response of a system to a fast change in one of its inputs in order to obtain information about the system dynamics [Abe04]. This is called *step response*. In the case of a vehicle, the maneuver starts with the vehicle driving straight ahead with constant speed of normally 100 km/h [RH84]. At a certain time t_0 , the steering wheel angle is changed to its stationary value δ_{st}^S with a high steering rate (*Rompe et al.* recommend a steering rate between $200^\circ/\text{s}$ and $500^\circ/\text{s}$) in such a way that the vehicle lateral acceleration ${}_v\ddot{y}$ reaches a value between 3 m/s^2 and 4 m/s^2 . Figure 4.1 shows schematically the step response of a state variable v (e.g. yaw rate $\dot{\psi}$, sideslip angle β or vehicle lateral acceleration ${}_v\ddot{y}$).

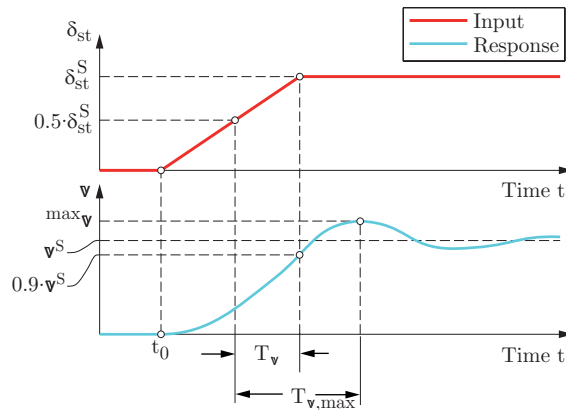


Figure 4.1.: Some assessment criteria and schematic representation of the step response of a considered state variable v to a step input of the steering angle δ_{st} .

Based on the control theory (see e.g. [Abe04]), the time point at which the steering wheel angle δ_{st} reaches 50 % of its stationary value δ_{st}^S is taken as reference to determine two of the assessment criteria related with this maneuver, i.e. the reaction time T_v and the time delay $T_{v,max}$. Small values of T_v and $T_{v,max}$ mean lower phase delay values and influence therefore the vehicle driving behavior positively. Additionally, the transient

overshoot \mathcal{O}_v can be calculated based on the maximum $^{max}_v$ and the steady state v^S values of the considered variable v as follows:

$$\mathcal{O}_v = \frac{^{max}_v - v^S}{v^S} \cdot 100 \% . \quad (4.1)$$

Small overshoot values as well as small values of the maximum sideslip angle $|^{max}\beta|$ are related with a better driving safety. Furthermore, the vehicle factor $TB_{\dot{\psi}\beta}$ can be determined as a function of the time delay of the yaw rate $T_{\dot{\psi},max}$ and the steady state value of the sideslip angle β^S as:

$$TB_{\dot{\psi}\beta} = T_{\dot{\psi},max} \cdot |\beta^S| . \quad (4.2)$$

According to *Mitschke et al.* [MW04], low values of the vehicle factor $TB_{\dot{\psi}\beta}$ are subjectively related with a better dynamic response of the vehicle by the driver. Table 4.1 summarizes the assessment criteria related with the maneuver step steer that are used in the present work.

Table 4.1.: Assessment criteria related with the maneuver step steer [Ros09].

	Assessment criteria	Symbol	Units	Requirement
Yaw rate	Reaction time	$T_{\dot{\psi}}$	s	small
	Time delay	$T_{\dot{\psi},max}$		
	Overshoot	$\mathcal{O}_{\dot{\psi}}$	%	
Lat. acc.	Reaction time	$T_v \ddot{y}$	s	
	Time delay	$T_v \ddot{y}_{,max}$		
	Overshoot	$\mathcal{O}_v \ddot{y}$	%	
	Maximum of sideslip angle	$ ^{max}\beta $	°	
	Vehicle factor	$TB_{\dot{\psi}\beta}$	s · °	

4.1.2. Open-loop sinusoidal steering input

The open-loop sinusoidal steering input is a relevant driving maneuver simulating a collision avoidance situation that can be simulated easily by means of a sinusoidal steering wheel movement with a duration of one period $T_{\delta_{st}} = 1/f_{\delta_{st}}$, as shown schematically in figure 4.2.

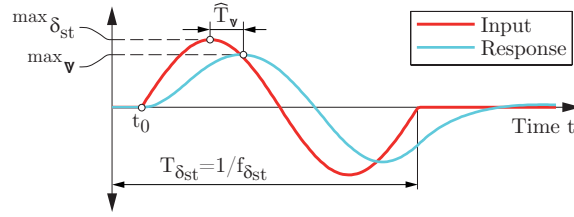


Figure 4.2.: Some assessment criteria and schematic representation of the open-loop sinusoidal steering input of a considered state variable v .

The time \hat{T}_v delay between the maximum of the steering wheel angle $^{max}\delta_{st}$ and the maximum of the considered state variable v is a measure of the dynamic behavior of the system and is used in the present work as assessment criteria. In general, lower values of \hat{T}_v are related with a good vehicle driving behavior. Furthermore, the maximum values of the sideslip angle $|^{max}\beta|$ and the vehicle lateral acceleration $|^{max}_v\ddot{y}|$ are taken as additional assessment criteria since small values of the sideslip angle β are an indication of proper driving stability and high values of the vehicle lateral acceleration $_v\ddot{y}$ are a sign of the vehicle's capability to avoid obstacles in critical driving situations. Table 4.2 summarizes the assessment criteria related with the maneuver open-loop sinusoidal steering input that are used in the present work.

Table 4.2.: Assessment criteria related with the maneuver open-loop sinusoidal steering input [Ros09].

Assessment criteria		Symbol	Units	Requirement
Time delay of yaw rate		$\hat{T}_{\dot{\psi}}$	s	small
Lat. acc.	Time delay	$\hat{T}_v \ddot{y}$		
	Maximum	$ ^{max}_v\ddot{y} $	m/s ²	high
Maximum sideslip angle		$ ^{max}\beta $	°	small

4.1.3. Open-loop frequency response

Based on the maneuver open-loop frequency response it is possible to determine the dynamic vehicle behavior as a function of the steering wheel angle excitation. As in the control theory, it is based on the fact, that the response of a vibration capable linear system to a harmonic input signal is also a harmonic output. Nevertheless, the magnitude and phase delay of the response is a function of the frequency and magnitude

of the input signal. Although this theory holds for linear systems, it is widespread used in the automotive industry to analyze the vehicle dynamic behavior taking the speed influence into consideration (see e.g. [RH84]).

The gain $G_v(f)$, i.e. the relation between the magnitudes of the input (steering wheel angle $\widehat{\delta}_{st}$) and the output (considered state variable \widehat{v}), is given in decibel and can be calculated as [RH84] (see also figure 4.3):

$$G_v(f) = \frac{\widehat{v}(f)}{\widehat{\delta}_{st}(f)} = 20 \cdot \log_{10} \left(\frac{v(f)}{\delta_{st}(f)} \cdot \frac{1}{G_{v,0}} \right). \quad (4.3)$$

By scaling with the steady state gain $G_{v,0}$ (i.e. $f = 0$ Hz), the curve of the gain starts by $G_v(f = 0 \text{ Hz}) = 0$ dB. This is advantageous since then the gain of different systems (vehicles) can be directly compared [RH84]. Moreover, the phase delay $\varphi_v(f)$ can be expressed as [Abe04]:

$$\varphi_v(f) = -T_{\varphi_v}(f) \cdot f \cdot 360^\circ, \quad (4.4)$$

where the frequency f corresponds to the frequency of the steering wheel angle $f_{\delta_{st}}$, i.e. $f = f_{\delta_{st}}$.

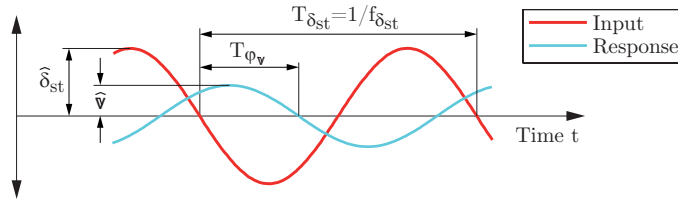


Figure 4.3.: Some assessment criteria and schematic representation of the open-loop frequency response of a considered state variable v .

Mitschke et al. as well as *Rompe et al.* propose following assessment criteria for this maneuver (see also [Ros09]):

- The vehicle controllability can be improved by minimizing the maximum value of the yaw rate gain $^{max}G_{\dot{\psi}}$ and increasing the frequency $f^{max}G_{\dot{\psi}}$ for which this maximum takes place.
- To guarantee a fast (direct) response of the vehicle over a large frequency range

and therefore to improve the vehicle driving behavior, the equivalent time delay

$$T_{eq} = \frac{1}{2 \cdot \pi \cdot f_{\dot{\psi}-45^\circ}} \quad (4.5)$$

must be minimized. This can be also expressed as a maximization of the frequency $f_{\dot{\psi}-45^\circ}$ for which the phase delay of the yaw rate $\dot{\psi}$ becomes smaller than -45° .

- The subjective vehicle handling behavior can be improved by maximizing the frequency $f_{G_{\dot{y}}-3 \text{ dB}}$ by which the gain $G_{\dot{y}}$ of the vehicle lateral acceleration \dot{y} becomes smaller than -3 dB .
- Large values of the phase delay $\varphi_{\dot{y}}(f)$ of the lateral acceleration are characteristic of hardly controllable vehicles. Therefore, this phase delay should be minimized. The value $\varphi_{\dot{y} \text{ 1 Hz}}$ by a frequency of $f = 1 \text{ Hz}$ is proposed as assessment criteria.

Table 4.3 summarizes the assessment criteria related with the maneuver open-loop frequency response that are used in the present work.

Table 4.3.: Assessment criteria related with the maneuver open-loop frequency response [Ros09].

	Assessment criteria	Symbol	Units	Requirement
Yaw rate	Maximum gain	$^{max}G_{\dot{\psi}}(f)$	dB	small
	Frequency for maximum gain	$f^{max}G_{\dot{\psi}}$	Hz	high
	Equivalent time delay	T_{eq}	s	small
Lat. acc.	Frequency for gain smaller than -3 dB	$f_{G_{\dot{y}}-3 \text{ dB}}$	Hz	high
	Phase delay by $f = 1 \text{ Hz}$	$\varphi_{\dot{y} \text{ 1 Hz}}$	$^\circ$	small

4.2. Control concept of a torque vectoring system for vehicles with in-wheel motors

In this chapter, the control concept of a torque vectoring system for vehicles with in-wheel motors is presented. The introduced approach is a simplified version of the *Vehicle Dynamics Controller - VDC* presented by *Niederkofler* [Nie11] and is based on the individual allocation of longitudinal tire forces ${}_W F_{T_i, x}$ (driving and braking) at

all four wheels to influence the yaw motion of the vehicle (see also [RND11]). Since the reaction forces and torques induced by the different longitudinal tire forces at the wheels of one axle are not transmitted to the steering system, as in torque vectoring systems with central motor or engine (see e.g. [HW09]), the presented approach can be applied both to two-wheel as well as to four-wheel powertrain architectures with torque vectoring on both axles (see also chapter 3.7.2).

Figure 4.4 presents an overview of the implemented control concept and its interaction with the other elements of the driver-vehicle-environment system (see also 2.1). The reference values $\hat{\mathbf{r}}$ are determined by the *reference values generator* based on the driver inputs

$$\hat{\mathbf{e}} = \begin{bmatrix} \delta_{st} & v\dot{x}^d \end{bmatrix}^T \quad (4.6)$$

corresponding to the steering wheel angle δ_{st} and the desired vehicle longitudinal speed¹ $v\dot{x}^d$. Afterwards, the reference control inputs $\hat{\mathbf{u}}$ for the *optimal longitudinal force allocation algorithm* are calculated by the *horizontal dynamics controller* based on the reference $\hat{\mathbf{r}}$ and the current values $\hat{\mathbf{y}}$. Finally, the *optimal longitudinal force allocation algorithm* determines the control inputs \mathbf{u} corresponding to the longitudinal forces at each individual wheel to be supplied by the electric motors. The individual components of the *Vehicle Dynamics Controller* are presented in detail in the following sections.

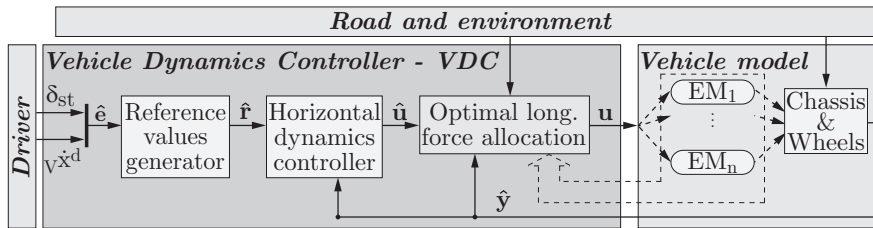


Figure 4.4.: Overview of the control concept implemented for the torque vectoring system with in-wheel motors [Nie11] (see also [RND11]).

4.2.1. Reference values generator

The main task of the *reference values generator* is to determine the reference values $\hat{\mathbf{r}}$ based on the driver inputs $\hat{\mathbf{e}}$ (see equation 4.6) to be used by the *horizontal dynamics*

¹In this work, it is assumed that the desired longitudinal speed $v\dot{x}^d$ is known or can be determined (e.g. as reference value of a *cruise control system*). It can also be interpreted as maneuver input or determined with a simplified vehicle model based on the accelerator pedal position (see [Nie11]).

controller. This is a challenging task that has become more important since the introduction of mechatronic systems in vehicles and is current focus of research in the field of vehicle dynamics (see e.g. [Nie11], [Ros09], [REH07] and [RHEL08]). According to the literature (see [Ore06], [And07] and [Raj06]), a combination of the desired values of the sideslip angle β^d , the yaw rate $\dot{\psi}^d$ and the vehicle longitudinal speed $v\dot{x}^d$ has been found to be appropriate to be used to control the horizontal vehicle dynamics. Therefore, the reference values vector $\hat{\mathbf{r}}$ is given by:

$$\hat{\mathbf{r}} = \begin{bmatrix} \beta^d & \dot{\psi}^d & v\dot{x}^d \end{bmatrix}^T, \quad (4.7)$$

where the desired vehicle longitudinal speed $v\dot{x}^d$ is assumed to be already contained in the driver inputs $\hat{\mathbf{e}}$. The value of the other two reference variables β^d and $\dot{\psi}^d$ are assumed to correspond to their steady state values β^S and $\dot{\psi}^S$ respectively. Model based approaches have proven to be efficient to determine them (see e.g. [RND11], [Nie11] and [Ros09]). Therefore, vehicle models with different complexities are used to obtain the corresponding steady state response for different values of the driver inputs δ_{st} and $v\dot{x}^d$. The result are three-dimensional maps

$$\hat{\mathbf{R}}_{\beta} = \mathcal{F}_1 \left(\delta_{st}, v\dot{x}^d \right), \quad (4.8a)$$

$$\hat{\mathbf{R}}_{\dot{\psi}} = \mathcal{F}_2 \left(\delta_{st}, v\dot{x}^d \right), \quad (4.8b)$$

having δ_{st} and $v\dot{x}^d$ as inputs and steady state values β^S or $\dot{\psi}^S$ as output, as shown schematically in figure 4.5. The driving behavior of a vehicle can be influenced (within the physical limits) by varying these three-dimensional maps (see e.g. [Ros09]). In all application cases using the torque vectoring system presented, $\hat{\mathbf{R}}_{\beta} = 0$ is chosen and $\hat{\mathbf{R}}_{\dot{\psi}}$ is determined through simulations using the nonlinear vehicle model introduced in chapter 2 with the model parameters given in the appendix B while driving on a flat road. This setup has evidenced good results to highlight the advantages and limitations of torque vectoring systems (see [RND11] and [Nie11]). An optimization of the mentioned $\hat{\mathbf{R}}_{\beta}$ is chosen and $\hat{\mathbf{R}}_{\dot{\psi}}$ goes beyond the scope of this work. Finally, the chosen setup can be interpreted as a reduction of the transient response of the yaw rate $\dot{\psi}$ and a simultaneous minimization of the sideslip angle β .

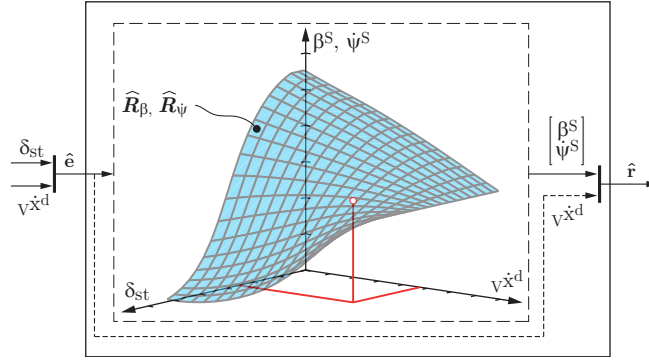


Figure 4.5.: Schematic representation of the *reference values generator* used to determine of the reference values $\hat{\mathbf{r}}$ based on steady state maps obtained with a reference vehicle model.

4.2.2. Horizontal dynamics controller

The main task of the horizontal dynamics controller is to determine the reference control inputs

$$\hat{\mathbf{u}} = \left[{}_V\hat{F}_{A, x} \quad {}_V\hat{M}_{A, z} \right]^T \quad (4.9)$$

needed to produce the desired horizontal vehicle movement specified by the reference values in $\hat{\mathbf{r}}$, where ${}_V\hat{F}_{A, x}$ corresponds to the reference control longitudinal force and ${}_V\hat{M}_{A, z}$ represents the reference control yaw moment around the vertical axis ${}_Vz$ of the vehicle coordinate system (see coordinate systems in chapter 2.2). This task can be mathematically expressed as the minimization of the difference

$$\Delta_e = \hat{\mathbf{r}} - \hat{\mathbf{y}} \quad (4.10)$$

between the reference value vector $\hat{\mathbf{r}}$ and the current state vector $\hat{\mathbf{y}}$ and is carried out by a longitudinal and by a lateral dynamics controller working in parallel, as can be seen in figure 4.6. These controllers are described in detail in the following sections.

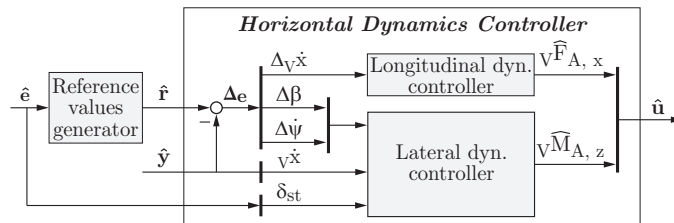


Figure 4.6.: Structure of the horizontal dynamics controller.

Longitudinal dynamics controller

The longitudinal dynamics controller (see figure 4.7) determines the reference control input ${}_V\widehat{F}_{A, x}$, corresponding to the control longitudinal force, based on the difference

$$\Delta_V\dot{x} = {}_V\dot{x}^d - {}_V\dot{x} \quad (4.11)$$

between the desired ${}_V\dot{x}^d$ and the current ${}_V\dot{x}$ longitudinal speed. Therefore, a proportional-integral controller with constant parameters K_P and K_I is used. The reference control input ${}_V\widehat{F}_{A, x}$ is obtained with a constant gain K_{F_x} . Furthermore, since the output power of the electric motors is limited (see chapter 3.7.6), an anti-wind-up strategy is implemented to optimize the controller efficiency (see [HD04] and [Abe04]). The difference between the signals after and before the saturation element is added to the input of the integrative element K_I . The parameter values can be found in [Nie11].

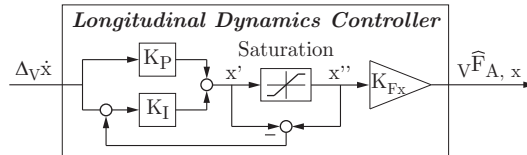


Figure 4.7.: Structure of the longitudinal dynamics controller.

Lateral dynamics controller

The main task of the lateral dynamics controller is to determine the reference control input ${}_V\widehat{M}_{A, z}$ based on the current errors of the sideslip angle $\Delta\beta$ and the yaw rate $\Delta\dot{\psi}$, where ${}_V\widehat{M}_{A, z}$ corresponds to the reference control yaw moment around the vertical axis ${}_Vz$ of the vehicle coordinate system (see coordinate systems in chapter 2.2). *Niederkofler* [Nie11] proposes a model based approach in which an extended linearized *single track vehicle model*, represented in the state space as

$$\dot{\mathbf{x}} = \mathbf{A} \cdot \mathbf{x} + \mathbf{B} \cdot \mathbf{u} + \mathbf{B}_c \cdot \mathbf{u}_c, \quad (4.12)$$

with the state vector \mathbf{x} composed by the sideslip angle β and the yaw rate $\dot{\psi}$

$$\mathbf{x} = \begin{bmatrix} \beta & \dot{\psi} \end{bmatrix}^T, \quad (4.13)$$

is used as basis. Here, the basic *single track vehicle model* has been extended by introducing the controllable input matrix \mathbf{B}_c and the controllable (driver independent) input \mathbf{u}_c , as presented in appendix D.1. Based on this extended vehicle model and according to the approach presented by *Niederkofler* [Nie11] and *Rosinger* [Ros09], a state controller (see figure 4.8) can be developed to regulate the error

$$\Delta_{e_{lat}} = \begin{bmatrix} \Delta\beta & \Delta\dot{\psi} \end{bmatrix}^T \quad (4.14)$$

in the control variables β and $\dot{\psi}$ relevant for the lateral dynamics, where $\Delta_{e_{lat}}$ is defined analogously to equation 4.10 as²

$$\Delta_{e_{lat}} = \hat{\mathbf{r}}_{lat} - \hat{\mathbf{y}}_{lat} \rightarrow \hat{\mathbf{y}}_{lat} = \hat{\mathbf{r}}_{lat} - \Delta_{e_{lat}} . \quad (4.15)$$

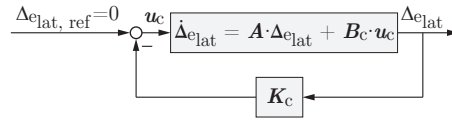


Figure 4.8.: Structure of the error controller for the lateral dynamics.

Based on this, equation 4.12 can be written as:

$$\dot{\hat{\mathbf{r}}}_{lat} - \dot{\Delta}_{e_{lat}} = \mathbf{A} \cdot \hat{\mathbf{r}}_{lat} - \mathbf{A} \cdot \Delta_{e_{lat}} + \mathbf{B} \cdot \mathbf{u} + \mathbf{B}_c \cdot \mathbf{u}_c . \quad (4.16)$$

Since

$$\dot{\hat{\mathbf{r}}}_{lat} = \mathbf{0} \quad (4.17)$$

is valid for a given working point, equation 4.16 is reduced to:

$$-\dot{\Delta}_{e_{lat}} = \mathbf{A} \cdot \hat{\mathbf{r}}_{lat} - \mathbf{A} \cdot \Delta_{e_{lat}} + \mathbf{B} \cdot \mathbf{u} + \mathbf{B}_c \cdot \mathbf{u}_c . \quad (4.18)$$

Furthermore, since a reference error $\Delta_{e_{lat}, ref} = \mathbf{0}$ is requested (see figure 4.8), it can be assumed that in steady state the state vector $\hat{\mathbf{y}}_{lat}$ correspond to the reference vector $\hat{\mathbf{r}}_{lat}$, i.e. $\hat{\mathbf{y}}_{lat} = \hat{\mathbf{r}}_{lat}$ and therefore

$$\dot{\Delta}_{e_{lat}} = \Delta_{e_{lat}} = \mathbf{0} , \quad (4.19a)$$

$$\mathbf{u}_c = \mathbf{0} . \quad (4.19b)$$

²The subscript *lat* is used to refer only to the control variables β and $\dot{\psi}$ relevant for the lateral dynamics.

With this equations 4.18 results in

$$\mathbf{0} = \mathbf{A} \cdot \widehat{\mathbf{r}}_{lat} + \mathbf{B} \cdot \mathbf{u} . \quad (4.20)$$

Finally, the steady state representation of the state controller can be found by introducing equation 4.20 in equation 4.18 and rearranging terms:

$$\dot{\Delta}_{e_{lat}} = \mathbf{A} \cdot \Delta_{e_{lat}} - \mathbf{B}_c \cdot \mathbf{u}_c . \quad (4.21)$$

According to figure 4.8, the controllable input \mathbf{u}_c is given as a function of the matrix \mathbf{K}_c of the proportional state controller and the error $\Delta_{e_{lat}}$ by:

$$\mathbf{u}_c(t) = -\mathbf{K}_c(t) \cdot \Delta_{e_{lat}}(t) . \quad (4.22)$$

The goal is to determine the controllable input $\mathbf{u}_c(t)$ and therefore the controller matrix $\mathbf{K}_c(t)$ needed to take the system 4.12 from an initial state characterized by $\Delta_{e_{lat}}(t_0)$ at the initial time t_0 into a rest position. Nevertheless, on the way from the initial state to the rest position, it is desired not only to minimize the error $\Delta_{e_{lat}}(t)$ but also to minimize the effort to do it, i.e. to minimize $\mathbf{u}_c(t)$. This can be mathematically formulated as to minimize the objective function [Nie11]

$$J_{lat} = \int_0^{\infty} (\Delta_{e_{lat}}^T(t) \cdot \mathbf{Q}_{lat} \cdot \Delta_{e_{lat}}(t) + \mathbf{u}_c^T(t) \cdot \mathbf{R}_{lat} \cdot \mathbf{u}_c(t)) \, dt , \quad (4.23)$$

where the symmetric and positive semi-definite matrix \mathbf{Q}_{lat} and the positive definite matrix \mathbf{R}_{lat} are introduced as weighting factors indicating the relative importance of the error $\Delta_{e_{lat}}(t)$ and the controllable input³ $\mathbf{u}_c(t)$. The process can be expressed as an optimization problem given by:

$$\min_{\mathbf{K}_c} J_{lat} . \quad (4.24)$$

For completely controllable plants, the solution of this problem is given by:

$$\mathbf{K}_c = \mathbf{R}_{lat}^{-1} \cdot \mathbf{B}_c \cdot \mathbf{P}_{lat} , \quad (4.25)$$

where the symmetric and positive definite matrix \mathbf{P}_{lat} corresponds to the solution of

³Although \mathbf{u}_c , \mathbf{K}_c and $\Delta_{e_{lat}}$ are all time-dependent variables, the explicitly indication of the time dependency will be avoided in the rest of the chapter for simplification reasons.

the matrix Riccati equation (see [Nie11] and [Ros09])

$$\mathbf{A}^T \cdot \mathbf{P}_{lat} + \mathbf{P}_{lat} \cdot \mathbf{A} - \mathbf{P}_{lat} \cdot \mathbf{B}_c \cdot \mathbf{R}_{lat}^{-1} \cdot \mathbf{B}_c^T \cdot \mathbf{P}_{lat} + \mathbf{Q}_{lat} = \mathbf{0}. \quad (4.26)$$

Niederkofler defines the matrix \mathbf{Q}_{lat} as a diagonal matrix

$$\mathbf{Q}_{lat} = \begin{bmatrix} Q_{\Delta\beta} & 0 \\ 0 & Q_{\Delta\dot{\psi}} \end{bmatrix} \quad (4.27)$$

with non-negative diagonal elements $Q_{\Delta\beta}$ and $Q_{\Delta\dot{\psi}}$ used to prioritize driving stability and vehicle driving behavior respectively. Additionally, for the case of the control yaw moment ${}_V\widehat{M}_{A, z}$ as the only reference control input, the matrix \mathbf{R}_{lat} (in general a diagonal matrix with positive diagonal elements) is reduced to a single element

$$\mathbf{R}_{lat} := \begin{bmatrix} R_{M_z} \end{bmatrix}. \quad (4.28)$$

With this, the output of the lateral dynamics controller is given by:

$$\mathbf{u}_c := \begin{bmatrix} {}_V\widehat{M}_{A, z} \end{bmatrix}. \quad (4.29)$$

The values of the controller parameters can be found in [Nie11].

4.2.3. Optimal longitudinal force allocation algorithm

The main task of this module of the torque vectoring control system is to optimally distribute the longitudinal tire forces⁴ ${}_WF_{T_i, x}$ in order to fulfill the requirements defined by the horizontal dynamics controller. Assuming small steering wheel angles $\delta_i \rightarrow 0$ as well as small pitch $\theta \rightarrow 0$ and roll angles $\phi \rightarrow 0$ leads to ${}_WF_{T_{fl}, x/y} \approx {}_VF_{T_{fl}, x/y}$. With this assumption and taking figure 4.9, the mentioned task of the optimal longitudinal

⁴While the right subscripts *fl* and *fr* are used to indicate the left and right wheels at the front axle, the right subscripts *rl* and *rr* correspond to the respectively wheels at the rear axle.

force allocation algorithm can be written as:

$$\underbrace{\frac{1}{2} \cdot \begin{bmatrix} 2 & 2 & 2 & 2 \\ -s_f & s_f & -s_r & s_r \end{bmatrix}}_{\boldsymbol{\gamma}_q} \cdot \underbrace{W \begin{bmatrix} F_{T_{fl}, x} \\ F_{T_{fr}, x} \\ F_{T_{rl}, x} \\ F_{T_{rr}, x} \end{bmatrix}}_{\mathbf{f}_q} = \underbrace{V \begin{bmatrix} \hat{F}_{A, x} \\ \hat{M}_{A, z} - M_{z, F_y} \end{bmatrix}}_{\hat{\mathbf{f}}_q}, \quad (4.30)$$

where s_f and s_r represent the front and rear track respectively and ${}_V M_{z, F_y}$ correspond to the yaw moment

$${}_V M_{z, F_y} = l_f \cdot ({}_W F_{T_{fl}, y} + {}_W F_{T_{fr}, y}) - l_r \cdot ({}_W F_{T_{rl}, y} + {}_W F_{T_{rr}, y}) \quad (4.31)$$

due to the lateral tire forces ${}_W F_{T_{i, y}}$ (it is assumed that the lateral tire forces ${}_W F_{T_{i, y}}$ can be measured or observed with enough accuracy).

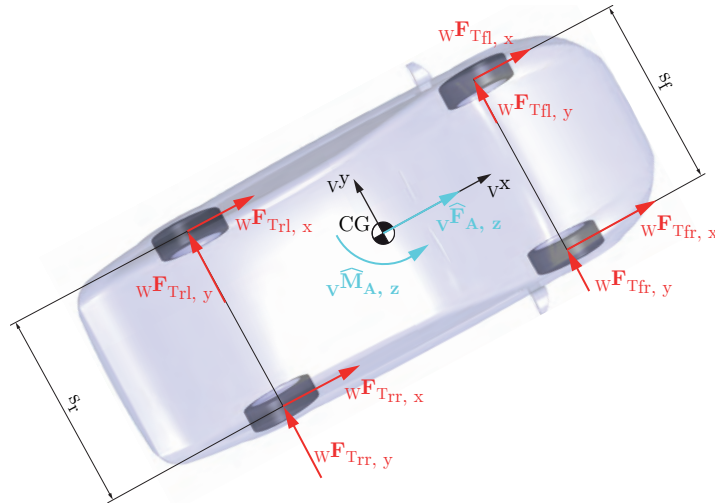


Figure 4.9.: Diagram depicting the task of the optimal force allocation algorithm (small steering angles δ_{st} are assumed). Turn to the left is exemplarily shown.

To fulfill this task, *Niederkofler* [Nie11] proposes the quadratic programming problem

$$\min_{\mathbf{f}_q} \mathbf{q}(\mathbf{f}_q) \quad (4.32)$$

subject to the restrictions

$$\mathbf{A}_q \cdot \mathbf{f}_q \leq \mathbf{b}_q, \quad (4.33)$$

where $\mathbf{q}(\mathbf{f}_q)$ correspond to the quadratic objective function

$$\mathbf{q}(\mathbf{f}_q) = \frac{1}{2} \cdot \mathbf{f}_q^T \cdot \mathbf{H}_q \cdot \mathbf{f}_q + \mathbf{s}_q^T \cdot \mathbf{f}_q . \quad (4.34)$$

Solving this problem, the output of the optimal longitudinal force allocation algorithm, i.e. the vector of the controlled inputs corresponding to ${}_C\mathbf{M}_{w_i, y, c}$, can be expressed as a function of the dynamic tire radius r_{dyn_i} as:

$$\mathbf{u} = {}_C\mathbf{M}_{w_i, y, c} = r_{dyn_i} \cdot {}_W\mathbf{F}_{T_i, x} . \quad (4.35)$$

The elements of this vector can be used afterwards as reference values for a subordinated electric motor controller based on the tire longitudinal slip as control variable (see e.g. [Wil11] and [Nie11]).

Quadratic objective function

It seems logical to involve the system of equations given by 4.30 in the objective function $\mathbf{q}(\mathbf{f}_q)$. Nevertheless, it is possible to notice that 4.30 is an under-determined system of equations, i.e. it has more unknown quantities than equations. Therefore, following changes are introduced (see [Nie11] and [RND11]):

Transformation in an over-determined system of equations: In a first step, the reference control input ${}_V\widehat{F}_{A, x}$ is considered to be distributed equally to all four wheels:

$$|{}_W\mathbf{F}_{T_i, x}| = \frac{1}{4} \cdot {}_V\widehat{F}_{A, x} . \quad (4.36)$$

Nevertheless, higher horizontal tire forces can be transmitted at wheels with higher vertical contact forces ${}_W F_{T_i, z}$ between the tire and the ground (as indicated in chapter 2.5.1) and with higher friction coefficients μ_{w_i} . Therefore and assuming that the friction coefficient μ_{w_i} can be estimated accurately enough (see e.g. [NLER11] and also [LEH11]) equation 4.36 is modified as proposed in [RND11] as follows:

$$|{}_W\mathbf{F}_{T_i, x}| = \underbrace{\frac{{}_V\widehat{F}_{A, x}}{4} \cdot \frac{{}_W F_{T_i, z}}{\sum_{i=1}^4 {}_W F_{T_i, z}} \cdot \frac{\mu_{w_i}}{\sum_{i=1}^4 \mu_{w_i}}}_{\Omega_q} . \quad (4.37)$$

This system of four additional equations can be introduced in 4.30 to obtain the over-determined system of equations:

$$\begin{bmatrix} \gamma_q \\ \mathbf{I}_{(4 \times 4)} \end{bmatrix} \cdot \mathbf{f}_q = \begin{bmatrix} \hat{\mathbf{f}}_q \\ \Omega_q \end{bmatrix}, \quad (4.38)$$

where $\mathbf{I}_{(4 \times 4)}$ corresponds to a 4×4 identity matrix.

Formulation as a minimization problem: The system of equations 4.38 is over-determined, i.e. there are more equations than unknowns and there are thus multiple solutions. To find the solution for which the individual longitudinal forces ${}_W F_{T_i, x}$ are minimized, the system of equations 4.38 is transformed into the least squares problem

$$\mathbf{q}(\mathbf{f}_q) = \left\| \mathbf{W}_q \cdot \begin{bmatrix} \gamma_q \\ \mathbf{I}_{(4 \times 4)} \end{bmatrix} \cdot \mathbf{f}_q - \mathbf{W}_q \cdot \begin{bmatrix} \hat{\mathbf{f}}_q \\ \Omega_q \end{bmatrix} \right\|_2^2, \quad (4.39)$$

where the diagonal 8×8 weighting matrix \mathbf{W}_q with non-negative elements $W_{1,1}$ to $W_{8,8}$ is introduced to prioritize the individual implicit optimization tasks. Observing the systems of equations 4.30 and 4.39 it can be concluded, that the first two elements on the diagonal of \mathbf{W}_q , i.e. $W_{1,1}$ and $W_{2,2}$, can be used to prioritize the longitudinal and the lateral vehicle dynamics respectively.

Finally, the objective quadratic function 4.39 can be written in the standard form of equation 4.34 with the Hessian matrix \mathbf{H}_q given by

$$\mathbf{H}_q = \nabla^2 \mathbf{q}(\mathbf{f}_q) = \begin{bmatrix} \frac{\partial^2 \mathbf{q}(\mathbf{f}_q)}{\partial f_{q,1} \partial f_{q,1}} & \dots & \frac{\partial^2 \mathbf{q}(\mathbf{f}_q)}{\partial f_{q,1} \partial f_{q,4}} \\ \vdots & \ddots & \vdots \\ \frac{\partial^2 \mathbf{q}(\mathbf{f}_q)}{\partial f_{q,4} \partial f_{q,1}} & \dots & \frac{\partial^2 \mathbf{q}(\mathbf{f}_q)}{\partial f_{q,4} \partial f_{q,4}} \end{bmatrix}, \quad (4.40)$$

and the vector \mathbf{s}_q expressed as

$$\mathbf{s}_q = \nabla \mathbf{q}(\mathbf{f}_q) - \mathbf{H}_q \cdot \mathbf{f}_q = \begin{bmatrix} \frac{\partial \mathbf{q}(\mathbf{f}_q)}{\partial f_{q,1}} \\ \vdots \\ \frac{\partial \mathbf{q}(\mathbf{f}_q)}{\partial f_{q,4}} \end{bmatrix} - \mathbf{H}_q \cdot \mathbf{f}_q. \quad (4.41)$$

Restrictions formulation

The maximum ${}^{\max}_W F_{T_i, x}$ and minimum ${}^{\min}_W F_{T_i, x}$ available longitudinal tire forces that can be transmitted depend on the currently transmitted lateral tire force ${}_W F_{T_i, y, in}$, on the current values of the vertical contact force ${}_W F_{T_i, z}$, and on the friction coefficient μ_{w_i} between tire and ground. Furthermore, they are limited by the maximum available torque of the electric motor(s). To account for these physical limitations, following restriction in the standard form of equation 4.33 is proposed (see also [RND11]):

$$\underbrace{\begin{bmatrix} \mathbf{I}_{(4 \times 4)} \\ -\mathbf{I}_{(4 \times 4)} \end{bmatrix}}_{\mathbf{A}_q} \cdot \mathbf{f}_q \leq \underbrace{\begin{bmatrix} {}^{\max}_W F_{T_i, x} \\ {}^{\min}_W F_{T_i, x} \end{bmatrix}}_{\mathbf{b}_q}, \quad (4.42)$$

where the value of the maximum ${}^{\max}_W F_{T_i, x}$ and the minimum ${}^{\min}_W F_{T_i, x}$ transmittable longitudinal tire force is given by:

$$\max \left({}^{\max}_W F_{T_i, x, ke}, {}_W F_{T_i, x, M_{EM}} \right), \quad (4.43a)$$

$$\min \left({}^{\min}_W F_{T_i, x, ke}, -{}_W F_{T_i, x, M_{EM}} \right). \quad (4.43b)$$

In equations 4.43, the tire dependant transmittable longitudinal forces (${}^{\max}_W F_{T_i, x, ke}$ and ${}^{\min}_W F_{T_i, x, ke}$) can be determined based on the Krempel's friction ellipse [Kre65] (see figure 4.10). Taking the extreme values of the longitudinal ${}^{\max} X_i$ and the lateral ${}^{\max} Y_i$ tire forces (see model for the horizontal tire dynamics in chapter 2.5.1) and the value of the currently transmitted lateral tire force ${}_W F_{T_i, y, in}$ (assumed to be measured or estimated accurately enough), the tire dependant transmittable longitudinal forces are given by:

$${}_W \begin{bmatrix} {}^{\max}_W F_{T_i, x, ke} \\ {}^{\min}_W F_{T_i, x, ke} \end{bmatrix} = \begin{bmatrix} 1 \\ -1 \end{bmatrix} \cdot \sqrt{\left[1 - \left(\frac{{}_W F_{T_i, y, in}}{{}^{\max} Y_i} \right)^2 \right]} \cdot {}^{\max} X_i^2. \quad (4.44)$$

Finally, neglecting the actuator dynamics⁵, the actuator limited force ${}_W F_{T_i, x, M_{EM}}$ can be approximated as a function of dynamic tire radius r_{dyn} and the maximum value of

⁵An approach accounting for the electric motor dynamics is presented by *Niederkofler* in [Nie11].

the electric motor torque ${}^{max}M_{EM}$ currently available as:

$$W^{F_{T_i, x, M_{EM}}} = {}^{max}M_{EM} \cdot r_{dyn} \cdot \quad (4.45)$$

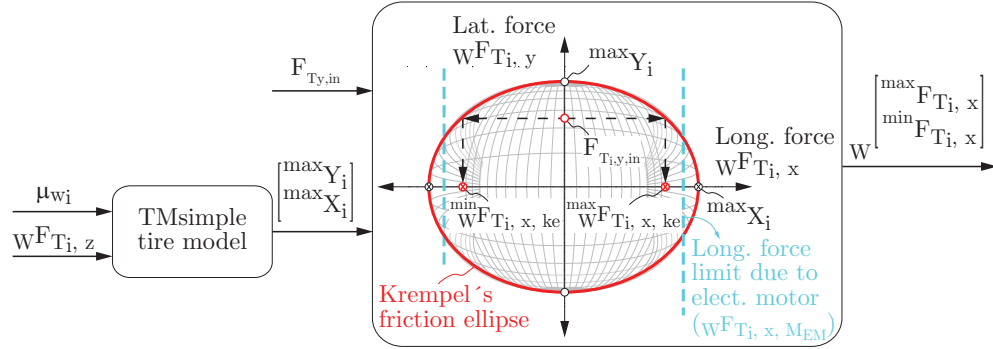


Figure 4.10.: Maximum available longitudinal tire force that can be transmitted.

4.3. Results

To highlight the advantages and limitations of the presented torque vectoring system (TVS) to improve the vehicle lateral dynamics, the two electric powertrain architectures with in-wheel motors (rear-wheel drive and four-wheel drive) and TVS (as shown in chapter 3.7.2) are compared with an electric four-wheel drive vehicle without TVS and an equally distributed torque to all four wheels (reference vehicle). A vehicle belonging to the subcompact vehicle class is considered (see chapter 3.7.1) and synchronous electric motors (see power and torque characteristics in table 3.11) are assumed. In the first part of this section, the general maneuver conditions (i.e. longitudinal speed, steering wheel angle and lateral acceleration) are defined. Therefor, the effect of the torque vectoring system on the individual tire forces is analyzed. Afterwards, the results corresponding to the driving maneuvers described in section 4.1 are presented.

4.3.1. General maneuver conditions

To determine the general maneuver conditions, i.e. longitudinal speed, steering wheel angle and lateral acceleration used for the simulations, two aspects are analyzed: on the one hand, the behavior of the horizontal forces with increasing lateral acceleration

$v\ddot{y}$, and on the other hand, the effect of the presented torque vectoring system on the horizontal tire forces. As mentioned before, an electric vehicle with a four-wheel drive powertrain and equally distributed torque to all four wheels (without torque vectoring system) is taken as reference. Furthermore, the steering wheel angle δ_{st} for each maneuver is determined based on the steady state maps of this reference vehicle depending on the desired values of the vehicle longitudinal speed $v\dot{x}^d$ and lateral acceleration $v\ddot{y}^d$ (cf. chapter 4.2.1).

Lateral acceleration

Figure 4.11 shows the behavior of the normalized horizontal tire forces ${}_W F_{T_i, x/y}$ for 50 %, 75 % and 100 % of the maximum steady state value of the lateral acceleration ${}^{max}v\ddot{y}^S \approx 7.4 \text{ m/s}^2$ for a step steer maneuver with a longitudinal speed of 100 km/h. The normalized horizontal tire forces are given as a function of the maximum horizontal tire forces ${}^{max}X_{i, z \text{ nom}}$ and ${}^{max}Y_{i, z \text{ nom}}$ for the nominal vertical contact force ${}_W F_{T_i, z \text{ nom}}$, and the maximum horizontal tire forces ${}^{max}X_{i, z}$ and ${}^{max}Y_{i, z}$ for the current vertical contact force ${}_W F_{T_i, z}$:

$${}^n F_{x_i} = {}_W F_{T_i, x} \cdot \frac{{}^{max}X_{i, z \text{ nom}}}{{}^{max}X_{i, z}}, \quad (4.46a)$$

$${}^n F_{y_i} = {}_W F_{T_i, y} \cdot \frac{{}^{max}Y_{i, z \text{ nom}}}{{}^{max}Y_{i, z}}, \quad (4.46b)$$

where ${}_W F_{T_i, x}$ and ${}_W F_{T_i, y}$ correspond, respectively, to the current longitudinal and lateral tire forces for the current vertical contact force ${}_W F_{T_i, z}$. Additionally, the relation

$$\chi_{Fz_i} = \frac{{}_W \bar{F}_{T_i, z}}{{}_W F_{T_i, z \text{ nom}}} \quad (4.47)$$

between the average ${}_W \bar{F}_{T_i, z}$ and the nominal ${}_W F_{T_i, z \text{ nom}}$ vertical contact force is indicated.

As can be seen in this figure, the combined normalized horizontal tire force

$${}^n F_i = \sqrt{{}^n F_{x_i}^2 + {}^n F_{y_i}^2} \quad (4.48)$$

approximates to the physical limit given by the Krempel's friction ellipse while increas-

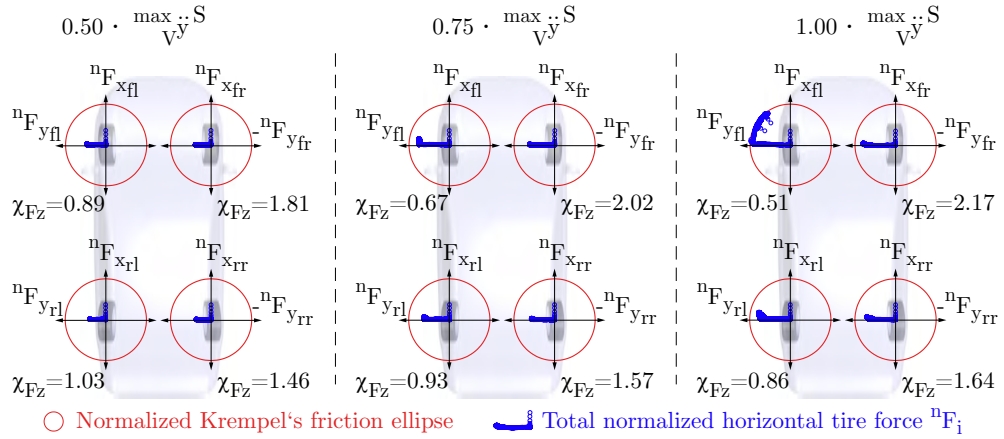


Figure 4.11.: Behavior of the horizontal tire forces during step steer maneuvers turning to the left at 100 km/h and different lateral accelerations $v\ddot{y}$ for the reference electric vehicle with a four-wheel drive powertrain architecture and no torque vectoring system (maximum steady state value of the lateral acceleration corresponds to $^{max}v\ddot{y}^S \approx 7.4 \text{ m/s}^2$).

ing the lateral acceleration. At the limit, i.e. when the lateral acceleration $v\ddot{y}$ equals the maximum steady state value $^{max}v\ddot{y}^S$, this force lies on the ellipse and the corresponding tire slides (see left front wheel for $v\ddot{y} = ^{max}v\ddot{y}^S$). Based on this and to guarantee a large operating range for the torque vectoring system (see also chapter 4.2.3), a maximum lateral acceleration corresponding to 50 % of its maximum steady state value is selected for the simulations.

Effect of the torque vectoring system on the horizontal tire forces

Figure 4.12 shows the behavior of the normalized horizontal tire forces for the different powertrain architectures considered. The results presented in this figure correspond to a step steer maneuver with a longitudinal speed of 100 km/h and the maximum steady state value of the lateral acceleration of the reference vehicle ($^{max}v\ddot{y}^S \approx 7.4 \text{ m/s}^2$).

As can be seen in figure 4.12, the force reserve, i.e. the distance to the Krempel's friction ellipse, of all tires is low. The total normalized horizontal tire force nF_i (see equation 4.48) of the front left tire lies actually on the Krempel's friction ellipse. Due to the declining influence of the vertical contact force ${}_wF_{T_i, z}$ on the horizontal tire forces (see [Wal06] and [MW04] as well as chapter 2.5.1), a reduction in the force reserve of a tire belonging to the front axle results in an increment of the understeering tendency.

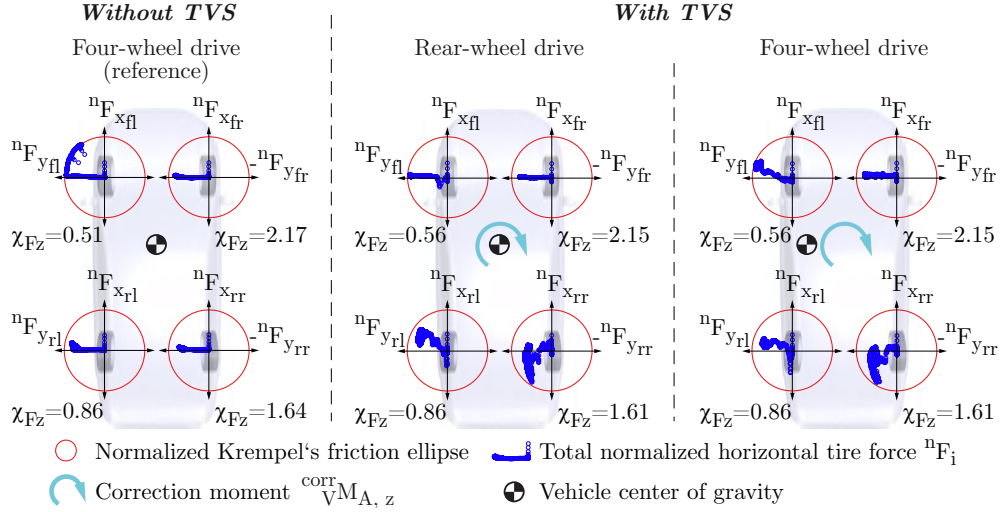


Figure 4.12.: Effect of the presented torque vectoring system (TVS) on the horizontal tire horizontal forces for the different powertrain configurations considered. The presented results correspond to a step steer maneuver turning to the left at $v \cdot \dot{x} = 100$ km/h and the maximum steady state value of the lateral acceleration for the reference vehicle $\overset{max}{V} \ddot{y}^S \approx 7.4$ m/s².

In the case of the vehicle with a rear-wheel drive powertrain, the presented torque vectoring system reduces the force demand at the front axle by varying the longitudinal tire forces at the rear. A reduction in the force demand means, in other words, an increase in the force reserve, which results in a reduction of the understeering tendency and therefore in a better cornering performance and a better driving behavior. Furthermore, the torque vectoring systems helps to minimize the reduction of the vertical contact force at the front left tire due to the force shifting during cornering. As a result, the understeering tendency of the vehicle is further reduced and the cornering performance further enhanced. Additionally, by varying the longitudinal tire forces, the torque vectoring system introduces a correcting yaw moment $\overset{corr}{M}_{A,z}$ around the vehicle center of gravity to try to achieve the goals imposed by the control concept presented in chapter 4.2, i.e. minimize the sideslip angle β and reduce the transient response of the yaw rate $\dot{\psi}$. As can be seen in figure 4.13, the reference vehicle is characterized by a negative sideslip angle. Therefore, a negative correcting yaw moment is needed to minimize it (see also figure D.1 in appendix D.1). It can be also seen, that while the transient response of the yaw rate can be reduced (i.e. the goal of the control strategy can be achieved), the sideslip angle does not vanish. This is due, on the one side to limitations in the torque and power of the considered motors, and on the other side to

the fact that the tire forces are approaching the physical limits. As can be appreciated in figure 4.12, in the case of the electric vehicle with two in-wheel motors at the rear axle, the rear right tire has practically no force reserve. In the case of the vehicle with four in-wheel motors, also the front left tire has almost no reserve.

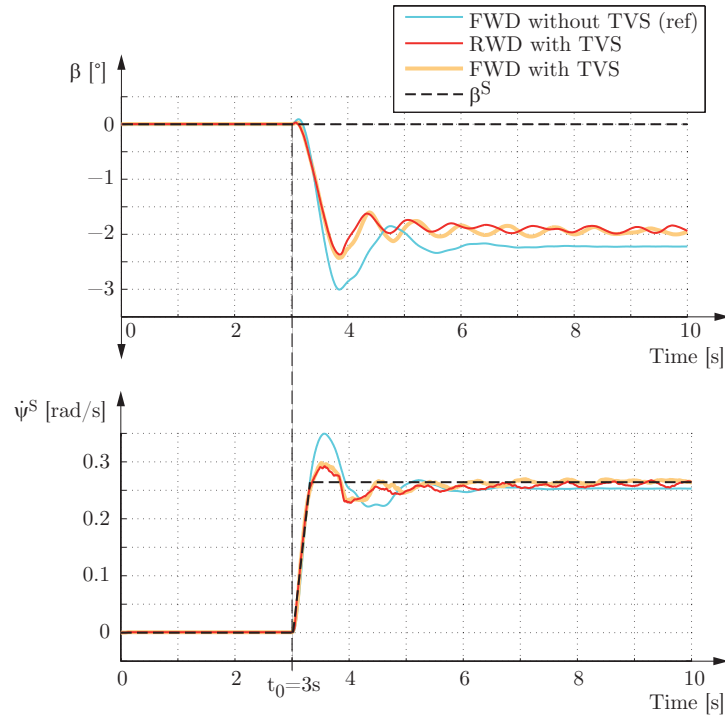


Figure 4.13.: Behavior of the sideslip angle β and the yaw rate $\dot{\psi}$ for the different powertrain configurations considered. The presented results correspond to a step steer maneuver turning to the left at $v \cdot \dot{x} = 100$ km/h and the maximum steady state value of the lateral acceleration for the reference vehicle ${}_{V}^{max} \ddot{y}^S \approx 7.4$ m/s².

The presented results agree with those published in the literature for a mechanical torque vectoring system (see [SUM06]). The advantage of the presented torque vectoring system based on in-wheel motors is the avoidance of the complicated mechanical components and the totally free allocation of the longitudinal tire forces.

Since it is assumed, that the total sum of the power and torque of the motors used in the considered electric powertrain architectures is approximately the same (see chapter 3.7.6), the results obtained for both configurations are not far away from each other (as can be deduced by taking a look at figures 4.12 and 4.13). Therefore, in the following sections, the results corresponding to the reference vehicle are compared with those of

the electric vehicle with a rear-wheel drive powertrain architecture.

Evaluation schema

To determine the performance of the presented torque vectoring system, the percentage of change

$$Change = \begin{cases} \frac{AC_{TVS} - AC_{ref}}{|AC_{ref}|} \cdot 100 \% & \text{if criteria should be maximized,} \\ \frac{AC_{ref} - AC_{TVS}}{|AC_{ref}|} \cdot 100 \% & \text{if criteria should be minimized,} \end{cases} \quad (4.49)$$

is calculated based on the value of the considered assessment criteria AC_{ref} and AC_{TVS} of the reference vehicle and the electric vehicle with a rear-wheel drive powertrain architecture respectively.

4.3.2. Step steer

This maneuver was carried out as follows: For a certain longitudinal vehicle speed and based on the steady state maps (see chapter 4.2.1), the steering wheel angle δ_{st} was adjusted to reach the desired steady state value of the lateral acceleration based on the steady state maps of the reference vehicle. According to the recommendations in the literature, a steering rate of $200^\circ/\text{s}$ was used for the simulations. As mentioned in chapter 4.3.1, approximately 50 % of the maximum lateral acceleration (${}^{max}_V \ddot{y}^S \approx 7.4 \text{ m/s}^2$) was sought for. Furthermore, with the aim to analyze the performance of the presented torque vectoring system for different speed conditions, longitudinal vehicle speeds ranging from 60 km/h to 120 km/h were used for the simulations.

Figure 4.14 shows exemplarily the behavior of the yaw rate $\dot{\psi}$, the sideslip angle β and the lateral acceleration ${}_V \ddot{y}$ for a step steer maneuver turning to the left at ${}_V \dot{x} = 100 \text{ km/h}$ and approximately 50 % of the maximum steady state value of the lateral acceleration.

It can be seen that the torque vectoring system tries to minimize the sideslip angle β . For the presented maneuver, a reduction of the sideslip angle of about 50 % is achieved. This is desirable, since a reduction in the sideslip angle β by increasing lateral acceleration ${}_V \ddot{y}^S$ would be perceived by a normal driver as a safety enhancement

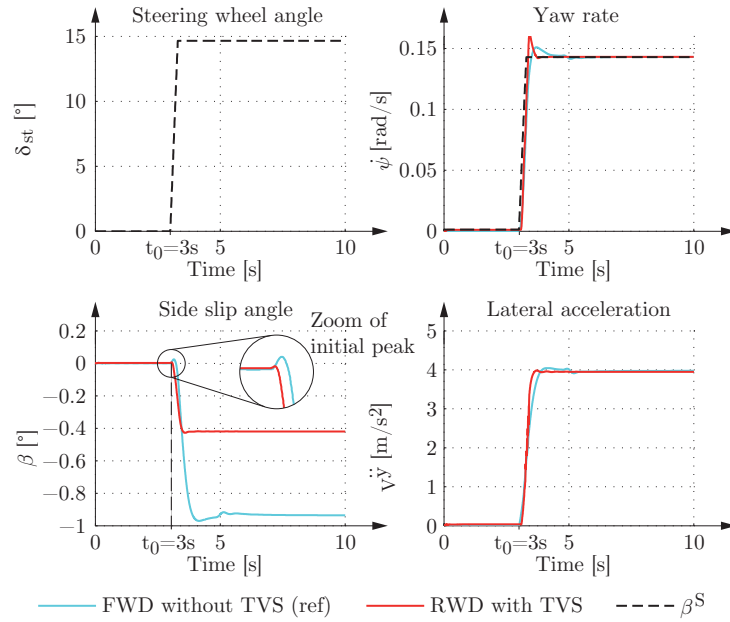


Figure 4.14.: Assessment variables for the step steer maneuver turning to the left at $v\dot{x} = 100$ km/h and approximately 50 % of the maximum steady state value of the lateral acceleration $\overset{max}{V}\ddot{y}^S \approx 7.4$ m/s².

(see e.g. [Wal06]). Additionally, the characteristic initial peak of the sideslip angle in the counter direction can be minimized. Furthermore, the reaction time and the time delay of both the yaw rate $\dot{\psi}$ and the lateral acceleration \ddot{v}_y can be reduced. This would be perceived by the driver as a driver performance enhancement. Nevertheless, the yaw rate present a higher overshoot by this longitudinal speed. As can be deduced from figure 4.15, a lower overshoot is obtained for speeds different than $v\dot{x} = 100$ km/h. A fine tuning of the controller parameters could improve this situation; however this would go beyond the scope of the present work.

Figure 4.15 presents the behavior of the considered assessment criteria (see table 4.1) with the vehicle longitudinal speed.

It can be seen, that the assessment criteria corresponding to the vehicle with the presented torque vectoring system behave better than for the reference vehicle in the entire considered longitudinal speed range. Based on this results and under the considered assessment criteria, it can be said that the presented torque vectoring system based on in-wheel motors enhance the overall driving performance of the considered vehicle in the step steer maneuver.

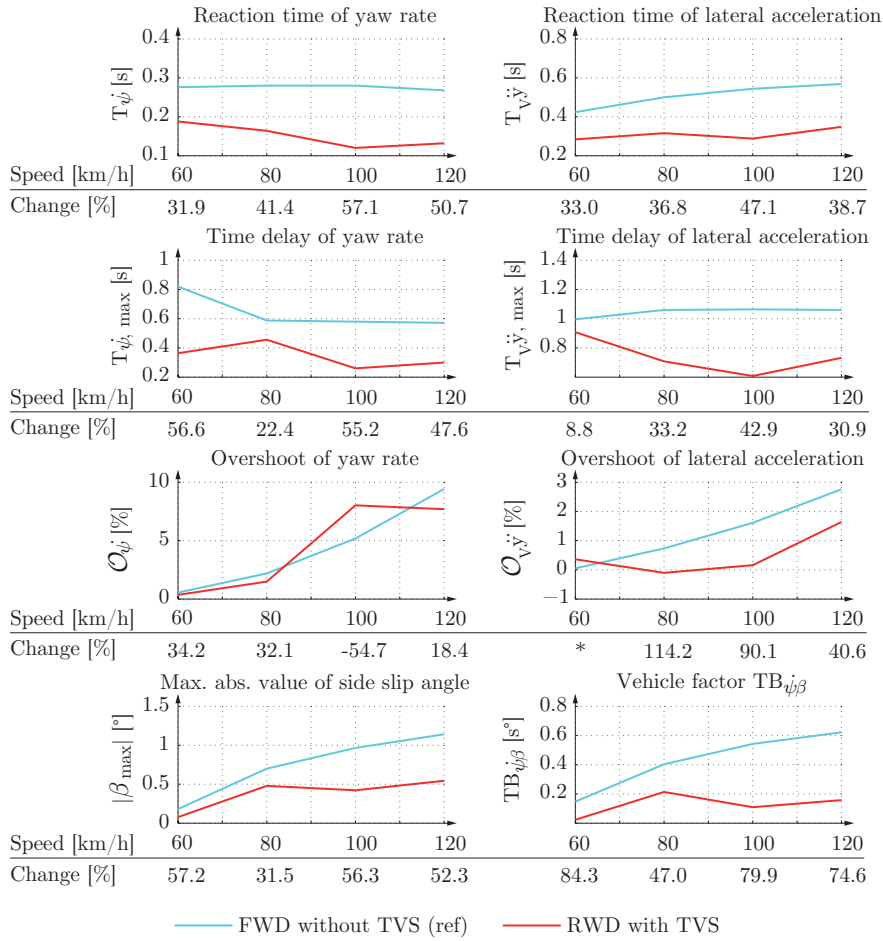


Figure 4.15.: Assessment variables for the step steer maneuver turning to the left at different longitudinal speeds and approximately 50 % of the maximum steady state value of the lateral acceleration $\overset{\max}{V}\ddot{y}^S \approx 7.4 \text{ m/s}^2$.

4.3.3. Open-loop sinusoidal steering input

To carry out this maneuver for a certain longitudinal vehicle speed, the maximum of the sinusoidal steering wheel angle signal was adjusted to reach the desired steady state value of the lateral acceleration based on the steady state maps of the reference vehicle. As mentioned in chapter 4.3.1, approximately 50 % of the maximum lateral acceleration ($\overset{\max}{V}\ddot{y}^S \approx 7.4 \text{ m/s}^2$) was sought for. Furthermore, with the aim to analyze the performance of the presented torque vectoring system for different speed conditions, longitudinal vehicle speeds ranging from 60 km/h to 120 km/h were used for the simulations.

Figure 4.16 shows exemplarily the behavior of the yaw rate $\dot{\psi}$, the sideslip angle β and the lateral acceleration $v\ddot{y}$ for an open-loop sinusoidal steering input maneuver at $v\dot{x} = 100$ km/h and approximately 50 % of the maximum steady state value of the lateral acceleration.

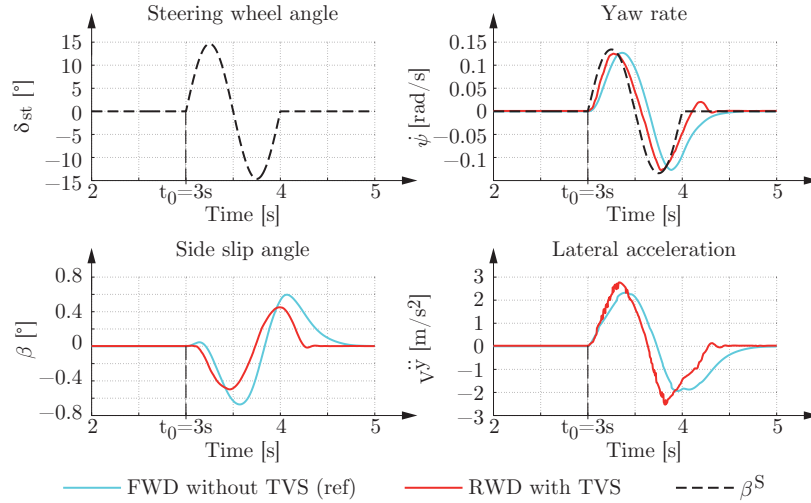


Figure 4.16.: Assessment variables for the open-loop sinusoidal steering input maneuver at $v\dot{x} = 100$ km/h and maximum lateral acceleration corresponding to approximately 50 % of the maximum steady state value ${}^{max}v\ddot{y}^S \approx 7.4$ m/s².

It can be seen in this figure, that the torque vectoring system reduces both the sideslip angle β and the transient response of the yaw rate $\dot{\psi}$. Furthermore, the maximum value of the achievable lateral acceleration is increased. This characteristics improve the subjective vehicle driving behavior.

Figure 4.17 presents the behavior of the considered assessment criteria (see table 4.2) with the vehicle longitudinal speed. It can be seen, that the assessment criteria corresponding to the vehicle with the presented torque vectoring system behave better than for the reference vehicle in the entire considered longitudinal speed range. Based on this results and under the considered assessment criteria, it can be said that the presented torque vectoring system based on in-wheel motors enhance the overall driving performance of the considered vehicle in the open-loop sinusoidal steering input maneuver.

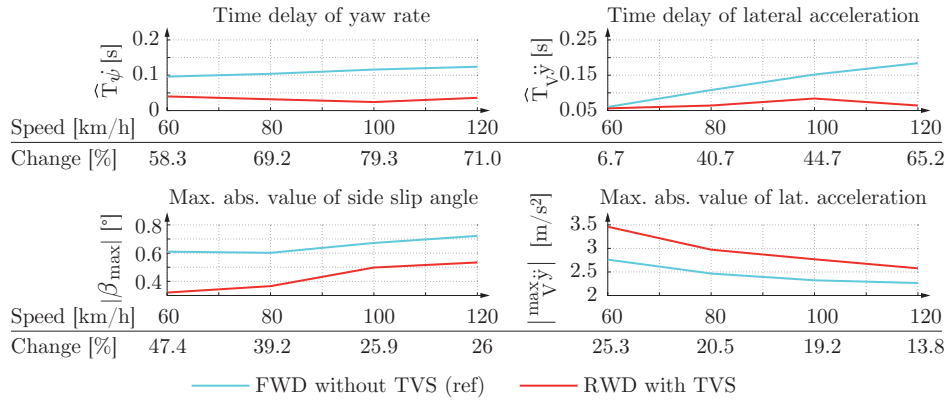


Figure 4.17.: Assessment variables for the open-loop sinusoidal steering input maneuver at different longitudinal speeds and approximately 50 % of the maximum steady state value of the lateral acceleration $\overset{max}{V} \ddot{y}^S \approx 7.4 \text{ m/s}^2$.

4.3.4. Open-loop frequency response

To analyze the frequency response of the vehicles with the two considered powertrain architectures presented in chapter 4.3.1, a sinus sweep signal with a frequency rate of $df_{\delta_{st}}/dt = 0.05 \text{ Hz/s}$ was used for the steering wheel angle δ_{st} . The frequency was varied from 0 Hz to 2 Hz to cover the relevant frequency range around 1 Hz for the lateral dynamics (see e.g. [MW04], [Wal06] and [Ros09]). The amplitude of this signal was chosen in such a way, so that the maximum achievable lateral acceleration corresponds to approximately 50 % of the maximum steady state value of this variable for the reference vehicle. Based on the results, the bode plot was determined.

Figure 4.18 shows a comparison of the bode plots for the yaw rate and the lateral acceleration for both the reference electric vehicle with a four-wheel drive powertrain and no torque vectoring system, and the electric vehicle with in-wheel motors at the rear axle and the presented torque vectoring system. In this figure, a longitudinal speed of $v_{\dot{x}} = 100 \text{ km/h}$ was simulated. It can be seen that it is possible to improve all considered criteria for this maneuver under the simulated conditions except for the maximum gain of the yaw rate.

Figure 4.19 presents the behavior of the considered assessment criteria (see table 4.3) with the longitudinal speed. It can be seen, that the assessment criteria corresponding to the vehicle with the presented torque vectoring system behave better than for the reference vehicle in the entire considered longitudinal speed range except for the maxi-

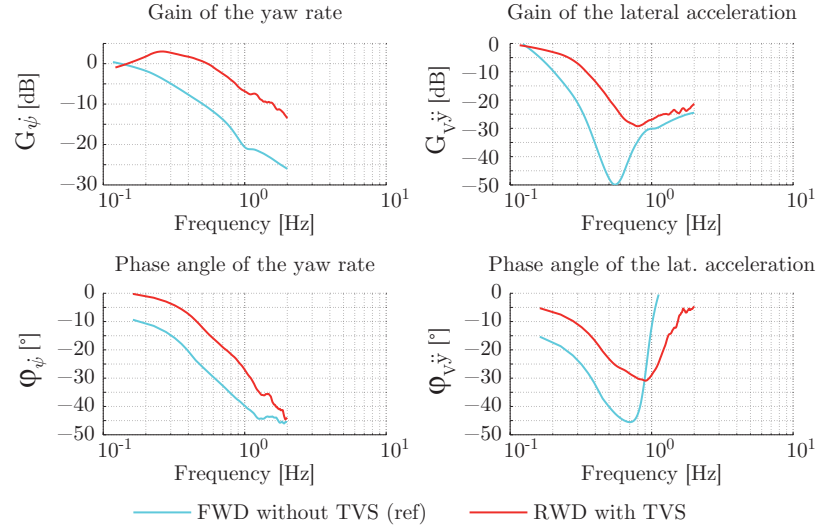


Figure 4.18.: Bode plots of the yaw rate and the lateral acceleration for the reference electric vehicle with a four-wheel drive powertrain architecture and no torque vectoring system, and the electric vehicle with two in-wheel motors at the rear axle with the presented torque vectoring system. The vehicle speed correspond to $v \dot{x} = 100$ km/h and the maximum lateral acceleration to approximately 50 % of the maximum steady state value ${}^{max}v \ddot{y}^S \approx 7.4$ m/s².

mum gain of the yaw rate. Since all the other criteria behave better, it can be said that the presented torque vectoring system based on in-wheel motors helps to enhance the overall driving performance of the considered vehicle in the analyzed maneuver.

Summary chapter 4: Lateral dynamics To analyze the advantages and limitations of in-wheel motors regarding the vehicle lateral dynamics, three different open-loop driving maneuvers were analyzed: step steer, open-loop sinusoidal steering input and open-loop frequency response. Based on the literature, different assessment criteria were presented to evaluate the performance of a given vehicle configuration in each of the analyzed driving maneuvers. Three different powertrain architectures were analyzed: an electric vehicle with a four-wheel drive powertrain and no torque vectoring system was taken as reference. This reference vehicle was compared with two electric vehicles with in-wheel motors and a rear-wheel drive and a four-wheel drive powertrain architecture respectively. A control concept for a torque vectoring system for these electric vehicles was presented. This concept consists of three components: The *reference values generator*, the *horizontal dynamics controller* and the *optimal force allocation algorithm*. The

4.3. Results

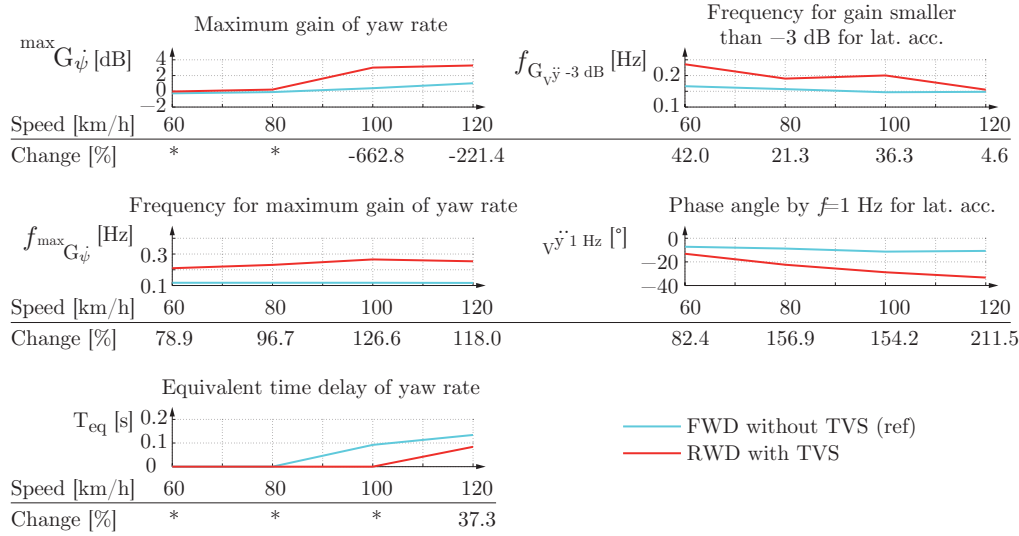


Figure 4.19.: Assessment variables for the open-loop frequency response change at different longitudinal speeds and approximately 50 % of the maximum steady state value of the lateral acceleration $\overset{max}{v}\ddot{y}^S \approx 7.4 \text{ m/s}^2$ (values marked with * are not calculable since the reference value AC_{ref} of the considered assessment criterion is very small).

reference values generator determines the reference values of the sideslip angle β , the yaw rate $\dot{\psi}$ and the vehicle longitudinal speed $v\dot{x}^d$ based on steady state maps of the vehicle to be controlled. These values are used as reference by the *horizontal dynamics controller* to build up the reference control inputs corresponding to the reference control longitudinal force $v\widehat{F}_{A, x}$ and the reference control yaw moment around the vertical axis $v\widehat{M}_{A, z}$. This values are taken by the third component, i.e. the *optimal force allocation algorithm*, to generate the control inputs corresponding to the longitudinal forces $wF_{T_i, x}$ at each of the wheels. This information can be used afterwards, for example, by a subordinated motor controller based on the tire longitudinal slip as control variable.

The obtained results showed that in-wheel motors in association with the presented torque vectoring system have substantial potential to enhance the lateral dynamics performance beyond the level of vehicles with a conventional four-wheel drive powertrain architecture without torque vectoring.

5. Vertical dynamics

Regarding the vehicle vertical dynamics, the influence of in-wheel motors is reflected mainly on the ride comfort and the driving safety. As presented in chapter 3.5.2, the in-wheel motors can add between 10 kg and 40 kg to the non-suspended mass. This changes, in first instance, the vibration behavior of the non-suspended mass itself. This leads to an alteration of the response of the tire vertical contact force ${}_W F_{T_i,z}$ and therefore on the horizontal tire forces ${}_W F_{T_i,x/y}$ (see chapter 2.5) to a certain road excitation. Since the horizontal tire forces are responsible for the vehicle driveability, it can be then concluded, that a variation on the non-suspended mass may influence the driving safety during safety relevant maneuvers (e.g. while driving in a curve on a bumpy road near the maximum lateral acceleration). Furthermore, the change on the vibration behavior of the non-suspended mass modifies the forces transmitted to the suspended mass and therefore also its vibration behavior. This influences correspondingly the vehicle ride comfort (see e.g. [RNW10] and [MK98]).

To analyze these effects this chapter is divided as follows: In the first part, different methods to assess the vehicle ride comfort and driving safety are presented. Afterwards, the influence of the increased non-suspended mass is presented and analyzed. In the final section, some methods to enhance the vehicle ride comfort and driving safety are presented.

5.1. Assessment of ride comfort and driving safety

Optimizing ride comfort and driving safety is one of the biggest trade-offs in vehicle design. In this section, some methods to evaluate the ride comfort level and the driving safety are presented. Afterwards, the trade-off between ride comfort and driving safety is explained based on the selected assessment criteria.

5.1.1. Ride comfort assessment

Perception of vibrations by human beings is influenced by several factors like age, state of health, mood, use of psychoactive substances and body position as well as by the application location, frequency and amplitude of the excitation signal. Moreover, vibrations are differently perceived from person to person, which makes the task of comfort assessing quite difficult. However, a lot of effort has been made to understand the influence of vibrations on human beings and to deduce guidelines to assess their effects. Although authors do not agree about the validity of the widespread used methods to assess ride comfort (see e.g. [Gri98]), there are, at present, three standards in Europe to assess comfort when the entire body is subjected to mechanical vibration (whole-body vibration): International Standard 2631-1:1997(E) [fSI97], British Standard 6841:1987 [Sta87] and the German Standard VDI 2057 (2002) [eV02]. An overview and a comparison of the standards can be seen in [Gri98], [LG98] and [PG02]. Moreover, some alternative methods to evaluate the ride comfort are presented in [Kna10], [Moh04], [Mar09] and [ST06].

Since it is widely used and alternative methods are not studied exhaustively, in this work, the International Standard 2631-1 is taken as basis. This standard takes the vehicle body acceleration as starting point for the comfort evaluation. Furthermore, it states, that the human perception of vibrations strongly depends on the frequency of excitation. Therefore, a series of filters W_i with different transfer functions are suggested to weight the magnitude of vibration depending on its frequency (or frequency content in the case of non harmonic signals), direction and application location (see figure 5.1).

Since human beings seem to be more sensitive to vibrations in the vertical direction ${}_V z$ (see [MG08], [Kna10] and [Len09]), the acceleration ${}_V \ddot{z}$ in this direction is taken as basis to evaluate the ride comfort in this work. Based on this, the frequency filter W_k is used to obtain the frequency weighted acceleration in order to evaluate the ride comfort (the mathematical description of this filter can be found in appendix E.1). It must be noticed in figure 5.1, that this filter present values higher than the unity in the frequency region in which the natural frequency of the internal organs as well as the head of average human beings is located, i.e. approximately between 4 Hz and 10 Hz (see e.g. [HEG11] and [Kna10]). According to this filter function, signals with a frequency (or frequency content) outside this region are considered to have a lower influence on the ride comfort. Therefore, many efforts during the design of a vehicle concentrate

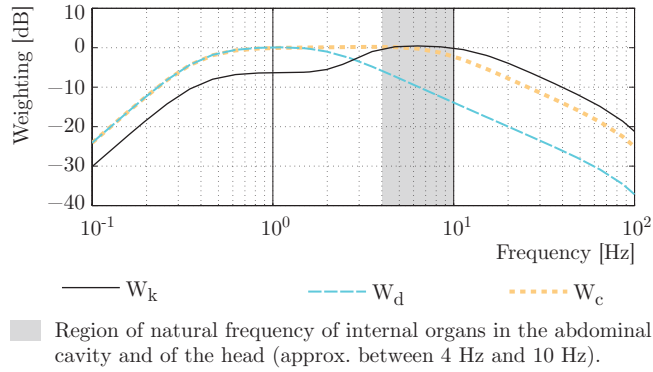


Figure 5.1.: Some frequency weighting curves for different directions and application locations according to the International Standard 2631-1:1997(E) [fSI97]: W_k : On seat surface in vertical direction ${}_V z$, W_d : On seat surface in horizontal directions ${}_V x$ and ${}_V y$, W_c : On seat-back in horizontal direction ${}_V x$.

in lowering the vertical acceleration in this non-advantageous frequency region (see e.g. [MW04]).

To avoid the big influence of the seat material on the vibration perceived by vehicle passengers (see e.g. [PG02]) and as usual in practical testing, the acceleration measured directly at the seat frame is considered. Additionally, due to the fact that road excitations in a range up to approximately 20 Hz are perceived as vibrations by human beings (see [MW04] and [Kna10]), the evaluation of ride comfort (while driving roads with harmonic excitation signals) is restricted to the frequency range (0 20] Hz in this work.

Depending on the nature of the excitation signal, different assessment criteria based on the measured (or simulated) vertical acceleration ${}_V \ddot{z}_P$ of a point P (e.g. at the seat frame) are defined in the International Standard 2631-1 to evaluate the comfort level. For harmonic or stochastic excitation signals without shocks, the *root mean square* (rms) given by

$${}_{V}^{rms} \ddot{z}_P(t) = \sqrt{\frac{1}{T_o} \cdot \int_0^{T_o} {}_V^w \ddot{z}_P^2(t) dt}, \quad (5.1)$$

is proposed, where T_o is the observation time and ${}_V^w \ddot{z}_P(t)$ correspond to the frequency weighted acceleration of the considered point P expressed as:

$${}_V^w \ddot{z}_P(t) = W_k(t) \cdot {}_V \ddot{z}_P(t). \quad (5.2)$$

For signals with shocks, the International Standard 2631-1 defines the *maximum transient vibration value* (mtvv) as:

$${}^{mtvv}{}_V\ddot{z}_P = \max({}^{rrms}{}_V\ddot{z}_P(t)) , \quad (5.3)$$

for a considered point P as the maximum of the *running root mean square* (rrms)

$${}^{rrms}{}_V\ddot{z}_P(t) = \sqrt{\frac{1}{\tau} \cdot \int_{t-\tau}^t {}^w{}_V\ddot{z}_P^2(t) dt} , \quad (5.4)$$

which corresponds to a series of rms-values calculated for each time t within a window of width τ along the entire observation time T_o .

5.1.2. Driving safety assessment

The effect of a changing vibration behavior of the non-suspended mass on the vehicle driving safety has not been exhaustively investigated in the literature and therefore there are no standardized or unified methods to evaluate it (see e.g. [RND11] and section 5.4). Nevertheless, the vertical movement of the center of the non-suspended masses ${}^Ez_{C_i}$ (see also equation 2.56 in chapter 2.5.2) is used by some authors to assess the vehicle driving safety since it affects the tire vertical contact force ${}^WF_{T_i,z}$ which determines the horizontal tire forces ${}^WF_{T_i,x/y}$ (see chapter 2.5) and hence the vehicle driving behavior and stability (see also [Hir09a], [Wal06] and [MW04]).

Another possibility to assess the vehicle driving safety is given by the wheel load factor (see e.g. [MW04])

$$\chi_{wl_i} = \frac{{}^{rms}{}_WF_{T_i,z}}{{}^SF_{T_i,z}} , \quad (5.5)$$

which defines the variation of the dynamical contact force ${}^WF_{T_i,z}$ between the tire and the ground as a function of the root mean square of the dynamic tire vertical contact force

$${}^{rms}{}_WF_{T_i,z} = \sqrt{\frac{1}{T_o} \cdot \int_0^{T_o} {}^WF_{T_i,z}(t) dt} \quad (5.6)$$

and its static value ${}^SF_{T_i,z}$ during the considered observation time T_o . Strong oscillations of a considered non-suspended mass i lead to strong variations of the tire vertical contact force ${}^WF_{T_i,z}$ and therefore to high values of the wheel load factor χ_{wl_i} . Moreover, values

of χ_{wl_i} near to 1 indicate a possible tire lifting.

While the wheel load factor χ_{wl_i} can be used to explain fundamental phenomena, different criteria must be taken into account to analyze realistic driving maneuvers (see e.g. [Ott87]). Some alternative criteria to assess the driving safety are presented in section 5.4, where the combined vehicle dynamics is analyzed.

5.1.3. Trade-off between ride comfort and driving safety

As explained in chapters 5.1.1 and 5.1.2, the root mean square value ${}^{rms}_V \ddot{z}_A$ of the frequency weighted vertical acceleration of the suspended mass and the wheel load factor χ_{wl_i} can be used to assess the ride comfort and the driving safety respectively. The quarter vehicle model presented in chapter E.2 of appendix E is taken as basis for the following fundamental analysis.

When driving on a road being described as a stochastic process characterized by a certain power spectral density $\Phi(\omega)$ (see chapter 2.6), the root mean square value of the frequency weighted vertical acceleration of the suspended mass ${}^{rms}_V \ddot{z}_A$ can be expressed in terms of the transfer function $W_k(\omega)$ of weighting filter proposed in the International standard 2631-1 [fSI97] (see chapters 5.1.1 and E.1) and the transfer function $G_{\ddot{z}_A/z_{road}}(\omega)$ for of the vertical acceleration of the suspended mass (see equation E.8 in chapter E.2) as¹ (see also [MW04]):

$${}^{rms}_V \ddot{z}_A = \left[\int_0^\infty (W_k(\omega))^2 \cdot \left(G_{\ddot{z}_A/z_{road}}(\omega) \right)^2 \cdot \Phi(\omega) \, d\omega \right]^{1/2}. \quad (5.7)$$

Analogously, the root mean square value ${}^{rms}_W F_{T_i,z}$ of the dynamic contact force between tire and ground can be expressed in terms of the corresponding transfer function $G_{F_{T_i,z}/z_{road}}(\omega)$ as (see equation E.11 in chapter E.2 for the transfer function):

$${}^{rms}_W F_{T_i,z} = \left[\int_0^\infty \left(G_{F_{T_i,z}/z_{road}}(\omega) \right)^2 \cdot \Phi(\omega) \, d\omega \right]^{1/2}. \quad (5.8)$$

¹Strictly speaking, the right term in equation 5.7 corresponds to the standard deviation of the frequency weighted acceleration ${}^{\sigma}_V \ddot{z}_A$, which is related with its root mean square value ${}^{rms}_V \ddot{z}_A$ by ${}^{rms}_V \ddot{z}_A = \sqrt{{}^{\sigma}_V \ddot{z}_A + \sigma^2}$. Nevertheless, since the mean value ${}_V \ddot{z}_A$ is zero for normally distributed stochastic processes (as assumed in chapter 2.6.2 for the road roughness), then ${}^{rms}_V \ddot{z}_A = {}^{\sigma}_V \ddot{z}_A$.

The wheel load factor χ_{wl_i} can be then obtained inserting equation 5.8 in equation 5.5.

The trade-off between ride comfort and driving safety can be explained using the so-called *conflict diagram* shown in figure 5.2. This diagram relates the driving safety and the ride comfort levels (here expressed in terms of the wheel load factor χ_{wl_i} and the root mean square ${}^{rms}_V \ddot{z}_A$ of the frequency weighted vertical acceleration of the suspended mass respectively) for different values of the static suspension spring stiffness $c_{b_i}^S$ and the linear damping coefficient $d_{b_i}^S$ of the shock absorber while driving with constant longitudinal speed ${}_V \dot{x}$ on a road characterized by a certain power spectral density $\Phi(\omega)$.

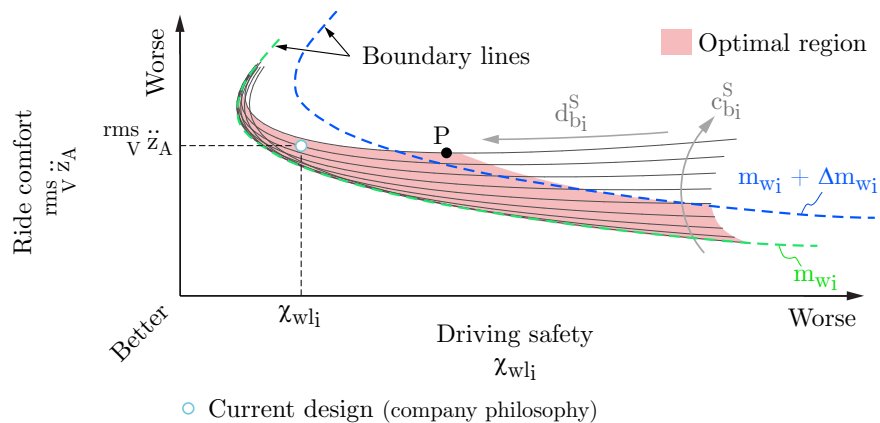


Figure 5.2.: Conflict diagram showing the trade-off between ride comfort and driving safety for a variation of the static suspension spring stiffness $c_{b_i}^S$ and the linear damping coefficient $d_{b_i}^S$ of the shock absorber while driving with constant longitudinal speed ${}_V \dot{x}$ on a road characterized by a certain power spectral density $\Phi(\omega)$. The ride comfort is evaluated based on the root mean square value of the frequency weighted vertical acceleration ${}^{rms}_V \ddot{z}_A$ of the suspended mass m_A , and the wheel load factor χ_{wl_i} is used to evaluate the driving safety. The boundary lines for unmodified m_{w_i} and increased $m_{w_i} + \Delta m_{w_i}$ non-suspended masses are depicted.

Starting at a point P on a line of constant static suspension spring stiffness $c_{b_i}^S$ and increasing the linear damping coefficient $d_{b_i}^S$ of the shock absorber, the driving safety level can be improved, i.e. the wheel load factor χ_{wl_i} can be reduced. However, the root mean square ${}^{rms}_V \ddot{z}_A$ of the frequency weighted vertical acceleration of the suspended mass increases resulting in a worse ride comfort level at the same time. This is the well known trade-off between ride comfort and driving safety (see e.g. [RNH11], [GM01], [Hir09a] and [MW04]). Nevertheless, there is a region called *optimal region* (see red region in figure 5.2) in which either the ride comfort level or the driving safety level

can be improved by changing $c_{b_i}^S$ and/or $d_{b_i}^S$. Outside this region, both ride comfort and driving level get worse.

Furthermore, it can be shown, that for a given value of the non-suspended mass m_{w_i} , the ride comfort and the driving safety levels cannot be improved beyond a boundary line by changing the static suspension spring stiffness $c_{b_i}^S$ or the linear damping coefficient $d_{b_i}^S$.

It is worth mentioning, that the selection of the static suspension spring stiffness $c_{b_i}^S$ and the linear damping coefficient $d_{b_i}^S$ is not always driven by the aim of optimizing ride comfort and driving safety but it is rather a matter of the philosophy of the vehicle manufacturing company and its desire to confer a distinctive flair to its product. While some companies producing sports cars give more importance to driving safety aspects, others related with large-scale production vehicles look after a more balanced relation between ride comfort and driving safety. It can be expected that the same philosophy will be kept in case of changing conditions, as increased non-suspended masses. Nevertheless, the validation of this hypothesis goes beyond the scope of the present work. Additionally, to account for the damping coefficient decrease over the life time, it is advisable to select a higher value during the early vehicle development phase.

5.2. Influence of increased non-suspended mass on ride comfort and driving safety

In this section, the influence of increased non-suspended masses on the ride comfort and the driving safety as a result of including an in-wheel motor (see also chapter 3.5.2) is presented. In the first part, the influence of the increased non-suspended masses m_{w_i} and their relation m_A/m_{w_i} with the suspended mass m_A on the objective evaluation criteria presented in chapters 5.1.1 and 5.1.2 are analyzed. Afterwards the results of test drives involving *normal drivers* and *experienced test drivers* are used as basis to establish the correlation between objective evaluation criteria and subjective perception. Furthermore, with the aim to identify a more "intuitive" variable producing similar effects on the subjective ride comfort perception of drivers and passengers as increased non-suspended masses, an approach based on the tire inflation pressure p_{T_i} is presented in the third part of this section.

5.2.1. Influence of the relation of the suspended to the non-suspended mass on the assessment criteria

As can be seen in figure 5.2, by increasing the non-suspended mass to $m_{w_i} + \Delta m_{w_i}$, both ride comfort and driving safety get worse. The boundary line characterizing the best ride comfort and driving safety levels achievable with a certain combination of the static suspension spring stiffness $c_{b_i}^S$ and the linear damping coefficient $d_{b_i}^S$ is shifted in a direction of worse ride comfort and driving safety levels. Since different performance requirements lead to different electric motor torques (see chapter 3.5.8) and therefore to different increments of the non-suspended mass (see chapter 3.5.2), the effect of the increased non-suspended masses on different vehicle segments (characterized by different suspended masses m_A and related with different performance requirements) is analyzed in this section (see also [RNH11]). Therefor, the quarter vehicle model presented in chapter E.2 of appendix E is taken as basis.

Table 5.1 presents the three different vehicle classes taken into account to analyze the effect of the relation m_A/m_{w_i} between the suspended mass m_A and the non-suspended mass m_{w_i} . Since the presented analysis is based on the quarter vehicle model² presented in chapter E.2, the relation m_{A_q}/m_{w_i} is used instead of m_A/m_{w_i} . Furthermore, it is assumed, that the suspended mass corresponding to the quarter vehicle m_{A_q} can be expressed as $m_{A_q} \approx m_A/4$, where m_A is given in terms of the vehicle mass in running order m_v by $m_A = m_v - (4 \cdot m_{w_i})$. The relation m_{A_q}/m_{w_i} is indicated in table 5.1 together with the standard non-suspended mass³ m_{w_i} for each analyzed vehicle class, and the considered additional non-suspended mass Δm_{w_i} . In comparison to the vehicle classes presented in table 3.3 of chapter 3.7.1, the additional vehicle class *D* corresponding to large sedans⁴ is also considered.

Figure 5.3 shows the conflict diagram for the three different vehicle classes listed in table 5.1. Additionally, the comfort bands specified in the international standard 2631-1:1997(E) [fSI97] are presented. It can be seen, that according to the considered evaluation criteria, the lower the relation m_{A_q}/m_{w_i} (i.e. for lower vehicle segments), the stronger is the effect of the increased non-suspended masses on ride comfort and driving safety. Nevertheless, based on the assumption that the effect of the increased non-

²The right subscript q is used to identify variables related with the quarter vehicle model.

³Measured or estimated value of non-suspended mass as corresponding to the series product without any additional weight.

⁴Vehicle classes definition according to [oE11].

Table 5.1.: Considered vehicle segments for the analysis of the influence of increased non-suspended masses on ride comfort and driving safety.

		Minicompact ^a	Subcompact ^a	Large
		A ⁻	B	D
Vehicle mass in running order	m_v [kg]	850	1200	2000
Standard non-suspended mass	m_{w_i}	40 ^b	50 ^c	60 ^c
Mass relation ^d	m_{A_q}/m_{w_i} [-]	4.3	5.0	7.3
Additional non-suspended mass	Δm_{w_i} [kg]	20 ^e	30 ^e	60 ^f

^a Further related properties can be found in table 3.3 in chapter 3.7.1.

^b Measured.

^c Estimated value of non-suspended mass as corresponding to the series product without any additional weight (based on [BS07]).

^d It is assumed that the mass m_{A_q} corresponding to the quarter vehicle (see appendix E.2) is given by $m_{A_q} \approx m_A/4$, where $m_A = m_v - (4 \cdot m_{w_i})$.

^e Estimated weight of an induction electric motor based on the results presented on table 3.11 in chapter 3.7.6. The active mass m_{EMact} as presented in figure 3.9 and an estimated value for the weight of the case and the gear box as presented in table 3.9 are considered.

^f Estimated by extrapolation based on the results for the other two vehicle classes presented in this table.

suspended masses on ride comfort is acceptable if the optimal region remains in the same comfort band, it can be concluded, that the considered increased non-suspended masses as corresponding to the performance requirements taken into account (see chapter 3.7.4) lead to an acceptable reduction in ride comfort for the analyzed vehicle segments. An approach involving subjective impressions of test drivers is presented in chapter 5.2.2 to further support this statement.

5.2.2. Subjective comfort assessment and correlation with simulation results

Describing the subjective comfort perception using objective individual independent numeric or verbal (e.g. comfortable, fairly comfortable, very uncomfortable, etc.) attributes is called *objectify*. Nevertheless, it is not an easy process, even for experienced test drivers (see e.g. [Len09] and [Kna10]). In this work, a group of persons composed of 34 *normal drivers* and 2 *experienced test drivers* was taken as population in order to determine the influence of increased non-suspended masses on the subjective perception of ride comfort.

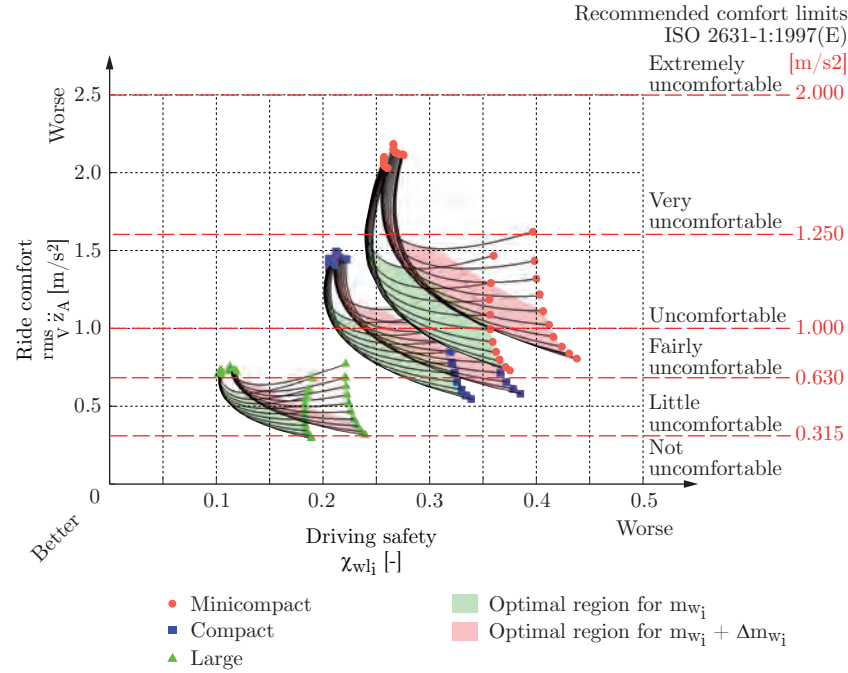


Figure 5.3.: Conflict diagram for different vehicle segments with and without increased non-suspended masses. Results obtained considering a street type *C* (see chapter 2.6.2) and a longitudinal vehicle speed of $v\dot{x} = 40$ km/h.

Test drives on the road presented in figure 2.20 (see also figure E.2-c in chapter E.3.1 of appendix E) with the test vehicle (see chapter B.1 in appendix B) and the conditions presented in table 5.2 were carried out. To evaluate the subjective road comfort perception, an evaluation scale ranging from 1 (very uncomfortable) to 10 (very comfortable) was proposed. For each considered longitudinal speed $v\dot{x}$, the configuration corresponding to the test vehicle without additional non-suspended masses ($\Delta m_{w_i} = 0$ kg), no additional load mass ($m_{load} = 0$ kg) and the tire inflation pressure recommended by the car manufacturer ($p_{T_i} = 2.3$ bar) was selected as reference and a grade of 5.5 in the proposed scale was assigned to it. Each test person was asked to subjectively evaluate the ride comfort of each test drive condition by comparing it with the reference configuration corresponding to the selected longitudinal speed. While grades lower than 5.5 indicated a worse subjective ride comfort perception in comparison with the reference condition, grades higher than 5.5 indicated a better subjective comfort perception.

Figure 5.4 presents the relative cumulative frequency⁵ of the grades given by all test

⁵See appendix A.1.

Table 5.2.: Test drive conditions used to determine the influence of increased non-suspended m_{w_i} masses on the subjective ride comfort perception.

Parameter	Symbol	Units	Values		
Additional non-suspended mass	Δm_{w_i}	[kg]	0 ^a	10	30
Additional load mass	m_{load}		0 ^a	400 ^b	
Longitudinal vehicle speed ^c	$v \dot{x}$	[km/h]	20	40	
Tire inflation pressure	p_{T_i}	[bar]	2.3 ^{a,d}	3.2	

^a Reference.

^b Corresponds to approximately two thirds of the maximum authorized additional load mass (see table B.1 in appendix B).

^c Held constant during each test drive.

^d Value recommended by the car manufacturer.

persons to the different test configurations considered. As can be seen in figure 5.4-a, increased non-suspended masses lead to a worse subjective ride comfort perception. It can also be seen, that while the longitudinal vehicle speed as well as the additional load mass (figures 5.4-a and 5.4-b respectively) do not clearly affect the subjective ride comfort perception, the increased tire inflation pressure strongly worsens it (figure 5.4-c).

With the purpose to establish a relation between the subjective ride comfort perception and the objective criteria presented in chapter 5.1.1, the different conditions presented in table 5.2 were simulated using the model presented in chapter 2. Due to the fact that the road excitation contains shocks (curb and pothole), the *maximum transient vibration value* ${}^{mtvv}\ddot{z}_A$ of the frequency weighted acceleration (see equation 5.3) at the driver's seat frame is used as evaluation criteria. Furthermore, since the answers of the test drivers are referred to the reference test condition, the relative *maximum transient vibration value*

$$\Delta {}^{mtvv}\ddot{z}_P = \frac{{}^{mtvv}\ddot{z}_{A_{ref}} - {}^{mtvv}\ddot{z}_{A_{mw}}}{{}^{mtvv}\ddot{z}_{A_{ref}}} \cdot 100 \quad (5.9)$$

is used, where ${}^{mtvv}\ddot{z}_{A_{ref}}$ and ${}^{mtvv}\ddot{z}_{A_{mw}}$ correspond to the frequency weighted acceleration at the driver's seat frame for the reference configuration and for the configuration with increased non-suspended masses respectively. Finally, since the small differences between the considered conditions were hardly perceived by the *normal drivers*, only the (independently obtained but unanimous) answers of the *experienced test drivers* are considered at this instance. Taking the subjective ride comfort perception of only

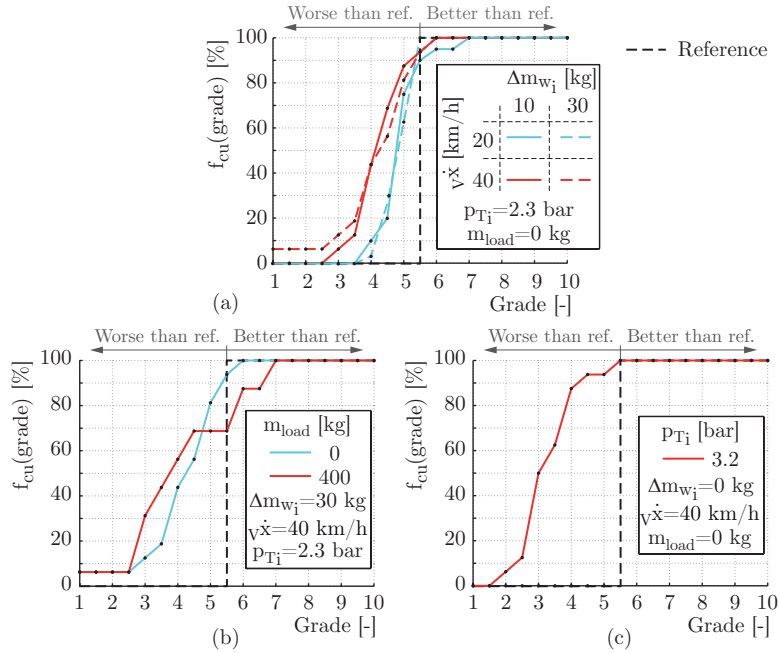
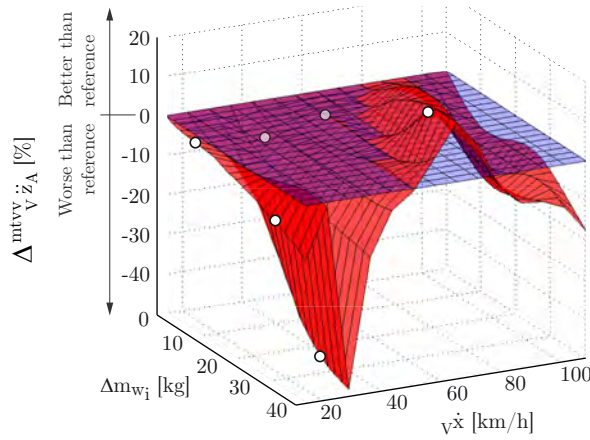


Figure 5.4.: Results of the survey regarding the subjective ride comfort perception while driving over the deterministic road excitation signal presented in figure 2.20: variation of the additional non-suspended mass Δm_{w_i} and the longitudinal vehicle speed v_x (a), variation of the additional load mass m_{load} (b), and variation of the tire inflation pressure p_{T_i} (c). The relative cumulative frequency $f_{cu}(\text{grade})$ of the grade given by all drivers (*normal drivers* and *experienced test drivers*) is presented.

experienced test drivers is a common praxis used to reduce the uncertainty and noise introduced by *normal drivers*, for which small comfort differences are difficult to objectify (see e.g. [Len09]).

The comparison between the subjective ride comfort perception of the *experienced test drivers* and the simulation results for different values of the longitudinal vehicle speed v_x is shown in figure 5.5. According to equation 5.9, the relative *maximum transient vibration value* $\Delta_{V\ddot{z}_A}^{mtvv}$ corresponding to the reference condition equals zero and the corresponding surface in figure 5.5 is therefore a horizontal plane. While positive values of $\Delta_{V\ddot{z}_A}^{mtvv}$ (above the plane corresponding to the reference condition) indicate a better subjective ride comfort perception, negative ones correspond to a worsening. In figure 5.5, the qualitative answer of the *experienced test drivers* (i.e. better or worse than the reference test condition) and not an absolute value is depicted. While a better subjective ride comfort perception is indicated with a point above the horizontal plane

corresponding to the reference condition, a worse perception is related with a point below it.



- Subjective comfort perception of *experienced test drivers*
- Reference configuration
- Configuration with increased non-suspended masses

Figure 5.5.: Comparison between the subjective ride comfort perception of the *experienced test drivers* and the simulation results for different values of the longitudinal vehicle speed $v_{\dot{x}}$. Reference configuration: test vehicle without increased non-suspended masses $m_{w_i} = 0$ kg, no additional load mass $m_{load} = 0$ kg and tire inflation pressure $p_{T_i} = 2.3$ bar.

Based on figure 5.5, following conclusions can be made:

- The tendency of the answers of the *experienced test drivers* can be qualitatively depicted with accuracy with the help of the model presented in chapter 2. The subjective ride comfort perception can be therefore estimated with the objective assessment criteria calculated based on the simulation results obtained with the presented vehicle model.
- The effect of increased non-suspended masses on the subjective perception of ride comfort and on the related objective evaluation criteria depends on the driving speed and is not always negative. Furthermore, a wide variation range of the analyzed variables (e.g. increased non-suspended mass m_{w_i} or longitudinal vehicle speed $v_{\dot{x}}$) must be considered in order to increase the validity of the analysis.
- Under the considered conditions, no remarkable differences in the ride comfort

subjective perception with and without increased non-suspended masses can be expected. Nevertheless, there is room for improvement.

The results obtained in this chapter support the conclusion made in chapter 5.2 regarding the acceptable ride comfort reduction related with increased non-suspended masses. This results also agree with those presented recently in the literature, which, based on test drives with vehicles with increased non-suspended masses, show no evidence of relevant subjective or objective worsening neither of the ride comfort nor of the driving safety (see e.g. [GFH10] and [GHKP12]).

5.2.3. Equivalence between the subjective ride comfort perception with increased non-suspended masses and increased tire inflation pressure

With the aim to identify a more "intuitive" variable producing similar effects on the subjective ride comfort perception of drivers and passengers as increased non-suspended masses, an approach based on the tire inflation pressure p_{T_i} is presented in this section.

Figure 5.6 shows the relative cumulative frequency⁶ $f_{cu}(grade)$ of the grades given by all test drivers when driving over the deterministic road excitation signal presented in figure 2.20 with increased non-suspended masses of $m_{w_i} = 20$ kg at both wheels of the rear axle and with increased tire inflation pressure of $p_{T_i} = 3.2$ bar. Both curves are approximated using a spline. It can be seen that the approximation lines present the same behavior. Therefore, it is assumed that a relation between the influence of increased non-suspended mass m_w and increased tire inflation pressure p_T can be established.

In this work an empirical linear relation according to

$$\Delta p_T = C_{mw \rightarrow p} \cdot \Delta m_w \quad (5.10)$$

is proposed, where the proportionality factor $C_{mw \rightarrow p}$ is given by

$$C_{mw \rightarrow p} = \frac{\Delta p_{T_i}}{\Delta m_{w_i}} \cdot \frac{\Delta g_{mw}}{\Delta g_p} . \quad (5.11)$$

The variables Δm_{w_i} and Δp_{T_i} correspond to the value of the additional non-suspended mass and the additional tire pressure used during the test drives related with the results

⁶See appendix A.1.

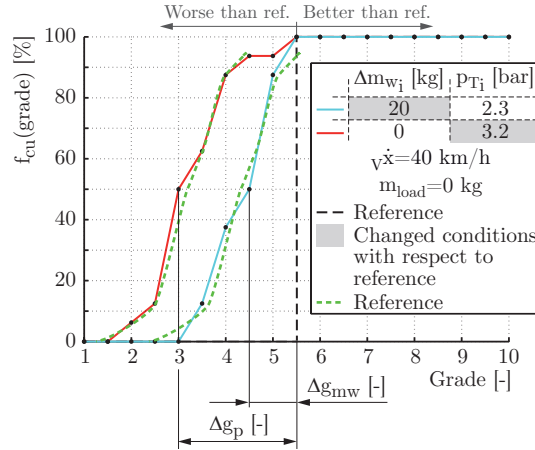


Figure 5.6.: Comparison between the subjective ride comfort perception with an additional non-suspended mass of $\Delta m_{w_i} = 20$ kg at both wheels of the rear axle and with an increased tire inflation pressure of $p_{T_i} = 3.2$ bar. The relative cumulative frequency $f_{cu}(grade)$ of the grade given by the *normal drivers* and the *experienced test drivers* is presented.

presented in figure 5.6 respectively, i.e. $\Delta m_{w_i} = 20$ kg and $\Delta p_{T_i} = 0.9$ bar. The terms Δg_{mw} and Δg_p indicate the difference between the reference and the approximation lines for the conditions with increased non-suspended masses and with increased tire inflation pressure respectively. Since this lines are approximately parallel, the mentioned terms are measured for a relative cumulative frequency⁷ $f_{cu}(grade) = 50$ %, resulting in

$$\Delta g_{mw} = 5.5 - 4.5 = 1.0 , \quad (5.12a)$$

$$\Delta g_p = 5.5 - 3.0 = 2.5 . \quad (5.12b)$$

With this, the proportionality factor becomes

$$C_{mw \rightarrow p} = \frac{0.9 \text{ bar}}{20 \text{ kg}} \cdot \frac{1.0}{2.5} = 0.018 \frac{\text{bar}}{\text{kg}} . \quad (5.13)$$

The approach presented in this section represents a possibility to easily carry out test drives aiming to estimate the subjective ride comfort perception of vehicles with increased non-suspended masses (at least at the rear axle) without using any special device to actually increase them.

⁷See appendix A.1.

5.3. Suspension systems to enhance the ride comfort and the driving safety

In this section, two non-conventional passive, a semi-active and an active suspension system aiming to enhance the ride comfort and the driving safety are presented. As presented in figure 5.7, beside the constructive differences and the production costs, the operating range, the system reaction time τ_{ws} and the energy demand distinguish these systems from each other. The considered concepts were presented in [RNW10] and [RNW11b], and the obtained results are considered by some authors as a reference point toward the electrification of vehicles using in-wheel motors (see e.g. [RA11]).

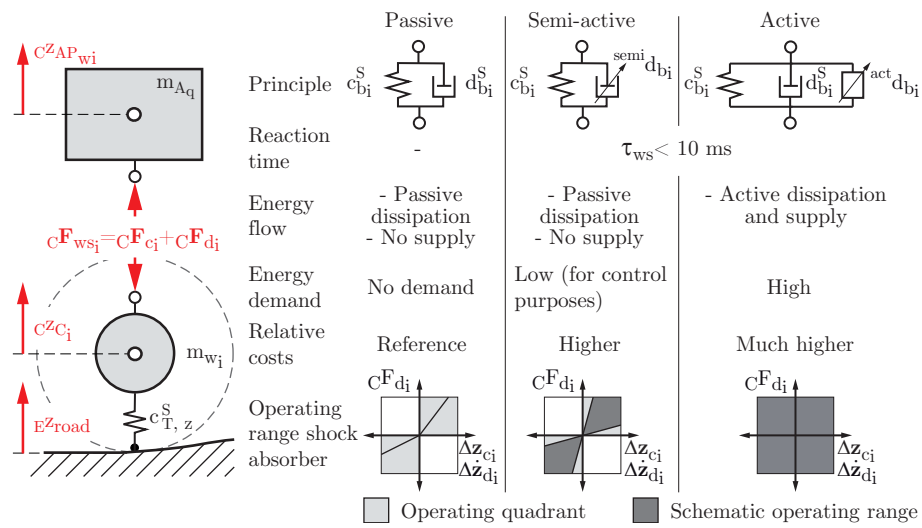


Figure 5.7.: Comparison of the considered suspension systems to enhance the ride comfort and the driving safety (see also [Nie11] and [HEG11]).

5.3.1. Passive suspension systems

Passive suspension systems do not need any energy supply. This makes them attractive for electrified vehicles (hybrid or pure electric ones), for which energy saving is even more important than for vehicles with traditional internal combustion engines. Higher energetic efficiency levels increase the driving range of electrified vehicles and make them attractive for typical vehicle customers and thus for series production. Beside the conventional passive suspension system presented in chapter 2.7, two alternative passive suspension systems are presented and analyzed in the present work: a concept

with eccentric electric motor and a concept using the electric motor as damping mass.

Eccentric concept

This concept can be used in vehicles with torsion beam axles. The electric motor is positioned eccentric with respect to the rotation axis of the wheel. Because the distance between the electric motor and the wheel must be kept constant, this concept is more suitable for torsion beam axles. The implementation in other axle types would lead to very complicated designs. Figure 5.8 shows a schematic representation of the eccentric concept used in a torsion beam axle. The electric motor m_{EM} is placed at distance l_{EM} from the wheel center m_{w_i} on the trailing arm of length l_{TA} . The torque is transmitted to the wheel using a belt (a chain transmission is also possible) tightened by a belt pulley.

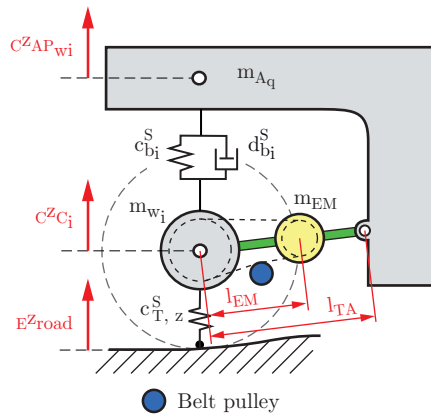


Figure 5.8.: Schematic representation of the eccentric concept.

The mass m_{EM} and the reduced moment of inertia ${}^{red}I_{EM}$ of the electric motor can be considered to be equivalent to the additional non-suspended mass

$$\Delta m_{w_i} = \frac{m_{EM} \cdot (l_{TA} - l_{EM})^2 + {}^{red}I_{EM}}{l_{TA}^2} \quad (5.14)$$

located at the wheel center. Neglecting the moment of inertia ${}^{red}I_{EM}$ of the electric motor, the total mass on the wheel $m_{w_i} + \Delta m_{w_i}$ depends only on the position of the electric motor on the trailing arm. Figure 5.9 shows the variation of additional non-suspended mass Δm_{w_i} as a function of the position l_{EM} of the electric motor mass m_{EM} on the trailing arm and of the non-suspended mass m_{w_i} without any additional

mass. Based on this figure, if the relation between the electric motor mass and the non-suspended mass without any additional mass correspond to $m_{EM}/m_{w_i} = 50\%$, the electric motor must be placed at a distance corresponding to $l_{EM} \approx 0.35 \cdot l_{TA}$ measured from the wheel center. As expected, placing the electric motor near the joint between the trailing arm and the suspended mass avoids increasing the non-suspended mass. Moreover, it can be seen on the figure, that small changes in the position l_{EM} of the motor mass m_{EM} lead to big changes on the additional non-suspended mass Δm_w .

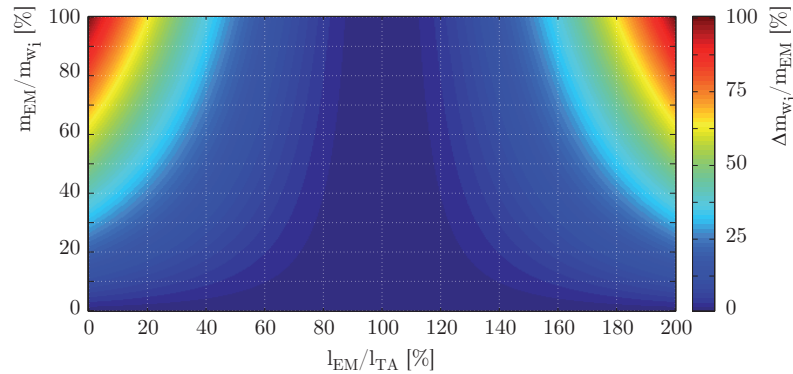


Figure 5.9.: Reduction of the additional non-suspended mass Δm_w for the eccentric concept.

Since it is sufficient to determine the total non-suspended mass $m_{w_i} + \Delta m_{w_i}$ and consider the system as an unmodified passive trailing arm suspension, the results of this concept are not going to be explicitly presented in the section 5.3.4 where the different systems described in the present chapter are compared.

Damping mass concept

The concept presented here corresponds to that first introduced by *Bridgestone* in 2004 (see [STN06] and [MTI⁺06]). As shown in figure 5.10-a, the electric motor is used as damping mass by suspending it on the wheel carrier over a spring and shock absorber system.

As can be seen in figure 5.10-b, the damping mass adds an additional degree of freedom to the vibrating system. The term

$${}^C\mathbf{F}_{DM_i} = {}^{DM}{}^C\mathbf{F}_{c_i} + {}^{DM}{}^C\mathbf{F}_{d_i} \quad (5.15)$$

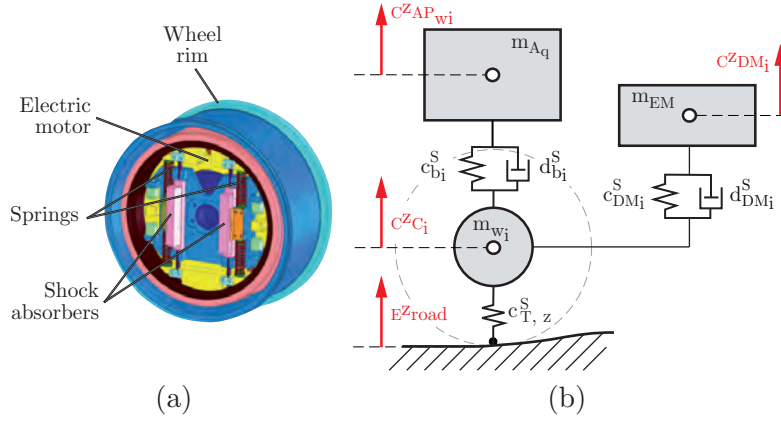


Figure 5.10.: Damping mass concept: mechanism of the *Advanced Dynamic Damper Motor* - ADM - mechanism as presented by *Bridgestone* (see [STN06] and [MTI⁺06]) (a), schematic representation with the motor mass m_{EM} being used as damping mass (b).

corresponding to the (vertical⁸) force related with the spring and shock absorber system of the damping mass and acting on the wheel carrier must be introduced in the equation 2.16 of linear momentum for the non-suspended masses (see chapter 2.4.2), which leads to the modified equation (see forces definition in the mentioned chapter):

$$\sum C \mathbf{F}_{w_i} = C \mathbf{F}_{T_i} - C \mathbf{F}_{ws_i} - C \mathbf{F}_{DM_i} + C \mathbf{G}_{w_i}. \quad (5.16)$$

The spring force

$${}^{DM} C \mathbf{F}_{c_i} = c_{DM_i}^S \cdot \Delta z_{DM_i} = c_{DM_i}^S \cdot (C z_{C_i} - C z_{DM_i}) \quad (5.17)$$

is assumed to present a linear behavior and can be described as a function of the static coefficient $c_{DM_i}^S$ of the spring of the damping mass suspension and the vertical displacements of the wheel carrier $C z_{C_i}$ and the damping mass $C z_{DM_i}$. The force of the shock absorber

$${}^{DM} C \mathbf{F}_{d_i} = d_{DM_i}^S \cdot \Delta \dot{z}_{DM_i} = d_{DM_i}^S \cdot (C \dot{z}_{C_i} - C \dot{z}_{DM_i}) \quad (5.18)$$

is also assumed to present a linear behavior and can be expressed in terms of the linear damping coefficient $d_{DM_i}^S$ of the shock absorber of the damping mass suspension and

⁸See assumption 2.2.

the vertical velocities of the wheel carrier ${}_C\dot{z}_{C_i}$ and the damping mass ${}_C\dot{z}_{DM_i}$.

The static spring coefficient $c_{DM_i}^S$ and the coefficient and linear damping coefficient $d_{DM_i}^S$ must be determined to avoid resonances between the damping mass and the suspended or the non-suspended mass. Analogously to equation 2.83 in chapter 2.7.1, the static spring coefficient $c_{DM_i}^S$ can be written in terms of the natural frequency f_{DM} of the damping mass, the statical tire vertical stiffness $c_{T_i, z}^S$ and the damping mass (corresponding in this case to the mass of the electric motor m_{EM}) as:

$$c_{DM_i}^S = \frac{m_{EM} \cdot (2 \cdot \pi \cdot f_{DM})^2 \cdot c_{T_i, z}^S}{c_{T_i, z}^S - m_{EM} \cdot (2 \cdot \pi \cdot f_{DM})^2}. \quad (5.19)$$

The linear damping coefficient can be determined analogously to equation 2.105 in chapter 2.7.2 as a function of the static spring coefficient $c_{DM_i}^S$ defined previously, the mass of the electric motor m_{EM} and the desired damping ratio ξ_{DM} for the damping mass as:

$$d_{DM_i}^S = 2 \cdot \xi_{DM} \cdot \sqrt{c_{DM_i}^S \cdot m_{EM}}. \quad (5.20)$$

In this work, the natural frequency⁹ of the damping mass was set to $f_{DM} = 5.5$ Hz and its damping ratio, as suggested by *Masaki et al.* [MTI⁺06], to $\xi_{DM} = 0.5$.

A similar system producing a similar effect as the damping mass described in this chapter but using the moment of inertia of a mass connected with one of the suspension control arms of an independent axle system is presented in [NR09] and analyzed in [Pür11].

5.3.2. Semi-active suspension system

Semi-active suspension systems can be considered to be an intermediate technology between active and passive suspension systems. While an active suspension system can supply and dissipate energy to and from the vibrating system composed by the suspended and the non-suspended mass, a semi-active suspension system can only dissipate it. Nevertheless and in comparison with traditional passive suspension systems with fixed properties leading to fixed amounts of dissipated energy (see chapter 2.7), semi-active suspension systems dissipate different amounts of energy by adjusting their

⁹The natural frequencies of the suspended and the non-suspended mass are around 1 Hz and 10 Hz respectively (see e.g. [Hir09a], [Wal06] and [MW04]).

properties depending on a predefined algorithm (see e.g. [Kar90] and [FHT⁺09]). In this regard, one of the most popular approaches for such systems is the semi-active *sky-hook* control strategy presented by *Karnopp et al.* [KCH74]. This strategy is based on the hypothesis, that an optimal ride comfort can be achieved by damping the vibrating suspended mass with respect to the *artificial sky* (or the horizon) and not with respect to the wheel body - real shock absorber - [HEG11]. Therefore, as shown in figure 5.11-a, the *idealized* sky-hook shock absorber is considered to be placed between the suspended mass m_{A_q} and the sky and not between the suspended mass and the non-suspended mass m_{w_i} as for a *real* one.

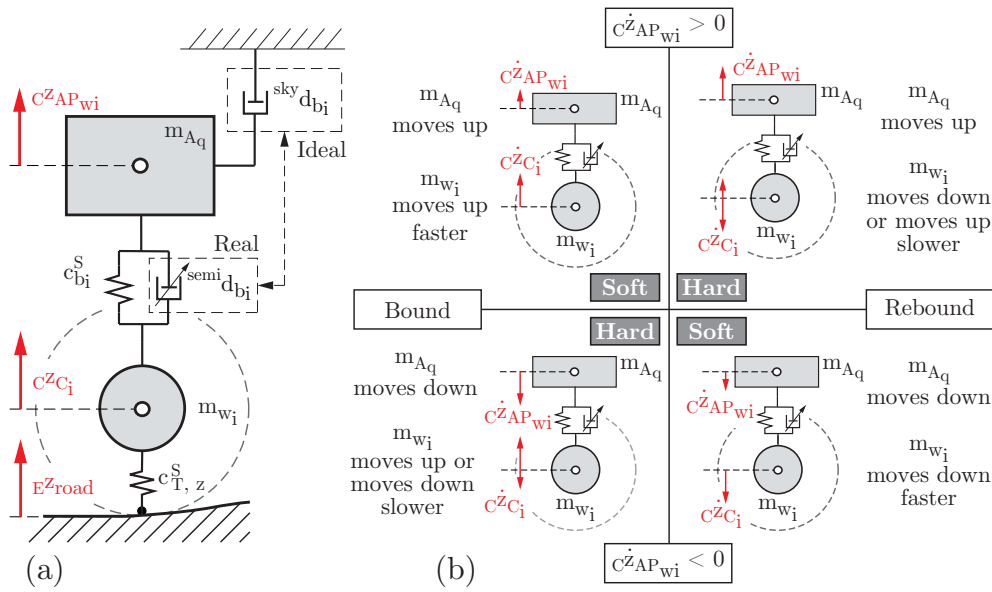


Figure 5.11.: Sky-hook control strategy for a variable shock absorber of a semi-active suspension system: schematic representation (a) and fundamental function [HEG11] (b).

It is then assumed that the time-dependent force¹⁰

$${}^{sky}F_{d_i} = {}^{sky}d_{b_i} \cdot C \dot{z}_{AP_{wi}} \quad (5.21)$$

of the *idealized* sky-hook shock absorber, which is described in terms of the time-dependent vertical¹¹ speed of the suspended mass $C \dot{z}_{AP_{wi}}$ and the (constant) linear

¹⁰To simplify the equations in this section, the time dependency is not explicitly indicated.

¹¹According to assumption 2.2, only vertical forces are considered for the wheel movement.

sky-hook damping coefficient $^{sky}d_{b_i}$, is equal to the time-dependent (linear) force

$${}_C\mathbf{F}_{d_i} = {}^{semi}d_{b_i} \cdot ({}_C\dot{\mathbf{z}}_{C_i} - {}_C\dot{\mathbf{z}}_{AP_{wi}}) \quad (5.22)$$

of the *real* shock absorber (see equation 2.95 in chapter 2.7.2), which is additionally a function of the time-dependent vertical speed of the non-suspended mass m_{w_i} . Based on these equations, the linear time-dependent semi-active damping coefficient ${}^{semi}d_{b_i}$ can be expressed as:

$${}^{semi}d_{b_i} = {}^{sky}d_{b_i} \cdot \frac{{}_C\dot{\mathbf{z}}_{AP_{wi}}}{{}_C\dot{\mathbf{z}}_{C_i} - {}_C\dot{\mathbf{z}}_{AP_{wi}}}. \quad (5.23)$$

Furthermore, a semi-active shock absorber uses the force ${}_C\mathbf{F}_{d_i}$ to enhance the ride comfort by reducing the amplitude of the suspended mass movement. To reach this goal, following strategy is proposed (see e.g. [KCH74] and [Kar90]): On the one hand, the linear semi-active damping coefficient is allowed to be varied in the given range

$${}^{min}d_{b_i} \leq {}^{semi}d_{b_i} \leq {}^{max}d_{b_i}. \quad (5.24)$$

On the other, as can be seen figure 5.11-b (see also [HEG11]), while only small values of the time-dependent force ${}^{semi}{}_C\mathbf{F}_{d_i}$ from the semi-active shock absorber are allowed to be transmitted when it acts in a direction tending to amplify the suspended mass movement, larger values can be transmitted to reduce the movement amplitude. Therefore, the resulting time-dependent reference semi-active shock absorber force ${}^{ref}{}_C\mathbf{F}_{d_i}$ can be expressed mathematically as:

$${}^{ref}{}_C\mathbf{F}_{d_i} = \begin{cases} {}^{semi}d_{b_i} \cdot ({}_C\dot{\mathbf{z}}_{C_i} - {}_C\dot{\mathbf{z}}_{AP_{wi}}); & \text{if } \text{sign}({}_C\dot{\mathbf{z}}_{AP_{wi}}) = \text{sign}({}_C\dot{\mathbf{z}}_{C_i} - {}_C\dot{\mathbf{z}}_{AP_{wi}}), \\ {}^{min}d_{b_i} \cdot ({}_C\dot{\mathbf{z}}_{C_i} - {}_C\dot{\mathbf{z}}_{AP_{wi}}); & \text{if } \text{sign}({}_C\dot{\mathbf{z}}_{AP_{wi}}) \neq \text{sign}({}_C\dot{\mathbf{z}}_{C_i} - {}_C\dot{\mathbf{z}}_{AP_{wi}}). \end{cases} \quad (5.25)$$

Since effects like the compressibility of the damper oil and the deformability of the pressure chamber of the damper affects the effectiveness of the control strategy (see e.g. [Nie06], [Kol07] and [RW95]), following transfer function, proposed by *Niemz* [Nie06], is used to consider the dynamic behavior of the system and obtain the time-dependent value of the actual resulting semi-active shock absorber force ${}^{semi}{}_C\mathbf{F}_{d_i}$ as a function of the time-dependent value of the reference one ${}^{ref}{}_C\mathbf{F}_{d_i}$ given by equation 5.25:

$${}^{semi}G(s) = \frac{{}^{semi}{}_C\mathbf{F}_{d_i}(s)}{{}^{ref}{}_C\mathbf{F}_{d_i}(s)} = \frac{1}{1 + 0.01 \cdot s}. \quad (5.26)$$

The values of the system parameters are presented in [RNW10].

5.3.3. Active suspension system

Active damping suspension systems can non only dissipate but also introduce energy into the vibrating system to enhance the ride comfort or improve the driving safety (see also figure 5.7). The control strategy presented in this chapter was introduced by *Karnopp* [Kar83] in 1983 and states that the ride comfort of a vehicle can be improved near the natural frequency of the suspended mass by introducing the active shock absorber force

$${}^{act}{}_C\mathbf{F}_{d_i}^* = {}^{act}d_{b_i} \cdot {}_C\dot{\mathbf{z}}_{AP_{wi}} \quad (5.27)$$

expressed in terms of the (constant) linear active damping coefficient ${}^{act}d_{b_i}$ and the vertical speed of the suspended mass ${}_C\dot{\mathbf{z}}_{AP_{wi}}$. Nevertheless, as presented in [RNW10], this force acts damping the movement of the suspended mass but not that of the non-suspended mass. Therefore, an additional passive shock absorber is introduced, as shown in figure 5.7. This additional shock absorber is modeled as a linear force element supplying a force

$${}^{act}{}_C\mathbf{F}_{d_i} = {}^{act}{}_C\mathbf{F}_{d_i}^* + d_{b_i}^S \cdot ({}_C\dot{\mathbf{z}}_{C_i} - {}_C\dot{\mathbf{z}}_{AP_{wi}}) . \quad (5.28)$$

The active shock absorber considered in this work is composed by an electric synchronous motor transmitting its torque to one of the transversal control arms of an independent axle system through a single stage gearbox. A maximum power of ${}^{act}P_{d_i} = 4000$ W by $|{}_C\dot{\mathbf{z}}_{C_i} - {}_C\dot{\mathbf{z}}_{AP_{wi}}| = 1.5$ m/s was assumed (see [RNW10]). Moreover, the system dynamics were taken into account by introducing a similar transfer function as that presented in equation 5.26 for the semi-active shock absorber. An approach to define the linear damping coefficient $d_{b_i}^S$ of the additional passive shock absorber as well as further details on the entire considered system were presented in [RNW10].

5.3.4. Comparison

In this section, the performance of the different suspension systems described in the present chapter (traditional passive, passive with electric motor used as damping mass, semi-active, and active system) regarding vehicles with increased non-suspended masses is presented. Since the effect of increased non-suspended masses on the driving safety is

analyzed in depth in chapter 5.4, the analysis is focused here on the performance of the systems regarding ride-comfort. The force-speed diagrams of the traditional passive, the semi-active and the active¹² suspension systems are presented in figure 5.12 [RNW10].

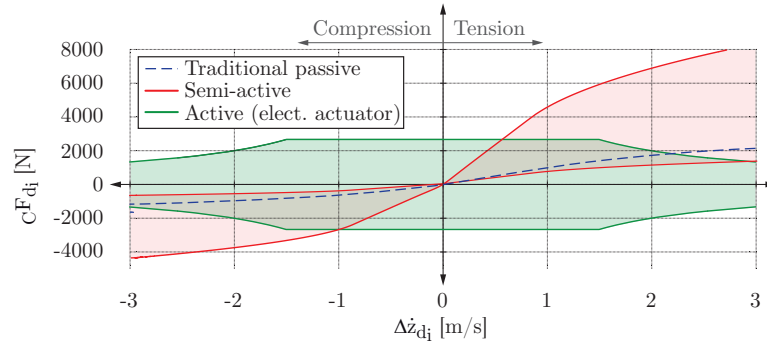


Figure 5.12.: Force-speed diagrams for the traditional passive, semi-active and active (only the curve corresponding to the electric actuator is presented) shock absorbers [RNW10].

To analyze different working conditions, the additional increased non-suspended mass Δm_{w_i} was varied simultaneously for all wheels in a range between 0 kg and 40 kg and the longitudinal vehicle speed $v\dot{x}$ was changed between 10 km/h and 110 km/h. For each value of the additional non-suspended mass, the vehicle with the traditional passive system consisting in a suspension spring and a passive shock absorber (see chapter 2.7) is taken as reference configuration. Straight ahead maneuvers driving over three different excitation signals were simulated: a deterministic signal (like that presented in figure 2.20), a stochastic signal corresponding to a road type C (see chapter 2.6.2) and a sinusoidal harmonic signal whose frequency f_{harm} was varied between 0.8 Hz and 20 Hz (see [RNW10] for the definition of this excitation). The relative change in the considered assessment criterium AC (see sections 5.1.1 and 5.1.2) for each excitation condition is calculated according to

$$\Delta AC = \frac{AC_{ref} - AC_{comp}}{AC_{ref}} \cdot 100 \% , \quad (5.29)$$

where AC_{ref} correspond to value of the assessment criterium for the reference configuration and AC_{comp} to the corresponding value for the configuration being compared. Positive values of ΔAC correspond to an improvement of the considered assessment criterium and negative ones to a worsening. Figure 5.13 presents the simulation results.

¹²Regarding the active suspension system, only the part corresponding to the electric actuator is presented in figure 5.12.

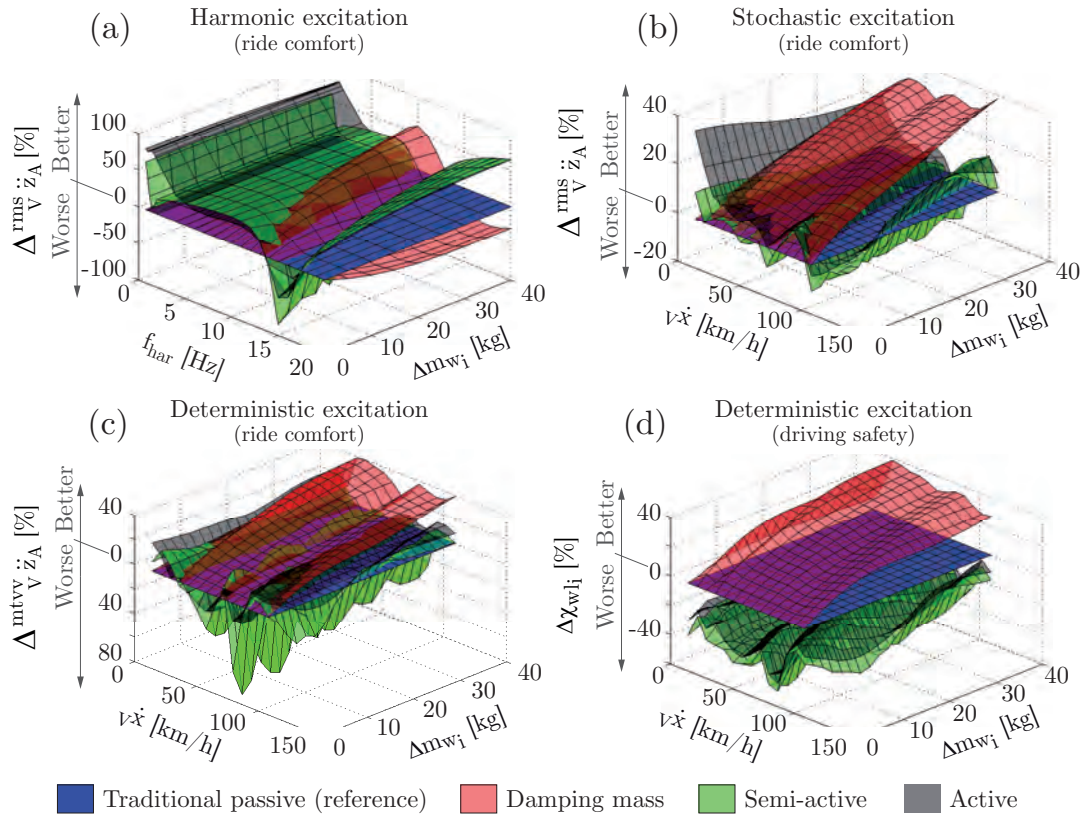


Figure 5.13.: Performance comparison for the different suspension systems considered as a function of the longitudinal driving speed v_x and for different additional non-suspended masses Δm_{w_i} while driving straight ahead over different excitation signals. Ride comfort change for sinusoidal harmonic excitation (a), ride comfort change for stochastic excitation road type C (b), ride comfort and driving safety change for deterministic excitation (see also [RNW10]).

Figure 5.13-a shows the *root mean square* ${}^{rms} \ddot{z}_A$ of the weighted vertical acceleration at the rails of the driver's seat for the sinusoidal harmonic excitation. It can be seen that in frequency ranges close to the natural frequency of the non-suspended mass (i.e. 10 Hz), the damping mass concept performs much better than the other suspension types. The reason why the controlled damping systems do not give satisfying results in this area can be found in the control algorithm itself. Both control strategies (semi-active and active) are designed to enhance vehicle comfort near the natural frequency of the suspended mass (i.e. 1 Hz) and in the region of the natural frequency of the internal organs, i.e. approximately between 4 Hz and 10 Hz (see also [HEG11] and [Kna10]). Outside this objective region, the control algorithm shows a worse performance than the reference

configuration.

The *root mean square* ${}^{rms}_V\ddot{z}_A$ of the weighted vertical acceleration at the rails of the driver's seat for the stochastic road excitation of type C (see chapter 2.6.2) is shown in figure 5.13-b. The active electric suspension system can improve the ride comfort behavior significantly in a wide speed range. Only at a small area by high speeds ($v\dot{x} > 70$ km/h) the traditional passive suspension system performs better compared to the active electric one. The semi-active system shows a similar behavior than that of the active concept except at low speeds, where the ${}^{rms}_V\ddot{z}_A(t)$ values for the semi-active system are up to 20 % higher. However, the damping mass concept shows the best performance in the entire analyzed region. This can be explained as follows: As shown in figure 5.13, the higher the non-suspended mass the greater the advantages of damping mass concept to enhance the ride comfort in comparison with the reference configuration. Additionally the frequency range in which the damping mass concept performs better than the reference configuration becomes wider by increasing the non-suspended mass. This result in an overall better behavior (at least regarding ride comfort) when the system is excited by broadband signals like the stochastic one presented in figure 5.13-b or the deterministic one presented in figures 5.13-c and -d.

The results for the deterministic excitation are presented in figure 5.13. The *maximum transient vibration value* ${}^{mtvv}_V\ddot{z}_A$ of the weighted vertical acceleration at the rails of the driver's seat is shown in figure 5.13-c and the wheel load factor in figure 5.13-d. This abruptly road impact represents the worst scenario for the controlled suspension systems. Due to the limitations of the system dynamics a phase delay between the actuator reference signal and the actual system response is caused. As consequence the performance of the controlled systems is highly sensitive to the vehicle speed. The ${}^{mtvv}_V\ddot{z}_A$ values presented in figure 5.13-c for the controlled suspension systems indicate a worsening (up to ≈ -80 %) of the ride comfort in the entire analyzed range with only few combinations of longitudinal speed and additional non-suspended mass for which a better performance (up to ≈ 20 % mainly for low speeds) can be achieved. Considering the driving safety criterium (wheel load factor χ_{wli}), the controlled systems cannot offer the performance of the traditional passive system. The reason therefor lies again in the comfort control law used (see chapters 5.3.2 and 5.3.3). On the other hand, the driving safety criterium can be improved significantly with the damping mass concept. The higher the non-suspended masses, the better the mentioned concept works and the greater the differences with the other suspension systems. As mentioned before, the driving safety of vehicles with in-wheel motors is analyzed in depth in chapter 5.4.

5.4. Driving safety enhancement of vehicles with in-wheel motors through torque vectoring

As mentioned before, in-wheel motors increase the non-suspended masses tending to lead to higher accelerations of the suspended mass and stronger fluctuations of the contact force between tire and ground while driving on uneven roads. The higher accelerations of the suspended mass tend to reduce the ride comfort and the stronger fluctuations of the contact force between tire and ground tend to worsen the driving safety (see sections 5.1.3, 5.2 and 5.3.4 as well as e.g. [RND11] and [MW04]).

The reduction of the transmittable horizontal tire forces as result of the stronger vertical wheel movements can destabilize the vehicle in extreme situations. Driving on a curve with a sinusoidal vertical perturbation exciting the natural frequency of the suspended mass is an example of such a situation [Müh93]. In this situation, the vehicle can become uncontrollable for a *normal* driver and constitutes a greater hazard potential as when driving or braking on an stochastically uneven road.

In the following sections, the potential of the torque vectoring system with in-wheel motors presented in chapter 4.2 to attenuate the mentioned hazard on a driving safety relevant maneuver by stabilizing the vehicle is analyzed (see also [RND11]). In the first section, the maneuver and the simulation conditions are described. Afterwards, some criteria to assess the driving safety under the described conditions are proposed. Finally, the results are presented and discussed.

5.4.1. Maneuver definition

To analyze the influence of the increased non-suspended masses related with the in-wheel motors on the vehicle lateral dynamics, an open-loop maneuver consisting in driving over a sinusoidal perturbation in a curve with constant longitudinal speed $v\dot{x}$ and constant steering wheel angle δ_{st} , as presented schematically in figure 5.14, is simulated.

As shown in table 5.3, the perturbation height was set to 25 mm. Two different wave lengths exciting the natural frequency of the suspended and the non-suspended masses (i.e. approximately 1 Hz and 10 Hz respectively) while driving with the mean value of the considered vehicle longitudinal speeds (i.e. $v\dot{x} = 80$ km/h) were simulated. The steering wheel angle δ_{st} is adjusted depending on the currently simulated longitudinal

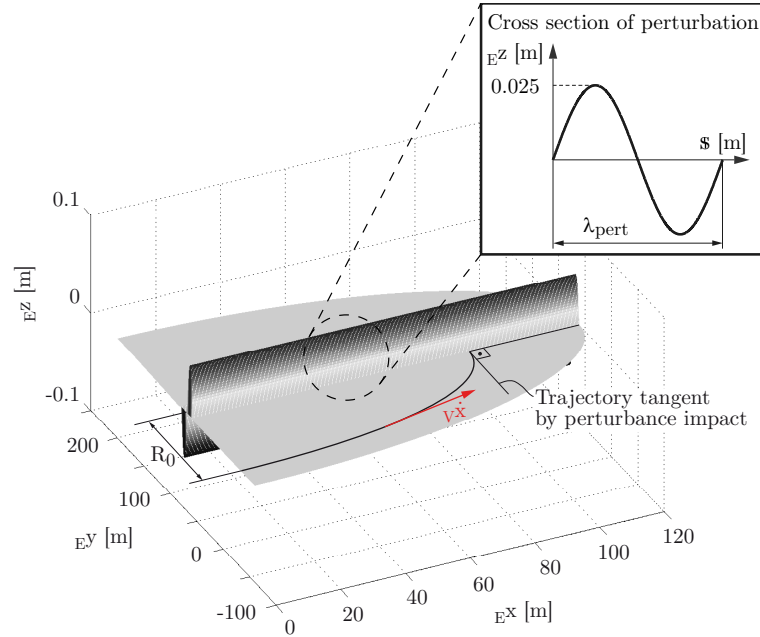


Figure 5.14.: Schematic representation of the driving maneuver and the road used to analyze the behavior of vehicles with in-wheel motors and torque vectoring system in driving safety relevant situations [RND11]. The variable s corresponds to the driven distance.

vehicle speed $v \dot{x}$ to reach a steady state value of the lateral acceleration of $v \ddot{y} \approx 7 \text{m/s}^2$ (see chapter 4.2.1). This value corresponds to approximately 95 % of the maximum achievable lateral acceleration. The initial position, characterized by R_0 in figure 5.14, was adjusted to guarantee that the vehicle reaches the perturbation in a perpendicular way. It must be mentioned, that the vehicle impacted the perturbation after having reached the steady state. Finally, the non-suspended masses were varied simultaneously at all wheels according to the values shown in table 5.3. The simulated maneuvers are characterized by the combination of all parameters presented in this table. Furthermore, in order to determine the potentials and limitations of the presented torque vectoring system (see chapter 4.2), each maneuver was simulated with and without torque vectoring system.

As in chapter 4, a vehicle belonging to the subcompact vehicle class (see chapter 3.7.1 with a four-wheel drive powertrain architecture (see figure 3.16 in chapter 3.7.2) and synchronous electric motors (see power and torque characteristics in table 3.11) is used as basis for the simulations.

5.4. Driving safety enhancement of vehicles with in-wheel motors through torque vectoring

Table 5.3.: Simulation conditions used to analyze the influence of increased non-suspended masses on the lateral dynamics of vehicles with in-wheel motors and torque vectoring.

Parameter	Symbol	Values	Units
Lateral acceleration	${}_v\ddot{y}$	7	[m/s ²]
Longitudinal vehicle speed	${}_v\dot{x}$	65, 80, 95	[km/h]
Additional non-suspended mass per wheel	Δm_{w_i}	0, 20, 40	[kg]
Wave length of the sinusoidal perturbation ^a	λ_{pert}	${}_v\dot{x}/1$ Hz, ${}_v\dot{x}/10$ Hz	[m]

^a Mean value of the analyzed longitudinal vehicle speeds: ${}_v\dot{x} = 22.2$ m/s (80 km/h)

5.4.2. Alternative driving safety assessment criteria

The influence of increased non-suspended masses on the driving safety while driving on roads with perturbations has not been extensively analyzed in the literature. Therefore, there are not standardized or widely used assessment criteria to evaluate the driving safety under these conditions. Beside the traditional criteria corresponding to the vertical wheel movement ${}_{Ez}z_{C_i}$ and the wheel load factor χ_{wl_i} proposed to evaluate the driving safety under *not so critical* driving situations (as presented in chapter 5.1), three alternative methods are presented in this chapter to assess the driving safety in critical driving situations (see also [RND11] and [Müh93]).

Sideslip angle difference

Since the sideslip angle β is an important magnitude used by drivers to perceive the driving behavior (see e.g. [MW04]), the side slip angle difference

$$\Delta\beta_{ref} = \max \left(\frac{|\beta(t) - \beta_{ref}(t)|}{|\beta_{ref}(t)|} \right) \cdot 100 \% \quad (5.30)$$

is proposed to assess the driving safety of the vehicle after the disturbance occurs. In equation 5.30, $\beta(t)$ indicates the actual value of the side slip angle and $\beta_{ref}(t)$ the corresponding value without disturbance. Due to the fact that the maneuver defined in section 5.4.1 corresponds to a stationary one and since the disturbance occurs after the steady state has been reached, the reference value $\beta_{ref}(t)$ of the sideslip angle can be replaced by its steady state value β^S (see chapter 4.2.1 for the determination of the

steady state values), i.e. $\beta_{ref}(t) = \beta^S$. Furthermore, the higher the side slip angle difference, $\Delta\beta_{ref}$ the worse the driving safety.

Deviation from the reference trajectory

The deviation from the reference trajectory is commonly used in the literature as criterion for the driving safety assessment (see e.g. [FMH⁺01] and [RND11]). Taking into account that the reaction time of the driver is about 1 s (see e.g. [ZBR97a], [ZBR97b] and [MW04]), the deviation of the vehicle's center of gravity from the reference trajectory one second after the disturbance occurs is proposed as assessment criteria for the driving safety as follows (see also [RND11]):

$$\Delta y_{1s} = \Delta_{E\mathbf{r}_{CG, ref}} \cdot \mathbf{n}_{traj} = (E\mathbf{r}_{CG} - E\mathbf{r}_{CG, ref}) \cdot \mathbf{n}_{traj}, \quad (5.31)$$

where $E\mathbf{r}_{CG}$ and $E\mathbf{r}_{CG, ref}$ are the position vectors of the vehicle's center of gravity in the earth-fixed axis system (see chapter 2.2) without (reference trajectory) and with disturbance (actual trajectory) respectively. Additionally, as can be seen in figure 5.15, \mathbf{n}_{traj} represents the unit vector perpendicular to the tangent to the reference trajectory.

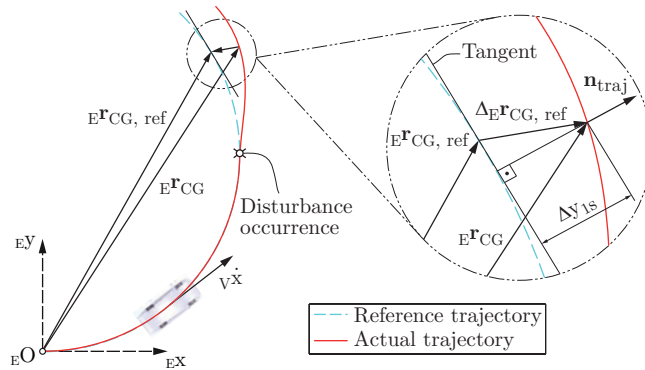


Figure 5.15.: Schematic representation for determining the deviation from the reference trajectory.

As stated by *Niederkofler* [Nie11], the acceptable limits for the deviation from the reference trajectory Δy_{1s} depend mainly on the traffic lane width. Taking into account the vehicle track (see also table B.1 in appendix B) and the design parameters of modern roads (see e.g. [Nat03]), allowable values of Δy_{1s} oscillate between 0.25 m and 1.25 m. Assuming that the maneuver defined in chapter 5.4.1 can occur mainly on highways and cross-country roads, $\Delta y_{1s} = 0.5$ m is taken as acceptable limit in this work.

Yaw acceleration characteristic value

The yaw reaction of a vehicle as a result of driver inputs (e.g. steering wheel angle δ_{st}) or actuator interventions (like those introduced by a torque vectoring system - see chapter 4 - or a single wheel steering system - see [Nie11]) constitutes an important criterium to assess the vehicle lateral dynamics (see also [Ros09]). Based on this fact and in order to evaluate the vehicle's reaction during driving safety relevant maneuvers while cornering (like that presented in chapter 5.4.1), the *yaw acceleration characteristic value*, introduced by *Otto* [Ott87] in 1987, has been successfully used [RND11] (see figure 5.16).

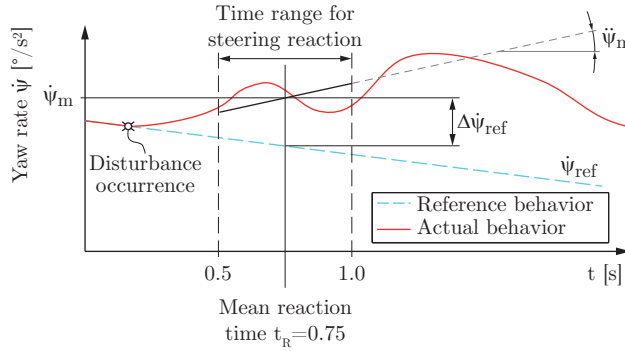


Figure 5.16.: Schematic representation for determining the yaw acceleration characteristic value.

Based on test drives, he established, that the magnitude of the steering reaction of a *normal* driver after the occurrence of a disturbance during a driving safety relevant maneuver while cornering mainly depends on two variables: on the one hand, it depends on the mean value of the yaw acceleration $\ddot{\psi}_m$ calculated within the reaction time range between 0.5 s and 1.0 s. On the other hand, the magnitude of the steering reaction depends on the yaw rate difference given by

$$\Delta\dot{\psi}_{ref} = \dot{\psi}_m - \dot{\psi}_{ref} , \quad (5.32)$$

where $\dot{\psi}_m$ correspond to mean value of the actual yaw rate calculated within the mentioned reaction time range and $\dot{\psi}_{ref}$ indicates the reference value of the yaw rate without disturbance. Due to the fact that the maneuver defined in section 5.4.1 corresponds to a stationary one and since the disturbance occurs after the steady state has been reached, the reference value $\dot{\psi}_{ref}$ of the sideslip angle can be replaced by its steady state value

$\dot{\psi}^S$ (see chapter 4.2.1 for the determination of the steady state values), i.e. $\dot{\psi}_{ref} = \dot{\psi}^S$. Based on this observations, *Otto* proposed the *yaw acceleration characteristic value* as follows:

$$Q_{\dot{\psi},ch} = \left| \frac{\Delta\dot{\psi}_{ref}}{t_R} + \ddot{\psi}_m \right|, \quad (5.33)$$

where $t_R = 0.75$ s corresponds to the mean reaction time. According to the results presented by *Otto* [Ott87], a driving situation in a curve can be managed by a *normal* driver if $Q_{\dot{\psi},ch} \leq 5$ °/s².

5.4.3. Results

The simulation results corresponding to the wave length of $\lambda_{pert} = 22.2$ m (excitation of the natural frequency of the suspended mass) and to the wave length of $\lambda_{pert} = 2.2$ m (excitation of the natural frequency of the non-suspended masses) are presented in figure 5.17-a and -b respectively. The wheel load factor $\chi_{wl_{rl}}$ of the curve inner wheel of the rear axle (rear left for which the rear subscript *rl* is used), the sideslip angle difference $\Delta\beta_{ref}$, the deviation from the reference trajectory Δy_{1s} and the yaw acceleration characteristic value $Q_{\dot{\psi},ch}$ are presented for both analyzed conditions, i.e. with and without torque vectoring system - TVS - (see sections 5.4.1 and 5.4.2).

Suitability of the proposed assessment criteria to identify driving safety critical situations

Based on the simulation results, there are two aspects that must be analyzed before the effect of the individual varied parameters is discussed. On the one hand, it must be determined whether the considered maneuver can be considered as critical for the driving safety. On the other hand, the suitability of the proposed assessment criteria to identify and evaluate the driving safety in such critical situations has to be analyzed. To address this issues, the results of the vehicle without torque vectoring system are analyzed.

By observing the results of the vehicle without torque vectoring system in figure 5.17-a, it can be noticed that perturbations exciting the natural frequency of the suspended mass produce strong yaw reactions resulting in high yaw acceleration characteristic values $Q_{\dot{\psi},ch}$ [°/s²]. The safety limit of 5 °/s² is exceeded by the considered vehicle

5.4. Driving safety enhancement of vehicles with in-wheel motors through torque vectoring

without torque vectoring system in the entire analyzed variation region. In contrast, this excitation produces only small fluctuations in the vertical contact force between tire and road leading to a better transmittability of horizontal tire forces (e.g. correcting forces applied by the torque vectoring system) and to a small load factor $\chi_{wl_{rl}}$. The lateral deviation from the reference trajectory Δy_{1s} varies between 2 cm and 3 cm and can be classified as non critical. The maximum sideslip angle difference adopts a more or less constant value of $\Delta\beta_{ref} = 30\%$.

As can be seen in figure 5.17-b, exciting the natural frequency of the non-suspended masses results in strong fluctuations of the vertical contact force between tire and ground. Therefore, the related assessment criterium, i.e. the wheel load factor $\chi_{wl_{rl}}$, adopts values that are approximately the double of those corresponding to the long wave excitation analyzed in the preceding paragraph. A deviation from the reference trajectory of approximately $\Delta y_{1s} = 0.65$ m results because of the high lateral acceleration (${}_V\ddot{y} = 7$ m/s²) and the mentioned stronger fluctuations in the vertical contact force between tire and ground. Since this value corresponds to near half of the vehicle's track (see vehicle parameters in table B.1 in appendix B), the situation can be classified as very critical. Moreover, while the yaw acceleration characteristic value $Q_{\dot{\psi},ch}$ is smaller as for the long wave excitation analyzed before, the sideslip angle difference $\Delta\beta_{ref}$ remains almost unchanged.

It can be concluded, that driving in a curve over a perturbation exciting the natural frequency of both the suspended and the non-suspended masses results in a safety critical situation. Furthermore, several assessment criteria must be considered to evaluate the driving safety in such situations. Based on the simulation results, the yaw acceleration characteristic value $Q_{\dot{\psi},ch}$ can be recommended to assess the driving safety while driving over perturbations exciting the natural frequency of the suspended mass. In the case of perturbations exciting the natural frequency of the non-suspended masses, the wheel load factor $\chi_{wl_{rl}}$ and the deviation from the reference trajectory Δy_{1s} lead to a better assessment. Finally, it was not possible to identify the safety critical situations based on the proposed sideslip angle difference $\Delta\beta_{ref}$.

Influence of the increased non-suspended mass

Considering the vehicle without torque vectoring system, the results reproduced the negative influence of increased non-suspended masses on the driving safety. Additional

non-suspended masses of $\Delta m_{w_i} = 40$ kg at each wheel increase the considered criteria between 40 % and 50 %.

Influence of the perturbation's wave length

Since the vehicle reactions concerning the vehicle lateral dynamics take place in a frequency range between 0 Hz and 2 Hz (see e.g. [MW04]), perturbations in a curve exciting the system *vehicle* in this range produce strong yaw reactions. As mentioned before, the yaw acceleration characteristic value $Q_{\psi, ch}$ can be used to identify these kind of critical safety situations. These results agree with those presented in the literature (see e.g. [Müh93] and [MW04]). Perturbations exciting the natural frequency of the non-suspended masses has a little influence on the yaw reaction of the vehicle but lead to big fluctuations in the vertical contact force between tire and ground and therefore to large deviations from the reference trajectory Δy_{1s} .

Influence of the longitudinal vehicle speed

The frequency of the excitation varies with the longitudinal vehicle speed. Since the gradient of the transfer function $G_{z_w/z_{road}}(\omega)$ (relating the vertical wheel movement and the vertical road excitation - see appendix E.2) in the proximity of the natural frequency of the suspended mass is relatively small, only a weak influence of the excitation frequency in this region and therefore of the longitudinal vehicle speed can be noticed. In contrast, the longitudinal vehicle speed has a stronger influence on the considered assessment criteria when driving over a perturbation exciting the natural frequency of the non-suspended masses because of the greater gradient of the mentioned transfer function in this region.

Suitability of the torque vectoring system to enhance the driving safety in critical situations

The frequency of the considered perturbation has a strong influence on the effectiveness of the torque vectoring system presented in chapter 4.2. For perturbations exciting the natural frequency of the suspended mass it is possible to reduce the value of the considered assessment criteria and therefore increase the driving safety. In contrast,

5.4. Driving safety enhancement of vehicles with in-wheel motors through torque vectoring

the torque vectoring system seems to have only a small effect when considering the perturbation exciting the natural frequency of the non-suspended masses. This can be explained since strong fluctuations of the vertical contact force between tire and ground reduce the transmittable horizontal tire forces and therefore also reduce the potential of the torque vectoring system to correct the vehicle reactions introduced by the perturbation. Furthermore, the better performance of the torque vectoring system with increasing non-suspended masses in the region near the natural frequency of the suspended mass (figure 5.17-a) measured in terms of the yaw acceleration characteristic value $Q_{\dot{\psi},ch}$ can be explained based on the fact that the influence of the suspended mass m_A over the non-suspended mass m_{w_i} decreases as m_{w_i} increases.

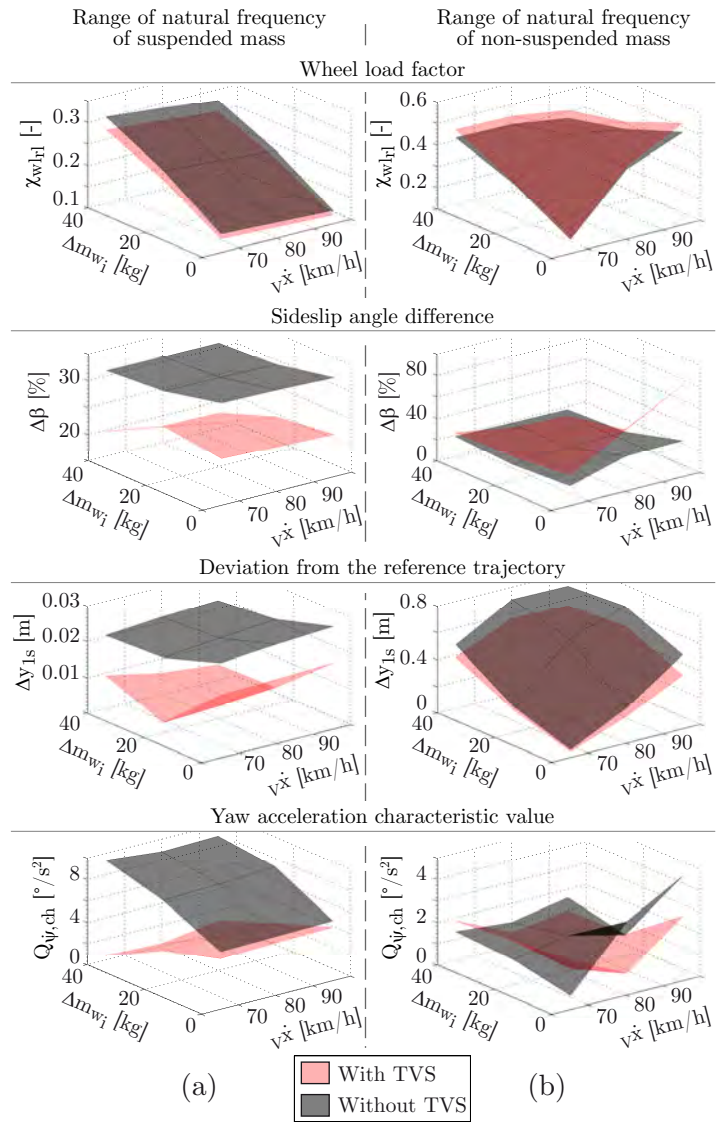


Figure 5.17.: Simulation results corresponding to the maneuver driving in a left curve over a sinusoidal perturbation with a wave length of $\lambda_{pert} = 22.2$ m (a) or $\lambda_{pert} = 2.2$ m (b). *TVS* stands for *Torque Vectoring System*. The wheel load factor is determined at the curve inner wheel, i.e. the rear left one (right subscript *rl*).

Summary chapter 5: Vertical dynamics The influence of the increased non-suspended masses on the ride comfort and driving safety of vehicles with in-wheel motors was analyzed. Therefore, the traditional objective assessment criteria was presented in the first part of the chapter. For the assessment of the ride comfort, criteria based on the frequency weighted acceleration, like the *root mean square* (for harmonic and stochastic excitation signals without shocks) and the *maximum transient vibration value* (for excitation signals with shocks), were used. The vertical wheel movement and the *wheel load factor* were taken as traditional assessment criteria to evaluate the driving safety. The so-called *conflict diagram* relating these criteria was taken as basis to exemplify the trade-off between ride comfort and driving safety. As a reference point, the comfort bands proposed in the international standard ISO 2631-1:1997(E) [fSI97] were introduced in this diagram. Based on this, it was shown, that ride comfort and driving safety can be improved only within a certain region (called *optimal region*) by changing the properties of a traditional passive suspension system. Furthermore, this diagram was used afterwards to analyze the influence of the increased non-suspended masses. The results showed that, according to the considered evaluation criteria, the lower the relation m_{A_q}/m_{w_i} (i.e. for lower vehicle segments), the stronger is the effect of the increased non-suspended masses on ride comfort and driving safety. Nevertheless, the *optimal region* of the considered vehicles (belonging to three different vehicle segments) remains within the same comfort band when considering the additional non-suspended masses introduced into the system by the electric motors determined in chapter 3 (see table 3.11). Based on the assumption that the effect of the increased non-suspended masses on ride comfort is acceptable if the optimal region remains in the same comfort band, it can be concluded, that the considered increased non-suspended masses, as corresponding to the performance requirements taken into account (see chapter 3.7.4), lead to an acceptable reduction in ride comfort for the analyzed vehicle segments.

In the second part of this chapter, the results of test drives carried out on a road consisting in an excitation signal with shocks (curb and pothole) with the aim to determine the subjective perception of *normal drivers* and *experienced test drivers* were presented. A total of 34 test persons were asked to drive with a modified test vehicle with a special device designed to increase the non-suspended masses at the rear axle from 40 kg up to 80 kg. Different longitudinal speeds, tire inflation pressures and vehicle load conditions were used. The results show that increased non-suspended masses tend to worsen the subjective ride comfort perception. Furthermore, while the longitudinal vehicle speed as well as additional load mass do not clearly affect the subjective ride comfort perception,

the increased tire inflation pressure strongly worsens it.

With the objective to establish a relation between the subjective ride comfort perception and the presented traditional objective assessment criteria, the conditions used for the test drives were simulated with the model presented in chapter 2. Based on this and since the small differences between the considered conditions were hardly perceived by the *normal drivers*, only the answers of the *experienced test drivers* were taken into account for this analysis. This is a common praxis used to reduce the uncertainty and noise introduced by *normal drivers*, for which small comfort differences are difficult to objectify (see e.g. [Len09]). The obtained results agree with those presented recently in the literature and can be summarized as follows:

- The tendency of the qualitative answers of the *experienced test drivers* can be depicted with accuracy with the help of the presented vehicle model. The subjective ride comfort perception can be therefore estimated with the objective assessment criteria calculated based on the simulation results obtained with it.
- The effect of increased non-suspended masses on the subjective perception of ride comfort and on the related objective evaluation criteria depends on the driving speed and is not always negative. Furthermore, a wide variation range of the analyzed variables (e.g. increased non-suspended mass m_{w_i} or longitudinal vehicle speed $v\dot{x}$) must be considered in order to increase the validity of the analysis.
- Under the considered conditions, no remarkable differences in the ride comfort subjective perception with and without increased non-suspended masses can be expected. Nevertheless, there is room for improvement.

Additionally, an approach based on the tire inflation pressure as a more "*intuitive*" variable producing similar effects on the subjective ride comfort perception as increased non-suspended masses was presented.

In the third part of the chapter, the potentials and limitations of two alternative passive suspension systems (eccentric concept and damping mass concept), a semi-active system and an active system to improve ride comfort and driving safety of vehicles with in-wheel motors were analyzed and compared with a conventional passive suspension system (reference) from a theoretical point of view. Using the validated vehicle model it was possible to analyze their performance regarding ride comfort and driving safety improvement under the consideration of different wheel masses, driving speeds

5.4. Driving safety enhancement of vehicles with in-wheel motors through torque vectoring

and excitation signals. Both alternative passive concepts analyzed present advantages regarding the considered assessment criteria for all considered conditions. Nevertheless, their design is associated with other problems like packaging, complex design or suitability for a wide range of axle systems (e.g. steered axles). Moreover, under the considered conditions, the damping mass concept showed improvements both in ride comfort and driving safety up to 40 % in comparison with the reference passive system. Greater improvements in ride comfort and driving safety were noticed with larger damping masses. The analyzed mechatronic systems present advantages in ride comfort (up to 10 %) mainly for low speeds. It was shown that, in general, the performance in ride comfort and driving safety of the active system is better than that of the semi-active system. Finally, it must be noticed, that from the systems analyzed, only the damping mass concept showed improvements in ride comfort and driving safety over the entire speed range, for all values of the non-suspended masses taken into account and for all considered excitations. Based on this and on the fact that this suspension system does not need external energy supply, it can be seen as the most interesting alternative to cope with the problems induced by the increased non-suspended masses related with in-wheel motors if the related challenges regarding package can be solved.

In the last part of the chapter, the effect of increased non-suspended masses on the driving safety of vehicles with in-wheel motors in realistic maneuvers was analyzed. Therefore, an open-loop maneuver representing a driving situation in a curve with different constant longitudinal speeds producing a lateral acceleration of 7 m/s^2 (about 95 % of the maximum achievable value) was simulated. Two different sinusoidal perturbations with a height of 25 mm and wavelengths adjusted to excite the natural frequency of the suspended and the non-suspended mass were used. To analyze the potentials and limitations of the *torque vectoring system* presented in chapter 4.2 to enhance the driving safety of vehicles with in-wheel motors, all scenarios were simulated with and without it.

While the traditional assessment criteria presented in section 5.1 are suited to carry out fundamental analysis, the investigation of the driving maneuver described in section 5.4.1 constitutes a more representative scenario to draw detailed conclusions about the influence of increased non-suspended masses on the driving safety of vehicles with in-wheel motors (as also presented recently in the literature). Furthermore, since the influence of increased non-suspended masses on the driving safety while driving on roads with perturbations has not been extensively analyzed in the literature, there are no standardized or widely used assessment criteria related. Therefore, four criteria were

proposed to assess the driving safety in such scenarios: the traditional *wheel load factor*, the *sideslip angle difference*, the *deviation from the reference trajectory* and the *yaw acceleration characteristic value*. Based on the results, following conclusions can be drawn:

- For both considered perturbations, the results showed that increased non-suspended masses negatively influence the driving safety. Doubling the non-suspended masses from 40 kg to 80 kg results in 40 % to 50 % higher values of the proposed assessment criteria.
- Several criteria must be considered to properly assess the vehicle driving safety in realistic scenarios.
- The *yaw acceleration characteristic value* can be used as basis to assess the driving safety while driving over perturbations exciting the natural frequency of the suspended mass. This kind of excitation results in strong yaw reactions that can be difficult to control for a *normal* driver.
- Perturbations exciting the natural frequency of the non-suspended masses lead to big fluctuations of the vertical contact force between tire and ground. Big lateral displacements result as a consequence. The *wheel load factor* or the *deviation from the reference trajectory* can be used to assess the driving safety in such cases.
- Variations of the excitation frequency (as a consequence of changes of the longitudinal speed or the wavelength) near the natural frequency of the non-suspended masses produce stronger effects on the driving safety as variations near the natural frequency of the suspended mass.
- The presented torque vectoring system helps to enhance the driving safety of vehicles with increased non-suspended masses in the entire considered variation range.

6. Mechanical component integration

The integration of the electric motor, a possibly needed gearbox, the brake system and the suspension control arms within the wheel has not been sufficiently analyzed and documented in the scientific literature and still represents one of the major open questions related with in-wheel motors. An innovative approach for the mechanical integration of in-wheel motors in several common single wheel suspension systems (e.g. McPherson, double wishbone, multi-link, control blade) is presented in this chapter (see also [RNA11b], [RNA11a] and [RN11]). It represents a synthesis process to be used for the design of single wheel suspension systems and particularly of suspension systems for vehicles with in-wheel motors.

The developed algorithm is based on a co-simulation between MATLAB® and CATIA V5®. MATLAB® is used as master for the control of the entire optimization process and for the interaction with the user. The suspension system kinematics is depicted using the kinematics module of CATIA V5®. The starting point of the entire process is a simplified CAD-model of the suspension system in which the in-wheel motor is to be integrated (reference). The behavior of the desired characteristic suspension parameters is determined in the first step. Afterwards simplified geometries representing the in-wheel motor are added to the CAD-model. At this stage, first collision problems can be visually identified. The next step corresponds to a fully automated optimization routine aiming to find the position of the suspension hardpoints for which the behavior of the characteristic suspension parameters (e.g. camber, toe, roll center position, scrub radius) remains as close as possible to that of the reference suspension system. This reduces the influence on the vehicle's driving behavior and on comfort aspects related with the suspension system. At the same time, collisions between the components are detected and avoided during the suspension movement (bound/rebound and steering) controlled by the algorithm. Two optimization algorithms were used and analyzed: the Nelder-Mead simplex algorithm (see [RN11] for an application example and also [NM65] for the principles of the Nelder-Mead simplex algorithm) and genetic algorithms (see

[RNA11a] and [RNA11b]). Since each step during the optimization can be visualized in CATIA V5®, the user can track the development of the entire process and has therefore total control over it.

6.1. Suspension characterization process and previous definitions

The driving behavior and comfort of a vehicle is strongly influenced by the performance of its suspension system (see e.g. [MW04]). It is therefore important to characterize it even in an early vehicle development phase. Generally speaking, this characterization process corresponds to the description of the three-dimensional wheel movement during bound/rebound and steering, and comprises the so-called suspension kinematics and the compliance analysis (see e.g. [Mat08]). While all suspension elements are considered as rigid bodies in the suspension kinematics analysis, elastic deformations due to the forces acting on the system are taken into account in the compliance analysis. Anyway, both cases are related with the behavior of the characteristic suspension parameters - CSP - (e.g. camber, toe and caster angle - see also [RSB01]) during bound/rebound and steering. In this work, all components of the considered suspension systems are assumed as rigid bodies (suspension arms and tire) and therefore only kinematics analysis are performed.

In a simplified way, a suspension system can be seen as a spatial mechanism composed of closed loops of bodies - suspension arms - connecting the wheel carrier to the suspended mass (or to the steering system) and transmitting the tire forces and torques to it. The effect of the transmitted forces on the suspended mass movement and therefore on the driving behavior and vehicle comfort depends on the spatial distribution of the suspension arms and on their relative movement during bound/rebound and/or steering. The points joining the suspension arms with the wheel carrier and suspended mass are called *hardpoints* and determine the suspension kinematics. The relationship between them and the suspension characteristic parameters is highly nonlinear and one hardpoint generally influences more than one parameter. Traditionally, positioning the hardpoints to obtain certain behavior of the suspension parameters is a "manual" task done by experienced suspension engineers. Furthermore, few automated approaches can be found in the literature (see e.g. [RN11], [RNA11a], [RNA11b], [NHuRH09], [AKH⁺02], [USSS02] and [SHK09]).

6.2. Suspension Kinematics Optimization System - KOS

In-wheel motors are not only related with increased non-suspended masses affecting ride comfort and driving safety (see chapter 5) but also with a complicated component integration within the rim, in which there is limited space anyway. The single wheel suspension systems used nowadays in passenger vehicles of the middle and upper classes (but also increasingly in compact vehicles) must be modified in order to integrate the electric motor and a possibly needed gearbox (see e.g. table 3.9 in chapter 3.7.6) within the rim. In this chapter, the Suspension **K**inematics **O**ptimization **S**ystem - KOS -, a novel automated approach developed in the context of the present research project to integrate the mentioned components in several kinds of (existing and future) single wheel suspension systems, is introduced (further details about KOS can be found in [Apo10]). The component integration shall fulfill two constraints:

- The characteristic suspension parameters - CSPs - shall meet a given target behavior in bound/rebound and during the steering motion. This target behavior is adjusted during the vehicle's early development phase to obtain a desired handling performance and certain comfort characteristics. Therefore, if the in-wheel motor is going to be integrated in an existing suspension system, the effects on the behavior of the characteristic kinematic parameters of the suspension should be minimized.
- Collisions between the different suspension elements (suspension control arms, electric motor, possibly needed gearbox, etc.) must be avoided.

The approach presented in this chapter corresponds to a synthesis process and is based, as mentioned before, on a co-simulation between MATLAB® and CATIA V5®. MATLAB® serves as master for the control of the entire optimization process and for the interaction with the user through a GUI¹. CATIA V5® is used to represent the suspension system kinematics [Böh10] and to depict the suspension components as volumes (for example, to detect collisions) [Apo10]. Further, since each step during the optimization cycle can be visualized in CATIA V5®, the user can track the development of the entire process and has therefore total control over it. Due to the fact that this approach combines typical core competencies of the design and the simulation departments, it can be seen as an interface between them.

¹Graphical User Interface

In the presented approach, the analysis and optimization of suspension systems can be done based on the twelve characteristic suspension parameters presented in table 6.1 (see for example [RSB01] for the definition of the different parameters and [Apo10] for the determination methods used in the presented Suspension Kinematics Optimization System - KOS).

Table 6.1.: Suspension parameters that can be used for the synthesis of suspension systems in the presented approach.

Parameter	Symbol	Parameter	Symbol
Camber angle	$^{susp}\gamma$	Roll center height ^{a,c}	$^{susp}z_{RC}$
Toe angle	$^{susp}\delta$	Roll center transversal position ^{b,c}	$^{susp}y_{RC}$
Caster angle	$^{susp}\tau$	Track change ^{c,d}	$^{susp}\Delta s_{f/r}$
Kingpin inclination	$^{susp}\sigma$	Wheel base alteration	$^{susp}\Delta L$
Scrub radius	$^{susp}r_{\sigma}$	Anti-dive angle	$^{susp}\varepsilon$
Caster offset	$^{susp}r_{\tau}$	Anti-squat angle	$^{susp}\kappa$

^a Measured from the ground.

^b Measured from the vertical symmetric plane of the vehicle.

^c Behavior can be determined for a parallel or a nonparallel vertical movement of the wheels belonging to the same axle as well as for the steering movement.

^d The right subscript f/r is used to refer either to the front axle - f - or to the rear one - r -.

Figure 6.1 shows the flow diagram of the presented Suspension Kinematics Optimization System. The starting point is either a simplified CAD-model² of the suspension system in which the in-wheel motor is to be integrated (see figure 6.2) or the target behavior of the suspension characteristic parameters. If the first option is chosen, then the target behavior of the suspension characteristic parameters can be determined in the first module "reference values". In the module "suspension system to be optimized", simplified geometries corresponding to the in-wheel motor and the possibly needed gearbox are integrated in the CAD-model. Based on the results of these two modules, the suspension kinematics is optimized in the third module "suspension kinematics optimization" considering the constraints described before.

²The suspension system is depicted in CATIA Kinematics as a skeleton-based CAD-structure with simplified geometries (see e.g. [Böh10]).

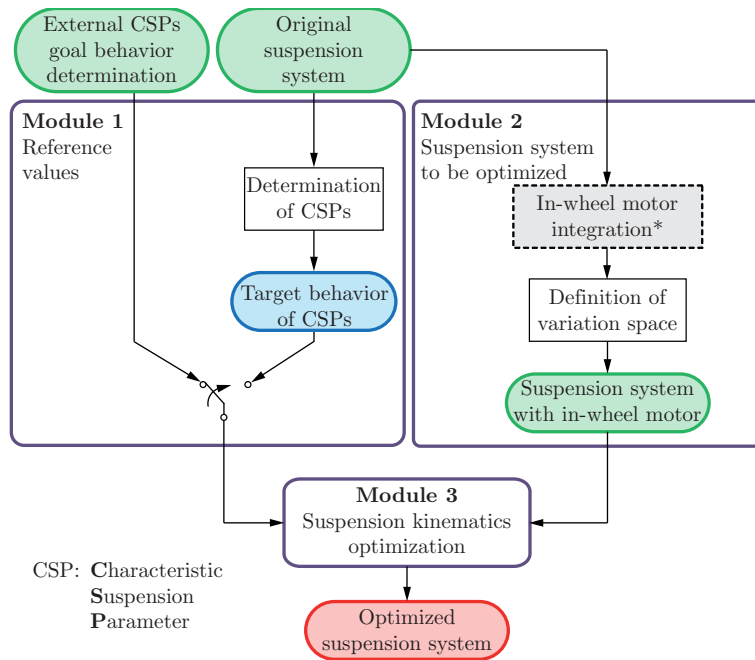


Figure 6.1.: Flow diagram of the synthesis process of the presented Suspension Kinematics Optimization System - KOS. To optimize the kinematics of suspensions without in-wheel motor, the simplified geometries (*) are not integrated in the CAD-model.

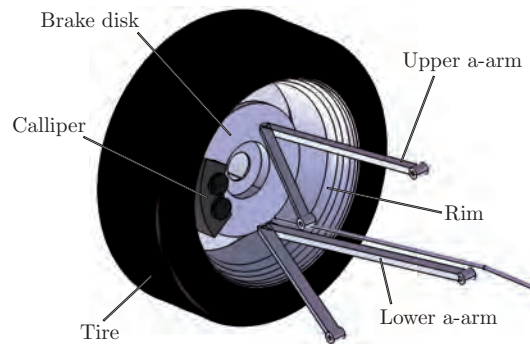


Figure 6.2.: Simplified CAD-model of the suspension system in which the in-wheel motor is to be integrated. The CAD-model of a double wishbone suspension system is exemplarily presented in this figure.

6.2.1. Module 1: Reference values

In this module, the target behavior of the suspension characteristic parameters is determined. Based on the desired range for the bound/rebound and the steering movement, all parameters shown in table 6.1 can be determined. It is also possible to choose just some of them to build up the set of target parameters to be used for the optimization in the module "*suspension kinematics optimization*".

6.2.2. Module 2: Suspension system to be optimized

The goal of this module is to integrate the in-wheel motor and prepare the suspension system for the optimization process of the third module. In the first step, simplified geometries corresponding to additional parts, in this case, the electric motor and a possibly needed gearbox, are integrated in the CAD-model of the suspension system (see figure 6.3-a). This process is carried out based on the dimensions and positions of the simplified geometries. Furthermore, collisions between the added geometries and the suspension components can already be visually recognized in this early development phase and, if desired, manually solved. It is important to highlight that the approach presented in this chapter is also applicable for suspensions without in-wheel motor. In this case, the simplified geometries corresponding to the electric motor and the gearbox are not integrated in the CAD-model.

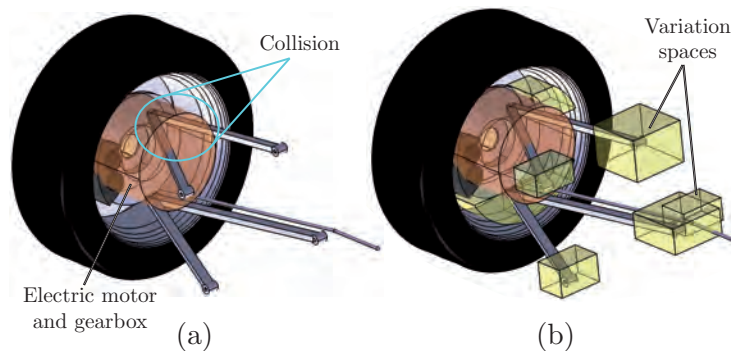


Figure 6.3.: Introduction of the simplified geometries corresponding to the electric motor and the possible needed gearbox in the simplified CAD-model (a). Definition of the variation space for each hardpoint belonging to the suspension system to be modified (b). The CAD-model of a double wishbone suspension system is exemplarily presented in this figure.

Another important step in this early development phase is the definition of the three-dimensional space in which the hardpoints can be varied by the optimization algorithm. This variation space is individually defined, directly in CATIA V5®[®], for each hardpoint and can correspond to any three-dimensional body (see figure 6.3-b).

6.2.3. Module 3: Suspension kinematics optimization

In this module, the hardpoints are varied within the defined three-dimensional variation spaces (see section 6.2.2) with the goal of obtaining a suspension system whose characteristic suspension parameters behave as similar as possible as the target behavior (see section 6.2.1). The inputs of this module are the CAD-model of the suspension system to be optimized (defined in section 6.2.2) and the target behavior of the characteristic suspension parameters. The mentioned task corresponds to an optimization problem, for which two optimization algorithms were implemented and analyzed (see also [RN11], [RNA11a], [RNA11b] and [Apo10]): The Nelder-Mead simplex algorithm and genetic algorithms.

Optimization process using the Nelder-Mead simplex algorithm

The simplex algorithm is an iterative and computationally efficient algorithm presented by *John A. Nelder* and *A. Mead* in 1965 [NM65] to optimize nonlinear problems. The flow diagram of the implemented optimization process is presented in figure 6.4.

In a first step, the behavior of the characteristic parameters of the suspension to be optimized (in this case it contains already the electric motor and the gearbox) is determined. Afterwards, it is compared with the target behavior determined in the first module. If the behavior of the characteristic parameters of the suspension being currently optimized do not fulfill the requirements specified by the fitness function ^{sus}J (see section 6.2.3), the position of the hardpoints is varied by the algorithm. If the requirements are fulfilled, the algorithm checks automatically for collisions using the appropriated tools of CATIA V5®[®]. In the case that there are collisions, the algorithm changes again the position of the hardpoints; otherwise, a suspension system with optimized kinematics (according to the framework described in this chapter) is obtained as output.

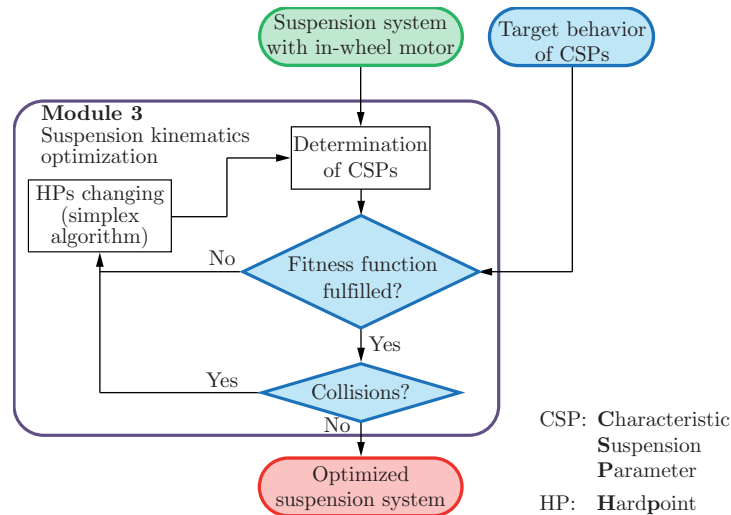


Figure 6.4.: Flow diagram of the optimization process using the Nelder-Mead simplex algorithm.

Optimization process using genetic algorithms

According to the science of artificial intelligence, genetic algorithms are a heuristic optimization approach belonging to the class of evolutionary algorithms [Gol89]. Based on a group of individuals (*population*) and inspired by nature, they reproduce the mechanisms of *selection*, *recombination* and *mutation* to find the optimum of a given problem (see figure 6.5). All individuals of a population are graded according to given evaluation criteria (fitness function ^{susp}J to be optimized - see section 6.2.3). Based on their fitness, some of them are selected as basis for the next generation of individuals. This new generation is obtained through combination and randomly change of the properties (analogous to the genes of any organism in the nature) of the selected individuals.

In this approach, each individual (suspension configuration) is characterized by the position of the hardpoints that should be optimized. Based on the suspension system with in-wheel motor (and gearbox), the initial *population* is generated randomly so that all hardpoints of each suspension configuration reside within their corresponding variation space.

It should be pointed out, that in comparison with, for example, gradient based algorithms, genetic algorithms are better suited to find global optima [Gol89].

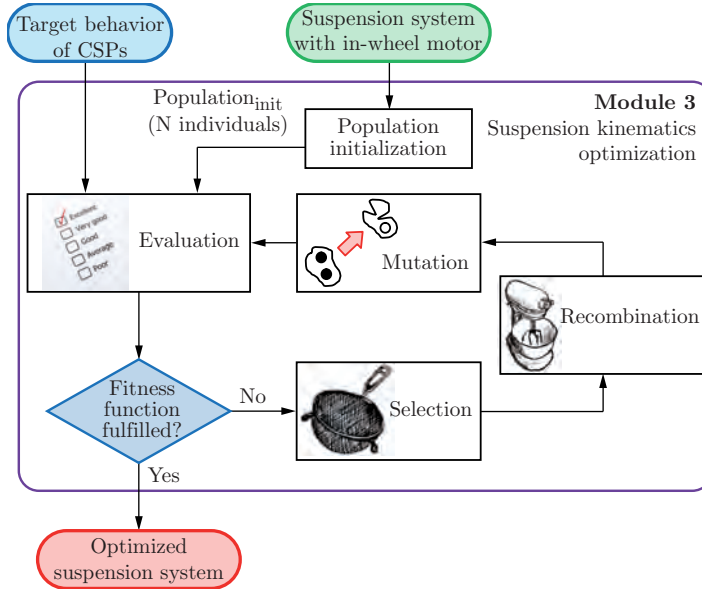


Figure 6.5.: Flow diagram of the optimization process using genetic algorithms.

Fitness function

Following fitness function is proposed to calculate the fitness value of each suspension configuration (see [RN11], [RNA11a], [RNA11b]):

$$\text{susp } J = \begin{cases} \sum_{i=1}^n \left(w_{om,i} \cdot w_i \cdot \sum_{k=2}^m \frac{\Delta P_{ik} + \Delta P_{i(k-1)}}{2} \cdot \Delta \zeta \right); & \text{if there are no collisions,} \\ \text{susp } J_{clash}; & \text{otherwise.} \end{cases} \quad (6.1)$$

This equation relates the number n of suspension parameters to be optimized (see table 6.1), the number m of static points analyzed during the suspension movement, the weighting factor $w_{om,i}$ to get the same order of magnitude for all selected suspension parameters, the weighting factor w_i and the normalized value P_{ik} for each parameter, which is given by

$$\Delta P_{ik} = \left| \frac{P_{ik} - GP_{ik}}{\max(GP_i) - \min(GP_i)} \right|, \quad (6.2)$$

where GP_{ik} corresponds to the target value of the parameter i in the position k .

A graphical explanation of the proposed fitting function is presented in figure 6.6. The difference between the characteristic parameters of the suspension configuration being

currently analyzed and of the original suspension system is defined as the area between the corresponding lines for each characteristic parameter P_i . This area is approximated as a sum of rectangular regions. Each rectangle (hatched area) is defined between two subsequent movements $\Delta\zeta$ of the suspension (where $\Delta\zeta = \Delta z_{c_i}$ for bound/rebound - see chapter 2.7.1 - or $\Delta\zeta = \Delta\delta_{st}$ for steering movements) and has a width corresponding to the mean value $\Delta\tilde{P}_{ik}$ of the normalized values related with the currently analyzed suspension parameter P_{ik} and $P_{i(k-1)}$.

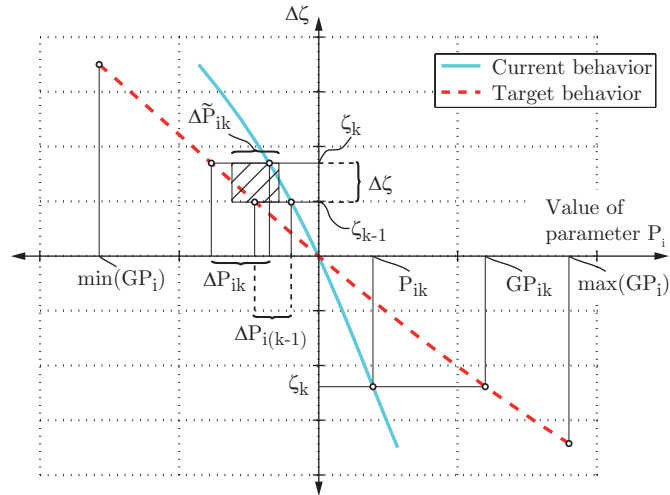


Figure 6.6.: Graphical explanation of the fitting function used by the implemented optimization algorithms.

In case of clashes between the suspension components, the penalty value $^{susp}J_{clash}$ is set, such that the corresponding suspension system is not further considered within the optimization process. Furthermore, the optimization loop is finished when a given maximum number of iterations is reached or when an individual with a fitness value smaller than a given threshold $^{susp}e_j$ is found. In the first case, the individual with the smallest fitness value corresponds to the best found solution.

6.3. Application cases

Based on the results presented in this work and on the detailed design of the electric motor presented by *Willberger* [Wil11], a prototype of the in-wheel motor concept for a

vehicle belonging to the minicompact class³ A^- including an air-cooled induction motor⁴ and a gearbox⁵ integrated in a rim with a diameter of 16 " was built (see figure 6.7). In this chapter, two single wheel suspension systems for rear axles with this concept are presented as application cases of the synthesis process introduced in chapter 6.2: a control blade and a double wishbone suspension system.

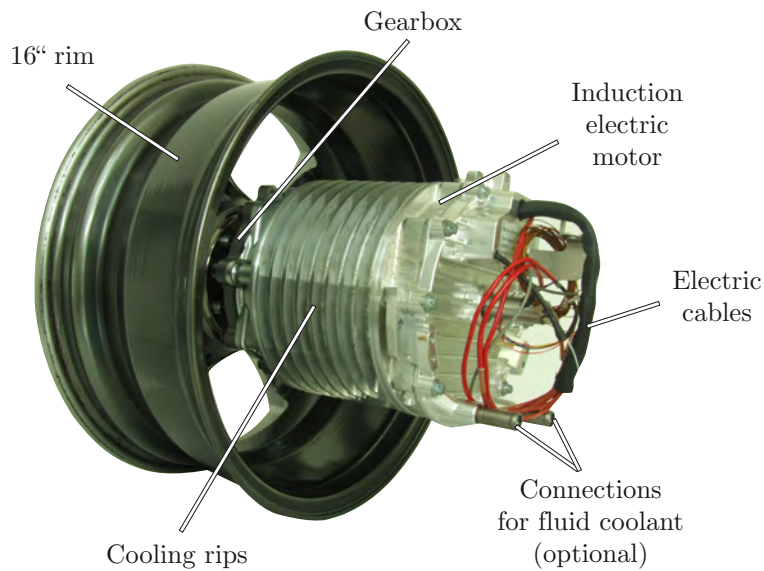


Figure 6.7.: In-wheel motor prototype with induction motor and gearbox for a vehicle belonging to the minicompact class A^- (see chapter 3.7 for the requirements and the characteristics of the electric motor and [Wil11] for its detailed electrical design).

For the optimization process described before in chapter 6.2, simplified geometries of the electric motor and the gearbox, with the dimensions specified in table 6.2, were considered.

The kinematic model used for both suspension systems is described in [HW09] (see also [Böh10]).

³See characteristics of the different vehicle segments in table 3.3 of chapter 3.7.1.

⁴See table 3.11 in chapter 3.7.

⁵See table 3.9 in chapter 3.7.

Table 6.2.: Dimensions of the considered simplified geometries for the considered induction motor and the gearbox. The dimensions of the electric motor as well as other aspects related with the detailed electric design can be found in [Wil11] (see also [Apo10]).

Component	Diameter	Length
	[mm]	
Electric motor	224	181
Gearbox	72	75

6.3.1. Control blade suspension system

For the synthesis of the control blade suspension system, the Nelder-Mead simplex algorithm presented in chapter 6.2.3 was used. The original suspension system corresponds to the control blade suspension system used at the rear axle in the Ford Focus from 1999. Further details were published in [RNW11a]. This suspension system is presented in figure 6.8 together with the control blade suspension system for the rear axle of passenger vehicles with in-wheel motors obtained with the approach presented in this work. Further details about the obtained suspension system were published in [RN11]. The position of the hardpoints belonging to the original and the modified double wishbone suspension system is presented in appendix F.1.



Figure 6.8.: Original control blade suspension system for the rear axle of the Ford Focus from 1999 [HEG11] (a). CAD-model of the control blade suspension system for the rear axle of passenger vehicles with in-wheel motors obtained with the approach presented in this work (b). A 16" rim is used.

The behavior obtained for all suspension parameters listed in table 6.1 is acceptable in

comparison with the behavior of those for the original suspension. Some of them are presented in figure 6.9. It should be mentioned, that an optimization process using the presented approach can take up to five hours on a PC running under Windows® XP (32-bit), two GB RAM and two GHz clock rate depending on the number of hardpoints to be varied.

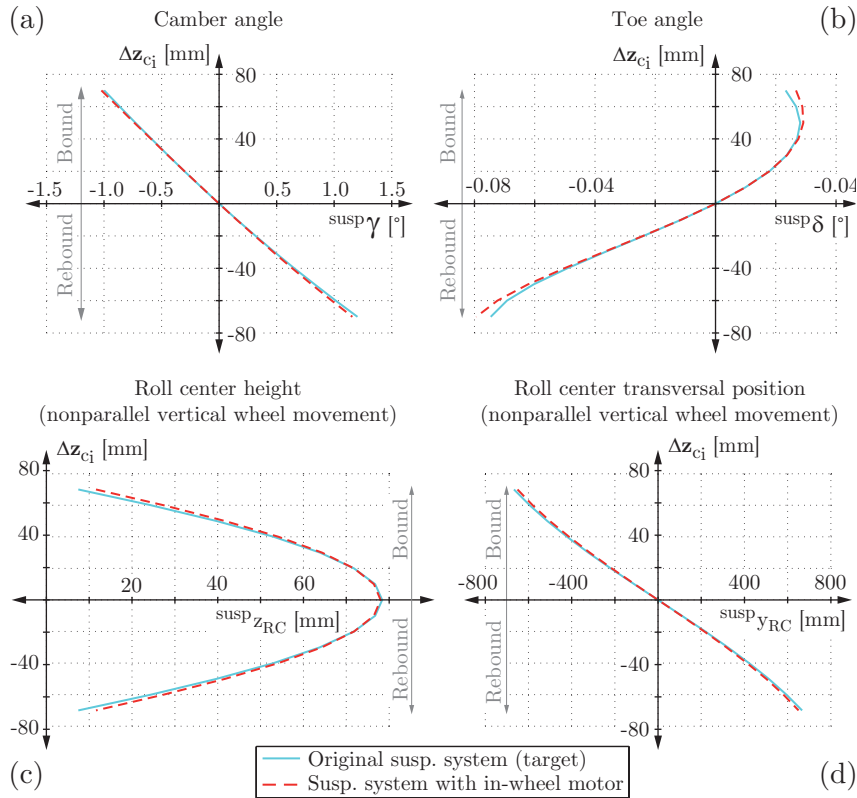


Figure 6.9.: Comparison of some suspension characteristic parameters for the presented control blade suspension system with in-wheel motors for rear axles: camber angle (a) and toe angle (b) as well as the roll center height (c) and transversal position (d) for a nonparallel vertical wheel movement.

6.3.2. Double wishbone suspension system

The approach based on genetic algorithms, as presented in chapter 6.2.3, was used for the synthesis of the double wishbone suspension system. The initial suspension kinematics is based on those of the formula student race vehicle of Graz University of Technology. Further details were published in [RNW11a]. Figure 6.8 presents the

double wishbone suspension system for the rear axle of passenger vehicles with in-wheel motors obtained with the approach presented in this work. Further details about the obtained suspension system were published in [RNA11a] and [RNA11b]. The position of the hardpoints belonging to the original and the modified double wishbone suspension system is presented in appendix F.2.

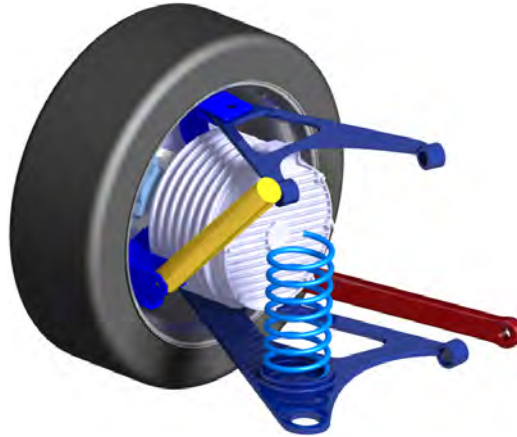


Figure 6.10.: CAD-model of the double wishbone suspension system for the rear axle of passenger vehicles with in-wheel motors obtained with the approach presented in this work. A 16" rim is used.

The behavior obtained for all suspension parameters listed in table 6.1 is acceptable in comparison with the behavior of those for the original suspension. In figure 6.11, some of them are presented. Depending on the number of hardpoints to be varied, the optimization time is about the double of that corresponding to the process based on the Nelder-Mead simplex algorithm.

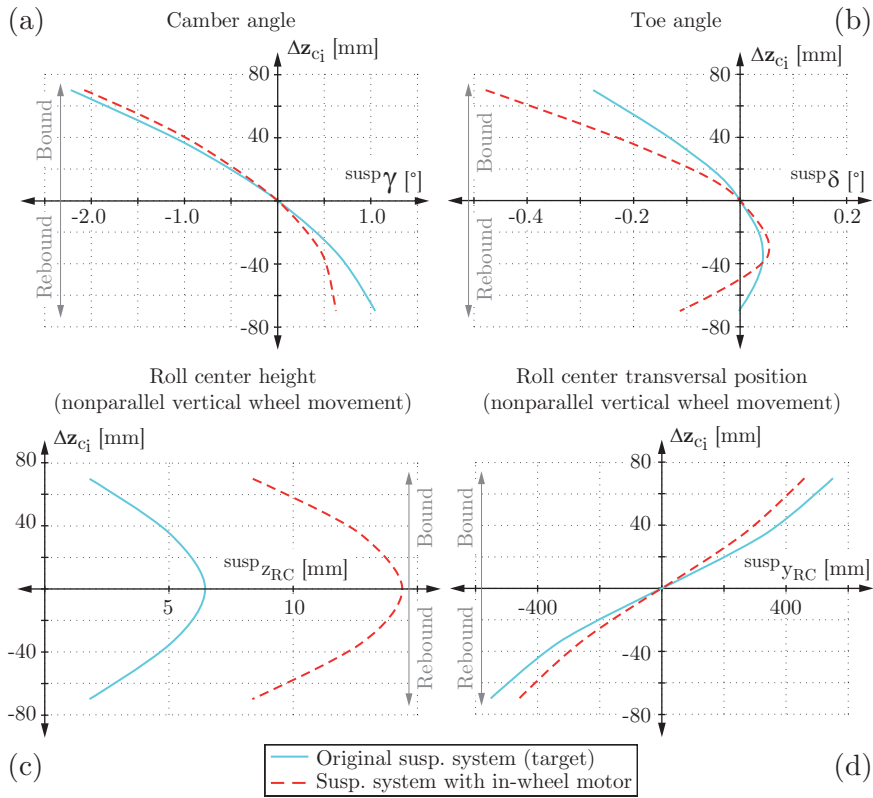


Figure 6.11.: Comparison of some suspension characteristic parameters for the presented double wishbone suspension system with in-wheel motors for rear axles: camber angle (a) and toe angle (b) as well as the roll center height (c) and transversal position (d) for a nonparallel vertical wheel movement.

Due mainly to the fact that the upper and lower control arms are joined (see points 5 and 7 in figure F.2), the double wishbone offers a narrower optimization margin than the control blade suspension system. As can be seen in figure 6.11, this results in greater differences between the target and the obtained behavior of the characteristic suspension parameters. The optimization margin can be expanded by decoupling one of both of the control arms mentioned (see e.g. [HEG11] and [Apo10]).

Figure 6.12-a shows the suspension kinematics optimization process schematically and figure 6.12-b presents the evolution of the fitness function value. It can be seen how the hardpoints position is changed over the iterations and how the fitness function value converges to a minimum.

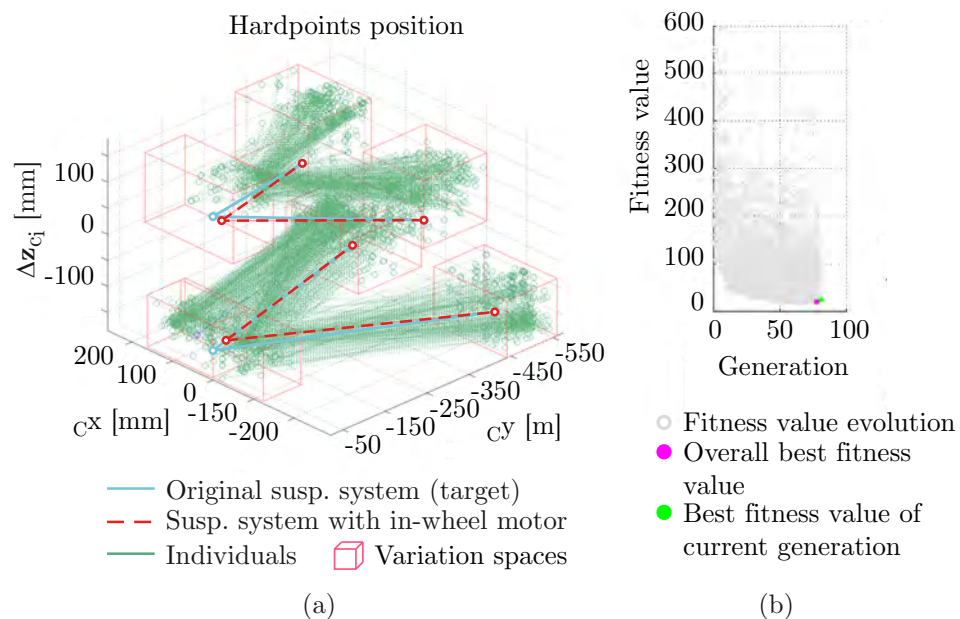


Figure 6.12.: Schematic representation of the suspension kinematics optimization process of a double wishbone suspension system using genetic algorithms (a). Evolution of the fitness function value (b).

Summary chapter 6: Mechanical component integration In this chapter, a novel approach to synthesize single wheel suspension systems was presented. It is called Suspension **K**inematics **O**ptimization **S**ystem - KOS - and is based on a co-simulation between MATLAB® and CATIA V5®. MATLAB® serves as master to control the entire optimization process and provides an interface for the user. CATIA V5® is used to represent the suspension system kinematics, to depict the suspension components as

volumes and to detect collisions between them.

With the presented approach, existing and future single wheel suspension systems, considered to be composed of rigid bodies, can be characterized based on twelve kinematic suspension parameters. Moreover, this approach enables the optimization of the suspension kinematics to reach a given target behavior of the suspension parameters. This can be used to modify a given single wheel suspension system to integrate in-wheel motors.

For the optimization process three different modules are used. The starting point for the optimization process is a simplified CAD model of the suspension system to be modified. In the first module, the target behavior of the suspension characteristic parameters is determined. In the second one, dummy geometries corresponding to the electric motor and the possibly needed gearbox are included in the CAD model. In the third module, the position of the suspension hardpoints is optimized to reach the target suspension parameters behavior and avoid collisions between the suspension components. Two optimization algorithms were implemented and compared: the Nelder-Mead simplex algorithm and genetic algorithms. Although the optimization time is about the double when using genetic algorithms, they are more suited to find global optima and can therefore reduce the number of times an optimization is to be started in order to find a kinematically optimized suspension system.

Two single wheel suspension systems, a control blade and a double wishbone suspension system, for passenger vehicles with in-wheel motors at the rear axle were presented as practical application examples. Using the presented approach, it was possible to reach the characteristic parameters behavior of the unmodified suspension systems avoiding collisions between the suspension components at the same time.

7. Summary and conclusions

In the early days of the automotive industry, electric vehicles were seen as a clean, quiet, comfortable, simple and easy to operate alternative in comparison with the other existing technologies, i.e. steam and internal combustion engines. These advantages assured them a market share of about 38 % by turn from the 19th to the 20th century in the United States of America. Nevertheless, technical, economic, political and socio-cultural factors inclined toward the internal combustion engines making them the most significant power source technology worldwide by the beginning of the 1940s. Since then, vehicles have become more complex, customers more exigent, society and politics more aware of environmental issues, and oil resources more expensive to be exploited. To cope with all demands, mobility and the vehicles itself must be redefined.

From the current point of view electric energy seems to be the most attractive main energy form for future vehicles. Additionally, in-wheel motors are a historical as well as a visionary solution toward the electrification of vehicles providing, at the same time, new alternatives to fulfill increasing exigences regarding passenger cell space, passive safety or styling. Moreover, since in-wheel motors constitute the shortest powertrain, energy losses can be reduced. These advantages make in-wheel motors interesting for original equipment manufacturers, suppliers and research institutions. Nevertheless, although more than 30 prototypes and concepts have been presented mainly in the last decade, no one has gained wide acceptance. This is maybe due to the lack of information and insufficient research in fields like the effect of increased non-suspended masses on ride comfort and driving safety, packaging within the rim, fail safe behavior, cooling of components, complex control strategies or high production costs. In this work, those aspects related with the mechanical integration of in-wheel motors were addressed. To provide a founded knowledge basis, the analysis of these aspects were carried out in different chapters, which are summarized as follows.

Chapter 1: Introduction. After a brief summary of the history of electric vehicles, a general introduction to the in-wheel motors technology, including advantages and open questions, was presented. Those open questions directly related to the mechanical integration of in-wheel motors in passenger vehicles were pointed out as the subject of study in the present work: determination of general characteristics of electric motors (torque, power and mass) and battery (energy and power capacity as well as battery mass), potentials and limitations of in-wheel motors to enhance the vehicle lateral dynamics, influence on the ride comfort and driving safety, and mechanical integration of components within the wheel.

Chapter 2: Simulation environment. In this chapter, the simulation environment MOVES², developed in the context of the present research project, involving the modular modeling of the *driver-vehicle-environment* system was introduced. The developed models of the vehicle, the tire, the road and the passive suspension system were described in detail. The vehicle model was considered to be composed of the suspended body and the non-suspended masses as well as of additional masses positioned on the suspended body via a spring-damper system. The tire model was divided into two sub-models depicting the horizontal and vertical tire dynamics. To model the uneven road, the widespread open source program OpenCRG[®], which is based on a *Curved Regular Grid* and is still being developed by several original equipment manufacturers, was implemented and extended to be able to model and simulate the road unevenness. Semi-physical approaches were developed to model the passive suspension system considered to be composed of a suspension spring and a shock absorber. This chapter finalized with the validation response of the entire model using measured data obtained with the test vehicle Opel Combo 1.6 CNG. For the validation of the stationary response, a steady state circular driving maneuver was used; for the transient response, a dynamic maneuver (reaching almost the physical limits) with varying longitudinal speed $v\dot{x}$ and an unsteady steering wheel angle input δ_{st} was taken as basis; and to validate the vertical dynamic behavior, a driving maneuver on a synthetic test track consisting in a curb followed by a pothole was used as reference.

Chapter 3: Longitudinal dynamics. This chapter focused on the determination of the battery and electric motor characteristics for vehicles with in-wheel motors on the basis of given performance requirements (e.g. maximum speed for different road inclinations, driving range or acceleration and climbing ability) and taking into account the power

demand of auxiliaries for this kind of vehicles. Therefore, optimization approaches using the Nelder-Mead simplex algorithm were developed and presented. Based on them, the torque and power (in nominal and overload service) as well as the approximated mass of induction and synchronous electric motors can be determined. Moreover, the battery mass as well as its energy and power capacity can be defined. Furthermore, the presented approaches were used to determine the characteristics of the mentioned electric components for electric vehicles belonging to three different vehicle classes: minicompact, subcompact and compact. Based on a regular modern Li-ion battery pack with an energy-to-mass ratio of 150 Wh/kg and a power-to-mass ratio of 300 W/kg, a battery mass of 135 kg for the minicompact, 205 kg for the subcompact and 290 kg for the compact vehicle class were obtained. Moreover, the results showed exemplarily that two electric motors with a nominal torque of about ${}^nM \approx 17.0$ Nm and a nominal power of approximately ${}^nP \approx 11.2$ kW are needed to meet the driving performance requirements of a vehicle belonging to the minicompact class and a rear-wheel drive powertrain architecture. A transmission ratio of around 9 was determined for this vehicle class based on the considered maximum rotational speed of the motor (11000 rpm) and the required maximum longitudinal vehicle speed (120 km/h). A comparison of the weight of vehicles with internal combustion engines and vehicles with in-wheel motors showed that a weight reduction of about (6 %) can be expected under the consideration of rational real world performance requirements covering most of the daily necessities of average drivers.

Chapter 4: Lateral dynamics. To analyze the advantages and limitations of in-wheel motors regarding the vehicle lateral dynamics, three different open-loop driving maneuvers were analyzed: step steer, open-loop sinusoidal steering input and open-loop frequency response. Based on the literature, different assessment criteria were presented to evaluate the performance of a given vehicle configuration in each of the analyzed driving maneuvers. A control concept for a torque vectoring system with optimal longitudinal tire force allocation was presented. Two electric powertrains (rear-wheel drive and four-wheel drive) with in-wheel motors and torque vectoring system were compared with a four-wheel drive electric powertrain without torque vectoring system. The obtained results showed that in-wheel motors in association with the presented torque vectoring system have substantial potential to enhance the lateral dynamics performance beyond the level of vehicles with a conventional four-wheel drive powertrain architecture without torque vectoring.

Chapter 5: Vertical dynamics. The influence of the increased non-suspended masses on the ride comfort and driving safety of vehicles with in-wheel motors was analyzed. Therefore, the traditional objective assessment criteria was presented in the first part of the chapter. The so-called *conflict diagram* relating these criteria was taken as basis to exemplify the trade-off between ride comfort and driving safety. The results showed that, the lower the relation between the suspended and the non-suspended mass m_{A_q}/m_{w_i} (i.e. for lower vehicle segments), the stronger is the effect of the increased non-suspended masses on ride comfort and driving safety. Furthermore, it was shown, that the considered increased non-suspended masses, as corresponding to the performance requirements taken into account in chapter 3, lead to an acceptable reduction in ride comfort for the analyzed vehicle segments.

In the second part of this chapter, the subjective perception of 34 test drivers while driving with a modified vehicle was presented. The results showed that no remarkable differences in the ride comfort subjective perception with and without increased non-suspended masses are to be expected. Furthermore, based on the simulation results, a good correlation between the subjective perception and the objective assessment criteria was found. Additionally, an approach based on the tire inflation pressure as a more "intuitive" variable producing similar effects on the subjective ride comfort perception as increased non-suspended masses was presented.

In the third part of the chapter, the potentials and limitations of two alternative passive suspension systems (eccentric concept and damping mass concept), a semi-active system and an active system to improve the ride comfort and driving safety of vehicles with in-wheel motors were analyzed and compared with a conventional passive suspension system (reference) from a theoretical point of view based on simulations. The results showed, that both alternative passive concepts analyzed present advantages regarding the considered assessment criteria for all considered conditions up to 40 % in comparison with the reference passive system. The analyzed mechatronic systems present advantages in ride comfort (up to 10 %) mainly for low speeds. Based on the results and on the fact that the damping mass concept does not need external energy supply, it can be seen as the most interesting alternative to cope with the problems induced by the increased non-suspended masses related to in-wheel motors if the related challenges regarding package can be solved.

In the last part of the chapter, the effect of increased non-suspended masses on the driving safety of vehicles with in-wheel motors in realistic maneuvers was analyzed.

Therefore, an open-loop maneuver representing a driving situation over a sinusoidal perturbation in a curve with different constant longitudinal speeds producing a lateral acceleration of about 95 % of the maximum achievable value was simulated. Due to the lack of suitable assessment criteria in the literature, four criteria were proposed to assess the driving safety in such scenarios. Based on the results, the suitability of the proposed evaluation criteria was shown and the ability of the presented torque vectoring system with in-wheel motors (chapter 4) to enhance the driving safety of vehicles with increased non-suspended masses was evidenced.

Chapter 6: Mechanical component integration. In this chapter, a novel optimization approach developed in the context of the present research project and based on a co-simulation between MATLAB® and CATIA V5® to synthesize single wheel suspension systems was presented. With this approach, existing and future single wheel suspension systems, considered to be composed of rigid bodies, can be characterized based on twelve characteristic kinematic suspension parameters. Moreover, this approach enables the optimization of the suspension kinematics to reach a given target behavior of the suspension parameters. This can be used to modify a given single wheel suspension system to integrate in-wheel motors. For the optimization process two optimization algorithms were implemented and compared: the Nelder-Mead simplex algorithm and genetic algorithms. Two single wheel suspension systems, a control blade and a double wishbone suspension system, for passenger vehicles with in-wheel motors at the rear axle were presented as practical application examples. Using the presented approach, it was possible to reach the characteristic parameters behavior of the unmodified suspension systems while avoiding collisions between the suspension components at the same time.

Final statements. An extensive and founded analysis of the visionary technology of in-wheel motors for applications in passenger vehicles was presented in this doctoral thesis. In contrast to published approaches, the characteristics of the electric components are the result of synthesis processes based on the driving performance requirements. Corresponding methodologies were developed and analyzed in detail. Furthermore, the advantages and limitations of in-wheel motors were evaluated using both theoretical and realistic scenarios.

New scientific findings complementing known scientific results were presented. It was possible to show that the increased non-suspended masses introduced by in-wheel motors

result in an acceptable reduction in ride comfort under the consideration of the realistic installed power needed for a given vehicle class. Moreover, it was highlighted that advanced functionalities can be easily implemented thanks to the additional degrees of freedom introduced by in-wheel motors. As an example, a control strategy for a torque vectoring system was presented. Using it, it was shown that, in comparison with vehicles with a conventional powertrain, the driving safety can even be improved. Furthermore, it was evidenced, that the difficulties regarding the mechanical integration of components within the wheel can be solved even for complex single wheel suspension systems.

Summarizing, in-wheel motors are a real and visionary alternative toward the electrification of vehicles. Nevertheless, further research is needed to answer some related open questions. The present thesis aimed to offer corresponding approaches from the methodological and engineering point of view in order to help bringing this technology to series production by clarifying some of those questions related with the determination of the electric components characteristics based on performance requirements, control strategies (e.g. torque vectoring system) to profit from the advantages of in-wheel motors to enhance the vehicle lateral dynamics, the analysis of the effects of the related increased non-suspended masses on ride comfort and driving safety, and the mechanical integration of components in single wheel suspension systems.

A. Appendix: Optimization methods and mathematics

A.1. Relative cumulative frequency

For a variable a assuming random values a_j with a certain frequency h , the relative cumulative frequency f_{cu} for a total of n observations or events is given by (see e.g. [BV08]):

$$f_{cu}(a_j) = \sum_{i=1}^j \frac{h_i}{n} \cdot 100 \% . \quad (\text{A.1})$$

The relative cumulative frequency $f_{cu}(a_j)$ gives insight into how often a particular occurrence a_j is greater than any other occurrence of the observed variable a . In figure A.1, the particular value a_j is said to be greater than $f_{cu}(a_j)$ -percent of all possible occurrences of the random variable a .

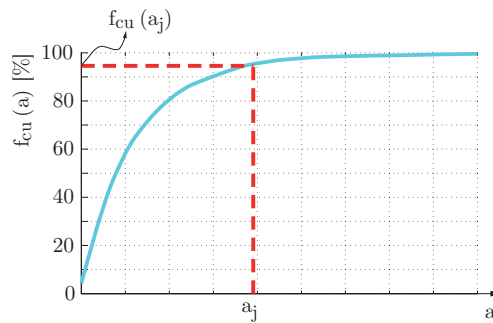


Figure A.1.: Relative cumulative frequency.

B. Appendix: Simulation environment

B.1. Vehicle parameters

An *Opel Combo 1.6 CNG* (year of construction 2007) was used as test vehicle and taken as reference for the parametrization and validation of the vehicle model presented in chapter 2. Most of the parameters are taken from the vehicle's technical data sheet or directly determined from measured data obtained on different test rigs (see [Kol09] and [Dür11]). The aerodynamic coefficients are based on values proposed in the literature (see [Dür11]). Other parameters were identified based on measured data from test drives using the identification routine implemented in the simulation environment (see [RNW10] and [Mar09]). All parameters are presented in table B.1.

B.2. Tire parameters

The Continental tires *ContiPremiumContactTM 2* 185/60 R 15 are used on the test vehicle and were taken as reference for the parametrization and validation of the model presented in chapter 2. The tire model parameters for the horizontal tire dynamics were determined based on measured data and are listed in table B.2. The model parameters for the vertical tire dynamics correspond to those suggested by *Schmeitz* [Sch04] for a tire similar to that used on the test vehicle.

B.3. Road parameters

The parameters used to reconstruct a road with certain roughness are taken from the literature (see [Bau87] and [fSI95]) and presented in table B.3. The values for Ω_0 and $\Phi_{road}(\Omega_0)$ depends on the desired road class (see chapter 2.6.2).

Table B.1.: Vehicle model parameters.

Parameter	Symbol	Value	Units
Vehicle mass in running order ^{a,b}	m_v	1571	
Maximum authorized additional load mass ^{a,b}	$^{max}m_{load}$	623	[kg]
Standard non-suspended mass ^c	$m_{w_i, Std.}$	40	
Wheel base ^b	L	2.716	
Front track ^b	s_f	1.417	[m]
Rear track ^b	s_r	1.440	
Distance center of gravity to front axle ^c	l_f	-1.3	
Height of center of gravity (from ground) ^c	h_{CG}	0.65	
Principal moments of inertia ^e	Around the ${}_Vx$ axis	${}_V I_{CGA, x}$	650
	Around the ${}_Vy$ axis	${}_V I_{CGA, y}$	1500
	Around the ${}_Vz$ axis	${}_V I_{CGA, z}$	2000
			[kg · m ²]
Moment of inertia of one wheel ^{f,g}	${}_C I_{w_i, z}$	2	
Tire inflation pressure (recomended value) ^{b,c}	p_{T_i}	2.3	[bar]
Engine mass ^e	m_{Eng}	170	[kg]
Engine position ^{e,h}	Along the ${}_Vx$ axis	${}_V^r O \rightarrow P_{Eng, x}$	1.4
	Along the ${}_Vy$ axis	${}_V^r O \rightarrow P_{Eng, y}$	0
	Along the ${}_Vz$ axis	${}_V^r O \rightarrow P_{Eng, z}$	0
			[m]
Engine suspension ^e	Vert. spring stiffness	c_{Eng}	596483
	Vert. damping coef.	d_{Eng}	4500
			[N/m]
Projected frontal area ^b	A_w	2.3	[m ²]
Drag coefficient ^d	C_d	0.35	
Lift coefficient ^d	C_l	0	[-]
Lateral drag coefficient ^d	C_s	0	

^a Vehicle mass definitions according to the Council Directive 92/21/EEC of 31 March 1992 of the European Union [Com92].

^b From technical data sheet of the test vehicle: *Opel Combo 1.6 CNG* (year of construction 2007).

^c Measured.

^d From the literature (see [Huc05]).

^e Identified.

^f Approximated by calculations.

^g Including tire, rim, brake disk and other rotating parts of the wheel carrier. See C.2 to calculate the reduced moment of inertia ${}_C I_{red w_i, z}$.

^h Measured from the vehicle's center of gravity with P_{Eng} as the engine attachment point (P_{Add_j} in equation 2.25).

B.3. Road parameters

Table B.2.: Tire model parameters.

	Parameter	Symbol	Value for		Units
			${}_W F_{T_i, z \text{ nom}} = 2500N$	$2 \cdot {}_W F_{T_i, z \text{ nom}}$	
Long. ^a	Peak	${}_W F_{T_i, x \text{ max}}$	2740	5480	[N]
	Saturation	${}^\infty F_{T_i, x}$	2130	4350	
	Initial stiffness	$d({}_W F_{T_i, x})_0$	430	1100	[N/%]
Lat. ^a	Peak	${}_W F_{T_i, y \text{ max}}$	2720	4990	[N]
	Saturation	${}^\infty F_{T_i, y}$	2600	4700	
	Initial stiffness	$d({}_W F_{T_i, y})_0$	51600	80200	[N/rad]
Pneu. trail ^a	Initial value	$(n_{v_i}/L_{T_i})_0$	0.24	0.50	[-]
	Slip for $n_{p_i} = 0$ m	$sl_{y_i}^0$	12	22	[%]
	Slip for ${}^\infty n_{p_i} = 0$ m	$sl_{y_i}^S$	22	19	
Stiffness ^a	Longitudinal	$c_{T_i, x}^S$	200		$\left[\frac{\text{kN}}{\text{m}} \right]$
	Lateral	$c_{T_i, y}^S$	100		
	Vertical	$c_{T_i, z}^S$	200		
	Rolling resistance coeff. ^b	f_{roll}	0.01		
	Contact patch length ^c	$\mathcal{P}_{l_{s_0}}$	0.8148		[-]
		$\mathcal{P}_{l_{s_1}}$	$6.645 \cdot 10^{-4}$		$[m/\sqrt{N}]$
		$\mathcal{P}_{l_{s_2}}$	$4.524 \cdot 10^{-6}$		$[m/N]$
	Cam ellipsis ^c	\mathcal{P}_a	1.2162		
		\mathcal{P}_b	1.0608		[-]
		\mathcal{P}_c	1.6481		
	Dynamic tire radius ^c	\mathcal{P}_{r_0}	0.3127		[m]
		\mathcal{P}_{r_1}	$-2.292 \cdot 10^{-4}$		$[m/\sqrt{N}]$
		\mathcal{P}_{r_2}	$1.176 \cdot 10^{-6}$		$[m/N]$
		\mathcal{P}_{r_3}	$1.265 \cdot 10^{-10}$		$[m/N^{3/2}]$
	Unloaded tire radius ^d	r_0	0.3159		[m]

^a From measurements.

^b Statical values according to *Hirschberg* [Hir09a].

^c According to *Schmeitz* [Sch04].

^d Calculated based on the tire dimensions (185/60 R 15).

Table B.3.: Parameters to reconstruct a road with certain roughness given a specific power spectral density Φ_{road} .

Parameter	Symbol	Value	Units
Form factor ^a	β_{P_1}	0.1	[-]
	β_{P_2}	1.6	
Correlation factor ^a	α_{road}	0.6	
Unevenness exponent ^b	w	2.0	

^a According to *Bauer* [Bau87].

^b According to the *ISO-Standard 8608:1995(E)* [fSI95].

B.4. Single-mass oscillator model parameters

The behavior of the functions corresponding to the speed parameter $\mathbb{C}_{T\omega}$ (see [RSB01] and [Wal06]) as well as to the static $c_{T_i, z}^S$ and dynamical $c_{T_i, z}^D$ tire stiffness coefficients (based on measures - see also [Mar09]) of the single-mass oscillator model is presented in figure B.1.

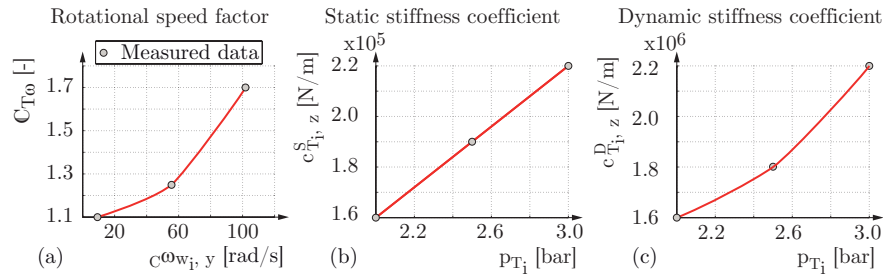


Figure B.1.: Tire vertical stiffness coefficients (see chapter 2.5.2): (a) Speed coefficient $\mathbb{C}_{T\omega}$ vs. tire rotational speed $C\omega_{w_i, y}$ as well as (b) static $c_{T_i, z}^S$ and (c) dynamical $c_{T_i, z}^D$ tire stiffness coefficients vs. tire inflation pressure p_{T_i} .

Figure B.2 shows the behavior of the obtained tire vertical force ${}_WF_{T_i}$ as a function of the effective tire vertical deflection ρ_{z_i} , the tire rotational speed $C\omega_{w_i, y}$ and the tire inflation pressure p_{T_i} . In the case of the influence of the tire inflation pressure p_{T_i} on the tire vertical force ${}_WF_{T_i}$, a high correlation between the measured data and the obtained curves can be observed (see also [Mar09]).

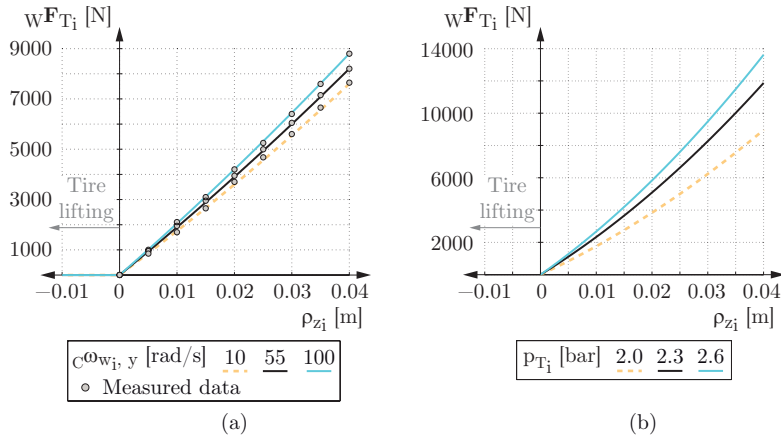


Figure B.2.: Behavior of the tire vertical force wF_{T_i} as a function of the effective tire vertical deflection ρ_{z_i} , the tire rotational speed $C\omega_{w_i, y}$ (a) and the tire inflation pressure p_{T_i} (b).

B.5. Passive suspension system parameters

The parameters used for the suspension spring and the shock absorber models described in chapter 2.7 are presented in table B.4. While the parameters for the spring were determined based on measured data¹, those related with the shock absorber were determined with the help of the identification routine implemented in the simulation environment MOVES² and presented in [RNW10] (see also [Mar09]). The corresponding characteristic curves are shown in figure B.3. For the spring, a high correlation between the obtained curves and the measured data is achieved.

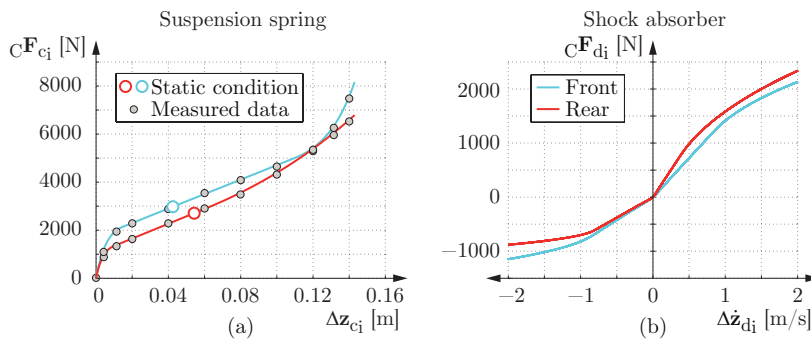


Figure B.3.: Suspension spring (a) and shock absorber (b) characteristic curves for the front and rear axle of the test vehicle.

¹The measured data is presented in [Dür11]

Table B.4.: Passive suspension system parameters.

	Parameter	Symbol	Value		Units	
			Front	Rear		
Suspension spring ^a	Natural frequency ^b	f_{Aq}	1.68	2.1	[Hz]	
	Static ground clearance	$\Delta z_{c_i}^S$	0.043	0.054		
	Limits of linear region	Bound	$\Delta z_{c_i, III_0}$	0.110	0.060	[m]
		Rebound	$\Delta z_{c_i, I_0}$	0.015	0.010	
	Exponential coefficient during bound	$n_{c,III}$	58	8.5	[-]	
Shock absorber ^c	Compression-tension relation parameter	γ_d	0.63	0.73		
	Damping ratio	ξ_d	0.27	0.32	[-]	
	Exponential coefficient during tension	$n_{d,T}$	0.438	0.433		
	Damper force relation factor in exponential region II	κ_d	0.586	0.703		
	Trigger speed of relief mechanisms	Compression	$\Delta \dot{z}_{d_i, C_0}$	-0.85	-0.81	[m/s]
Tension		$\Delta \dot{z}_{d_i, T_0}$	0.85	0.38		

^a Determined based on measurements (see [Dür11] for the measured data).

^b In the literature, a value between 1.0 Hz and 2.2 Hz is recommended (see e.g. [MW04]).

^c Identified based on the driving maneuver presented schematically in figure 2.20 (see also [Mar09]).

C. Appendix: Longitudinal dynamics

C.1. Equations of motion for the longitudinal vehicle dynamics

Figure C.1 shows the simplified model for the longitudinal vehicle dynamics according to *Hirschberg* [Hir09a]. In this model, the vehicle is considered to be composed of a suspended mass (right subscript A) and two axles, one at the front and one at the rear (right subscripts f and r respectively). Furthermore, it is assumed that the effective wheel radius r_{dyn} is the same for the front and the rear wheels. Additionally, a left subscript is used to indicate the coordinate system in which a variable is defined. For example, in figure C.1 the left subscript V is used to indicate the vehicle coordinate system¹.

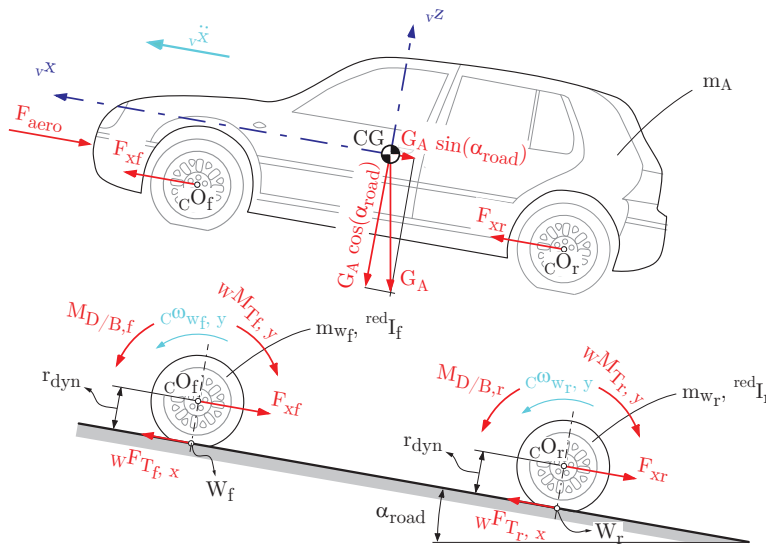


Figure C.1.: Model of the longitudinal vehicle dynamics [Hir09a].

¹See the German standard DIN 70000 [fN94] for the definition of the road vehicles, vehicle dynamics and road-holding ability vocabulary.

From equation 2.4, the equation of linear momentum of the suspended mass m_A in the v_x direction results in:

$$m_A \cdot v \ddot{x} = F_{xf} + F_{xr} - F_{aero} - F_{climb}, \quad (\text{C.1})$$

where F_{xf} and F_{xr} correspond to the reaction force between the suspended mass and the front and rear axles respectively. Furthermore, F_{aero} is the aerodynamic force and F_{climb} the necessary force to overcome a road with a given inclination α_{road} .

Analogously and applying also the principle of conservation of the angular momentum to the axles results in:

$$m_{w_{f/r}} \cdot v \ddot{x} = {}_W F_{T_{f/r}, x} - F_{x,f/r}, \quad (\text{C.2})$$

$${}^{red} I_{f/r} \cdot {}_C \dot{\omega}_{w_{f/r}, y} = M_{D/B,f/r} - r_{dyn} \cdot {}_W F_{T_{f/r}, x} - {}_W M_{T_{f/r}, y}. \quad (\text{C.3})$$

In equations C.2 and C.3 the subscript f/r was used to denote variables corresponding to both the front and the rear axle. In this sense, ${}_W F_{T_{f/r}, x}$ indicates the longitudinal tire force, $M_{D/B,f/r}$ corresponds to the driving (subscript D) or braking (subscript B) torque², and ${}_W M_{T_{f/r}, y}$ is the torque due to the rolling resistance (see equation 2.41 in chapter 2.5.1). Moreover, r_{dyn} is the dynamic tire radius, ${}^{red} I_{f/r}$ denotes the reduced moment of inertia and ${}_C \dot{\omega}_{w_{f/r}, y}$ corresponds to the angular acceleration of the wheels at the front and rear axle respectively.

Taking into account the equation 2.30a for the longitudinal tire slip and neglecting the artificial velocity v_N , the rotational speed of the wheels ${}_C \dot{\omega}_{w_{f/r}, y}$ can be written as a function of the vehicle longitudinal speed as

$${}_C \omega_{w_{f/r}, y} = \frac{v \dot{x}}{r_{dyn}} \cdot s_{f/r}^*, \quad (\text{C.4})$$

where the generalized tire slip $s_{f/r}^*$ is defined as:

$$s_{f/r}^* = \begin{cases} \frac{1}{1 - sl_{x_{f/r}}}; & \text{while driving (i.e. } v \dot{x} > 0 \text{ m/s),} \\ 1; & \text{for a free rolling wheel (i.e. } v \dot{x} = 0 \text{ m/s), or} \\ 1 + sl_{x_{f/r}}; & \text{while braking (i.e. } v \dot{x} < 0 \text{ m/s).} \end{cases} \quad (\text{C.5})$$

²In figure C.1, positive driving torques $M_{D,f/r}$ and/or negative braking torques $M_{B,f/r}$ are depicted.

Equations C.4 and C.5 can also be used to find the relation between the rotational acceleration of the tires ${}_C\dot{\omega}_{w_{f/r}, y}$ and the longitudinal acceleration of the vehicle ${}_V\ddot{x}$.

Rearranging equations C.1 and C.2 results in:

$$(m_A + m_{w_f} + m_{w_r}) \cdot {}_V\ddot{x} = {}_W F_{T_f, x} + {}_W F_{T_r, x} - F_{aero} - F_{climb} . \quad (C.6)$$

Solving equation C.3 for ${}_W F_{T_{f/r}, x}$ leads to:

$$\begin{aligned} {}_W F_{T_{f/r}, x} = \frac{1}{r_{dyn}} \cdot \left(M_{D/B, f/r} - {}_W M_{T_{f/r}, y} - {}^{red}I_{f/r} \cdot {}_C\dot{\omega}_{w_{f/r}, y} \right) = \\ \frac{M_{D/B, f/r}}{r_{dyn}} - F_{roll, f/r} - \frac{{}^{red}I_{f/r}}{r_{dyn}} \cdot {}_C\dot{\omega}_{w_{f/r}, y} , \quad (C.7) \end{aligned}$$

where ${}_W M_{T_{f/r}, y}/r_{dyn}$ has been replaced by the rolling resistance force $F_{roll, f/r}$.

Inserting equation C.7 in equation C.6 and taking into account the relation between the rotational acceleration of the tires ${}_C\dot{\omega}_{w_{f/r}, y}$ and the longitudinal acceleration of the vehicle ${}_V\ddot{x}$ (see equations C.4 and C.5), leads to:

$$\begin{aligned} \left(m_v + \frac{{}^{red}I_f \cdot s_f^* + {}^{red}I_r \cdot s_r^*}{r_{dyn}^2} \right) \cdot {}_V\ddot{x} = \\ \left(\frac{M_{D/B, f} + M_{D/B, r}}{r_{dyn}} \right) - (F_{roll, f} + F_{roll, r}) - F_{aero} - F_{climb} , \quad (C.8) \end{aligned}$$

where the sum of the suspended mass m_A and wheel masses $m_{w_{f/r}}$ has been replaced by the total vehicle mass or mass in running order³ m_v :

$$m_v = m_A + m_{w_f} + m_{w_r} . \quad (C.9)$$

According to the Council Directive 92/21/EEC of 31 March 1992 of the European Union [Com92], the mass m_v includes the suspended mass m_A and the non-suspended masses (m_{w_f} and m_{w_r}) as well as a 75kg driver. Moreover, it is assumed here, that in the case of electric vehicles, the mass of the battery m_{Batt} is also included in m_v .

³Vehicle mass definitions according to the Council Directive 92/21/EEC of 31 March 1992 of the European Union [Com92].

Furthermore, with the general rolling resistance force

$$F_{roll} = F_{roll,f} + F_{roll,r} \quad (\text{C.10})$$

and the general driving/braking force

$$\frac{M_{D/B}}{r_{dyn}} = \frac{M_{D/B,f} + M_{D/B,r}}{r_{dyn}}, \quad (\text{C.11})$$

equation C.8 can be rewritten as

$$\left(m_v + \frac{{}^{red}I_f \cdot s_f^* + {}^{red}I_r \cdot s_r^*}{r_{dyn}^2} \right) \cdot v \ddot{x} = \frac{M_{D/B}}{r_{dyn}} - F_{roll} - F_{aero} - F_{climb}. \quad (\text{C.12})$$

By neglecting the tire slip ($sl_{x_f/r} = 0$), the equation

$$\frac{M_{D/B}}{r_{dyn}} = F_{x_{resistance}} \quad (\text{C.13})$$

approximately holds in the quasi-stationary equilibrium, where the quasi-stationary total resistance force $F_{x_{resistance}}$ can be expressed as a function of the the total reduced moment of inertia for both axles ${}^{red}I = {}^{red}I_f + {}^{red}I_r$ (see chapter C.2) as

$$F_{x_{resistance}} = \left(m_v + \frac{{}^{red}I}{r_{dyn}^2} \right) \cdot v \ddot{x} + F_{roll} + F_{aero} + F_{climb}, \quad (\text{C.14})$$

or in the compact form:

$$F_{x_{resistance}} = F_v \ddot{x} + F_{roll} + F_{aero} + F_{climb}. \quad (\text{C.15})$$

Equation C.13 states that in the quasi-stationary equilibrium, the necessary force to produce a certain (instantaneous) longitudinal movement of the vehicle, corresponds to the sum of all resistance forces. Furthermore, equations C.13, C.14 and C.15 can be used for the synthesis process described in chapter 3 in order to determine the nominal torque and power of the electric motors as well as the battery mass to drive a certain cycle.

C.2. Determination of the reduced moment of inertia

The reduced moment of inertia ${}^{red}I_{f/r}$ is an auxiliary variable corresponding to the moment of inertia of a simplified equivalent dynamical system embracing all rotatory powertrain components connected to the wheels of an axle (including the wheels itself). To assure the equivalence, both systems have to show the same dynamic behavior. This is possible when the kinetic energy of the reduced system ${}^{red}E_k$ is the same as the kinetic energy of the original (powertrain) system 0E_k :

$${}^{red}E_k = {}^0E_k . \quad (C.16)$$

Taking into account the rotational acceleration $\ddot{\psi}_i$ and the moments of inertia I_i of the n different powertrain components, equation C.16 can be written as:

$$\frac{{}^{red}I_{f/r} \cdot \ddot{\psi}_{f/r}^2}{2} = \sum_1^{i=n} \frac{I_i \cdot \ddot{\psi}_i^2}{2} . \quad (C.17)$$

Considering a powertrain composed of rigid bodies, the rotational accelerations $\ddot{\psi}_i$ of the different powertrain components are related with the rotational acceleration $\ddot{\psi}_{f/r}$ of the considered axle⁴ through

$$\ddot{\psi}_i = i_{i \rightarrow f/r} \cdot \ddot{\psi}_{f/r} , \quad (C.18)$$

where $i_{i \rightarrow f/r}$ correspond to the total transmission ratio along the part of the powertrain between the component i and the considered wheel at the front f or at the rear r axle.

Introducing equation C.18 in equation C.17 and simplifying the rotational acceleration of the considered axle $\ddot{\psi}_{f/r}$, the reduced moment of inertia ${}^{red}I_{f/r}$ can be expressed as:

$${}^{red}I_{f/r} = \sum_1^{i=n} I_i \cdot i_{i \rightarrow f/r}^2 . \quad (C.19)$$

⁴The right subscript f is used for the front axle and right subscript r for the rear one.

C.3. Driving cycles

General information about the driving cycles considered in this work is presented in the following sections.

C.3.1. ARTEMIS

The Assessment and Reliability of Transport Emission Models and Inventory Systems - abbreviated ARTEMIS - was an EU-Project carried out between 2000 and 2004. The participants were 36 organizations from 15 countries (Europe and Israel) involved in research topics of transportation. The goal was the development of a harmonized emission model for road, rail, air and ship transportation systems in order to provide consistent emission assessments in Europe. One of the main topics of ARTEMIS was the analysis and establishment of driving cycles representing modern driving patterns in Europe. Field tests conducted between 1980 and 2004 have been analyzed to identify reasonable driving patterns and create representative city, road and highway driving cycles [BM07].

C.3.2. HYZEM

The main goal of the European Hybrid Technology Development Approaching Efficient Zero Emission Mobility - abbreviated HYZEM - project was the assessment of hybrid vehicles potentials in Europe [And04]. Between 1994 and 1997 14 OEMs and research institutions from eight European countries undertook special efforts to derive typical traffic situations in Europe in order to set up more realistic driving cycles for urban, road and highway scenarios [And04]. Nowadays, HYZEM cycles are widely used by scientific communities in order to assess fuel consumption and pollutant emissions, especially when designing hybrid and electric vehicles [NBW06].

C.3.3. INRETS

The INRETS cycle family was derived at the Institut National de Recherche sur les Transports et leur Sécurité. The data were obtained by measuring driving patterns using about 30 passenger cars in France in the late eighties [And04].

C.3.4. NEDC

The *New European Driving Cycle* - NEDC is a modal standardized cycle widely used in Europe (see [Uni07]). It is composed of two successive parts representing a city (called ECE) and a highway cycle (EUDC). Some authors argue that realistic consumption and emission information could not be obtained using the NEDC because it does not represent a real driving pattern (see e.g. [And04]). Nevertheless, it is widespread used for compatibility reasons since this driving cycle has been used for long time and there is therefore a lot of information based on it that otherwise would not be comparable.

C.3.5. FTP-75

This driving cycle used in North America was initially specified in 1975 as *Federal Test Procedure* in the *Code of Federal Regulations* number 40 (*Protection of Environment*) part 86 (*Control of emissions from new and in-use highway vehicles and engines*) and is known as *FTP-75* [oE00]. It corresponds to a transient standardized cycle representing a typical driving in the United States and consisting of three phases: cold start, transient and hot start.

C.3.6. Japan-10-15

This modal standardized driving cycle created initially in 1983 is specified in the Japanese standard JISHA 899 *Technical Standard for 10-15-Mode Exhaust Emission Measurement for Gasoline-Fueled Motor Vehicles* from the *Japan Industrial Safety and Health Association* - JISHA.

C.3.7. Energy storage device

There are several ways to store the energy in a vehicle, as presented in figure C.2.

Chemical energy sources have been traditionally used in vehicles due to their higher energy-to-mass ratio $E_{Batt\ specific}$ compared to other energy storages, as can be seen in figure⁵ C.3-a. Nevertheless, actual studies estimate the maximum of the worldwide oil

⁵The energy-to-mass ratio of gasoline and diesel corresponds to their lower heating value - LHV - (see

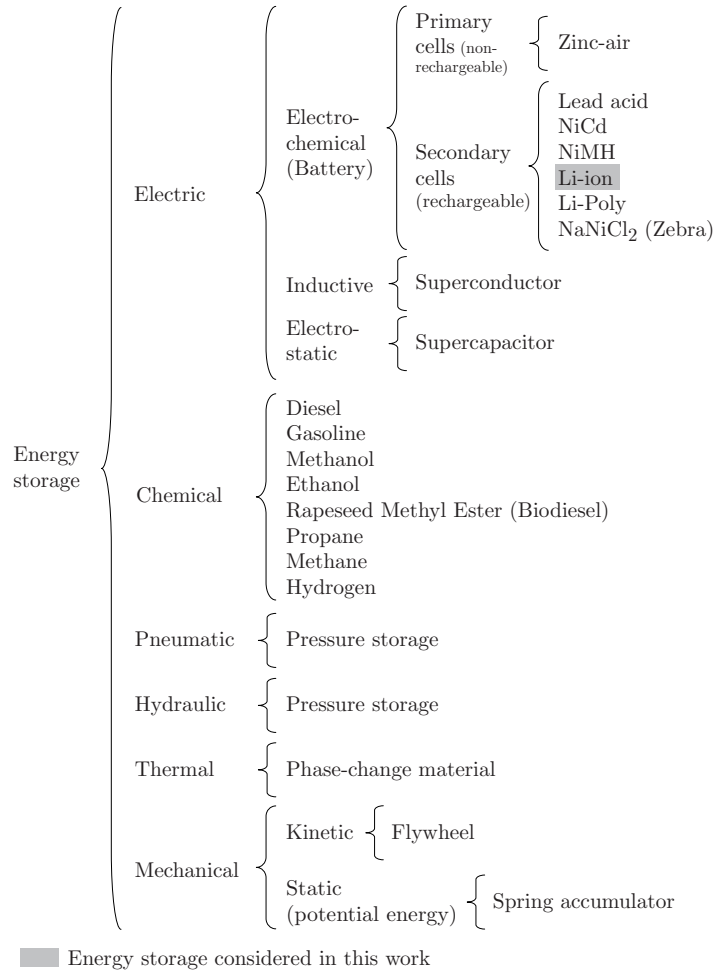


Figure C.2.: Energy storage classification [Hof09].

production curve to be reached in the coming twenty to thirty years followed by a strong fall (see e.g. [Kon09], [MC09] [SZ08]). Therefore, the automotive industry is moving toward alternative energy sources, from which the electrochemical ones (the batteries) seem to be the most attractive alternative (see e.g. [WFO09], [Hof09] and [She09]). Furthermore, since not all the energy needed during the entire lifetime of the vehicle can be stored in a battery with acceptable volume and weight, rechargeable batteries made of so-called secondary cells are considered. However, there is still a long way to fulfill the requirements of actual automotive customers used to drive vehicles with internal combustion engines regarding safety, costs, lifetime, cycle stability, drive range

e.g. [WFO09]). The power-to-mass ratio $P_{Batt\ specific}$ depends on the engine technology (see e.g. [Bit09]).

(or indirectly the energy-to-mass ratio) and the driving performance (related with the power-to-mass ratio). Nonetheless, some authors suggest that the driving performance requirements and therefore the design requirements of modern and future vehicles must be reevaluated since statistics show that in crowded regions (as in Europe), most trips are undertaken in urban areas, lasting five kilometers in average, with 1.1 persons per vehicle and at speeds that are below 20 km/h in 85 % of the cases [Hir11], [BH11].

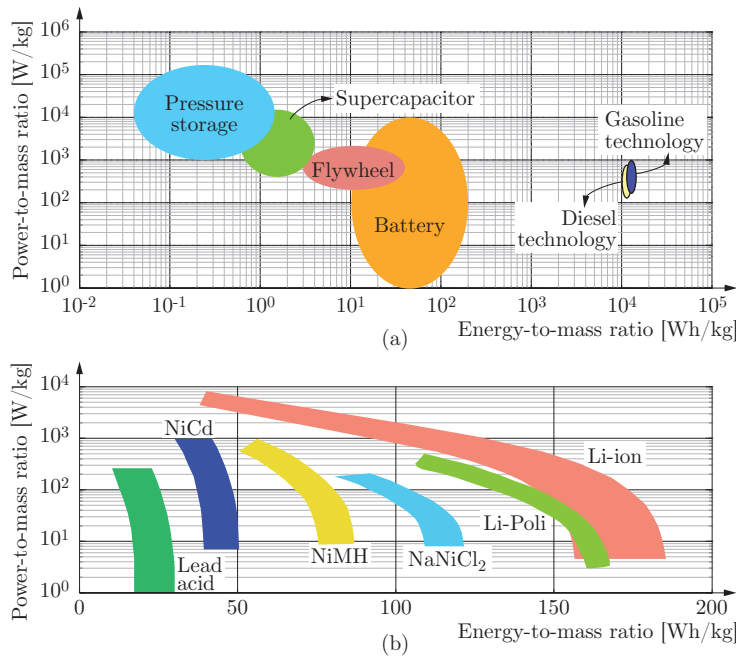


Figure C.3.: Ragone chart: Energy-to-mass and Power-to-mass ratios for different energy storage and converter technologies (see e.g. [WFO09], [Hof09], [Bit09], [vdBVvM⁺06] and [CC00]).

Due to its cycle stability and comparatively high energy-to-mass ratio (see figure C.3-b), the nickel-metal hydride battery has been widely used until now in several applications concerning electric and hybrid vehicles. Nevertheless, its future as main energy storage is limited because of its relative short lifetime and restricted optimization possibilities to enhance its energy-to-mass ratio [WFO09]. The nominal efficiency of nickel-metal hydride batteries is around 70 % [Hof09].

Most research efforts are concentrated worldwide nowadays in the development of lithium-ion batteries. The reason is the strong potential of this battery technology to reach high energy-to-mass ratios in comparison with the other battery technologies presented in figure C.3. Furthermore, lithium-ion batteries are characterized by low self-

discharge, high cycle stability and quite good nominal efficiency (up to 93 %) [WFO09], [Hof09], [Ise09]. Lithium-ion batteries are however related with some disadvantages when used in automotive applications. Mechanical damages can lead to leakages and excessive charges or discharges can result in thermal runaway. Under this condition, the temperature within a battery cell can increase. If the resulting heat cannot be dissipated by the battery cooling system, other cells can get damaged and a chain reaction starts. Since damaged cells can explode (depending on their chemical composition), a fail safe condition must be guaranteed through e.g. pressure relief valves or non-flammable foam [WFO09]. Moreover, based on the current industrial technical knowledge, the optimization potential of this kind of battery is chemically limited to energy-to-mass ratios about 200 Wh/kg and power-to-mass ratios about 10000 W/kg [WFO09]. Therefore, application oriented research to develop battery technologies capable to fulfill all customers expectations is strongly needed. However, the lithium-ion battery is going to be taken as basis for further analysis in this work as it seems to be the most promising technology considering the current knowledge in this area.

Information about other energy storage technologies can be found in [WFO09], [Hof09], [WB06] or [Ise09].

C.4. Electric motors

Figure C.4 shows a classification of electric motors [Hof09]. In this section, the synchronous motor with permanent magnets and the induction motor are described and analyzed since they seem to be the most attractive electric motor types for the automotive industry on the way toward the electrification of the powertrain of passenger vehicles (see e.g. [Wil11]). As stated in chapter 3.5, the expression *synchronous motor* is used in this work to refer to the synchronous motor with permanent magnets. More information about other motor types can be found, for example, in [BT09], [Ise02], [WFO09], [Hof09], [WB06] and [Wil11].

Additionally, an approach to determine the torque and power of the two considered electric motor types is presented. This approach can be used in the early design phase to set the motor specifications to fulfill given driving performance requirements (as described in the section 3.2).

Synchronous and induction motors belong to the so called *alternating current motors*

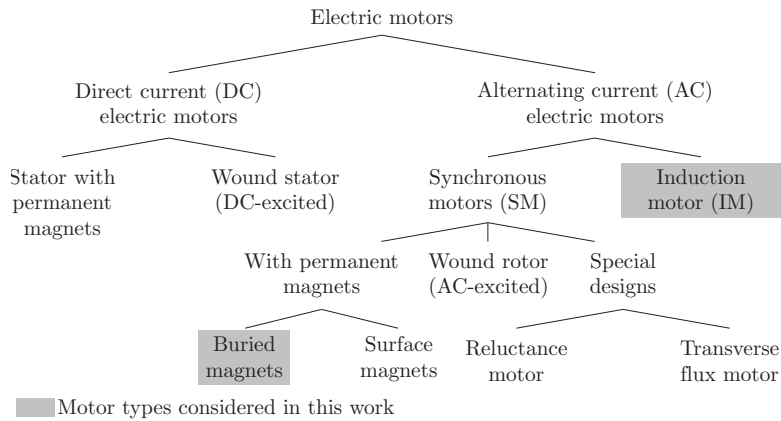


Figure C.4.: Classification of electric motors [Hof09].

or briefly AC-motors. This kind of electric motors are characterized by interleaved phase coils (windings) distributed along the periphery of the stator. When connected to a three phase power system⁶ they produce a rotatory magnetic field whose frequency f_{rmf} depends on the frequency of the power supply f_{supp} and on the number of pole-pairs p_{EM} according to [Ise02]:

$$f_{rmf} = \frac{f_{supp}}{p_{EM}} . \quad (C.20)$$

It can be distinguished between synchronous and induction AC-motors depending on the layout of the rotor [Ise02]. Figure C.5 shows a comparison between the design of these two electric motors considered in this work.

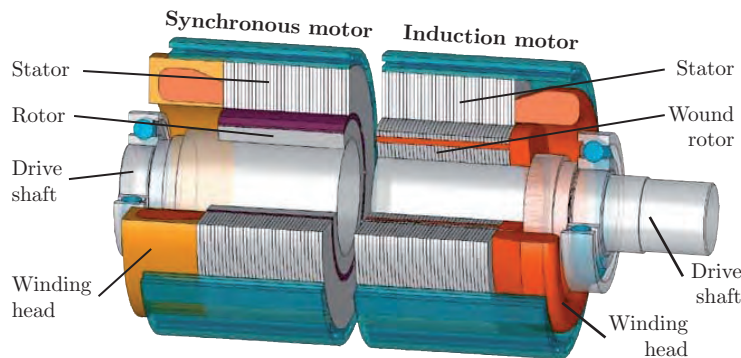


Figure C.5.: Comparison of the design of induction (with wound rotor) and synchronous motors [Hof09].

⁶Three phase windings are the most used for high power while two phase windings are suitable for residential applications with low power requirements (below some kW) [BT09].

C.4.1. Induction motor

The operating principles of this kind of motors were introduced by the Italian Galileo Ferraris and the Yugoslav Nicola Tesla in 1885 and 1887 respectively. Afterwards, the Russian Michail von Dolivo-Dobrowolsky presented the first three-phase induction motor in 1889 [Kol11]. Nowadays, about 95 % of all driving propulsion systems are induction motors. This is mainly due to its robustness, its low production and maintenance costs, as well as its easy and robust design. Though until now the induction motors were operated mainly at a continuous rotational speed (e.g. pumps, ventilators or compressors), modern power electronics makes it possible to use them in controlled powertrains with variable rotational speed (e.g. traction powertrains or lifts).

When a three phase induction motor is star or delta connected to a three phase alternating power system, an alternating current flows through the conductors of each phase in the stator. These currents are 120° phase delayed in time. Because the phases in the stator are also $120^\circ/p_{EM}$ spatially displaced, a rotatory field with a frequency f_{rmf} (see C.20) or a synchronous rotational speed

$$\omega_{syn} = 2 \cdot \pi \cdot f_{rmf} = 2 \cdot \pi \cdot \frac{f_{supp}}{p_{EM}} \quad (\text{C.21})$$

arises in the air gap (space between the rotor and the stator of an induction motor⁷) [Kol11]. This rotatory field induces a voltage in the uninsulated conductors of the cage rotor or in the windings of the wound rotor. The circuit diagram of a three phase induction motor connected to a power supply with a voltage U_{supp} and a frequency f_{supp} can be seen in figure C.6 [Ise02].

It must be pointed out, that cage rotors are more robust than wound rotors and that wound rotors are used normally in applications with limited variable speed [BT09]. Therefore, induction motors with cage rotor are more suitable than traction motors in passenger vehicles.

Alternating currents arise also in the rotor due to the induced voltage. These currents produce a rotatory magnetic field in the rotor as well. Due to the interaction of the magnetic fields, a tangential force (Lorentz force) arises in the air gap producing a torque.

⁷The air gap of induction motors varies from approximately 0.3 mm (for low powers) to about 3.0 mm (for large powers) [BT09].

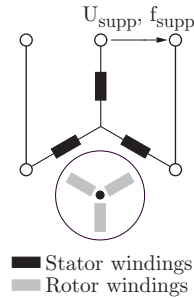


Figure C.6.: Circuit diagram of a three phase induction motor [Ise02].

According to Lenz's law, the rotor moves in the direction of the rotatory magnetic field to counteract the source of the induced voltage. The smaller the difference between the rotational speed of the rotor $\omega_{rot, IM}$ and the rotational speed of the magnetic field n_s , the weaker the induced voltage in the rotor. This difference can be expressed as the slip s_{IM} :

$$s_{IM} = \frac{\omega_{syn} - \omega_{rot, IM}}{\omega_{syn}} = 1 - \frac{\omega_{rot, IM}}{\omega_{syn}} . \quad (C.22)$$

No voltage would be induced if the slip s_{IM} becomes zero. Nevertheless, under normal circumstances, this situation never occurs due to friction effects (e.g. in bearings or due to the air). The rotational speed of the rotor is always smaller than the synchronous rotational speed ($\omega_{rot, IM} < \omega_{syn}$) and the absolute value of the slip is always greater than zero ($s_{IM} > 0$). Therefore, this electric motor is also called asynchronous motor [Kol11].

The nominal efficiency of induction motors (by nominal torque and power) varies with the output power and is about 80 % to 90 % [Vog88]. More details as well as the mathematical and physical description of induction motors used as power units in passenger powertrains can be found in [Wil11].

C.4.2. Synchronous motor

The North-American Charles S. Bradley and the German Friedrich August Haselwander submitted patent applications regarding a three phase synchronous AC-generator in March and July of 1887 respectively (see [KK04] and [HP90]). Since then, the syn-

chronous motors have been widely used mainly as electric generators in power plants (e.g. hydraulic or wind power plants) but also as automobile alternators, small power actuators in automobiles (e.g. electric power steering assist) and other applications with a wide spectrum of speed and power [BT09]. While they have been mainly operated at constant speeds, modern power electronics makes it possible to use them in controlled powertrains with variable rotational speed [Ise02]. Additionally, modern power electronics avoids also the use of a start-up device (starter), which constitutes, otherwise, a disadvantage of synchronous motors compared with other motor types [WB06].

The stator design of a synchronous motor is very similar to that of an induction motor. Nevertheless, in contrast to the induction motor, in which the magnetic field in the rotor is induced by the magnetic field in the stator, windings supplied with direct current (figure C.7-a) or permanent magnets create the magnetic field in the rotor of the synchronous motor. The rotor moves then synchronously with the rotatory magnetic field of the stator with a rotational speed (see equation C.21).

$$\omega_{rot, SM} = \omega_{syn} . \quad (C.23)$$

The permanent magnets can be distributed on the rotor surface or can be buried in the rotor itself (see e.g. [WB06] and [Kol11] for other forms of buried magnets). As stated before, the expression *synchronous motor* is used in this work to refer to synchronous motors with buried permanent magnets. The use of magnets in this kind of electric motors reduces the mechanical and electrical complexity avoiding windings in the rotor and the contact between moving parts (no abrasion and simplification of maintenance). It should be pointed out, that in the traditional layout with the rotor placed within the stator (internal rotor), the fixation of the magnets on and in the rotor is related with some problems due to the centrifugal force. This has led to the use of this kind of motors in applications with low power requirements [WFO09]. This problem does not arise when the stator is placed within the rotor (external rotor). However, the fixation problem is being resolved to some extent for traditional designs with internal rotor and the use of this kind of motors in higher power applications is expected to be possible [BSK06]. Nevertheless, the synchronous motor with buried permanent magnets is still the most used electric motor type for the electrification of the powertrain of passenger vehicles (see e.g. [Hof09] and [WB06]). The nominal efficiency of induction motors (by nominal torque and power) varies with the output power and is about 92 % to 99 %

[Vog88]. Figure C.7 presents the circuit diagram of synchronous motors with wound rotor (a) and with buried permanent magnets (b).

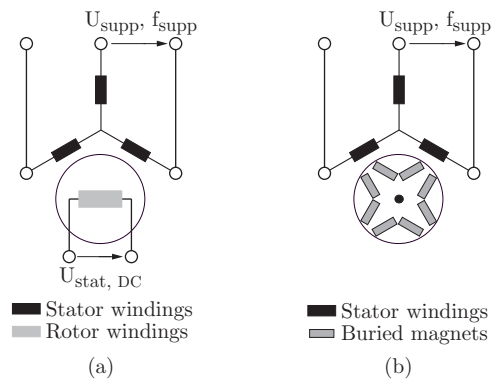


Figure C.7.: Circuit diagram of a three phase induction motor [Ise02] with wound stator (a) and with buried permanent magnets (b).

C.4.3. Comparison of the structural and operational characteristics of synchronous and induction motors

As stated before, synchronous and induction motors seem to be the most attractive technologies for the automotive industry toward the electrification of the powertrain of passenger vehicles. Nevertheless, there is no unique preference for any of these two motor types. Their structural and operational advantages and disadvantages are described by [Wil11] as presented in table C.1 (see also [Hof09], [WFO09] and [WB06]). Based on this information, it is evident, that while synchronous motors have structural advantages, induction motors have operational advantages. Therefore, it is a priori not possible to decide between these two kinds of motors for the electrification of the powertrain of passenger vehicles. Each application case must be analyzed individually to state the suitability of each motor type.

C.4.4. Efficiency of induction and synchronous electric motors

The efficiency plays a very important role when selecting the motor type to be used to electrify the powertrain of a vehicle since it determines the energy consumption of the vehicle. Figure C.8 shows representative efficiency characteristic diagrams of induction and synchronous motors with a traditional flux control according to Willberger [Wil11].

Table C.1.: Advantages and disadvantages of synchronous and induction motors [Wil11]

	Criteria		Induction motor		Synchronous motor
Structural	Torque density Φ_{EM}	o	Φ_{EM} depends on optimization criteria and heat transfer conditions. High Φ_{EM} leads to high losses.	++	Φ_{EM} depends on optimization criteria and heat transfer conditions. High number of poles have high Φ_{EM} and high losses.
	Active mass $m_{EM_{act}}$ or Volume [Hof09]	o	Wounds in rotor increase the motor weight.	++	Magnetic field in rotor through magnets \Rightarrow less $m_{EM_{act}}$
Operational	Efficiency η_{EM}	+	Copper and iron losses in stator. Copper losses in rotor.	++	Copper and iron losses in stator. Very low losses in rotor.
	Drag loss (decoupling mechanism)	++	No drag losses (no decoupling mechanism necessary).	-	Permanent excitation of rotor due to permanent magnets (decoupling mechanism recommendable / necessary).
	Overloading capacity	++	High, since high rotor temperatures are permissible.	+	Low, since high temperatures lead to demagnetization.
	High speed service	++	η_{EM} increases in the field weakening region. Breakdown torque $\sim \omega^{-2}$. High optimization potential to increase η_{EM} .	+	η_{EM} drops down in the field weakening region. Breakdown torque $\sim \omega^{-1}$.
	Fail safe	++	Idle speed and short circuit are safe states.	-	Short circuit \Rightarrow Alternating torque, brake torque Idle speed \Rightarrow Drag torque
Costs	Production	+	Relative low production cost.	o	Awaited cost increase in row materials for magnets.

– Very bad - Bad o Neutral + Good ++ Very good

It can be seen, that while the efficiency of synchronous motors is higher at partial loads in nominal service (under the nominal torque nM and up to the nominal rotational speed ${}^n\omega$), the induction motor presents higher efficiency values in overload service and in the field weakening region. Based on this, it can be deduced, that the type of electric motor to be selected depends on the operating points of the considered application.

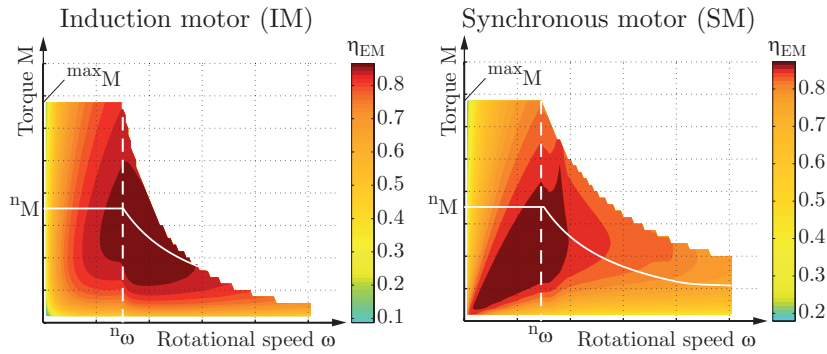


Figure C.8.: Schematic steady state efficiency characteristic diagrams of induction (a) and synchronous (b) motors [Wil11].

The automotive industry prefers synchronous motors (with permanent magnets) as induction motors to electrify the powertrain of passenger vehicles because, among other things, of their higher nominal efficiency⁸ (see e.g. [WFO09], [Hof09] and [WB06] as well as chapters C.4.2 and C.4.3). The energy consumption in a driving cycle for a vehicle using synchronous motors is lower than for the same vehicle using induction motors. These synchronous motors are normally controlled using conventional power electronics with a constant flux control strategy in the region of constant torque (see figure 3.7), as presented by Hofmann [Hof09]. Nevertheless a variable flux control can be implemented in the power electronics with the aim of reducing losses in the entire operating range of both synchronous and induction motors [WH10], [Wil11]. Using this strategy, the efficiency of induction motors in the region of constant torque and nominal service can be increased up to 45 % while the efficiency of synchronous motors (with permanent magnets) can be increased in the region of constant torque and overload service up to 5 % [Wil11]. Representative efficiency characteristic diagrams of induction and synchronous motors using a variable flux control strategy are presented in figure C.9. Additionally, using the variable flux control, the energy consumption is pretty much the same for both electric motor types in the New European Driving Cycle - NEDC - (see chapter C.3.4).

⁸The nominal efficiency of an electric motor is defined at nominal torque nM and nominal Power nP .

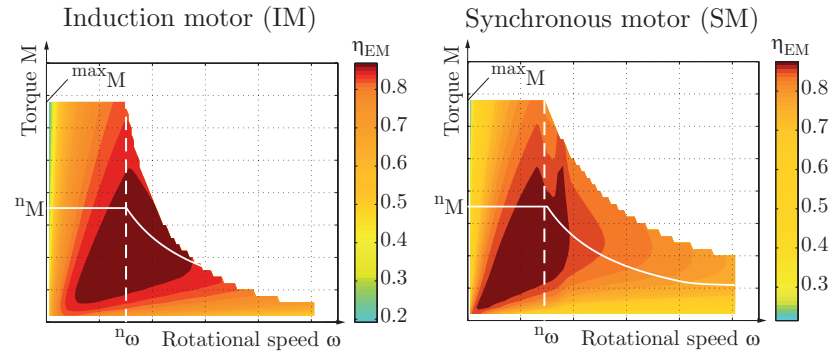


Figure C.9.: Schematic steady state efficiency characteristic diagrams of induction (a) and synchronous (b) motors with variable flux control [Wil11].

Summarizing, not only the general characteristics of the electric motor type (as presented in chapters C.4.1, C.4.2 and C.4.3) and its nominal efficiency but furthermore the application scenario and the control strategy must be taken into account to select an electric motor type to be used for the electrification of the powertrain of a passenger vehicle.

C.4.5. Comparison between the traction force diagrams of a vehicle with internal combustion engine and a vehicle with electric motor(s)

Figure C.10 shows the traction force diagram for a vehicle with internal combustion engine and a vehicle with electric motor(s). It should be noticed, that the curve illustrated in this figure, representing the electric motor, can be obtained in nominal service for both an induction and a synchronous motor. Nevertheless, the curve corresponding to the overload service is considered since most of the driving conditions with a normal passenger car correspond to operating points far away from the full load curve and those near it normally do not correspond to a permanent working condition (see e.g. [Wil11] and [Lun09]). Although the results are slightly different when considering the overload service of both motor types, in figure C.10 the curve of a synchronous motor (SM) is presented exemplarily.

While in a vehicle with electric motor(s) the maximum torque in nominal (nM) or overload (${}^{max}M$) service is available from standstill (${}_V\dot{x} = 0$ km/h), in a concept with internal combustion engine a speed converter (clutch) is needed to bridge the gap to reach the engine idle speed. Thus, in a concept with electric motor(s), the maximum

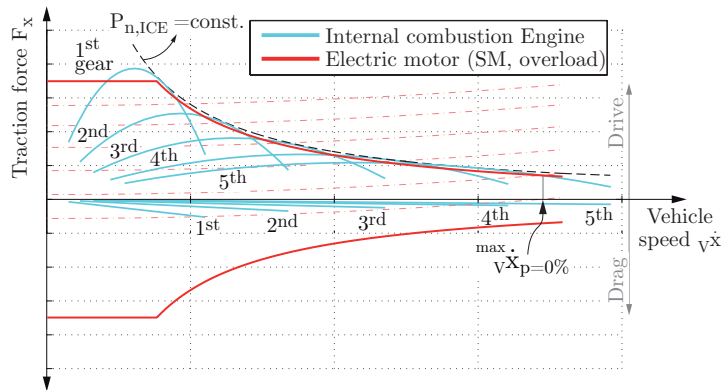


Figure C.10.: Comparison between the steady state traction force diagrams of a vehicle with internal combustion engine - ICE - (see also [HW09]) and a vehicle with electric motor(s). The curve of a synchronous motor (SM) in overload service is shown exemplarily. For the ICE, only the maximum torque for all gears is presented. Both the ICE and the electric motor presented lead to similar driving performances (e.g. same maximum longitudinal speed $\overset{max}{V} \dot{x}_{p=0} \%$ on flat road.).

excess traction force and therefore the climbing and acceleration ability are available from standstill. Furthermore, due to the fact that the maximum torque remains constant until the nominal rotational speed of the engine ${}^n\omega$, the excess traction force and hence the climbing and acceleration ability show a more constant behavior than in a vehicle with internal combustion engine.

It is worth noting, that the traction curves presented in figure C.10 for both the internal combustion engine and the electric motor lead to similar driving performances. This can be concluded from the similar excess traction forces that can be obtained in both cases. Nevertheless, a very important difference between both concepts are the gaps between the curve corresponding to the internal combustion engine and the line of constant power. In the case of a synchronous motor (as presented in the figure), these gaps are not present. This leads to a more uniform driving performance avoiding, for example, frequent gear shifting when driving uphill in a vehicle with internal combustion engine. This difference together with the overloading ability of electric motors suggests also, that an electric motor with lower nominal power could lead to a very similar driving performance as that offered by a corresponding internal combustion engine.

Another important aspect concerns the behavior of the output power. While in a vehicle with internal combustion engine a gearbox is needed to adjust the traction force

depending on the power requirements and the current driving speed, in an electric vehicle a gearbox is not strictly necessary. A transmission (with constant or variable ratio) can be used to adjust the speed range reducing, at the same time, the nominal torque nM and therefore the motor weight (see also [Hof09]).

C.5. Power electronics

As stated before in chapter 3.4.1, lithium-ion batteries are considered as energy storage devices for further analysis in this work. When working in the corresponding state of charge range, these batteries supply a nearly constant direct current. This current must be converted before being supplied to the alternating current motors considered in this work (see chapter 3.5). Generally speaking, the electric energy can be converted in four different ways, as shown in figure C.11. The energy stored in the battery must be converted using a DC/AC converter before being supplied to the electric motors. To be able to recuperate kinetic energy while braking, the alternating current must be converted again in direct current to be supplied to the battery. Furthermore, a DC/DC converter must be used to supply electric energy to auxiliaries with a lower voltage than that of the battery used to supply the electric motors (called also traction battery).

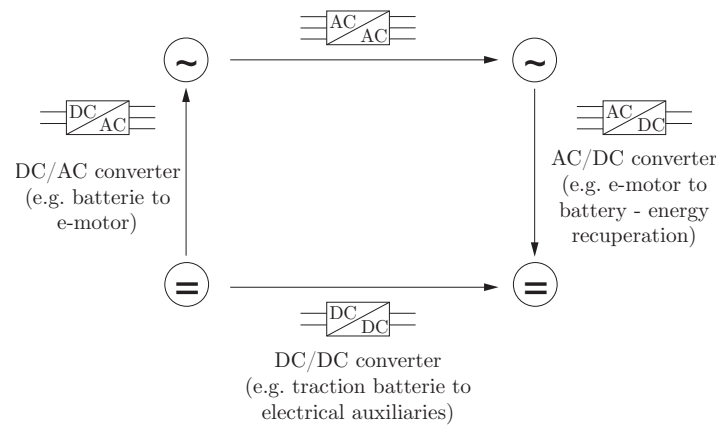


Figure C.11.: Electric energy conversion (see [WFO09] and [Hof09]).

In theory, the frequency f_{rmf} of the rotatory magnetic field (see also equation C.21), the voltage in the stator $V_{stat, IM}$, the number of pole-pairs p_{EM} and the slip s_{IM} can be used to control the rotational speed $\omega_{rot, IM}$ and the torque M_{EM} of an induction motor. Nevertheless, the slip s_{IM} results from the applied load torque and the number of

pole-pairs p_{EM} cannot be continuously varied during operation. Therefore, the voltage in the stator $V_{stat, IM}$ and the frequency of the rotatory field f_{rmf} , which depends on the frequency of the power supply f_{supp} (as shown in equation C.20), are used. This is shown in figure C.12 for an induction motor. In this figure, some so-called operating characteristic curves are presented. Each curve corresponds to a constant synchronous speed of the rotatory field in the stator $\omega_{syn i}$ (see equation C.21). In idle state, the rotatory speed of the rotor $\omega_{rot, IM}$ is the same as the synchronous speed of the magnetic flux in the stator ω_{syn} . Under this condition, there is no slip s_{IM} (see equation C.22) and no output torque M_{EM} is supplied, as shown exemplarily in figure for a certain synchronous speed $\omega_{syn i}$. If the load applied on the output of the electric motor is increased, the speed of the rotor $\omega_{rot, IM}$ decreases leading to a new operating point characterized by a higher slip s_{IM} and therefore by a higher output torque M_{EM} . Furthermore, the synchronous rotatory speed $\omega_{syn i}$ can be increased by increasing the frequency of the rotatory magnetic field f_{rmf} according to C.21. By keeping the load constant, this would lead to another operating point at a higher output speed.

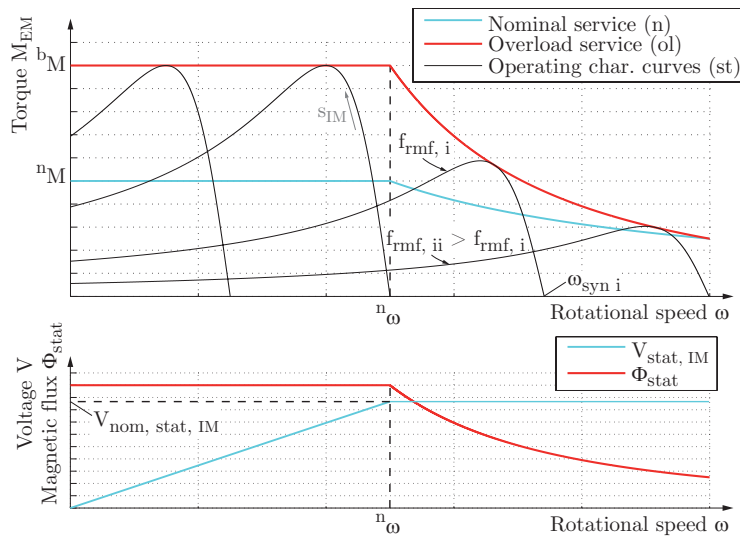


Figure C.12.: Operational characteristic curves of an induction motor in steady state for different frequencies of the rotatory field f_{rmf} .

For rotational speeds under the nominal one $n\omega$ (region of constant torque), an operating point can be reached by varying the frequency of the rotatory field in the stator f_{rmf} . In this region, the stator voltage $V_{stat, IM}$ is linearly varied with the frequency f_{rmf} up to the nominal voltage $V_{nom, stat, IM}$ to avoid influencing the breakdown torque M_b and to maintain the magnetic flux Φ_{stat} constant, which is given by [Spr09]:

$$\Phi_{stat} \sim \frac{V_{stat, IM}}{f_{rmf}}. \quad (C.24)$$

For higher rotational speeds ($\omega_i > n\omega$), the voltage $V_{stat, IM}$ is kept constant ($V_{nom, stat, IM}$) resulting in a weakening of the magnetic flux [Hof09]. This behavior gives the name to this kind of motor. Furthermore, the power electronics changes the phase sequence of the alternating current to change the direction of rotation of the electric motor.

The power electronics to control the synchronous motor is similar to that explained before for induction motors. In both cases, the nominal efficiency of the power electronics is around 93 % [WFO09].

C.6. Dimensioning of electric motors: Four-wheel drive powertrain architecture

Figure C.13 presents the traction force diagram for the considered vehicles with a four-wheel drive powertrain architecture. These results are very similar to those presented in chapter 3.7.6, figure 3.18. Since the same vehicle mass was considered for vehicles with two and four in-wheel motors, the main difference arises because of the moment of inertia of the additional electric motors and the transmission ratio of their corresponding gearboxes.

C.7. Weight of different electric vehicles (EV) in comparison with their counterparts with internal combustion engine (ICE)

Table C.2 shows the weight of different electric vehicles (EV) in comparison with their counterparts with internal combustion engine (ICE). The approach to estimate the mass m_{v0} of the corresponding vehicle without mechanical powertrain and fuel tank as well as the mass of the power electronics $m_{PE\ total}$ is presented in table 3.12, chapter 3.7.6. The battery mass can be found in table 3.8, chapter 3.7.5. To approximate the mass of the electric motors, the mass of one electric motor for the subcompact vehicle A

C.7. Weight of different electric vehicles (EV) in comparison with their counterparts with internal combustion engine (ICE)

Table C.2.: Weight of different electric vehicles (EV) in comparison with their counterparts with internal combustion engine (ICE).

Two in-wheel motors (rear-wheel drive)								
			2xIM			2xSM		
			A^-	A	B	A^-	A	B
EM	Individual ^a	m_{EM}	20.2	30.0	34.6	16.9	25.0	28.9
	Total	$m_{EM\ total}$	40.5	60.0	69.2	33.7	50.0	57.8
			[kg]					
Mass EV ^b		$m_{v, EV}$	810.5	995.0	1169.2	803.6	986.2	1159.0
Rel. weight change ^c		Δm_v	[-4.6]	[-5.2]	[-2.6]	[-5.5]	[-6.1]	[-3.4]
			[%]					

Four in-wheel motors (four-wheel drive)								
			4xIM			4xSM		
			A^-	A	B	A^-	A	B
EM	Individual ^a	m_{EM}	10.1	15.0	17.3	8.4	12.5	14.4
	Total	$m_{EM\ total}$	40.5	60.0	69.2	33.7	50.0	57.7
			[kg]					
Mass EV ^b		$m_{v, EV}$	840.5	1025.0	1199.2	833.5	1016.2	1188.8
Rel. weight change ^c		Δm_v	[-1.1]	[-2.4]	[-0.1]	[-1.9]	[-3.2]	[-0.9]
			[%]					

^a The mass of an electric motor for the subcompact vehicle class was approximated to 25 kg (synchronous motor) and 30 kg (induction motor). This values take into account the active mass of the electric motor (see chapter 3.5.2), bearings and housing. The mass of the electric motors for the other vehicle classes was obtained proportionally based on their nominal torque ⁿ M (see also table 3.11).

^b Vehicle mass in running order $m_{v, EV} = m_{v0} + m_{EM\ total} + m_{PE\ total} + m_{Batt}$ (see also table 3.12).

^c $\Delta m_v = (m_{v, EV} - m_{v, ICE})/m_{v, EV}$ (see also table 3.12).

was estimated as 25 kg (synchronous motor) and 30 kg (induction motor) based on chapter 3.5.2. The mass of one electric motor for the other vehicle classes considered was approximated proportionally to its individual nominal torque (see table 3.11 in chapter 3.7.6).

Based on this approach, it can be concluded, that no appreciable weight change for an electric vehicle in comparison with its counterpart with internal combustion engine is to be expected. Therefore, the assumption made in chapter 3.7 concerning similar masses for these kind of vehicles can be assumed as valid for the calculations presented there.

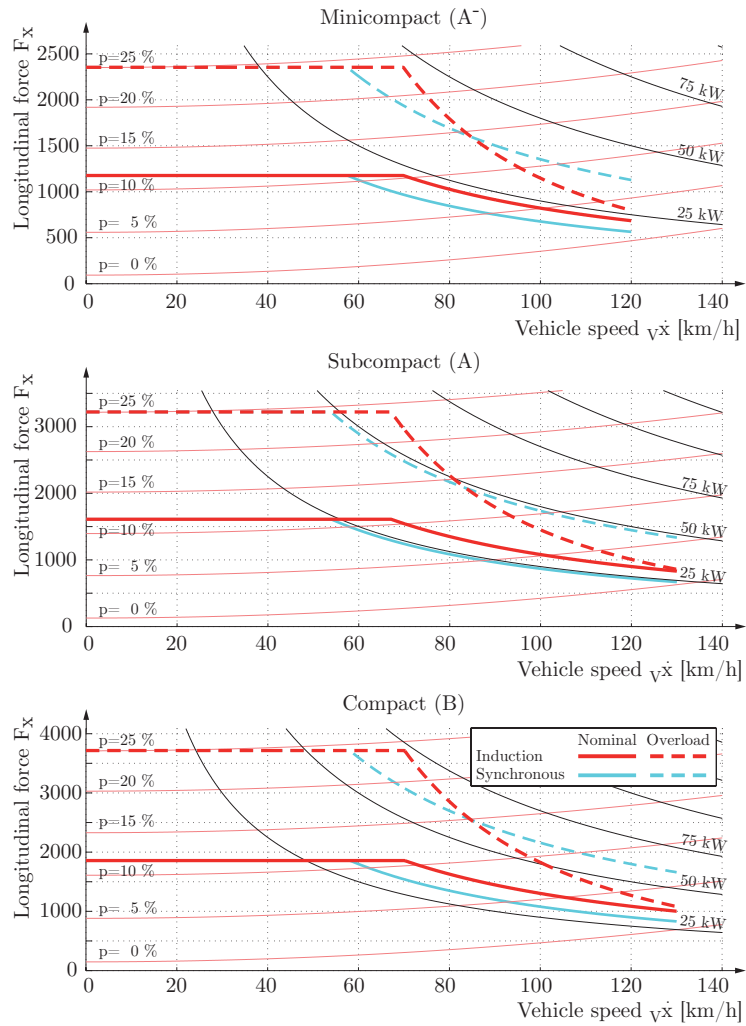


Figure C.13.: Steady state traction force diagrams for the vehicles with four in-wheel motors.

D. Appendix: Lateral dynamics

D.1. Single track vehicle model

The single track vehicle model as shown in figure D.1 was presented by *Rieker* and *Schunck* in 1940 [RS40]. It is a simple vehicle model needing few parameters and leading to usefully results to understand the fundamental behavior of vehicles and the influence of vehicle (e.g. wheelbase and weight distribution) and tire parameters [Wal06]. It serves also as basis for the design of vehicle dynamics controllers (see e.g. [Ros09]).

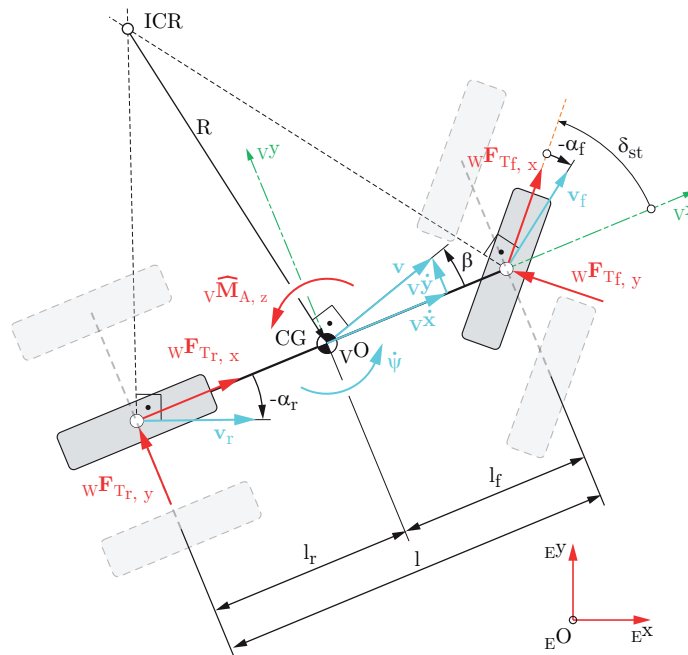


Figure D.1.: Simplified single track vehicle model.

This model is based on following simplifications (see e.g. [Wal06]):

- The wheel contact points W of the wheels belonging to the same axle (i.e. front

or rear axle) are assumed to coincide along the vehicle long axle.

- The height of the vehicle center of gravity is considered to be zero. Therefore, pitch and roll movements are neglected and the rotational speed of the suspended mass ${}_V\omega_{A, z}$ around its vertical axis is approximately equal to the yaw rate $\dot{\psi}$ (i.e. ${}_V\omega_{A, z} \approx \dot{\psi}$).
- The mass and the moment of inertia of the suspended and all the non-suspended masses are assumed to be concentrated in the common center of gravity and given by m_v and $I_{v, z}$.
- The longitudinal vehicle speed ${}_V\dot{x}$ is assumed as constant for a given operating point and becomes therefore a model parameter.
- The influence of the vehicle suspension (e.g. mechanical trail) are neglected.
- Small values of the steering wheel angle δ_{st} are assumed.

As proposed by *Niederkofler* [Nie11], the single track vehicle model is used in this work as basis for the design of the horizontal dynamics controller presented in chapter 4.2.2, with the state vector \mathbf{x} composed by the sideslip angle β and the yaw rate $\dot{\psi}$:

$$\mathbf{x} = \begin{bmatrix} \beta & \dot{\psi} \end{bmatrix}^T . \quad (\text{D.1})$$

Since the mass properties of the suspended and the non-suspended mass are assumed to be concentrated on the center of gravity of the entire vehicle (total vehicle mass m_v and equivalent moment of inertia around the vertical axis $I_{v, z}$), the equations of motion for the single track vehicle can be deduced based on those presented in chapter 2.4.1. Taking into account the linear momentum along the vehicle transversal axis ${}_V y$ and the angular momentum around the center of gravity (see chapter 2.4.1), the equations of motion describing the lateral dynamics of the single track vehicle model can be written in terms of the total vehicle mass m_v , the total moment of inertia of the vehicle around its vertical axis $I_{v, z}$, the vehicle lateral acceleration ${}_V\ddot{y}$, the yaw acceleration $\ddot{\psi}$, the yaw rate $\dot{\psi}$, the vehicle longitudinal speed ${}_V\dot{x}$, the lateral tire forces ${}_W F_{T_{f/r}, y}$ at each individual front and rear tire¹ and the distances $l_{f/r}$ from the vehicle center of gravity

¹The right subscripts f and r are used to denote variables at the front and rear axles respectively.

to the front and rear axles (see also [Hir09a]):

$$\begin{bmatrix} m_v & 0 \\ 0 & I_{v,z} \end{bmatrix} \cdot \begin{bmatrix} {}_V\ddot{y} \\ \ddot{\psi} \end{bmatrix} = m_v \cdot \begin{bmatrix} -\dot{\psi} \cdot {}_V\dot{x} \\ 0 \end{bmatrix} + \begin{bmatrix} 2 \cdot ({}_W F_{T_f, y} + {}_W F_{T_r, y}) \\ 2 \cdot ({}_W F_{T_f, y} \cdot l_f + {}_W F_{T_r, y} \cdot l_r) + {}_V \widehat{M}_{A, z} \end{bmatrix}. \quad (\text{D.2})$$

The term ${}_V \widehat{M}_{A, z}$ is introduced as an external additional yaw moment to influence the lateral dynamics of the vehicle. As presented in chapter 4.2.2, ${}_V \widehat{M}_{A, z}$ correspond in this work to the control yaw moment that is used as reference by the optimal longitudinal force allocation algorithm (see chapter 4.2.3) to determine the individual longitudinal tire forces ${}_W F_{T_i, x}$.

Assuming lateral accelerations not greater than approximately 3 m/s^2 (see e.g. [Wal06]) and small steering wheel angles $\delta_{st} \ll 1$ rad, the lateral tire forces, as presented in chapter 2.5.1, can be simplified to (see also [Hir09a]):

$${}_W F_{T_f, y} = -c_{\alpha, f} \cdot \left(-\delta_{st} + \frac{{}_V \dot{y} + \dot{\psi} \cdot l_f}{{}_V \dot{x}} \right), \quad (\text{D.3a})$$

$${}_W F_{T_r, y} = -c_{\alpha, r} \cdot \left(\frac{{}_V \dot{y} - \dot{\psi} \cdot l_r}{{}_V \dot{x}} \right), \quad (\text{D.3b})$$

where $c_{\alpha, f/r}$ correspond to the tire cornering stiffness (assumed as constant) of the front and rear tires respectively (see e.g. [Hir09a], [Wal06] or [MW04] for the explanation of this parameters and [Nie11] for the parameter values).

Furthermore, assuming small values of the sideslip angle β and considering that the magnitude of the total horizontal speed v of the vehicle can be expressed in terms of the magnitude of the longitudinal ${}_V \dot{x}$ and lateral ${}_V \dot{y}$ speeds as

$$v = \sqrt{({}_V \dot{x})^2 + ({}_V \dot{y})^2}, \quad (\text{D.4})$$

following relations can be established for a given operating point (where $\dot{v} = 0$ is valid):

$${}_V \dot{x} = v \cdot \cos(\beta) \rightarrow {}_V \dot{x} \approx v, \quad (\text{D.5a})$$

$${}_V\dot{y} = v \cdot \sin(\beta) \rightarrow {}_V\dot{y} \approx v \cdot \beta, \quad (\text{D.5b})$$

$${}_V\ddot{y} = \dot{v} \cdot \sin(\beta) + \dot{\beta} \cdot v \cdot \cos(\beta) \rightarrow {}_V\ddot{y} \approx \dot{\beta} \cdot v. \quad (\text{D.5c})$$

Introducing equations D.3 and D.5 in the system of equations D.2, the equations of motion for the extended single track vehicle model can be written in the state space in terms of the state vector given by equation D.1, the input vector

$$\mathbf{u} = \begin{bmatrix} \delta_{st} \end{bmatrix}, \quad (\text{D.6})$$

and the controllable input vector

$$\mathbf{u}_c = \begin{bmatrix} {}_V\widehat{M}_{A, z} \end{bmatrix} \quad (\text{D.7})$$

as:

$$\dot{\mathbf{x}} = \mathbf{A} \cdot \mathbf{x} + \mathbf{B} \cdot \mathbf{u} + \mathbf{B}_c \cdot \mathbf{u}_c, \quad (\text{D.8})$$

where

$$\mathbf{A} = 2 \cdot \begin{bmatrix} -\frac{c_{\alpha,f} + c_{\alpha,r}}{m_v \cdot {}_V\dot{x}} & \frac{-c_{\alpha,f} \cdot l_f + c_{\alpha,r} \cdot l_r}{m_v \cdot ({}_V\dot{x})^2} - \frac{1}{2} \\ \frac{-c_{\alpha,f} \cdot l_f + c_{\alpha,r} \cdot l_r}{I_{v, z}} & -\frac{c_{\alpha,f} \cdot l_f^2 + c_{\alpha,r} \cdot l_r^2}{I_{v, z} \cdot {}_V\dot{x}} \end{bmatrix}, \quad (\text{D.9a})$$

$$\mathbf{B} = 2 \cdot \begin{bmatrix} \frac{c_{\alpha,f}}{m_v \cdot {}_V\dot{x}} & \frac{c_{\alpha,f} \cdot l_f}{I_{v, z}} \end{bmatrix}^T, \quad (\text{D.9b})$$

$$\mathbf{B}_c = \begin{bmatrix} 0 & \frac{1}{I_{v, z}} \end{bmatrix}^T. \quad (\text{D.9c})$$

E. Appendix: Vertical dynamics

E.1. Frequency filter for the seat in vertical direction

According to the International Standard 2631-1 [fSI97], the transfer function of the filter W_k (see also figure 5.1) used to obtain the frequency weighted vertical acceleration ${}^w_V\ddot{z}_P$ based on the measured (or simulated) vertical acceleration ${}_V\ddot{z}_P$ of a point P is given as a function of the frequency $\omega = 2 \cdot \pi \cdot f$ by:

$$W_k(\omega) = \frac{{}^w_V\ddot{z}_P}{{}_V\ddot{z}_P} = W_{k,h}(\omega) + W_{k,l}(\omega) + W_{k,t}(\omega) + W_{k,s}(\omega), \quad (\text{E.1})$$

where

$$W_h(\omega) = \left| \frac{1}{1 + \frac{\sqrt{2} \cdot \mathbb{k}_1}{j \cdot \omega} + \left(\frac{\mathbb{k}_1}{j \cdot \omega}\right)^2} \right|, \quad (\text{E.2a})$$

$$W_l(\omega) = \left| \frac{1}{1 + \frac{\sqrt{2} \cdot j \cdot \omega}{\mathbb{k}_2} + \left(\frac{j \cdot \omega}{\mathbb{k}_2}\right)^2} \right|, \quad (\text{E.2b})$$

$$W_t(\omega) = \left| \frac{1 + \frac{j \cdot \omega}{\mathbb{k}_3}}{1 + \frac{j \cdot \omega}{\mathbb{K}_1 \cdot \mathbb{k}_3} + \left(\frac{j \cdot \omega}{\mathbb{k}_3}\right)^2} \right|, \quad (\text{E.2c})$$

$$W_s(\omega) = \left| \frac{1 + \frac{j \cdot \omega}{\mathbb{K}_2 \cdot \mathbb{k}_4} + \left(\frac{j \cdot \omega}{\mathbb{k}_4}\right)^2}{1 + \frac{j \cdot \omega}{\mathbb{K}_2 \cdot \mathbb{k}_5} + \left(\frac{j \cdot \omega}{\mathbb{k}_5}\right)^2} \cdot \left(\frac{\mathbb{k}_4}{\mathbb{k}_5}\right)^2 \right|, \quad (\text{E.2d})$$

and j correspond to the imaginary unit.

The values of the coefficients k_i and K_n are defined in the mentioned International Standard 2631-1 and reproduced in table E.1.

Table E.1.: Coefficients of the frequency filter W_k used to weight the vertical acceleration according to the International Standard 2631-1 [fSI97].

Parameter	Value	Units
k_1	$2 \cdot \pi \cdot 0.4$	
k_2	$2 \cdot \pi \cdot 100$	$\left[\frac{\text{rad}}{\text{s}} \right]$
k_3	$2 \cdot \pi \cdot 12.5$	
k_4	$2 \cdot \pi \cdot 2.37$	
k_5	$2 \cdot \pi \cdot 3.35$	
K_1	0.63	$[-]$
K_2	0.91	

E.2. Quarter vehicle model

The simplified quarter vehicle model, as presented in figure E.1, is composed by two masses m_{A_q} and m_w representing the mass of a vehicle corner¹ and a non-suspended mass respectively, each having the movement in vertical direction as only degree of freedom. They are connected by the suspension system, which in the case of a passive system is composed by a suspension spring and a shock absorber. The system is excited by the road unevennesses indicated by z_{road} in figure E.1. Furthermore, since it is assumed that both m_{A_q} and m_w have only one degree of freedom (movement in the vertical direction z) and that the system without excitation remains in steady state under the action of the gravitational force, the movement of both masses can be described in a single coordinate system, for which, therefore, no special index is used. Finally, in most cases the tire damping, as explained in chapter 2.5.2 is neglected.

According to equations 2.1 and 2.3, the equation of linear momentum for the suspended m_{A_q} and for the non-suspended mass m_w can be then written as:

$$\sum F_A = F_c + F_d = m_{A_q} \cdot \ddot{z}_A, \quad (\text{E.3a})$$

¹Considering the total mass of the vehicle m_A to be homogeneously distributed over its volume, the mass of a vehicle corner m_{A_q} would correspond to a quarter of its total mass, i.e. $m_{A_q} = m_A/4$.

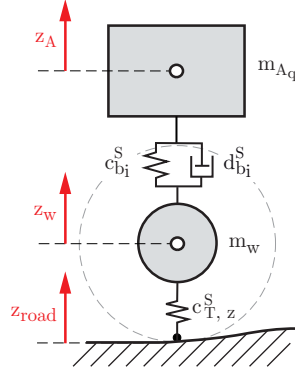


Figure E.1.: Simplified quarter vehicle model.

$$\sum F_w = -F_c - F_d + F_T = m_w \cdot \ddot{z}_w . \quad (\text{E.3b})$$

Considering a linear system, the suspension spring force F_c , the shock absorber force F_d and the force of the spring representing the tire vertical stiffness F_T can be expressed according to equations 2.80, 2.95 and 2.62 respectively as:

$$F_c = c_b^S \cdot \Delta z_c = c_b^S \cdot (z_w - z_A) , \quad (\text{E.4a})$$

$$F_d = d_b^S \cdot \Delta \dot{z}_d = d_b^S \cdot (\dot{z}_w - \dot{z}_A) , \quad (\text{E.4b})$$

$$F_T = c_{T,z}^S \cdot \rho z_i = c_{T,z}^S \cdot (z_{road} - z_w) , \quad (\text{E.4c})$$

where $z_{A/w}$ and $\dot{z}_{A/w}$ correspond to the displacement or the vertical speed of the quarter vehicle mass m_{Aq} and the non-suspended mass m_w respectively. With the state vector

$$\mathbf{x} = [z_A \quad z_w \quad \dot{z}_A \quad \dot{z}_w]^T , \quad (\text{E.5})$$

the equations of motion of the quarter vehicle model can be written in state space as:

$$\dot{\mathbf{x}} = \begin{bmatrix} \mathbf{0}_{(2 \times 2)} & \mathbf{I}_{(2 \times 2)} \\ -\mathbf{M}^{-1} \cdot \mathbf{C} & -\mathbf{M}^{-1} \cdot \mathbf{D} \end{bmatrix} \cdot \mathbf{x} + \begin{bmatrix} \mathbf{0}_{(2 \times 1)} \\ \mathbf{M}^{-1} \cdot \mathbf{u}(t) \end{bmatrix} , \quad (\text{E.6})$$

where the mass-matrix \mathbf{M} , the stiffness matrix \mathbf{C} , the damping matrix \mathbf{D} and the time-dependent input vector $\mathbf{u}(t)$ are given by:

$$\mathbf{M} = \begin{bmatrix} m_{Aq} & 0 \\ 0 & m_w \end{bmatrix} , \quad (\text{E.7a})$$

$$\mathbf{C} = \begin{bmatrix} c_b^S & -c_b^S \\ -c_b^S & c_b^S + c_{T,z}^S \end{bmatrix}, \quad (\text{E.7b})$$

$$\mathbf{D} = \begin{bmatrix} d_b^S & -d_b^S \\ -d_b^S & d_b^S \end{bmatrix}, \quad (\text{E.7c})$$

$$\mathbf{u}(t) = \begin{bmatrix} 0 \\ c_{T,z}^S \cdot z_{road}(t) \end{bmatrix}. \quad (\text{E.7d})$$

From the state space representation E.6, the transfer function for the vertical acceleration of the suspended mass in the frequency domain

$$G_{\ddot{z}_A/z_{road}}(\omega) = \frac{K_{q1} \cdot (j\omega)^3 + K_{q2} \cdot (j\omega)^2}{K_{q3} \cdot (j\omega)^4 + K_{q4} \cdot (j\omega)^3 + K_{q5} \cdot (j\omega)^2 + K_{q6} \cdot (j\omega) + K_{q7}}, \quad (\text{E.8})$$

as a measure of the ride comfort (see chapter 5.1.1), and the transfer function for the vertical movement of the non-suspended mass in the frequency domain

$$G_{z_w/z_{road}}(\omega) = \frac{K_{q8} \cdot (j\omega)^2 + K_{q1} \cdot (j\omega) + K_{q2}}{K_{q3} \cdot (j\omega)^4 + K_{q4} \cdot (j\omega)^3 + K_{q5} \cdot (j\omega)^2 + K_{q6} \cdot (j\omega) + K_{q7}}, \quad (\text{E.9})$$

as a measure of the driving safety (see chapter 5.1.2), can be obtained. The coefficients K_{q1} to K_{q8} are functions of the system parameters:

$$K_{q1} = d_b^S \cdot c_{T,z}^S, \quad (\text{E.10a})$$

$$K_{q2} = c_b^S \cdot c_{T,z}^S, \quad (\text{E.10b})$$

$$K_{q3} = m_{A_q} \cdot m_w, \quad (\text{E.10c})$$

$$K_{q4} = (m_{A_q} + m_w) \cdot d_b^S, \quad (\text{E.10d})$$

$$K_{q5} = m_{A_q} \cdot (c_b^S + c_{T,z}^S) + m_w \cdot c_b^S, \quad (\text{E.10e})$$

$$K_{q6} = d_b^S \cdot c_{T,z}^S, \quad (\text{E.10f})$$

$$K_{q7} = c_b^S \cdot c_{T,z}^S, \quad (\text{E.10g})$$

$$K_{q8} = m_{A_q} \cdot c_{T,z}^S. \quad (\text{E.10h})$$

By multiplying equation E.9 by the statical tire stiffness coefficient in vertical direction $c_{T,z}^S$ (see equation 2.62 in chapter 2.5.2 and also chapter B.4 in appendix B) the transfer

function for the contact force ${}_W F_{T_i,z}$ between the tire and the ground

$$G_{{}_W F_{T_i,z}/z_{road}}(\omega) = G_{\ddot{z}_w/z_{road}}(\omega) \cdot \mathcal{C}_{T_i,z}^S, \quad (\text{E.11})$$

can be obtained.

E.3. Test drives with additional non-suspended masses

To analyze the subjective effect of increased non-suspended masses on the ride comfort while driving over the deterministic road excitation signal presented in figure 2.20, test drives with different non-suspended masses were carried out with different additional non-suspended masses Δm_{w_i} (see chapter E.3.1) and the subjective perception of *normal drivers* and *experienced test drivers* were collected with the help of a questionnaire (see chapter E.3.2).

E.3.1. Device to increase the non-suspended masses for test drives

The device presented in figure E.2-a was designed as part of the present work to be able to simulate increased non-suspended masses Δm_{w_i} in a range from 10 kg to 35 kg. The device consist of steel discs of 5 kg and 10 kg that can be attached to the wheel hub with the help of an adapter (see also figure E.2-b). Since the effect of the increased non-suspended masses on the suspension components and therefore on the driving safety were unknown at the time the test drives were carried out, the device was designed to be attached only on the wheel hubs of the rear axle of the test vehicle presented in chapter B.1 in appendix B in order to reduce any possible risk.

E.3.2. Questionnaire to collect the subjective ride comfort perception of test drivers

The questionnaire presented in figure E.3 was used to collect the subjective comfort perception of both the *normal drivers* and the *experienced test drivers*. It allowed to take the perceptions for a combination of different values of the additional non-suspended masses at the rear axle Δm_{w_i} , the longitudinal vehicle speed ${}_V \dot{x}$, the tire inflation pressure p_{T_i} and the additional load mass m_{load} . For each longitudinal speed, the

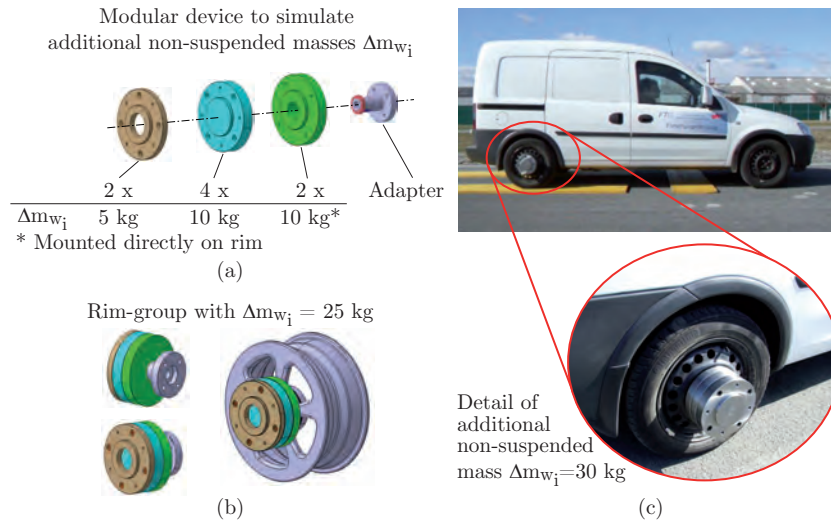


Figure E.2.: Modular device to simulate increased non-suspended masses Δm_{w_i} : Components (a), rim and device configuration corresponding to an additional non-suspended mass of $\Delta m_{w_i} = 25$ kg (b), picture of the test drives carried out with an additional non-suspended mass of $\Delta m_{w_i} = 30$ kg at the rear axle while driving on the deterministic signal presented in figure 2.20 consisting in a curb followed by a pothole with a height of $Ez_{road} = 27$ mm.

reference vehicle configuration was assumed to correspond to the test vehicle (see chapter B.1 in appendix B) without additional non-suspended masses (i.e. $\Delta m_{w_i} = 0$ kg), no additional load (i.e. $m_{load} = 0$ kg) and the tire inflation pressure recommended by the car manufacturer (i.e. $p_{T_i} = 2.3$ bar). For this configuration, a grade of 5.5 in the proposed evaluation scale ranging from 1 to 10 was assigned. Values lower than the reference are related with a worse and higher values with a better ride comfort perception.

Questionnaire to collect the subjective ride comfort perception while driving with increased non-suspended masses on a deterministic signal consisting in a curb followed by a pothole of 27mm of height

Personal data
 Date: _____
 Name: _____
 Gender: M F
 Age: _____

Evaluation scale
 1 2 3 4 5 6 7 8 9 10
 ← Uncomfortable | Comfortable →

Please evaluate the ride comfort based on the evaluation scale presented top right. As reference, take your personal ride comfort perception while driving with the vehicle without any additional non-suspended mass ($\Delta m_{wi}=0$ kg) and no additional load mass ($m_{load}=0$ kg).

		Tire inflation pressure $p_{Ti}=2.3$ bar		
		Vehicle speed $v\dot{x}=20$ km/h		
		$v\dot{x}=50$ km/h		
		$p_{Ti}=3.2$ bar		
Empty $m_{load}=0$ kg	$\Delta m_{wi}=0$ kg	$\Delta m_{wi}=50$ kg	$\Delta m_{wi}=60$ kg	$\Delta m_{wi}=0$ kg
	Grade: 5,5 Driver <input checked="" type="checkbox"/> Passeng. <input type="checkbox"/> Comment: Reference for $v\dot{x}=20$ km/h	Grade: Driver <input type="checkbox"/> Passeng. <input type="checkbox"/> Comment:	Grade: Driver <input type="checkbox"/> Passeng. <input type="checkbox"/> Comment:	Grade: Driver <input type="checkbox"/> Passeng. <input type="checkbox"/> Comment: Reference for $v\dot{x}=55$ km/h
Loaded $m_{load}=40$ kg	$\Delta m_{wi}=0$ kg	$\Delta m_{wi}=50$ kg	$\Delta m_{wi}=60$ kg	$\Delta m_{wi}=0$ kg
	Grade: Driver <input type="checkbox"/> Passeng. <input type="checkbox"/> Comment:	Grade: Driver <input type="checkbox"/> Passeng. <input type="checkbox"/> Comment:	Grade: Driver <input type="checkbox"/> Passeng. <input type="checkbox"/> Comment:	Grade: Driver <input type="checkbox"/> Passeng. <input type="checkbox"/> Comment:

Figure E.3.: Questionnaire used to collect the subjective ride comfort perceptions of normal drivers and experienced test drivers while driving with additional non-suspended masses Δm_{wi} .

F. Appendix: Mechanical component integration

F.1. Control blade suspension system

The position of the hardpoints belonging to the original and the modified control blade suspension system for passenger vehicles with in-wheel motors at the rear axle is presented in table F.1. See figure F.1 for the numbering of the presented hardpoints.

Table F.1.: Position of the hardpoints corresponding to the control blade suspension system (see [Apo10]). Positions are measured in the wheel center axis system ${}_C O$ (see chapter 2.2).

Hardpoint Nr. ^a	Original susp. system			With in-wheel motor		
	${}_C x$	${}_C y$	${}_C z$	${}_C x$	${}_C y$	${}_C z$
[mm]						
1	0.0	0.0	0.0	0.0	0.0	0.0
2	125.0	-136.5	-118.3	125.0	-136.5	-118.3
3	-101.0	-115.6	-114.9	-101.0	-115.6	-114.9
4	127.5	-358.8	-100.2	127.5	-358.8	-100.2
5	-118.7	-605.4	-93.2	-118.7	-605.4	-93.2
6 ^b	59.4	-89.1	130.1	56.3	-84.9	145.2
7 ^b	72.0	-374.5	131.0	97.2	-378.4	129.5
8	513.3	-150.0	15.2	513.3	-150.0	15.2

^a Numbering according to figure F.1.

^b Modified hardpoint.

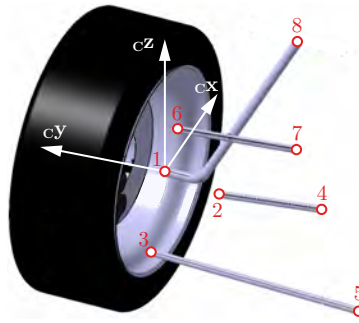


Figure F.1.: Wheel center axis system cO (see chapter 2.2) and schematic representation of the hardpoints belonging to the control blade suspension system.

F.2. Double wishbone suspension system

The position of the hardpoints belonging to the original and the modified double wishbone suspension system for passenger vehicles with in-wheel motors at the rear axle is presented in table F.2. See figure F.2 for the numbering of the presented hardpoints.

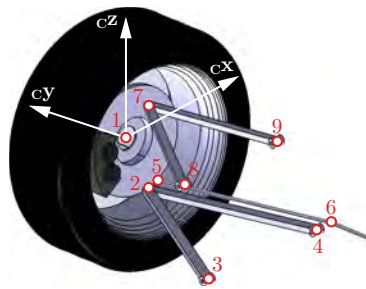


Figure F.2.: Wheel center axis system cO (see chapter 2.2) and schematic representation of the hardpoints belonging to the double wishbone suspension system.

Table F.2.: Position of the hardpoints corresponding to the double wishbone suspension system (see [Apo10]). Positions are measured in the wheel center axis system ${}_C O$ (see chapter 2.2).

Hardpoint Nr. ^a	Original susp. system			With in-wheel motor		
	${}_C x$	${}_C y$	${}_C z$	${}_C x$	${}_C y$	${}_C z$
	[mm]					
1	0.0	0.0	0.0	0.0	0.0	0.0
2 ^b	-30.0	-50.0	-150.0	16.4	-71.9	-129.2
3 ^b	-150.0	-500.0	-150.0	-230.7	-518.0	-113.4
4 ^b	200.0	-500.0	-150.0	247.8	-544.6	-177.5
5 ^b	-50.0	-30.0	-120.0	-101.1	-42.0	-114.9
6 ^b	-200.0	-500.0	-150.0	-226.6	-528.2	-115.7
7 ^b	-40.0	-60.0	100.0	13.8	-106.8	177.6
8 ^b	-150.0	-380.0	50.0	-150.4	-401.1	161.5
9 ^b	150.0	-380.0	50.0	179.2	-323.5	119.6

^a Numbering according to figure F.2.

^b Modified hardpoint.

Bibliography

- [AB06] J. Andreasson and T. Bünthe. Global chassis control based on inverse vehicle dynamics models. *Vehicle System Dynamics*, 44:321–328, 2006.
- [Abe04] D. Abel. *Mess- und Regelungstechnik*. Aachener Forschungsgesellschaft Regelungstechnik e.V. (AFR), Aachen, 2004.
- [AHG06] P. J. Allen, A. Hameed, and H. Goyder. Automotive damper model for use in multi-body dynamic simulations. *Proceedings of the Institution of Mechanical Engineers, Part D: Journal of Automobile Engineering*, 220(9):1221–1233, 2006.
- [AJV⁺06] M. André, R. Joumard, R. Vidon, P. Tassel, and P. Perret. Real-world European driving cycles, for measuring pollutant emissions from high- and low-powered cars. *Atmospheric Environment*, 40(31):5944–5953, 2006.
- [AKB06] J. Andreasson, C. Knobel, and T. Bünthe. On road vehicle motion control—striving towards synergy. In *Proceedings of the 8th International Symposium on Advanced Vehicle Control*, pages 20–24, 2006. Taipei.
- [AKH⁺02] K. Ahn, W. Kim, W. Hwang, H. E. Im, D. Kim, and C. Oh. A Study on optimization of hard points for double wishbone type suspension. In *Proceedings of the International Symposium on Advanced Vehicle Control - AVEC'02*, September 2002.
- [And04] M. André. Real-world driving cycles for measuring cars pollutant emissions - Part A: The ARTEMIS European driving cycles. Technical Report INRETS-LTE 0411, INRETS, 2004.
- [And06] M. André. Real-world driving cycles for measuring cars pollutant emis-

- sions - Part B: Driving cycles according to vehicle power. Technical Report INRETS-LTE 0412, INRETS, 2006.
- [And07] J. Andreasson. *On generic road vehicle motion modelling and control*. PhD thesis, Royal Institute of Technology, Stockholm, Sweden, 2007.
- [Apo10] J. E. Wilson Aponte. Development of a Suspension Kinematics Optimization System - KOS . Master's thesis, Universidad Nacional de Colombia, 2010. (In cooperation with the Institute of Automotive Engineering at Graz University of Technology).
- [Aso08] K. Asogawa. Variable wheel positioning in a vehicle, 2008. Patent document number: EP 1902926 A1.
- [Atk02] K. Atkinson. Modelling a road using spline interpolation. *Reports on Computational Mathematics*, 145:1–17, 2002.
- [BA06] T. Bunte and J. Andreasson. Global chassis control based on inverse vehicle dynamics models providing minimized utilisation of the tyre force potential. In *19th IAVSD Symposium*, 2006.
- [Bau87] R. Bauer. Erzeugung von Räumlichen Fahrbahnmodellen für Komfortuntersuchungen im Labor. Master's thesis, Institute of Mechanics, Vienna University of Technology, 1987.
- [BBS08] C. Borroni-Bird and M. Shabana. Chevrolet Sequel: Reinventing the Automobile. In SAE International, editor, *Proceedings of the SAE World Congress and Exhibition*. SAE International, 2008.
- [BDD⁺06] F. N. Büchi, A. Delfino, P. Dietrich, S. A. Freunberger, R. Kötz, D. Laurent, P. Magne, D. Olsommer, G. Paganelli, A. Tsukada, P. u. W. Varenne, and D. Walser. Elektrisches Antriebskonzept mit einer Brennstoffzelle und einem Supercapacitor - Ergebnisse mit dem Hy-Light-Fahrzeug. In *VDI Berichte 1975*, 2006.
- [Bes09] S. Best. Den Scheibenläufer motor neu definiert. *KFZ-Elektronik*, 6(6):73–74, Juni 2009.
- [Böh10] D. Böhm. Darstellungs- und Simulationsmethoden in der konzept-

- tionellen Fahrwerksentwicklung . Master's thesis, Institute of Automotive Engineering, Graz University of Technology, 2010.
- [BH11] C. Buksnowitz and W. Hirschberg. Reasonability of the Drive Power of Passenger Cars Available in Europe in 2010. In *Proceedings of the 13th EAEC Congress*, Valencia, Spain, 2011.
- [BHS⁺11] J. Brembeck, L. M. Ho, A. Schaub, C. Satzger, J. Tobolar, J. Bals, and G. Hirzinger. Romo - The robotic electric vehicle. In *Proceedings of the 22nd IAVSD International Symposium on Dynamics of Vehicle on Roads and Tracks*, 2011.
- [Bit09] O. Bitsche. Vom Verbrennungsmotor zum Elektrofahrzeug. In *ÖAMTC Expertenforum*, Wien, September 2009.
- [BJ88] F. P. Beer and E. Russell Johnston. *Vector Mechanics for Engineers: Dynamic*. McGrawHill, 1988.
- [BM07] P. Boulter and I. McCrae. Assessment and Reliability of Transport Emission Models and Inventory Systems - ARTEMIS. Technical Report UPR/IE/044/07, TRL Limited, 2007.
- [Bog06] K. Bogsjö. Development of analysis tools and stochastic models of road profiles regarding their influence on heavy vehicle fatigue. *Vehicle System Dynamics*, 44(sup1):780–790, 2006.
- [Bog08] K. Bogsjö. Coherence of road roughness in left and right wheel-path. *Vehicle System Dynamics*, 46(sup1):599–609, 2008.
- [BPR0] K. Bogsjö, K. Podgórski, and I. Rychlik. Models for road surface roughness. *Vehicle System Dynamics*, 0(0):1–23, 0.
- [BS07] H. H. Braess and U. Seiffert. *Vieweg Handbuch Kraftfahrzeugtechnik*. Vieweg Teubner, 2007.
- [BSK06] A. Binder, T. Schneider, and M. Klohr. Fixation of buried and surface-mounted magnets in high-speed permanent-magnet synchronous machines. *Industry Applications, IEEE Transactions on*, 42(4):1031, july-aug. 2006.

- [BT09] I. Boldea and L. Tutelea. *Electric machines: steady state, transients, and design with MATLAB*. Taylor and Francis, 2009.
- [BV08] U. Bankhofer and J. Vogel. *Datenanalyse und Statistik: Eine Einführung für Ökonomen im Bachelor*. Gabler, 2008.
- [CC00] T. Christen and M. W. Carlen. Theory of Ragone plots. *Journal of Power Sources*, 91(2):210, 2000.
- [Cho02] R. Choudhury. Well-to-wheel analyse des energieverbrauchs und der treibhausgas-emissionen von fortschrittlichen kraftstoff/fahrzeug-systemen - Eine europäische studie. In *Hart World Fuels Conference*, 2002.
- [Com92] European Commission. Council directive 92/21/EEC of 31 March 1992 on the masses and dimensions of motor vehicles of category M1, 1992.
- [Cor08] S. Cornel. *Alternative Antriebe für Automobile*, volume 2. Auflage. Springer Verlag, 2008.
- [dB09] Y. de Boer. How the Energy Sector can deliver on a Climate Agreement in Copenhagen. Technical report, International Energy Agency (IEA), 2009.
- [Dór06] S. Dóra. A survey of conventional and alternative methods for digital simulation of stochastic processes. In *Proceedings of the Mini Conference on Vehicle System Dynamics, Identification and Anomalies*, Budapest, Hungary, 2006.
- [Dür11] J. Dürnberger. Fahrdynamische Untersuchung einer elektrischen Einzelradlenkung. Master’s thesis, Institute of Automotive Engineering, Graz University of Technology, 2011.
- [DSR97] S. Duym, R. Stiens, and K. Reybrouck. Evaluation of shock absorber models. *Vehicle System Dynamics*, 27(2):109–127, 1997.
- [Duc04] P. Duclou. RoadXML Format Specification 2.3.0. Technical report, So-geclair, 2004.
- [EBMG10] M. Euchler, T. Bonitz, D. Mitte, and M. Geyer. Bewertung der

- Fahrsicherheit eines Elektrofahrzeugs bei stationärer Kreisfahrt. *Automobiltechnische Zeitschrift - ATZ*, 03:206–213, 2010.
- [EGW11] L. Eckstein, R. Göbbels, and R. Wohlecker. Benchmarking des Elektrofahrzeugs Mitsubishi I-MIEV. *Automobiltechnische Zeitschrift - ATZ*, 12:964–970, 2011.
- [EPRT07] J. Edelmann, M. Plöchl, W. Reinalter, and W. Tieber. A passenger car driver model for higher lateral accelerations. *Vehicle System Dynamics*, 45(12):1117–1129, 2007.
- [eTr] eTraction. The Wheel - A revolution in motion. Available at <http://www.e-traction.com/TheWheel.htm>. Accessed on 30.03. 2012.
- [eV02] Verein Deutscher Ingenieure e.V. (VDI). VDI Norm 2057, Blatt 1 / Part 1: Einwirkung mechanischer Schwingungen auf den Menschen - Ganzkörperschwingungen. Technical report, Verein Deutscher Ingenieure e.V. (VDI), 2002.
- [FAL04] J. Fredriksson, J. Andreasson, and L. Laine. Wheel force distribution for improved handling in a hybrid electric vehicle using nonlinear control. In *43rd IEEE Conference on Decision and Control, 2004. CDC*, volume 4, 2004.
- [Fer11] X. Bas Ferrer. Development of an Environment Framework for a Modular Vehicle Simulation System. Master’s thesis, Technical University of Catalonia, 2011. (In cooperation with the Institute of Automotive Engineering at Graz University of Technology).
- [FHT⁺09] C. Früh, J. Hermann, M. Tietke, M. Niestegge, F. Scheyhing, A. Neteler, G. Steller, M. Lauer, M. Decker, and R. Michalski. Komfort bei erlebbarer Dynamik und Agilität. *Automobiltechnische Zeitschrift - Die neue E-Klasse von Mercedes-Benz*, 01:128–143, 2009.
- [Fia06] E. Fiala. *Mensch und Fahrzeug*. Vieweg and Sohn Verlag, Wiesbaden, 2006.
- [FJM⁺98] S. Friedmann, C. Jones, D. Mesiti, M. André, P. Carminot, M. Audinet, A. Künzer, W. Kriegler, R. Heath, N. Kyriakis, P. Dietrich, C. Reulein,

- W. Josefowitz, and A. Lasso. Entwicklung von Bewertungswerkzeugen für Hybridantriebe (Das EUCAR Projekt HYZEM: Hybrid Technology approaching efficient Zero Emission Mobility). In *VDI Bericht 1378*, 1998.
- [FMH⁺01] R. Freitag, M. Moser, M. Hartl, J. Koepf, and L. Eckstein. Anforderungen an das Sicherheitskonzept von Lenksystemen mit Steer-by-Wire Funktionalität. In *VDI Berichte 1646*, 2001.
- [fN94] Deutsches Institut für Normung. DIN 70000 - Fahrzeugdynamik und Fahrverhalten. Standard, 1994.
- [FS10] A. Fandre and M. Schwab. RMOD-K V7 / OpenCRG Roadmodule: Interface to OpenCRG Version 1.0.1. In *Proceedings of the 1st OpenCRG workshop*, 2010.
- [fSI95] International Organization for Standardization (ISO). ISO 8608:1995(E) Mechanical vibration - Road surface profiles - Reporting of measured data. Standard, 1995.
- [fSI97] International Organization for Standardization (ISO). ISO 2631-1:1997(E) - Mechanical vibration and shock - Evaluation of human exposure to whole-body vibration - Part 1: General requirements. Standard, 1997.
- [fSI03] International Organization for Standardization (ISO). ISO 7401:2003 Road vehicles. Lateral transient response test methods. Open-loop test methods. Standard, 2003.
- [fSI04] International Organization for Standardization (ISO). ISO 4138 - Passenger cars - Steady-state circular driving behavior - Open-loop test methods. Standard, 2004.
- [GB07] A. Gallrein and M. Bäcker. CDTire: a tire model for comfort and durability applications. *Vehicle System Dynamics*, 45(sup1):69–77, 2007.
- [GCDB05] A. Gallrein, J. De Cuyper, W. Dehandschutter, and M. Bäcker. Parameter identification for LMS CDTire. *Vehicle System Dynamics*, 43(sup1):444–456, 2005.

- [Geo08] N. Georgano. *Electric Vehicles*. Shire, 2008.
- [GFH10] B. Gombert, R. Fischer, and W. Heinrich. Elektrische Radnabenmotoren - Konstruktionskriterien und Fahrzeugintegration. *Automobiltechnische Zeitschrift - ATZ elektronik*, 01:8–14, 2010.
- [GG06] B. Gombert and P. Gutenberg. Die Elektronische Keilbremse Meilenstein auf dem Weg zum Elektrischen Radantrieb. *Automobiltechnische Zeitschrift - ATZ*, 108(11):904–913, 2006.
- [GH10] M. Gipser and G. Hofmann. Stiff and Deformable Digital Roads for FTire: Experiences with Regular Grid Roads. In *Proceedings of the 1st OpenCRG workshop*, 2010.
- [GHKP12] M. Gröninger, F. Horch, A. Kock, and H. Pleiteit. Elektrischer Radnabenmotor. *Automobiltechnische Zeitschrift elektronik - ATZ*, 01:46–50, 2012.
- [Gip05] M. Gipser. FTire: A physically based application-oriented tyre model for use with detailed MBS and finite-element suspension models. *Vehicle System Dynamics*, 43(SUPPL.):76–91, 2005.
- [GM01] M. Gobbi and G. Mastinu. Analytical description and optimization of the dynamic behaviour of passively suspended road vehicles. *Journal of Sound and Vibration*, 245(3):457–481, 2001.
- [Gmb10] VIRES Simulationstechnologie GmbH. Open CRG: User Manual. Technical report, 2010.
- [Gol89] D. E. Goldberg. *Genetic algorithms in search, optimization, and machine learning*. Addison-Wesley Pub. Co, 1989.
- [Gom07] B. Gombert. Neue Fahrzeugkonzepte erfordern einen ganzheitlichen Ansatz in der Integrationsstrategie - Am Beispiel der Elektronik und Sensorik im Fahrzeug. In *Proceedings of the 2nd Munich Network Mobilitätsforum*. Munich Network, November 2007. München.
- [Gom10] B. Gombert. Vom intelligenten Radlager zum Robot Wheel. In *Proceedings of the Schaeffler Kolloquium*, 2010.

-
- [Grä10] G. Gräfe. Präzise kinematische Vermessung von Teststrecken für Simulationsanwendungen mit Hochleistungs-Laserscannern. In *Proceedings of the 1st OpenCRG workshop*, 2010.
- [Gri98] M. J. Griffin. A comparison of standardized methods for predicting the hazards of whole-body vibration and repeated shocks. *Journal of Sound and Vibration*, 215(4):883–914, 1998.
- [Gös08] B. Göschel. Elektrifizierung Antrieb. Lecture notes, Institute for Internal Combustion Engines and Thermodynamics, Graz University of Technology, 2008.
- [GWL11] M. Graf, F. Wiesbeck, and M. Lienkamp. Fahrdynamikauslegung des Elektrofahrzeugs Mute. *Automobiltechnische Zeitschrift - ATZ*, 06:452–457, 2011.
- [HBWH11] T. Hüsemann, C. Bachmann, S. Winter, and D. Henrichmüller. Mobile Prüfstandstechnik zur Messung von Reifen-Fahrbahn-Reibwerten. *Automobiltechnische Zeitschrift - ATZ*, 06:504–508, 2011.
- [HD04] M. Horn and N. Dourdoumas. *Regelungstechnik - Rechnerunterstützter Entwurf zeitkontinuierlicher und zeitdiskreter Regelkreise*. Pearson Studium, 2004.
- [HEG11] B. Heiing, M. Ersoy, and S. Gies. *Fahrwerkhandbuch: Grundlagen, Fahrdynamik, Komponenten, Systeme, Mechatronik, Perspektiven*. Springer Fachmedien Wiesbaden, 2011.
- [Hei01] A. J. Heinen. Wheel provided with driving means, 2001. Patent document number: WO 01/54939 A2.
- [Hir09a] W. Hirschberg. Fahrzeugdynamik. Lecture notes, Institute of Automotive Engineering (Graz University of Technology), 2009.
- [Hir09b] W. Hirschberg. TMsimple: A simple to use tyre model. Technical report, Institute of Automotive Engineering (Graz University of Technology), 2009.
- [Hir09c] W. Hirschberg. Tyre - The Essential Component for Traction and Ve-

- hicle Dynamics. In *Proceedings of the 9th European All-Wheel Drive Congress Graz*, Graz, Austria, 2009.
- [Hir11] W. Hirschberg. Fahrzeug-Auslegung heute und morgen. In *Proceedings of ÖVK-Vortragsreihe*, Steyr, Austria, 2011.
- [HLSB08] L. Hofmann, J. Leohold, W. Steiger, and T. Böhm. twinDRIVE - Ein Schritt in Richtung Elektromobilität. *VDI Berichte*, 2030:3–20, 2008.
- [Hof09] P. Hofmann. *Hybridfahrzeuge: Ein alternatives Antriebskonzept für die Zukunft*. Springer, 2009.
- [Hon] Honda. Tokio Motor Show 2005: FCX Concept. Available at <http://world.honda.com/Tokyo2005/fcx/>. Accessed on 30.03. 2012.
- [HP90] A. Heertje and M. Perlman. *Evolving technology and market structure: studies in Schumpeterian economics*. University of Michigan Press, Ann Arbor, Mich., 1990.
- [HRW02] W. Hirschberg, G. Rill, and H. Weinfurter. User-Appropriate Tyre-Modelling for Vehicle Dynamics in Standard and Limit Situations. *Vehicle System Dynamics*, 38(2):103–125, 2002.
- [HRW07] W. Hirschberg, G. Rill, and H. Weinfurter. Tire model TMeasy. *Vehicle System Dynamics*, 45(Suppl. 1):101–119, 2007.
- [HSA⁺08] E. Hoepke, B. Stefan, W. Appel, H. Brähler, U. Dahlhaus, T. Esch, S. Kopp, and B. Rhein. *Nutzfahrzeugtechnik*. Number 5. Vieweg + Teubner, 2008.
- [Huc05] W. Hucho. *Aerodynamik des Automobils*. Vieweg Verlag, 2005.
- [HW06] T. Hüsemann and M. Woehrmann. Reifenmessungen als Grundlage der Reifen- und Fahrdynamiksimulation. In *Proceedings of the CTI Fachkonferenz "Aktive Beeinflussung von Längs- und Querdynamik zur Steigerung der Fahrsicherheit"*, Würzburg, Germany, 2006.
- [HW09] W. Hirschberg and H. M. Waser. Kraftfahrzeugtechnik. Lecture notes, Institute of Automotive Engineering (Graz University of Technology), 2009.

-
- [HWJ00] W. Hirschberg, H. Weinfurter, and C. Jung. Ermittlung der Potenziale zur LKW-Stabilisierung durch Fahrdynamiksimulation. In *VDI Berichte 1559*, 2000.
- [HY07] K. Handa and H. Yoshida. Development of Next-Generation Electric Vehicle "i-MiEV". Technical review 19, Mitsubishi Motors, 2007.
- [Høy08] K. G. Høyer. The History of Alternative Fuels in Transportation: The Case of Electric and Hybrid Cars. *Utilities Policy*, 16(2):63–71, 2008.
- [Ise02] R. Isermann. *Mechatronische Systeme: Grundlagen*. Springer, 2002.
- [Ise09] R. Isermann. *Elektronisches Management motorischer Fahrzeugantriebe: Elektronik, Modellbildung, Regelung und Diagnose für Verbrennungsmotoren, Getriebe und Elektroantriebe*. Vieweg+Teubner Verlag, 2009.
- [JA08] M. Jonasson and J. Andreasson. Exploiting autonomous corner modules to resolve force constraints in the tyre contact patch. *Vehicle System Dynamics*, 46(7):553–573, 2008.
- [JAJT10] M. Jonasson, J. Andreasson, B. Jacobson, and A. S. Trigell. Global force potential of over-actuated vehicles. *Vehicle System Dynamics*, 48(9):983–998, 2010.
- [Jon07] M. Jonasson. Aspects of Autonomous Corner Modules as an Enabler for New Vehicle Chassis Solutions. Master's thesis, Royal Institute of Technology, Stockholm, Sweden, 2007.
- [JW06] M. Jonasson and O. Wallmark. Stability of an electric vehicle with permanent magnet in-wheel motors during electrical faults. In *Proceedings of the 22nd International Battery Hybrid and Fuel Cell Electric Vehicle Symposium and Exposition*, Yokohama, Japan, 2006.
- [KA10] F. Knogler and H. Antensteiner. Geschichte der Firma Magna Powertrain. Innovationsveranstaltung der MAGNA Powertrain 2010, 2010.
- [Kar83] D. Karnopp. Active damping in road vehicle suspension systems. *Vehicle System Dynamics*, 12(6):291–316, 1983.
- [Kar90] D. Karnopp. Design principles for vibration control systems using semi-

- active dampers. *Journal of Dynamic Systems, Measurement and Control, Transactions of the ASME*, 112(3):448–455, 1990.
- [KCH74] D. Karnopp, M. J. Crosby, and R. A. Harwood. Vibration control using semi-active force generators. *J Eng Ind Trans ASME*, 96 Ser B(2):619–626, 1974.
- [Kel10] G. Kelz. *Modulare Modellbildung und Simulation von hybriden Antriebssträngen*. PhD thesis, Institute of Automotive Engineering, Graz University of Technology, 2010.
- [KH11] J. Käsgen and R. Heim. Product Development and Testing Requirements for Electric Wheel Hub Motors. In *Proceedings of Internationales Symposium "Innovative Fahrzeug-Getriebe"*, Berlin, Germany, 2011.
- [KIA] KIA. Fuel Cell Electric Vehicle Platform. Available at <http://www.kiapress.com/presskits/motorshows/frankfurt2007/kiasall-newfcevplatformmakeeuropeandebut.aspx>. Accessed on 30.03.2012.
- [KK04] G. Klempner and I. Kerszenbaum. *Operation and Maintenance of Large Turbo-Generators*. John Wiley and Sons, 2004.
- [KK12] M. Kimmerstorfer and M. König. Erweiterung der Modellkomplexität der Simulationsumgebung MOVES² auf Fahrzeugniveau: Viertel- und Einspurmodell. Projekt fahrzeugtechnik, Institut für Fahrzeugtechnik der Technischen Universität Graz, 2012.
- [Kna10] P. Knauer. *Objektivierung des Schwingungskomforts bei instationärer Fahrbahnanregung*. PhD thesis, Institute of Automotive Technology, Technical University Munich, 2010.
- [Kol07] C. Koletzko. *Untersuchung des Einflusses von Verstelldaempfern auf das Wankverhalten von PKW unter Beruecksichtigung einer aktiven Wankstabilisierung*. PhD thesis, Institute of Automotive Technology, Technical University Munich, 2007.
- [Kol09] D. Kollreider. *Identifikation der Reifeneigenschaften als Grundlage zur Fahrdynamikbewertung*. PhD thesis, Institute of Automotive Engineering, Graz University of Technology, 2009.

-
- [Kol11] J. Kolar. Power Electronic Systems. Lecture notes, Power Electronic Systems Laboratory, ETH Zurich, 2011.
- [Kon09] A. E. Kontorovich. Estimate of global oil resource and the forecast for global oil production in the 21st century. *Russian Geology and Geophysics*, 50(4):237, 2009.
- [Kre65] G. Krempel. *Experimenteller Beitrag zur Untersuchung am Kraftfahrzeugreifen*. PhD thesis, Karlsruhe Institute of Technology, 1965.
- [KS09] S. Koller and M. Schmuck. Batteries and Supercapacitors. Lecture notes, Institute for Chemistry and Technology of Materials, Graz University of Technology, 2009.
- [KSS11] U. Knödel, F. Stein, and H. Schlenkermann. Variantenvielfalt der Antriebskonzepte für Elektrofahrzeuge. *Automobiltechnische Zeitschrift - ATZ*, 08:553–557, 2011.
- [KTSY07] K. Kawakami, H. Tanabe, H. Shimizu, and H. Yoshida. Advanced redundancy technology for a drive system using in-wheel motors. *World Electric Vehicle Journal*, 1(1):46–53, 2007.
- [KWLH10] G. Krebs, R. Weber, S. Leppelsack, and U. Hochberg. Elektrische Radnabenmotoren für leichte Stadtfahrzeuge. *Automobiltechnische Zeitschrift - ATZ elektronik*, 01:20–27, 2010.
- [LEH11] C. Lex, A. Eichberger, and W. Hirschberg. Systematische Bewertung von Methoden zur Ermittlung des Kraftschlussbeiwerts zwischen Reifen und Fahrbahn und deren Anwendungspotentiale in Fahrerassistenzsystemen. *Automobiltechnische Zeitschrift - ATZ*, 12:991–997, 2011.
- [Len09] S. Lennert. *Zur Objektivierung von Schwingungskomfort in Personenkraftwagen - Untersuchung der Wahrnehmungsdimensionen*. VDI - Fortschritt-Berichte, Reihe 12, 2009.
- [LG98] C. H. Lewis and M. J. Griffin. A comparison of evaluations and assessments obtained using alternative standards for predicting the hazards of whole-body vibration and repeated shocks. *Journal of Sound and Vibration*, 215(4):915–926, 1998.

- [LSW00] D. Laurent, M. Sebe, and D. Walser. Assembly comprising a wheel and a suspension integrated into the wheel, 2000. Patent document number: US 6,113,119.
- [Lun09] M. Lunanova. *Optimierung von Nebenaggregaten: Maßnahmen zur Senkung der CO₂-Emission von Kraftfahrzeugen*. Vieweg+Teubner Verlag, 2009.
- [Ma95] Kruth J.P. Ma, W. Parameterization of randomly measured points for least squares fitting of B-spline curves and surfaces. *Computer-Aided Design*, 27(9):663–675, 1995.
- [Mar09] M. Marini. Modular Vehicle Model for Comfort and Safety Assessment. Master’s thesis, Università di Cagliari, 2009. (In cooperation with the Institute of Automotive Engineering at Graz University of Technology).
- [Mat08] W. Matschinsky. *Die Radführungen der Strassenfahrzeuge*, volume 2. Springer Berlin Heidelberg New York, 2008.
- [MBBB10] W. J. Mitchell, C. E. Borroni-Bird, and L. D. Burns. *Reinventing the automobile - Personal urban mobility for the 21st century*. MIT press, 2010.
- [MC09] G. Maggio and G. Cacciola. A variant of the Hubbert curve for world oil production forecasts. *Energy Policy*, 37(11):4761, 2009.
- [MG08] M. Morioka and M. J. Griffin. Absolute thresholds for the perception of fore-and-aft, lateral, and vertical vibration at the hand, the seat, and the foot. *Journal of Sound and Vibration*, 314(1-2):357–370, 2008.
- [Müh93] M. Mühlmeier. *Bewertung von Radlastschwankungen im Hinblick auf das Fahrverhalten von Pkw*. PhD thesis, Institute of Automotive Engineering, Braunschweig University of Technology, 1993.
- [MK98] M. Mitschke and B. Klingner. Schwingungskomfort im Kraftfahrzeug. *ATZ Automobiltechnische Zeitschrift*, 100(1):18–24, 1998.
- [Moh04] D. Mohr. Eine einfache Methode zur Beurteilung stoßhaltiger Ganzkörper-Schwingungen. In *VDI Bericht 1821*, 2004.

- [MTI⁺06] N. Masaki, K. Tashiro, H. Iwano, G. Nagaya, Y. Wakao, and Y. Abe. Entwicklung eines Radnabenantriebssystems mit dynamischem Dämpfungssystem. In *Proceedings of the 15th Aachen Colloquium "Automobile and Engine Technology"*, Aachen, Germany, 2006.
- [MW04] M. Mitschke and H. Wallentowitz. *Dynamik der Kraftfahrzeuge*. Springer, 2004.
- [Nat03] H. Natzschka. *Strassenbau: Entwurf und Bautechnik*. Vieweg Teubner, 2003.
- [NBW06] H. Neudorfer, A. Binder, and N. Wicker. Analyse von unterschiedlichen Fahrzyklen fuer den Einsatz von Elektrofahrzeugen. *Elektrotechnik und Informationstechnik*, 123(7-8):352–360, 2006.
- [NDR11] H. Niederkofler, J. Dürnberger, and A. E. Rojas Rojas. Electrical single wheel steering sytem for future suspension systems. In *Proceedings of the 13th European Automotive Congress*, 2011. Valencia.
- [NHuRH09] A. Niersmann, J. Hoffmann, and F. Kuecuekay und R. Henze. Eigenschaftbasierte Fahrwerksauslegung durch Inversion der Achskinematik. In *VDI Berichte 2086*, 2009.
- [Nie06] T. Niemz. *Reducing braking distance by control of semi-active suspensions*. PhD thesis, Darmstadt University of Technology, 2006.
- [Nie10] H. Niederkofler. Mechatronisches Federbein für Kraftfahrzeuge, 2010. Invention disclosure at Graz University of Technology.
- [Nie11] H. Niederkofler. *Analyse radselektiv eingreifende Fahrdynamikregelsysteme für die Anwendung in elektromechanischen Corner-Modulen*. PhD thesis, Institute of Automotive Engineering, Graz University of Technology, 2011.
- [Nis] Nissan. Pivo2 Concept Car. Available at <http://www.nissan-global.com/EN/PIVO2/index.html>. Accessed on 30.03. 2011.
- [NIT08] S. Nishioka, H. Iwano, and K. Tashiro. In-wheel motor system, 2008. Patent document number: EP 1961602 A1.

- [NJT08] V. Nachtigal, K. P. Jäker, and A. Trächtler. Development and control of a quarter-vehicle testbed for a fully active x-wire demonstrator. In Society of automotive engineers of Japan, editor, *9th International symposium on advanced vehicle control - AVEC08*, volume 9. Society of automotive engineers of Japan, October 2008.
- [NLER11] H. Niederkofler, C. Lex, A. Eichberger, and A. E. Rojas Rojas. Potentialanalyse von aktiven Fahrwerks- und Antriebssystemen für die Anwendung in Fahrerassistenzsystemen in kritischen Fahrsituationen. In *VDI Berichte 2137*, Hannover, Germany, 2011.
- [NM65] J. A. Nelder and R. Mead. A simplex method for function minimization. *Comput.J.*, 7:308–313, 1965.
- [NR09] H. Niederkofler and A. E. Rojas Rojas. Torsionales Schwingungstilger System für Kraftfahrzeuge, 2009. Invention disclosure at Graz University of Technology.
- [NR10a] H. Niederkofler and A. E. Rojas Rojas. Toward eCorner: Energy efficient design of mechatronic suspension systems. In *Proceedings of the FISITA World Automotive Congress*, Budapest, Hungary, 2010.
- [NR10b] H. Niederkofler and M. Rudolf. Mechanisches Fail-Safe System für Fahrzeuge mit Einzelradlenkung, 2010. Invention disclosure at Magna Steyr Fahrzeugtechnik AG and Co KG.
- [NRD11] H. Niederkofler, A. E. Rojas Rojas, and J. Dürnberger. Development of a single wheel steer-by-wire system: Implementation aspects and failure handling. In *22nd International Symposium on Dynamics of Vehicles on Roads and Tracks*, 2011. Manchester.
- [oE00] United States Department of Energy. 40 CFR part 86: Control of Emissions from New and In-Use Highway Vehicles and Engines. Final rule, United States Environmental Protection Agency, Certification Division, 2000.
- [oE11] United States Department of Energy. Fuel Economy Guide 2012. Annual report, U.S. Environmental Protection Agency, Office of Energy Efficiency and Renewable Energy, 2011.

-
- [Oer11] C. Oertel. RMOD-K Formula Documentation. Technical report, Fachhochschule Brandenburg, 2011.
- [OF01] C. Oertel and A. Fandre. Simulation: Das reifenmodellsystem RMOD-K - Ein Beitrag zum virtuellen fahrzeug. *ATZ Automobiltechnische Zeitschrift*, 103(11):1074, 2001.
- [Ore06] R. Orend. *Integrierte Fahrdynamikregelung mit Einzelradaktorik - Ein Konzept zur Darstellung des Fahrdynamischen Optimums*. PhD thesis, University of Erlangen-Nuremberg, 2006.
- [Ott87] H. Otto. *Lastwechselreaktion von Pkw bei Kurvenfahrt*. PhD thesis, Institute of Automotive Engineering, Braunschweig University of Technology, 1987.
- [Pac06] H. B. Pacejka. *Tyre and vehicle dynamics*. Butterworth-Heinemann, 2006.
- [PB97] H. B. Pacejka and I. J. M. Besselink. Magic Formula Tyre Model with Transient Properties. *Vehicle System Dynamics*, 27(sup001):234–249, 1997.
- [PE07] M. Plöchl and J. Edelmann. Driver models in automobile dynamics application. *Vehicle System Dynamics*, 45(7-8):699–741, 2007.
- [PG02] G. S. Paddan and M. J. Griffin. Effect of seating on exposures to whole-body vibration in vehicles. *Journal of Sound and Vibration*, 253(1):215–241, 7 November 2000 through 9 November 2000 2002.
- [Pis04] S. Pischinger. *Energiewandlungsmaschinen II*. Lehrstuhl für Verbrennungskraftmaschinen der RWTH-Aachen, Aachen - Germany, 2004.
- [Pür11] M. Pürscher. Torsional Oscillator System - TOS. Bachelor’s Thesis, 2011. Institute of Automotive Engineering, Graz University of Technology.
- [Pro] Protean electric. Hi-Pa Drive. Available at <http://www.proteanelectric.com>. Accessed on 30.03. 2012.
- [RA11] J. Rauh and D. Ammon. System dynamics of electrified vehicles: some facts, thoughts, and challenges. *Vehicle System Dynamics*, 49(7):1005–

- 1020, 2011.
- [Raj06] R. Rajamani. *Vehicle dynamics and control*. Springer, 2006.
- [Rau08] J. Rauh. OpenCRG - The open standard to represent high precision 3D road data in vehicle simulation tasks on rough roads for handling, ride comfort, and durability load analyses. In *Proceedings of the 1st OpenCRG workshop*, 2008.
- [REH07] W. Rosinger, S. Eitzinger, and W. Hirschberg. Entwurf eines Sollwertgenerators für Fahrdynamikregelsysteme. In M. Horn, M. Hofbaur, and N. Dourdoumas, editors, *Proceedings des 15. Steirisches Seminar über Regelungstechnik und Prozessautomatisierung*, pages 117–139, 17.09. - 20.09.2007 2007. Leibnitz.
- [RH84] K. Rompe and B. Heissing. *Objektive Testverfahren für die Fahreigenschaften von Kraftfahrzeugen*. Verlag TÜV Rheinland, 1984.
- [RHELS08] W. Rosinger, W. Hirschberg, S. Eitzinger, and D. Lindvai-Soos. Improving driver-car performance through advanced reference value computation for vehicle dynamic control systems. In *Proceedings of the 9th International Symposium on Advanced Vehicle Control*, pages 282–287, Kobe, 2008.
- [Ric52] S. O. Rice. *Mathematical analysis of random noise*. Bell Telephone Labs., Inc., New York, 1952.
- [Ril94] G. Rill. *Simulation von Kraftfahrzeugen*. Vieweg, 1994.
- [RKuML11] M. Rosenberger, M. Kirschneck, and T. Koch und M. Lienkamp. Integration der elektrischen Antriebsmotoren in die ABS-Regelung. In *Proceedings of the 2nd Münchner Automobiltechnisches Kolloquium*, Munich, Germany, 2011.
- [RMB08] J. Rauh and M. Mössner-Beigel. Tyre simulation challenges. *Vehicle System Dynamics*, 46(sup1):49–62, 2008.
- [RN11] A. E. Rojas Rojas and H. Niederkofler. Synthesis of suspension systems for passenger vehicles with in-wheel motors. In *Proceedings of the 13th*

-
- European Automotive Congress*, 2011. Valencia.
- [RNA11a] A. E. Rojas Rojas, H. Niederkofler, and J. E. Wilson Aponte. Co-Simulation for the synthesis of suspension systems for passenger vehicles with in-wheel motors based on genetic algorithms. In *Proceedings of ChassisTech*, 2011. Munich.
- [RNA11b] A. E. Rojas Rojas, H. Niederkofler, and J. E. Wilson Aponte. Optimización de la cinemática de suspensiones para vehículos con motores eléctricos en las ruedas. In *Proceedings of the V Congreso Internacional de Ingeniería Mecánica y III de Ingeniería Mecatrónica*, Bogotá - Colombia, 2011. Universidad Nacional de Colombia.
- [RND11] A. E. Rojas Rojas, H. Niederkofler, and J. Duernberger. Analyse der Fahrsicherheit von Fahrzeugen mit Radnabenmotoren auf unebener Fahrbahn. In *Proceedings of the 2nd Münchner Automobiltechnisches Kolloquium*, Munich, Germany, 2011.
- [RNFD11] A. E. Rojas Rojas, H. Niederkofler, X. Bas Ferrer, and J. Duernberger. Modular modeling of vehicles with innovative powertrain systems. In *Proceedings of 13th EAEC European Automotive Congress*, June 13-16 2011. Valencia.
- [RNH11] A. E. Rojas Rojas, H. Niederkofler, and W. Hirschberg. Mechanical Design of In-Wheel Motor Driven Vehicles with Torque-Vectoring. In *Proceedings of the SAE-Brasil Congresso*, Sao Paulo, Brasil, 2011.
- [RNW10] A. E. Rojas Rojas, H. Niederkofler, and J. Willberger. Comfort and safety enhancement of passenger vehicles with in-wheel motors. In *Proceedings of the SAE 2010 World Congress and Exhibition*, Detroit, U.S.A., 2010.
- [RNW11a] A. E. Rojas Rojas, H. Niederkofler, and J. Willberger. Mechanical Design of In-Wheel Motor Driven Vehicles . In Magna Powertrain and Co KG, editors, *EAWD 11 European All-Wheel Drive Congress Graz* , April 2011 2011. Graz, Österreich.
- [RNW11b] A. E. Rojas Rojas, H. Niederkofler, and J. Willberger. Riding on in-wheel motors. *Automotive Engineering International*, 119(1):30–33,

- 2011.
- [Ros09] W. Rosinger. *Sollgrößengenerierung für Fahrdynamikregelsysteme*. PhD thesis, Institute of Automotive Engineering, Graz University of Technology, 2009.
- [RS40] P. Riekert and T. E. Schunck. Zur Fahrmechanik des gummibereiteten Kraftfahrzeugs. *Archive of Applied Mechanics*, 11(3):210–224, 6 January 1940.
- [RS86] J. Reimpell and P. Sponagel. *Fahrwerktechnik: Reifen und Räder*. Vogel-Buchverlag, Würzburg, 1986.
- [RSB01] J. Reimpell, H. Stoll, and J. Betzler. *The Automotive Chassis: Engineering Principles*. Butterworth Heinemann, Great Britain, 2001.
- [RW95] P. Redlich and H. Wallentowitz. Vehicle Dynamics with Adaptive or Semi-Active Suspension Systems Demands on Hardware and Software. *JSAE Review*, 16(2):218–223, 1995.
- [SBBH11] A. Schaub, J. Brembeck, D. Burschka, and G. Hirzinger. Robotisches Elektromobil mit kamerabasiertem Autonomieansatz. *Automobiltechnische Zeitschrift elektronik - ATZ*, 02:10–16, 2011.
- [SBJ07] A. J. C. Schmeitz, I. J. M. Besselink, and S. T. H. Jansen. TNO MF-SWIFT. *Vehicle System Dynamics*, 45(sup1):121–137, 2007.
- [SBRH11] T. Smetana, T. Bierman, M. Rohe, and W. Heinrich. E-Drive with Electrically Controlled Differential. *ATZautotechnology*, 11:52–57, October 2011.
- [Sch01] A. Schmeitz. An efficient dynamic ride and handling tyre model for arbitrary road unevennesses. In *VDI Berichte 1632*, 2001.
- [Sch03] R. Schneider. Grundlagen der Simulationstechnik. Lecture notes, Rheinisch-Westfälische Technische Hochschule Aachen, 2003.
- [Sch04] A. J. C. Schmeitz. *A semi-empirical three-dimensional model of the pneumatic tyre rolling over arbitrarily uneven road surfaces*. PhD thesis, Delft University of Technology, 2004.

-
- [She09] Shell Deutschland Oil GmbH. Shell PKW-Szenarien bis 2030 - Fakten, Trends und Handlungsoptionen für nachhaltige Auto-Mobilität. Scenario report, 2009.
- [Shi05] H. Shimizu. In-Wheel Motor for Electric Automobiles, 2005. Patent document number: US 6,942,049 B2.
- [SHK09] A. Schlecht, B. Heißing, and H. Krome. Entwicklung einer schwingungsunempfindlichen Vorderachskinematik mit Hilfe von Optimierungsmethoden. In *VDI Berichte 2086*, 2009.
- [Sim06] B. Simeon. Numerik gewöhnlicher Differentialgleichungen. Lecture notes, Department of Mathematics, Technical University Munich, 2006.
- [Sov09] B. K. Sovacool. Early Modes of Transport in the United States: Lessons for Modern Energy Policymakers. *Policy and Society*, 27(4):411–427, 3 2009.
- [Spr09] E. Spring. *Elektrische Maschinen: Eine Einführung*. Springer, 2009.
- [ss10] Cosin scientific software. Cosin road modeling: Documentation and User’s Guide. Technical report, 2010.
- [ST06] K. Strandemar and B. Thorvald. Ride diagram: A tool for analysis of vehicle suspension settings. *Vehicle System Dynamics*, 44(SUPPL. 1):913–920, 2006.
- [Sta87] British Standards. BS 6841:1987 - Guide to measurement and evaluation of human exposure to whole-body mechanical vibration and repeated shock. Standard, 1987.
- [STN06] Y. Suzuki, K. TASHIRO, and Y. Nakamura. In-wheel motor system, 2006. Patent document number: EP 1702784 A1.
- [Sto04] J. Stockmar. *Das große Buch der Allradtechnik*. Pietsch Verlag, 2004.
- [SUM06] K. Sawase, Y. Ushiroda, and T. Miura. Left-right torque vectoring technology as the core of super all wheel control (s-awc). *Mitsubishi Motors Technical Review*, 18:16–23, 2006.

- [SZ08] J. Schindler and W. Zittel. Zukunft der weltweiten Erdölversorgung. Technical report, Energy Watch Group, 2008.
- [TM4] TM4. TM4 Wheel Motor. Available at <http://www.tm4.com/en/home.aspx>. Accessed on 30.03. 2012.
- [TYSS06] E. Tabo, T. Yoshina, Y. Sekine, and R. Saito. Technology Status and Future of Clean-Energy Vehicles. Technical review, Mitsubishi Motors, 2006.
- [Uni07] European Union. M6 Richtlinie zur Angleichung der Rechtsvorschriften der Mitgliedstaaten über Maßnahmen gegen die Verunreinigung der Luft durch Emissionen von Kraftfahrzeugen., 2007.
- [USSS02] H. Urabe, Y. Sato, T. Shudo, and S. Shibuya. Suspension Characteristic Study using Genetic Algorithm. In *Proceedings of the International Symposium on Advanced Vehicle Control 2002 - AVEC'02*, September 2002.
- [vdBVvM⁺06] P. van den Bossche, F. Vergels, J. van Mierlo, J. Matheys, and W. van Autenboer. SUBAT: An assessment of sustainable battery technology. In Elsevier, editor, *Journal of Power Sources*, volume 162, pages 913–919, November 2006.
- [Vog88] K. Vogt. *Berechnung rotierender elektrischer Maschinen*. VEB Verlag Technik, Berlin, 1988.
- [Vol] Volvo. Volvo ReCharge Concept: Ground-breaking plug-in hybrid with a range of 100 km on battery power and with a combustion engine for back-up power. Available at <https://www.media.volvocars.com/global/enhanced/engb/Media/Preview.aspx?mediaid=16895>. Accessed on 30.03. 2012.
- [VS10] W. Verstedden and A. Schmeitz. OpenCRG: support in MF-Tyre and MF-Swift 6.1.2. In *Proceedings of the 1st OpenCRG workshop*, 2010.
- [Wal04] H. Wallentowitz. *Längsdynamik von Kraftfahrzeugen*. fka - Forschungsgesellschaft Kraftfahrwesen mbH Aachen, Aachen, 2004.

-
- [Wal06] H. Wallentowitz. *Vertikal- und Querdynamik von Kraftfahrzeugen*. fka - Forschungsgesellschaft Kraftfahrwesen mbH Aachen, Aachen - Germany, 2006.
- [WARN10] J. Willberger, M. Ackerl, A. E. Rojas, and H. Niederkofler. Motor Selection Criteria and Potentials of Electrified All Wheel Drive Concepts for Passenger Cars by Add-on Wheel Hub Motors on the Rear Axle. In *Proceedings of the SAE 2010 World Congress and Exhibition*, Detroit U.S.A., 2010.
- [WB06] M. Wiel and C. Bergelt. Untersuchungen zu entwicklungstechnischen Potenzialen hocheffizienter Antriebe. Kurzstudie, Sächsisches Landesamt für Umwelt und Geologie, 2006.
- [Wei08] C. Weinberger. Erhebung von verkehrs-, energie- und umweltrelevanten Fahrzeugdaten. Master's thesis, Institute of Automotive Engineering, Graz University of Technology, 2008.
- [WFO09] H. Wallentowitz, A. Freialdenhoven, and I. Olschewski. *Strategien zur Elektrifizierung des Antriebsstranges: Technologien, Märkte und Implikationen*. Vieweg + Teubner, 2009.
- [WH10] J. Willberger and M. Hirz. Energy Efficient Operation of In-wheel Motors for 4 Wheel Driven Passenger Cars. In *Proceedings of the FISITA World Automotive Congress*, Budapest, Hungary, 2010.
- [Wil07] J. Willberger. Design Principles for Simulating Flexible Bodies Focusing a Double Wishbone Suspension. Master's thesis, Institute of Automotive Engineering, Graz University of Technology, 2007.
- [Wil11] J. Willberger. *AC Motor Design for Passenger Cars - Design and Energy Efficient Control of In-Wheel Motors*. PhD thesis, Institute of Automotive Engineering, Graz University of Technology, 2011.
- [WJ02] M. Wright and B. Jaques. A Brief History of the Lunar Roving Vehicle. Technical report, Marshall Space Flight Center, 2002.
- [WRN09] J. Willberger, A. E. Rojas Rojas, and H. Niederkofler. Energy efficiency and potentials of electric motor types for wheel hub applications. In

Proceedings of the 9th International Conference on Engines and Vehicles, Capri, Italy, 2009.

- [ZBR97a] A. Zomotor, H. Braess, and R. Rönitz. Verfahren und Kriterien zur Bewertung des Fahrverhaltens von Personenkraftwagen Teil 1. *ATZ Automobiltechnische Zeitschrift*, 99:780–786, 1997.
- [ZBR97b] A. Zomotor, H. Braess, and R. Rönitz. Verfahren und Kriterien zur Bewertung des Fahrverhaltens von Personenkraftwagen Teil 2. *ATZ Automobiltechnische Zeitschrift*, 100:236–242, 1997.
- [Zet02] S. Zetterström. Electromechanical steering, suspension, drive and brake modules. In *56th Vehicular Technology Conference*, volume 56, pages 1856–1863, 24 September 2002 through 28 September 2002 2002. Vancouver, BC.

List of Figures

1.1. Electric tricycle presented by W. E. Ayrton and J. Perry in 1882 [Geo08].	1
1.2. Market share by technology at the turn from the 19 th to the 20 th century (see [Sov09]) and in the coming decades (see [She09] and [dB09]).	2
1.3. Oil production forecast worldwide (see [MC09] and [Kon09]).	3
1.4. Development and establishment of technologies on the way toward the vehicle electrification.	4
1.5. Electric powertrain architectures (rear wheel drive is shown exemplarily).	4
1.6. Lohner-Porsche ” <i>Semper Vivus</i> ”: Pure electric vehicle with two DC-in-wheel motors mounted on the front wheels.	7
1.7. Representative research and development projects in the field of electro-mechanical corner modules: (a) the <i>Advanced Dynamic Damper Motor</i> prototype of Bridgestone (see [MTI ⁺ 06] and [NIT08]), (b) the <i>Active Wheel</i> prototype of Michelin (see [BDD ⁺ 06], and [LSW00]), (c) the <i>eCorner</i> concept of Siemens VDO (see [Gom07] and [Gom10]), and (d) the <i>Autonomous Corner Module</i> concept of Volvo (see [Zet02] and [Jon07]).	8
2.1. Driver-vehicle-environment system (control loop).	14
2.2. Vehicle and wheel coordinate systems (based on the German standard [fN94]).	15
2.3. Schematic representation of the interaction between implemented vehicle, road and tire models.	26
2.4. Individual tire force vs. slip; approach according to TMsimple [Hir09b].	27
2.5. Interpolation of the combined tire forces in steady state [Hir09b].	28
2.6. Pneumatic trail n_{p_i}/l_{s_i} and self aligning torque ${}_W M_{T_i, z}$ as a function of the lateral slip sl_{y_i}	32
2.7. Schematic representation of the tire model for the vertical tire dynamics consisting of the location algorithm, the enveloping model and the single-mass oscillator model.	33

2.8. Triangulation method to determine whether a point is within a polygon or not.	34
2.9. Enveloping model: Two cams model (a) and movement of the W point (b).	36
2.10. Model of the tire vertical contact force ${}_W F_{T_i, z}$	40
2.11. Three-dimensional road with obstacles generated with the <i>Curved Regular Grid</i> approach of OpenCRG® and the simulation environment MOVES ²	41
2.12. Power spectral density of some common road types and approximation according to the international standard ISO 8608:1995(E) [fSI95] and to J. G. Parchilowskij (see [MW04]).	43
2.13. Rice method to reconstruct a road based on a given power spectral density.	44
2.14. Three-dimensional road model according to <i>J. F. Parkhilowskij</i> (see [Hir09a] and [Bau87]).	46
2.15. Characteristic deformation-force curve of the suspension spring according to the developed model.	49
2.16. Model of the shock absorber: characteristic speed-force curve divided in a region I of low and a region II of high deflection speeds (a) and behavior of the deviation Δd_{b_i} within the region I with respect to the value of the static damping coefficient $d_{b_i}^S$ (b).	52
2.17. Measurement system used for the model validation with the test vehicle (Opel Combo 1.6 CNG).	57
2.18. Comparison between simulation results and measured data obtained with the test vehicle for the steady state circular driving maneuver with a constant reference trajectory radius $R_t = 44$ m and increasing longitudinal speed ${}_V \dot{x}$: absolute position ${}_E y$ vs. ${}_E x$ of the center of gravity of the vehicle (a), longitudinal vehicle speed ${}_V \dot{x}$ (b), steering wheel angle δ_{st} (c), roll angle ϕ (d), difference sideslip angle $\Delta\beta$ (e), and yaw rate $\dot{\psi}$ (f). Figures (d), (e) and (f) are plotted against the lateral acceleration ${}_V \ddot{y}$ (see also [Dür11] and [Nie11]).	58
2.19. Comparison between simulation results and measured data obtained with the test vehicle for a dynamic maneuver: vehicle longitudinal speed ${}_V \dot{x}$ (a), steering wheel angle δ_{st} (b), sideslip angle β (c) and yaw rate $\dot{\psi}$ (d) over the time t (see also [Dür11] and [Nie11]).	59

2.20. Schematic representation of the test track consisting in a curb followed by a pothole with a height of ${}^E z_{road} = 27$ mm which was used to obtain the measured data taken as basis for the validation of the vertical dynamics behavior of the developed vehicle model (a), and corresponding road profile height ${}^E z_{road}$ (b).	60
2.21. Comparison between simulation results and measured data obtained with the test vehicle for driving over the synthetic road (figure 2.20) consisting in a curb followed by a pothole with a height of ${}^E z_{road} = 27$ mm: Suspended ${}^V \ddot{z}_A$ and non-suspended mass ${}^C \ddot{z}_C$ acceleration at the front left (a and c respectively - right subscript <i>fl</i>) and rear right (b and d respectively - right subscript <i>rr</i>) corners of the vehicle over the time t . Vehicle longitudinal speed ${}^V \dot{x} = 11.11$ m/s, wheel mass $m_{w_i} = 40$ kg, tire inflation pressure $p_{T_i} = 2.6$ bar and no additional load mass $m_{load} = 0$ kg (see also [Mar09]).	61
3.1. Quasi-stationary total longitudinal resistance force $F_{x_{resistance}}$ for a sub-compact electric vehicle with a single stage gearbox (see tables 3.3 and 3.5) as function of the longitudinal speed ${}^V \dot{x}$ while driving on a road with constant inclination ($\alpha_{road} = const.$) and with a longitudinal acceleration ${}^V \ddot{x} = 0.5$ m/s ²	65
3.2. Two different approaches toward the electrification of vehicles.	66
3.3. Aspects considered to describe the desired driving performance.	67
3.4. Considered driving cycles: ARTEMIS, HYZEM, INRETS, NEDC, FTP-75 and Japan-10-15.	69
3.5. Maximum longitudinal acceleration as function of the longitudinal speed for the different standardized (dotted and/or dashed lines) and non-standardized (continuous lines) driving cycles considered.	71
3.6. Flow diagram of the iterative process used to determine the characteristics of the needed battery for a certain driving cycle (battery mass as well as power and energy capacities).	74
3.7. Schematic steady state torque-speed curves for induction and synchronous motors in nominal and overload service.	76
3.8. Steady state four-quadrants operation of induction (IM) and synchronous motors (SM).	77
3.9. Active mass $m_{EM_{act}}$ of induction and synchronous motors as function of the nominal torque ⁿ M and the nominal power ⁿ P	78

3.10. Theoretical maximum recuperable kinetic energy while braking (steady state diagram).	79
3.11. Steady state traction force (a) and power (b) diagrams of a synchronous (SM) and an induction (IM) motor with an overspeed limited maximum speed on flat road. The theoretical maximum speed on flat road in nominal service is also indicated.	80
3.12. Steady state traction force (a) and power (b) diagrams illustrating the different electric motor - gearbox layouts: layout for maximum theoretical speed, electric motor overspeed limited layout, and underspeeding layout.	82
3.13. (a) Steady state traction force diagram and excess traction force, (b) steady state power defined climbing and acceleration ability.	84
3.14. Influence of the vehicle mass on the steady state power defined climbing and acceleration ability. The example is based on a synchronous motor. Vehicle mass definitions according to the Council Directive 92/21/EEC of 31 March 1992 of the European Union [Com92].	85
3.15. Flow diagram of the optimization process used to determine the torque and power characteristics of an electric motor.	87
3.16. Schematic representation of the considered powertrain architectures.	90
3.17. Cumulative frequency of the power while braking $P_{\dot{x}<0}$ for a compact vehicle (B) during the HYZEM driving cycle (most extreme case from those presented in table 3.7).	96
3.18. Steady state traction force diagrams for the different vehicles considered with two in-wheel motors.	99
3.19. Steady state operation points of the electric motors of a minicompact vehicle (A^-) with a rear-wheel drive powertrain architecture for different driving cycles.	101
4.1. Some assessment criteria and schematic representation of the step response of a considered state variable v to a step input of the steering angle δ_{st}	106
4.2. Some assessment criteria and schematic representation of the open-loop sinusoidal steering input of a considered state variable v	108
4.3. Some assessment criteria and schematic representation of the open-loop frequency response of a considered state variable v	109
4.4. Overview of the control concept implemented for the torque vectoring system with in-wheel motors [Nie11] (see also [RND11]).	111

4.5. Schematic representation of the *reference values generator* used to determine of the reference values $\hat{\mathbf{r}}$ based on steady state maps obtained with a reference vehicle model. 113

4.6. Structure of the horizontal dynamics controller. 113

4.7. Structure of the longitudinal dynamics controller. 114

4.8. Structure of the error controller for the lateral dynamics. 115

4.9. Diagram depicting the task of the optimal force allocation algorithm (small steering angles δ_{st} are assumed). Turn to the left is exemplarily shown. 118

4.10. Maximum available longitudinal tire force that can be transmitted. 122

4.11. Behavior of the horizontal tire forces during step steer maneuvers turning to the left at 100 km/h and different lateral accelerations $v\ddot{y}$ for the reference electric vehicle with a four-wheel drive powertrain architecture and no torque vectoring system (maximum steady state value of the lateral acceleration corresponds to approximately 7.4 m/s²). 124

4.12. Effect of the presented torque vectoring system (TVS) on the horizontal tire horizontal forces for the different powertrain configurations considered. The presented results correspond to a step steer maneuver turning to the left at 100 km/h and the maximum steady state value of the lateral acceleration for the reference vehicle of approximately 7.4 m/s². 125

4.13. Behavior of the sideslip angle β and the yaw rate $\dot{\psi}$ for the different powertrain configurations considered. The presented results correspond to a step steer maneuver turning to the left at 100 km/h and the maximum steady state value of the lateral acceleration for the reference vehicle of approximately 7.4 m/s². 126

4.14. Assessment variables for the step steer maneuver turning to the left at 100 km/h and approximately 50 % of the maximum steady state value of the lateral acceleration corresponding to approximately 7.4 m/s². 128

4.15. Assessment variables for the step steer maneuver turning to the left at different longitudinal speeds and approximately 50 % of the maximum steady state value of the lateral acceleration corresponding to approximately 7.4 m/s². 129

4.16. Assessment variables for the open-loop sinusoidal steering input maneuver at 100 km/h and maximum lateral acceleration corresponding to approximately 50 % of the maximum steady state value of approximately 7.4 m/s². 130

4.17. Assessment variables for the open-loop sinusoidal steering input maneuver at different longitudinal speeds and approximately 50 % of the maximum steady state value of the lateral acceleration corresponding to approximately 7.4 m/s ²	131
4.18. Bode plots of the yaw rate and the lateral acceleration for the reference electric vehicle with a four-wheel drive powertrain architecture and no torque vectoring system, and the electric vehicle with two in-wheel motors at the rear axle with the presented torque vectoring system. The vehicle speed correspond to 100 km/h and the maximum lateral acceleration to approximately 50 % of the maximum steady state value of approximately 7.4 m/s ²	132
4.19. Assessment variables for the open-loop frequency response change at different longitudinal speeds and approximately 50 % of the maximum steady state value of the lateral acceleration corresponding to approximately 7.4 m/s ² (values marked with * are not calculable since the reference value AC_{ref} of the considered assessment criterion is very small).	133
5.1. Some frequency weighting curves for different directions and application locations according to the International Standard 2631-1:1997(E) [fSI97]: W_k : On seat surface in vertical direction ${}_V z$, W_d : On seat surface in horizontal directions ${}_V x$ and ${}_V y$, W_c : On seat-back in horizontal direction ${}_V x$	137
5.2. Conflict diagram showing the trade-off between ride comfort and driving safety for a variation of the static suspension spring stiffness $c_{b_i}^S$ and the linear damping coefficient $d_{b_i}^S$ of the shock absorber while driving with constant longitudinal speed ${}_V \dot{x}$ on a road characterized by a certain power spectral density $\Phi(\omega)$. The ride comfort is evaluated based on the root mean square value of the frequency weighted vertical acceleration ${}_V \ddot{z}_A^{rms}$ of the suspended mass m_A , and the wheel load factor χ_{w_i} is used to evaluate the driving safety. The boundary lines for unmodified m_{w_i} and increased $m_{w_i} + \Delta m_{w_i}$ non-suspended masses are depicted.	140
5.3. Conflict diagram for different vehicle segments with and without increased non-suspended masses. Results obtained considering a street type C (see chapter 2.6.2) and a longitudinal vehicle speed of ${}_V \dot{x} = 40$ km/h.	144

5.4.	Results of the survey regarding the subjective ride comfort perception while driving over the deterministic road excitation signal presented in figure 2.20: variation of the additional non-suspended mass Δm_{w_i} and the longitudinal vehicle speed $v\dot{x}$ (a), variation of the additional load mass m_{load} (b), and variation of the tire inflation pressure p_{T_i} (c). The relative cumulative frequency $f_{cu}(grade)$ of the grade given by all drivers (<i>normal drivers</i> and <i>experienced test drivers</i>) is presented.	146
5.5.	Comparison between the subjective ride comfort perception of the <i>experienced test drivers</i> and the simulation results for different values of the longitudinal vehicle speed $v\dot{x}$. Reference configuration: test vehicle without increased non-suspended masses $m_{w_i} = 0$ kg, no additional load mass $m_{load} = 0$ kg and tire inflation pressure $p_{T_i} = 2.3$ bar.	147
5.6.	Comparison between the subjective ride comfort perception with an additional non-suspended mass of $\Delta m_{w_i} = 20$ kg at both wheels of the rear axle and with an increased tire inflation pressure of $p_{T_i} = 3.2$ bar. The relative cumulative frequency $f_{cu}(grade)$ of the grade given by the <i>normal drivers</i> and the <i>experienced test drivers</i> is presented.	149
5.7.	Comparison of the considered suspension systems to enhance the ride comfort and the driving safety (see also [Nie11] and [HEG11]).	150
5.8.	Schematic representation of the eccentric concept.	151
5.9.	Reduction of the additional non-suspended mass Δm_w for the eccentric concept.	152
5.10.	Damping mass concept: mechanism of the <i>Advanced Dynamic Damper Motor</i> - ADM - mechanism as presented by <i>Bridgestone</i> (see [STN06] and [MTI ⁺ 06]) (a), schematic representation with the motor mass m_{EM} being used as damping mass (b).	153
5.11.	Sky-hook control strategy for a variable shock absorber of a semi-active suspension system: schematic representation (a) and fundamental function [HEG11] (b).	155
5.12.	Force-speed diagrams for the traditional passive, semi-active and active (only the curve corresponding to the electric actuator is presented) shock absorbers [RNW10].	158

5.13. Performance comparison for the different suspension systems considered as a function of the longitudinal driving speed $v\dot{x}$ and for different additional non-suspended masses Δm_{w_i} while driving straight ahead over different excitation signals. Ride comfort change for sinusoidal harmonic excitation (a), ride comfort change for stochastic excitation road type C (b), ride comfort and driving safety change for deterministic excitation (see also [RNW10]).	159
5.14. Schematic representation of the driving maneuver and the road used to analyze the behavior of vehicles with in-wheel motors and torque vectoring system in driving safety relevant situations [RND11]. The variable s corresponds to the driven distance.	162
5.15. Schematic representation for determining the deviation from the reference trajectory.	164
5.16. Schematic representation for determining the yaw acceleration characteristic value.	165
5.17. Simulation results corresponding to the maneuver driving in a left curve over a sinusoidal perturbation with a wave length of $\lambda_{pert} = 22\sqrt{2}$ m (a) or $\lambda_{pert} = 2\sqrt{2}$ m (b). <i>TVS</i> stands for <i>Torque Vectoring System</i> . The wheel load factor is determined at the curve inner wheel, i.e. the rear left one (right subscript <i>rl</i>).	170
6.1. Flow diagram of the synthesis process of the presented Suspension Kinematics Optimization System - KOS. To optimize the kinematics of suspensions without in-wheel motor, the simplified geometries (*) are not integrated in the CAD-model.	179
6.2. Simplified CAD-model of the suspension system in which the in-wheel motor is to be integrated. The CAD-model of a double wishbone suspension system is exemplarily presented in this figure.	179
6.3. Introduction of the simplified geometries corresponding to the electric motor and the possible needed gearbox in the simplified CAD-model (a). Definition of the variation space for each hardpoint belonging to the suspension system to be modified (b). The CAD-model of a double wishbone suspension system is exemplarily presented in this figure. . . .	180
6.4. Flow diagram of the optimization process using the Nelder-Mead simplex algorithm.	182
6.5. Flow diagram of the optimization process using genetic algorithms. . . .	183

6.6.	Graphical explanation of the fitting function used by the implemented optimization algorithms.	184
6.7.	In-wheel motor prototype with induction motor and gearbox for a vehicle belonging to the minicompact class A^- (see chapter 3.7 for the requirements and the characteristics of the electric motor and [Wil11] for its detailed electrical design).	185
6.8.	Original control blade suspension system for the rear axle of the Ford Focus from 1999 [HEG11] (a). CAD-model of the control blade suspension system for the rear axle of passenger vehicles with in-wheel motors obtained with the approach presented in this work (b). A 16" rim is used.	186
6.9.	Comparison of some suspension characteristic parameters for the presented control blade suspension system with in-wheel motors for rear axles: camber angle (a) and toe angle (b) as well as the roll center height (c) and transversal position (d) for a nonparallel vertical wheel movement.	187
6.10.	CAD-model of the double wishbone suspension system for the rear axle of passenger vehicles with in-wheel motors obtained with the approach presented in this work. A 16" rim is used.	188
6.11.	Comparison of some suspension characteristic parameters for the presented double wishbone suspension system with in-wheel motors for rear axles: camber angle (a) and toe angle (b) as well as the roll center height (c) and transversal position (d) for a nonparallel vertical wheel movement.	189
6.12.	Schematic representation of the suspension kinematics optimization process of a double wishbone suspension system using genetic algorithms (a). Evolution of the fitness function value (b).	190
A.1.	Relative cumulative frequency.	199
B.1.	Tire vertical stiffness coefficients (see chapter 2.5.2): (a) Speed coefficient $C_{T\omega}$ vs. tire rotational speed ${}_C\omega_{w_i, y}$ as well as (b) statical $c_{T_i, z}^S$ and (c) dynamical $c_{T_i, z}^D$ tire stiffness coefficients vs. tire inflation pressure p_{T_i}	204
B.2.	Behavior of the tire vertical force ${}_W F_{T_i}$ as a function of the effective tire vertical deflection ρ_{z_i} , the tire rotational speed ${}_C\omega_{w_i, y}$ (a) and the tire inflation pressure p_{T_i} (b).	205
B.3.	Suspension spring (a) and shock absorber (b) characteristic curves for the front and rear axle of the test vehicle.	205
C.1.	Model of the longitudinal vehicle dynamics [Hir09a].	207

C.2. Energy storage classification [Hof09].	214
C.3. Ragone chart: Energy-to-mass and Power-to-mass ratios for different energy storage and converter technologies (see e.g. [WFO09], [Hof09], [Bit09], [vdBVvM ⁺ 06] and [CC00]).	215
C.4. Classification of electric motors [Hof09].	217
C.5. Comparison of the design of induction (with wound rotor) and synchronous motors [Hof09].	217
C.6. Circuit diagram of a three phase induction motor [Ise02].	219
C.7. Circuit diagram of a three phase induction motor [Ise02] with wound stator (a) and with buried permanent magnets (b).	221
C.8. Schematic steady state efficiency characteristic diagrams of induction (a) and synchronous (b) motors [Wil11].	223
C.9. Schematic steady state efficiency characteristic diagrams of induction (a) and synchronous (b) motors with variable flux control [Wil11].	224
C.10. Comparison between the steady state traction force diagrams of a vehicle with internal combustion engine - ICE - (see also [HW09]) and a vehicle with electric motor(s). The curve of a synchronous motor (SM) in overload service is shown exemplarily. For the ICE, only the maximum torque for all gears is presented. Both the ICE and the electric motor presented lead to similar driving performances (e.g. same maximum longitudinal speed on flat road.).	225
C.11. Electric energy conversion (see [WFO09] and [Hof09]).	226
C.12. Operational characteristic curves of an induction motor in steady state for different frequencies of the rotatory field f_{rmf}	227
C.13. Steady state traction force diagrams for the vehicles with four in-wheel motors.	230
D.1. Simplified single track vehicle model.	231
E.1. Simplified quarter vehicle model.	237
E.2. Modular device to simulate increased non-suspended masses Δm_{w_i} : Components (a), rim and device configuration corresponding to an additional non-suspended mass of $\Delta m_{w_i} = 25$ kg (b), picture of the test drives carried out with an additional non-suspended mass of $\Delta m_{w_i} = 30$ kg at the rear axle while driving on the deterministic signal presented in figure 2.20 consisting in a curb followed by a pothole with a height of ${}^E z_{road} = 27$ mm.	240

E.3. Questionnaire used to collect the subjective ride comfort perceptions of *normal drivers* and *experienced test drivers* while driving with additional non-suspended masses Δm_{w_i} 241

F.1. Wheel center axis system ${}_C O$ (see chapter 2.2) and schematic representation of the hardpoints belonging to the control blade suspension system. 244

F.2. Wheel center axis system ${}_C O$ (see chapter 2.2) and schematic representation of the hardpoints belonging to the double wishbone suspension system. 244

List of Tables

- 1.1. Advantages and open questions related with in-wheel motors in comparison with a traditional powertrain architecture with internal combustion engine. 5
- 1.2. Recent concepts and research activities in the field of in-wheel motors for automotive applications in **Asia** and **North America**. 11
- 1.3. Recent concepts and research activities in the field of in-wheel motors for automotive applications in **Europe**. 12

- 3.1. Characteristic kinematic parameters of the considered driving cycles. . . 70
- 3.2. Average power demand of auxiliaries for an electric vehicle [WFO09]. . . 88
- 3.3. Assumed parameters of the considered vehicle classes. 89
- 3.4. General properties of the electric powertrain components. 91
- 3.5. Driving performance requirements. 93
- 3.6. Additional battery mass $\Delta m_{Batt_{Aux}}$ needed to cover the energy demand of electric auxiliaries for an electric vehicle belonging to the vehicle classes minicompact to compact in the different driving cycles. 94
- 3.7. Energy and power demands as well as the needed battery mass for the different considered driving cycles. Highlighted background cells correspond to the dominant factor in the considered driving cycle. 95
- 3.8. Battery mass m_{Batt} needed for the considered vehicles in order to fulfill the driving range specified in table 3.5 (see battery properties in table 3.4). 96
- 3.9. Transmission ratio of the gearbox used between the electric in-wheel motors and the wheel hub for the different vehicles considered. 96
- 3.10. Weighting factors used to determine the power and torque characteristics of the electric motor(s). 97
- 3.11. Electric motor characteristics for vehicles with two and four in-wheel motors. 98

3.12. Comparison of the weight of a vehicle with internal combustion engine (ICE) and an electric vehicle (EV) with a rear-wheel drive powertrain architecture for the different vehicle classes considered.	102
4.1. Assessment criteria related with the maneuver step steer [Ros09].	107
4.2. Assessment criteria related with the maneuver open-loop sinusoidal steering input [Ros09].	108
4.3. Assessment criteria related with the maneuver open-loop frequency response [Ros09].	110
5.1. Considered vehicle segments for the analysis of the influence of increased non-suspended masses on ride comfort and driving safety.	143
5.2. Test drive conditions used to determine the influence of increased non-suspended m_{w_i} masses on the subjective ride comfort perception.	145
5.3. Simulation conditions used to analyze the influence of increased non-suspended masses on the lateral dynamics of vehicles with in-wheel motors and torque vectoring.	163
6.1. Suspension parameters that can be used for the synthesis of suspension systems in the presented approach.	178
6.2. Dimensions of the considered simplified geometries for the considered induction motor and the gearbox. The dimensions of the electric motor as well as other aspects related with the detailed electric design can be found in [Wil11] (see also [Apo10]).	186
B.1. Vehicle model parameters.	202
B.2. Tire model parameters.	203
B.3. Parameters to reconstruct a road with certain roughness given a specific power spectral density Φ_{road}	204
B.4. Passive suspension system parameters.	206
C.1. Advantages and disadvantages of synchronous and induction motors [Wil11]	222
C.2. Weight of different electric vehicles (EV) in comparison with their counterparts with internal combustion engine (ICE).	229
E.1. Coefficients of the frequency filter W_k used to weight the vertical acceleration according to the International Standard 2631-1 [fSI97].	236

F.1. Position of the hardpoints corresponding to the control blade suspension system (see [Apo10]). Positions are measured in the wheel center axis system ${}_C O$ (see chapter 2.2).	243
F.2. Position of the hardpoints corresponding to the double wishbone suspension system (see [Apo10]). Positions are measured in the wheel center axis system ${}_C O$ (see chapter 2.2).	245